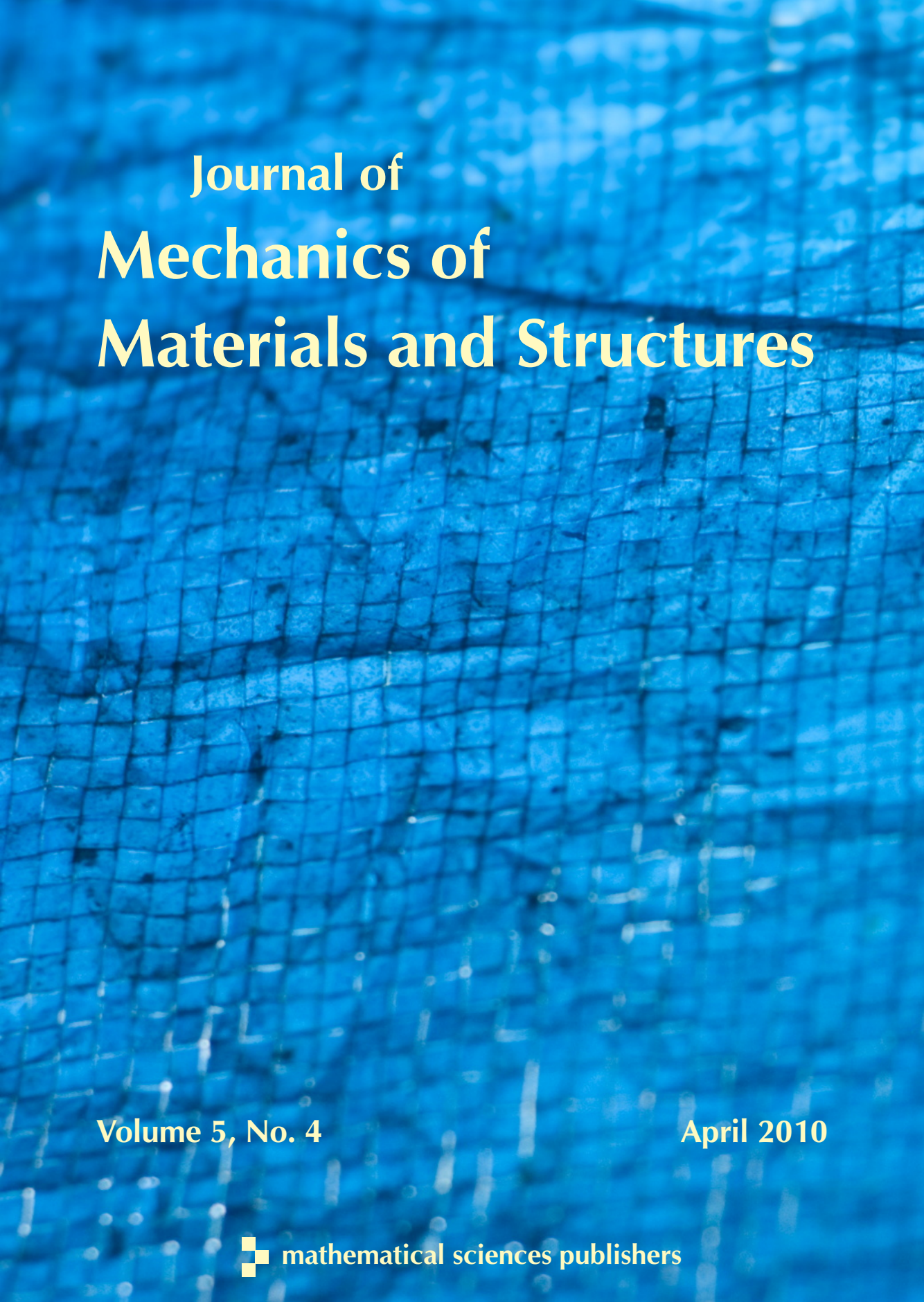

Volume 5, No. 4 April 2010

mathematical sciences publishers

JOURNAL OF MECHANICS OF MATERIALS AND STRUCTURES

http://www.jomms.org

Founded by Charles R. Steele and Marie-Louise Steele

Cover design: Alex Scorpan

Cover photo: Mando Gomez, www.mandolux.com

See inside back cover or http://www.jomms.org for submission guidelines.

JoMMS (ISSN 1559-3959) is published in 10 issues a year. The subscription price for 2010 is US $500/year for the electronic version, and $660/year (+$60 shipping outside the US) for print and electronic. Subscriptions, requests for back issues, and changes of address should be sent to Mathematical Sciences Publishers, Department of Mathematics, University of California, Berkeley, CA 94720–3840.

JoMMS peer-review and production is managed by EditFLOW™ from Mathematical Sciences Publishers.

PUBLISHED BY

mathematical sciences publishers

http://www.mathscipub.org

A NON-PROFIT CORPORATION

Typeset in LaTeX

JOURNAL OF MECHANICS OF MATERIALS AND STRUCTURES
Vol. 5, No. 4, 2010

MECHANICAL BEHAVIOR OF SILICA NANOPARTICLE-IMPREGNATED KEVLAR FABRICS

ZHAOXU DONG, JAMES M. MANIMALA AND C. T. SUN

This study presents the development of a constitutive model for in-plane mechanical behavior of five styles of plain woven Kevlar fabrics impregnated with silica nanoparticles. The neat fabrics differed in fiber type, yarn count, denier, weave tightness and strength, and varying proportions (4, 8, 16 and 24% by weight) of nanoparticles were added to enhance the mechanical properties of the fabric. It was found that fabrics impregnated with nanoparticles exhibit significant improvement in shear stiffness and a slight increase in tensile stiffness along the yarn directions over their neat counterparts. A constitutive model was developed to characterize the nonlinear anisotropic properties of nanoparticle-impregnated fabrics undergoing large shear deformation. The parameters for the model were determined based on uniaxial (along yarn directions) and 45° off-axis tension tests. This model was incorporated in the commercial FEA software ABAQUS through a user-defined material subroutine to simulate various load cases.

1. Introduction

Kevlar® fiber is a high modulus, high strength and low density para-aramid synthetic fiber. In comparison to high strength steel, Kevlar has much better strength to weight ratio. It is a good candidate for use as a soft body protection material. The fibers are tightly woven into fabrics and multiple layers of fabrics are used in many soft body armors. The primary goal of soft armor design is to reduce the weight while maintaining the protection level. Hence, weight and performance are the two major criteria that must be balanced in selecting soft body armors.

The mechanical behavior of Kevlar fabrics under uniaxial tensile loading has been extensively studied previously. Raftenberg and Mulkern [2002] performed uniaxial tension tests on Kevlar KM2 yarn and fabric to obtain stress versus displacement curves. They also obtained bilinear, exponential and quartic least square error fits to the data. The shear response of E-glass fabrics of various weave styles was studied in [Mohammed et al. 2000] using picture frame tests. The locking angle was determined for each type of weave. A material model based on the theory of elasticity including the effect of fiber inextensibility was applied to analyze the experimental data and a microstructural analysis was done to predict the shear locking angle. Peng et al. [2004] address the issue of comparing fabric shear test data obtained from different testing methods. It was found that the normalization method to be employed depended on the experimental configuration of the test. Lomov et al. [2006] investigated the factors affecting the validity of data obtained from picture frame tests on glass/PP woven fabrics. They also report that yarn pretension caused difference in the shear resistance measured for the fabric. Controlling the pretension

Keywords: Kevlar fabric, soft armor, nanoparticle, constitutive model.

in the yarn during sample preparation and standardizing testing procedures were recommended to obtain more accurate shear response using the picture frame test. Further, we cite [Harrison et al. 2004; Lebrun et al. 2003; Milani et al. 2010] as comparative studies on the evaluation of the in-plane shear behavior of fabrics using the bias extension and the picture frame tests.

Researchers have been continuously looking for ways to lighten body armors without compromising on performance. One way is to create stronger and lighter fibers by producing new materials and processes. Another method is to tailor the structure and composition of existing fabrics to achieve better performance. Lee et al. [2003] reported a significant enhancement in ballistic performance of Kevlar woven fabrics when impregnated with a shear thickening fluid (STF). The STF used was a colloid of ethylene glycol and highly concentrated silica nanoparticles. The viscosity of the STF increases significantly above a critical shear rate. This novel STF-fabric material offers good ballistic resistance and flexibility. However, the enhancement mechanisms and the exact role of STF in strengthening the fabric are still not well understood. In [Decker et al. 2007; Kalman et al. 2009] it was demonstrated that STF Kevlar fabrics offered better stab resistance properties than neat Kevlar by restricting the yarn mobility. Tan et al. [2005] impregnated Twaron® fabrics with a water based silica colloid. Improvement in ballistic resistance was observed, and they attributed it to the increase in projectile-fabric and interyarn friction.

Many different approaches like simplified orthogonal pin-jointed bars to model yarns, unit cell based models, equivalent homogenized continuum models and detailed three-dimensional models incorporating individual yarns and weave patterns with contact definitions have been used to analyze and model woven fabric material behavior. King et al. [2005] developed a continuum constitutive model for woven fabrics in which the fabric yarn structural configuration is related to the macroscopic deformation through an energy minimization method. Lin et al. [2009] developed a finite element model to predict the shear force versus shear angle response of a plain woven fabric. The fabric was modeled at the yarn scale by assuming yarn behavior to be that of a three-dimensional orthotropic solid. In [Grujicic et al. 2009], a meso-scale (yarn level) unit cell was developed and its properties were used to model plain woven Kevlar 129 fabric as a continuum surface via a user-defined material subroutine in ABAQUS. The properties of the unit cell were obtained from contact forces and shear response of a solid FEM model of cross yarns in a single unit cell.

In the present study, dry silica nanoparticles were used to reinforce Kevlar fabrics. Unlike the STF-fabric material, these nanoparticle-fabric composites do not contain any fluid and thus minimizes the weight added to neat fabrics. Uniaxial and 45° off-axis tension tests were done to evaluate the in-plane mechanical properties of the fabrics using an MTS servo-hydraulic load frame. It was found that the nanoparticles significantly increased the in-plane shear stiffness, while only slightly influenced the tension behavior along yarn directions. All the tested fabrics exhibited highly nonlinear behavior in shear deformation and large relative rotations between cross yarns. A constitutive model was developed using a method similar to the classical laminated plate theory in conjunction with the incremental deformation approach to characterize the nonlinear anisotropic properties of nanoparticle-impregnated fabrics undergoing large deformation. This model was incorporated in the commercial FEA software ABAQUS via a user-defined material (UMAT) subroutine to simulate the mechanical response of Kevlar fabrics. Validation of the model was done by comparing the numerical results to experimental load displacement curves for a 30° off-axis tension test and static indentation tests. The simulations agree well with the experimental results until the onset of failure.

Fabric style	K310	K706	K720	K745	K779
Fiber type	Comfort	KM-2	129	29	159
Fiber modulus (GPa)	87.0	80.0	99.7	73.0	97.2
Yarn size (denier)	400	600	1420	3000	200
Weight (g/m^2)	122	180	258	475	132
Warp count (yarns/in)	35.5	34	20	17	70
Weft count (yarns/in)	35.5	34	20	17	70
Warp strength (lbs/in)	530	775	978	1600	385
Weft strength (lbs/in)	530	880	992	1800	530
Thickness (mm)	0.18	0.23	0.36	0.61	0.18

Table 1. Manufacturer's product data of five styles of plain woven Kevlar fabrics.

2. Experimental methods

2.1. ***Material preparation.*** Five styles of Kevlar fabrics from Hexcel® were studied. The fabric specifications given by the manufacturer are listed in Table 1. These fabrics differ in fiber type, yarn size, yarn count, weave tightness, thickness, strength and weight. All the styles were, however, plain woven fabrics. Figure 1 shows the weave texture of these fabrics. K779 style has a fine, tight weave; K310 and K706 have medium weaves; K720 and K745 are thick and heavy styles with coarse and loose yarns. The fabric properties are sensitive to ultraviolet radiation and moisture absorption. Hence the fabric rolls were stored in a closed dry container and the samples were oven dried to remove ambient moisture prior to testing.

Plain woven fabrics have two orthogonal yarn directions — warp and weft — in the undeformed configuration (Figure 2a). Although the fabric is balanced and has the same yarn count in the warp and weft directions, their strengths are different. It is therefore necessary to identify them. If the selvage is still on the fabric, the yarns that are parallel to the selvage are the warp yarns. Alternatively, the warp and weft yarns can be distinguished by their waviness. Due to the weaving process, the warp yarns have more waviness than the weft yarn. Figure 2b shows an extracted warp and weft yarn from K720 style fabric.

A water-based silica nanoparticle colloid (Snowtex® ST-ZL) marketed by Nissan Chemical was used to impregnate nanoparticles into the fabric. According to the manufacturer's specifications, the silica

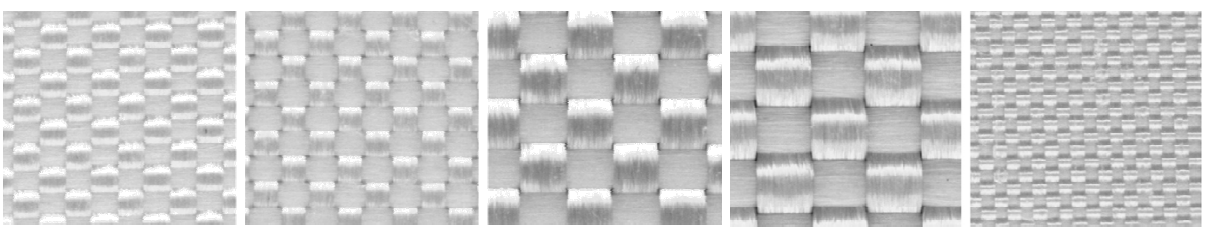

Figure 1. Optical images of five styles of plain woven Kevlar fabrics. (Each image corresponds to 6.4 × 6.4 mm. The fabrics are bright yellow; the images were postprocessed to black and white to enhance the contrast.)

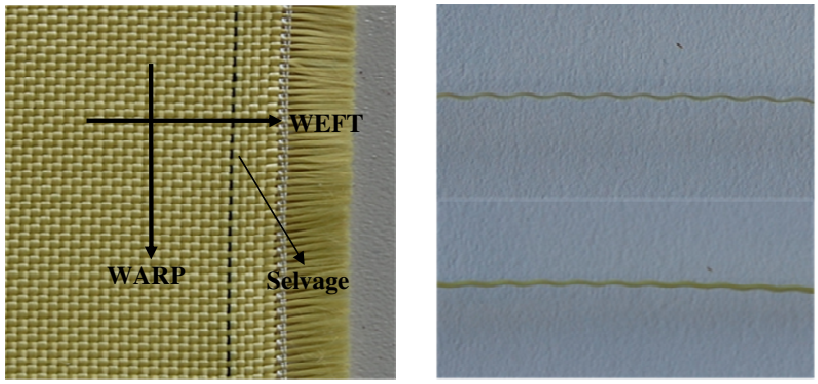

(a) Selvage on K720 (b) Warp (above) and weft yarns (K720)

Figure 2. Identifying warp and weft yarns in the fabric: warp yarns are wavier than weft yarns.

particle size was 70∼100 nm and the particle concentration was 40∼41% by weight. To impregnate the silica nanoparticles into the fabric, a square piece of fabric of dimensions 150 × 150 mm was cut from the bulk fabric roll. The weight of the fabric was measured and recorded using an OHAUS® analytical balance. It was then soaked into the silica colloid and the percentage by weight of the solution added to the fabric was controlled. The soaked piece was oven dried at 80° C for 30 minutes to remove the water leaving silica nanoparticles adhered to the fabric. The final nanoparticle weight additions to the neat fabrics are controlled to be 4, 8, 16 and 24%. The resulting nanoparticle impregnated fabric remained quite flexible albeit not as much as the neat fabric. Figure 3 shows the scanning electron micrograph (SEM) of K706 with 24 wt% of silica nanoparticles. Samples were imaged with an FEI Nova NanoSEM field emission scanning electron microscope. The image was obtained using back-scatter detector in low vacuum mode. The image reveals that silica nanoparticles did not form a uniform coating on the fabric surface but accumulated in the space between fibers. Abrading the surface of the treated fabric dislodges only the particles adhering to the surface but the particles in the interfiber spaces remain undisturbed.

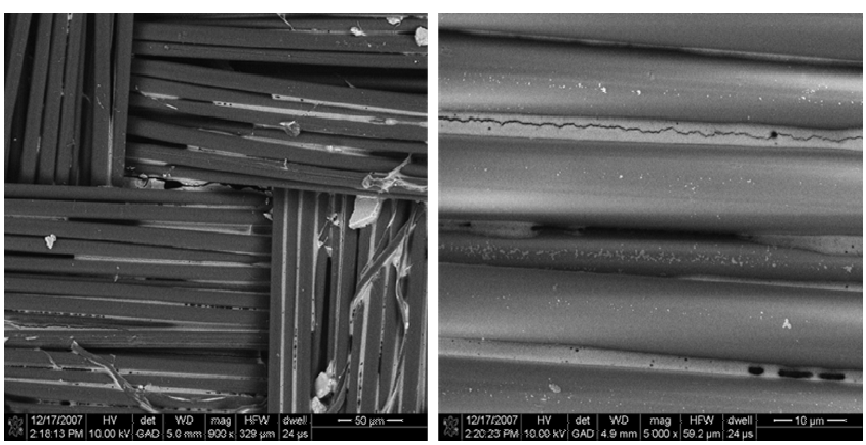

Figure 3. SEM image of K706 fabric with 24 wt% silica nanoparticles.

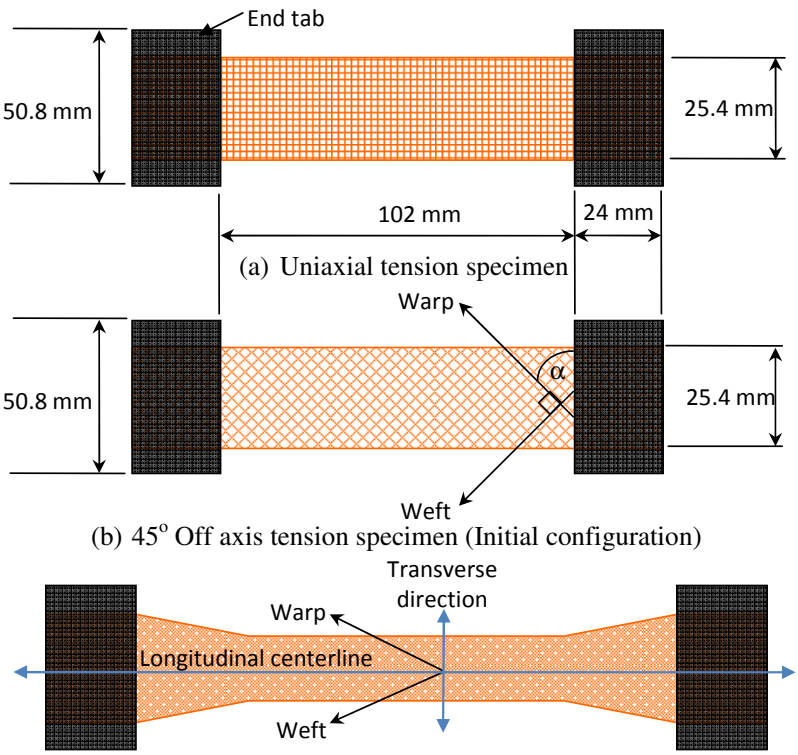

Figure 4. Diagram of tension test specimen.

2.2. ***Uniaxial tension tests.*** To evaluate the yarn direction stiffness of the fabrics, quasistatic uniaxial tension tests were performed on the neat and nanoparticle impregnated fabrics. The fabrics (single layer) with different wt% additions of nanoparticles were tested in both the warp and the weft directions. To prepare the specimens for the test, the neat and treated fabrics were cut into a rectangular piece of 25.4 mm in width and 150 mm in length along the yarn directions. Hard end tabs were bonded using epoxy adhesive to both ends leaving a gauge length of 102 mm between the tabs. Figure 4a shows the dimensions of the final specimen. A 100 KN MTS load frame was used in this test. The crosshead speed was set to 0.1 mm/second. The specimen was aligned and gripped using hydraulic grips during the test. No slippage at the grips was noticed during testing.

2.3. ***Off-axis tension tests.*** Picture frame tests are widely used to evaluate the in-plane shear properties of woven fabrics [Mohammed et al. 2000; Peng et al. 2004; Lomov et al. 2006]. The stress field in the picture frame is usually assumed to be uniform. When shear deformation is small, the fabric does not wrinkle and the uniform stress assumption is reasonable. However, the fabric wrinkles under large shear deformations. This results in nonuniform stress distributions and the accuracy of the test result is not guaranteed.

In view of the foregoing, we employed a 45° off-axis tension (bias extension) test to determine the fabric shear property. The specimen size was the same as that used in the uniaxial tension tests. Parts b and c of Figure 4 show the initial and deformed configurations. The yarn orientation angle α is the

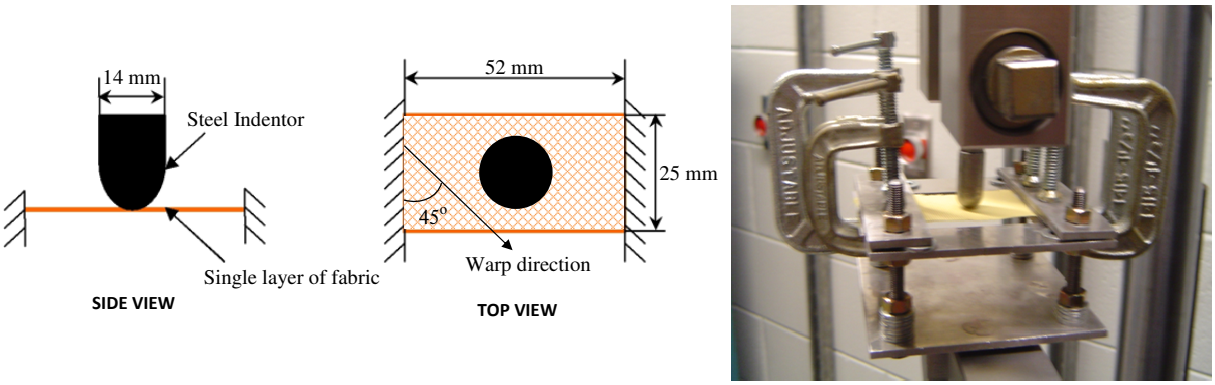

Figure 5. Left: schematic diagram of static indentation test. Right: indentation test on neat K706.

acute angle made by the warp direction yarn with the short (25 mm) edge of the specimen, as shown in Figure 4b. The specimens were cut in such a way that this angle was 45° in the undeformed state. As the warp and weft directions in the fabric are orthogonal to each other initially, this test has a symmetric configuration with respect to both yarn directions. The specimens were tabbed and tested with same experimental setup as the uniaxial tension tests. No slippage at the grips was noticed during testing.

The uniaxial and the 45° off-axis tension tests are used to obtain the material parameters for the constitutive model. In order to validate the model, one of the load cases used was a 30° off-axis tension test. The test was done using K706 fabric style with the same specimen dimensions and test conditions as for the 45° off-axis tension tests.

2.4. ***Indentation test.*** Under a transverse ballistic impact, the major mode of deformation in Kevlar fabrics is the out-of-plane displacement. Static indentation tests display certain correlations especially with regard to deformed profile, yarn pull-out behavior and indentor-yarn diameter size effects to the behavior of the fabric during ballistic impact. However, in ballistic tests, dynamic phenomena such as strain rate dependence and wave propagation effects become evident. To evaluate the accuracy of the proposed constitutive model, a static indentation test was done. The indentation test setup and specimen dimensions are schematically shown in Figure 5, left. A single layer of K706 Kevlar fabric with a yarn orientation angle of 45° was wrapped and clamped without slack between the grips of the test fixture such that two opposite edges are fixed and the other two edges are free. A hemispherical indentor of diameter 14 mm was pushed against the fabric at a crosshead speed of 0.1 mm/second using an MTS load frame and the load versus displacement response was recorded. No slippage at the gripped edges was noticed until onset of failure. Figure 5, right, shows an indentation test in progress.

3. Experimental results

3.1. ***Uniaxial tension tests.*** The uniaxial tension tests for the fabrics show two distinct regimes in the load displacement plots. In the initial loading phase the fabric has a linear behavior with low modulus. The axial strain occurs during this phase primarily because of the uncrimping of the axial yarns in the woven fabric. In the absence of any applied transverse tension, the actual phenomenon is one of crimp interchange whereby the axial yarns get straightened while the transverse yarns take up additional crimp.

However, once the axial yarns become uncrimped, the transverse yarns remain in position and no pullout is noticed. In the later loading phase the axial yarns undergo elongation with a relatively higher modulus. The yarn elongation response is also linear until the fabric fails by the breakage of axial yarns. The failure location depends on the location of any local defects but occurs at a definite load and is obtained consistently in repeated tests. The uniaxial response is thus markedly bilinear. The results show that, in general, the weft yarns are stronger than the warp yarns and also display a stiffer response. The addition of nanoparticles to the fabrics seems to increase the uniaxial strength and stiffness only slightly as evidenced by the plots presented in Figure 6. Nonetheless, we make a few observations of interest.

Firstly, as the deformation progresses, it is noticed that the width of the specimen remains more or less unchanged. Unlike a homogenous solid, the deformation in fabrics is largely governed by interaction between yarns at the cross over points in the weave. But once the crimp interchange process is complete after the initial loading phase, no transverse yarn pull out is noticed, which indicates that the width of the specimen (distance between outer most axial yarns) remains the same as the initial width of the specimen. This was noted to be the case for all the specimens tested and thus an assumption of negligible lateral contraction is made for the fabric loaded in uniaxial tension.

As the crimp interchange process reduces the yarn waviness in the axial direction while increasing it in the transverse direction, the variation of the overall thickness of the fabric is very small. Variability in the load sensed by individual axial yarns is reduced by ensuring high precision in the specimen fabrication process and alignment and gripping procedure for the test. However one of the factors affecting the scatter in the failure location (apart from any local defects) may be the slight difference in pretension induced due to errors in the aforesaid procedures. Owing to the existence of these conditions in the fabric during the uniaxial tension test, it is reasonable to assume a state of uniform axial stress and strain field. Hence, engineering stress versus strain can be reported using the initial specimen dimensions, which are presented in Figure 6. The thickness of woven fabrics is measured using ASTM D1777-96 standard. The thickness values as quoted by the manufacturer (Table 1) are used to calculate the fabric cross sectional area. The warp and weft fabric strengths as obtained from the tests (Table 2) differ from the manufacturer supplied values given in Table 1. The average difference between measured and supplied value is about 16%. As the manufacturer's test procedure is not supplied with the material data sheet, the variation in the measured strength values is attributed to difference in test methods and conditions. The axial mechanical properties of the fabric are obtained from the test results using a bilinear curve fit. The strength values assume significance only in the context of failure prediction which is not dealt with in the present study.

Secondly, a comparison of the load displacement curves for various styles of fabrics shows a slight departure from the typical trend for certain styles. In general it is noted that the weft direction has lower strains to complete uncrimping, higher moduli in both load regimes and greater strength. This is explained by the fact that the weft yarns are much less wavy than warp yarns and as a consequence

Fabric style	K310	K706	K720	K745	K779
Weight (g/m^2)	127	178	254	435	127
Warp strength (lbs/in)	630	760	1220	1770	390
Weft strength (lbs/in)	730	970	1290	1910	670

Table 2. Neat fabric weights and strengths measured in this study.

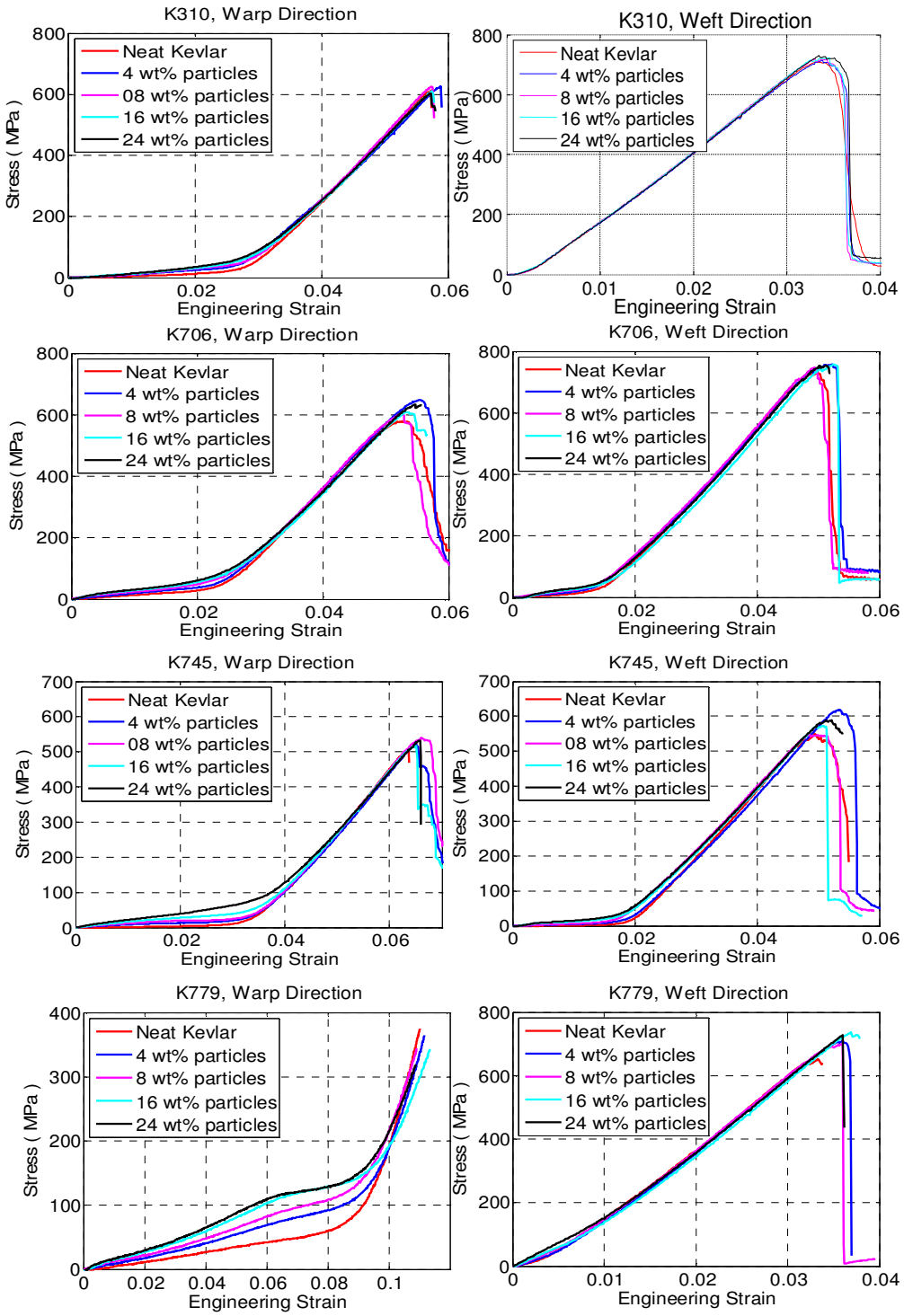

Figure 6. Engineering stress versus strain curves from uniaxial tension tests for five styles of Kevlar fabrics with different wt% of nanoparticle addition.

are fully uncrimped at lower strain values. The bilinear transition strain for most neat and treated fabric styles is between 0.01 and 0.03. However, K310 and K779 styles are exceptions. Among the five styles of fabric tested, K779 and K310 have the finest and the second finest weave respectively. Both these fabrics are tightly woven with very close yarn spacing. The steep rise in the weft direction load displacement curves for K310 and K779 is due to their fine weave which causes the yarn to become fully uncrimped at very low strains. This is less evident in the warp direction because of its relatively higher waviness.

The mechanism by which the addition of nanoparticles increases the stiffness of the fabric is conjectured to be due to increase in the friction between the yarns. As the nanoparticles are embedded in the interyarn and interfiber spaces, they restrict the relative yarn mobility. This effect becomes more pronounced in the case of fine weave fabrics in comparison to coarse weave as the nanoparticles are lodged in very small gaps between the tightly woven yarns. In the case of the warp direction response for K779, because of the high waviness and fine weave, the initial resistance to applied strain is due to a combination of elongation of the yarns and uncrimping as the nanoparticles lock the yarns in place relative to each other. Once the frictional resistance due to the nanoparticles is overcome a short plateau phase is observed when the uncrimping process is completed and thereafter the yarns undergo axial elongation alone until failure. This could be the reason for the high dependence of the initial load displacement response of weft direction K779 fabric on the percentage weight addition of nanoparticles.

3.2. ***Off-axis tension tests.*** The mechanical behavior exhibited by neat and treated fabrics in a 45° off-axis tension test offer numerous insights. The load displacement curves are highly nonlinear and the addition of nanoparticles to the fabric causes a significant increase in its shear rigidity and failure strength. Figure 7 presents the load versus displacement plots for five styles of Kevlar fabrics with different wt% additions of nanoparticles.

In an off-axis tension test, the deformation of the fabric is dependent on the specimen dimensions, yarn orientation angle, yarn count in warp and weft directions and the nanoparticle loading of the fabric. For balanced plain woven Kevlar fabrics with the same yarn count in warp and weft directions, a 45° off-axis tension (bias extension) test produces a deformation that is symmetric about the longitudinal center line of the specimen (Figure 4c). Distinct shear regions are observed in the specimen during deformation [Harrison et al. 2004; Lebrun et al. 2003]. The central region *C*, as shown in Figure 8 (page 539) has a pure shear deformation as the yarns experience only rotations relative to each other, while the region A remains undeformed and region B has a shear angle half that in region C. Due to the rotation of the yarns, region *C* displays large transverse contraction. The length of region *C* depends on the specimen dimensions and yarn count of the fabric. The load displacement curves show a steep rise after a critical value of displacement is reached in each case. This occurs because as the yarn rotations progress, a limiting angle is reached when adjacent yarns become compactly packed without any interyarn spacing. This angle is referred to as the locking angle for fabrics. After the locking angle is reached the shear rigidity of the fabric is driven by the compression of individual yarns in the transverse direction which causes a greater load to be sensed per unit displacement. In the postlocking deformation, out-of-plane wrinkling of the fabrics occur. Failure initiation occurs thereafter by the slipping of the yarns at the interface between shear regions C and B. Unlike the uniaxial tension test, the failure does not occur at a well defined load but progresses gradually as weft and warp yarns slip over each other at cross over points. The oscillatory behavior in the curves at displacements close to failure is due to this phenomenon

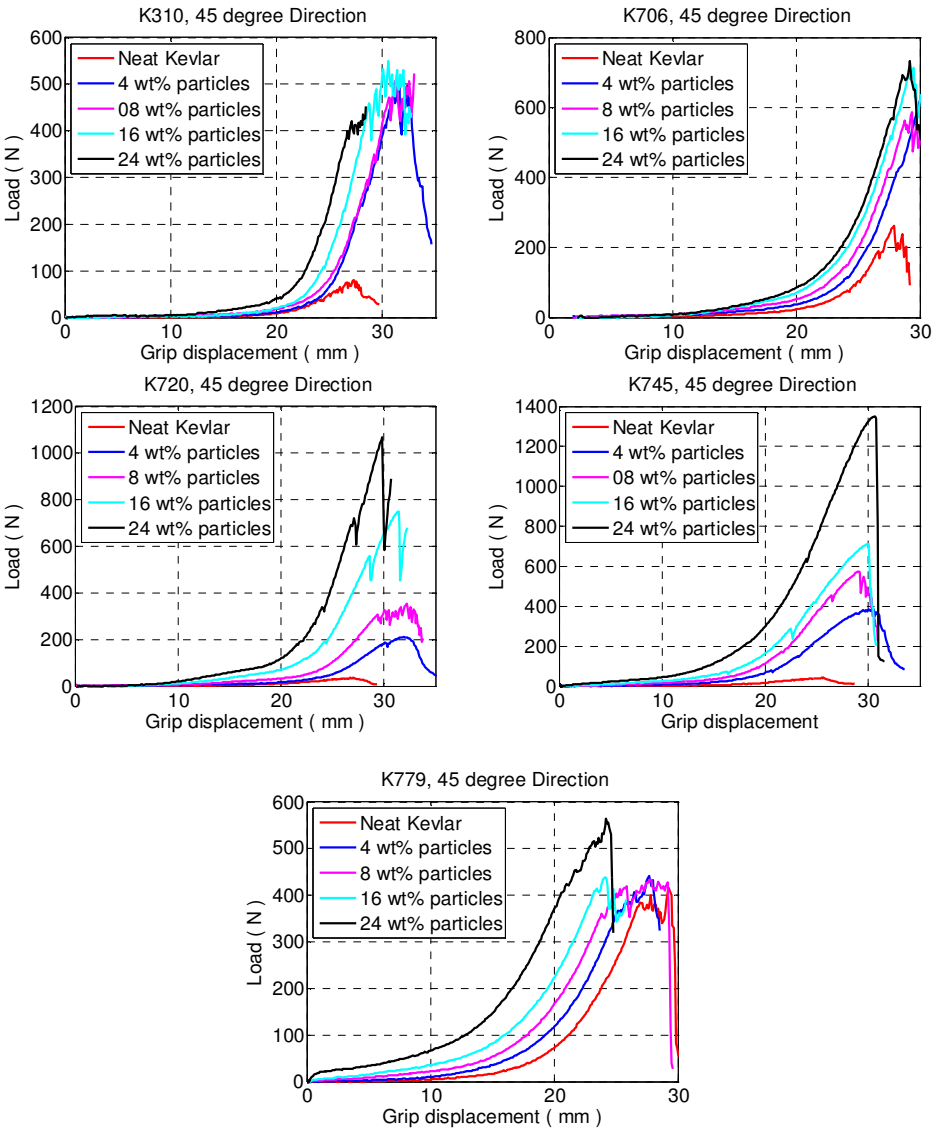

Figure 7. Load versus displacement curves from 45° off-axis tension tests for five styles of Kevlar fabrics with different wt% addition of nanoparticles.

of yarn sliding at corners. The maximum load is sensed during the yarn sliding phase after which the curve falls rapidly as the two portions of the specimen separate. The failure location was always observed to be at either the upper or lower shear region interfaces. The addition of nanoparticles did not affect the location of failure. However, treated fabrics display a more definite failure load as the enhanced load carrying ability diminishes rapidly once the nanoparticles that lock the relative motion between adjacent yarns are dislodged. This reinforces the inference that the nanoparticles enhance the shear rigidity by increasing the interyarn and intrayarn friction in woven fabrics.

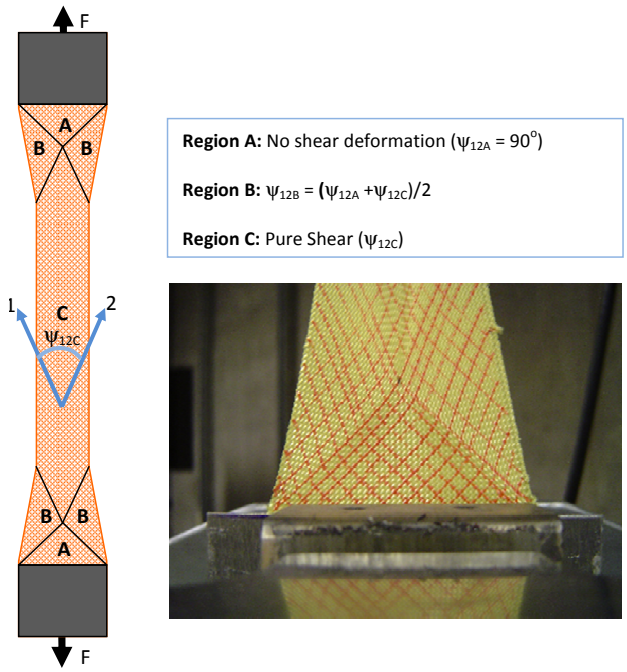

Figure 8. Shear regions in a 45° off-axis tension test: schematic diagram and actual deformation.

The load displacement plots (Figure 7) demonstrate that substantial enhancement of shear rigidity and strength is achieved by the addition of nanoparticles to the fabric. The effect is greater for coarse weave fabrics which have low rigidity in the neat condition. K745 (the coarsest weave among the five styles) registers a failure load of nearly 26 times that of its neat strength with an addition of 24% by weight of nanoparticles. In comparison, fine weave fabrics that have higher interyarn friction in the neat state due to their smaller yarn size and interyarn spacing, show lower sensitivity to the percentage of nanoparticles added. K779, for example, shows a proportional increase in stiffness with increase in the amount of nanoparticles added but the failure load remains more or less the same. It is surmised that the impregnation of nanoparticles in the fabric imparts an additional mechanism of frictional interaction between the yarns which acts in conjunction with the inherent interyarn friction present in neat fabrics. In the case of fine weave fabrics like K779, the effect of the neat fabric friction is predominant and hence the fabric shows lower increase in failure load with increase in nanoparticle addition. The fabric styles K310, K706 and K720 show varying degrees of increase in shear rigidity and failure loads. An important factor that influences the behavior of silica nanoparticle impregnated fabrics is the uniformity of the distribution of nanoparticles in the fabric. Although, the process is controlled to ensure that the nanoparticle colloid soaks the fabric evenly and remains undisturbed during the drying process, SEM images reveal that there is agglomeration of particles in interyarn spaces. Hence, to a certain extent, variability in the failure load of the fabric may be attributed to the nonuniform distribution of nanoparticles in the fabric.

3.3. ***Indentation test.*** Indentation test was conducted for validation of the constitutive model. The deformation and failure of Kevlar fabrics in a static indentation test depends on the fabric style, indentor size

and boundary conditions. As a 45° yarn orientation was used, large out-of-plane deformation occurs before failure initiation. Unlike the off-axis tension test, the yarn rotations in the specimen are not uniform. The indentor load is initially small as the out-of-plane deformation is accommodated by uncrimping of yarns. Once the rotations of the yarns are close to the locking value, a steep rise in the indentor load is noticed. Further transverse displacement leads to the onset of failure by the sliding (unraveling) of yarns at cross over points at the corner of the clamped edges of the specimen.

4. Constitutive modeling

The uniaxial and off-axis tension tests reveal that Kevlar fabrics have very high stiffness in both yarn directions, but a very low in-plane shear resistance. Addition of nanoparticles produces a substantial increase in shear rigidity while only a small increase is obtained in the axial stiffness. The tensile strains in yarn directions are small because of high stiffness in these directions. However, an in-plane shear loading can cause very large changes in the angle between the warp and weft yarns due to their relative rotations. This behavior makes the modeling of the fabric as a homogenized continuum rather difficult. In addition, for nanoparticle impregnated fabrics, the effect of the nanoparticles on the mechanical behavior must be included in the constitutive equations.

To simplify this task, we adopt an incremental deformation approach in setting up the constitutive model in conjunction with a procedure that resembles the classical laminated plate theory. As the response of the fabrics is highly nonlinear, an incremental deformation approach is used. At every increment, the fabric deforms through the interaction of the warp and weft families of yarns. This interaction is simplified by modeling the warp and weft yarns as two separate plies in a composite laminate. Once the incremental constitutive equations are established, they can be implemented as a user defined subroutine in the commercial finite element code ABAQUS/ Standard to perform numerical simulations.

A set of coordinate systems are established as shown in Figure 9. The fabric is assumed to lie in the x-y plane with the warp and weft yarns initially assumed to be oriented at angles α and β respectively to the positive x direction of the global coordinate system x-y. An angle measured anticlockwise from the positive x direction is represented as positive and an angle measured clockwise is represented as negative. As the out-of-plane thickness of the fabric is very small compared to the specimen in-plane dimensions, an assumption of a state of plane stress is made. For plain woven fabrics the warp and weft directions are orthogonal to each other in the undeformed condition. As the fabric undergoes large shear deformations, the yarns rotate relative to each other and the angle between them in the deformed state

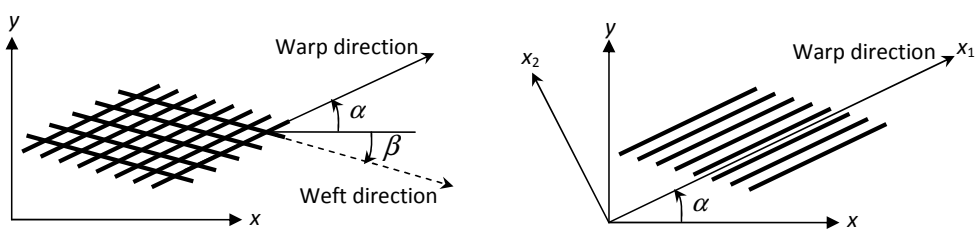

Figure 9. Left: global coordinate system (x, y) and yarn orientations. Right: Local coordinate system (x_1, x_2) for the warp layer.

(θ) can become much larger or smaller than 90°. Two local coordinate systems, $(x_1, x_2)_\alpha$ and $(x_1, x_2)_\beta$ are established for the warp and the weft layers respectively such that the x_1 direction is along the yarn direction in each layer.

At each incremental step, a single layer of Kevlar fabric of thickness T is modeled as the composite of two layers of unidirectional fibers. The effective mechanical properties of each layer are modeled as a two-dimensional orthotropic solid and the fabric is modeled as the laminate consisting of two fiber layers. Considering the warp layer, the incremental stress-strain relations for this layer are formulated in the local coordinate system as

$$\begin{Bmatrix} \Delta\sigma_{11} \\ \Delta\sigma_{22} \\ \Delta\sigma_{12} \end{Bmatrix} = \begin{bmatrix} \dfrac{E_1^\alpha}{1-\nu_{12}\nu_{21}} & \dfrac{\nu_{12}^\alpha E_2^\alpha}{1-\nu_{12}^\alpha\nu_{21}^\alpha} & 0 \\ \dfrac{\nu_{12}^\alpha E_2^\alpha}{1-\nu_{12}^\alpha\nu_{21}^\alpha} & \dfrac{E_2^\alpha}{1-\nu_{12}^\alpha\nu_{21}^\alpha} & 0 \\ 0 & 0 & G_{12}^\alpha \end{bmatrix} \begin{Bmatrix} \Delta\varepsilon_{11} \\ \Delta\varepsilon_{22} \\ \Delta\gamma_{12} \end{Bmatrix}, \tag{1}$$

where the superscript α denotes the warp layer and E_1^α, E_2^α and ν_{12}^α are the yarn direction modulus, transverse modulus and in-plane Poisson's ratio for the layer. The uniaxial tension tests show that for an applied tensile load in the yarn directions, the fabric structure does not have any overall contraction in the transverse direction. The yarns themselves (which are formed by bundles of fibers) may contract leading to an increase in the free space between yarns, but the overall transverse dimension of the specimen remains unchanged. Thus from a continuum perspective, the in-plane Poisson's ratio for a layer of unidirectional yarns (warp or weft) is negligible and is set to zero which simplifies Equation (1) to

$$\begin{Bmatrix} \Delta\sigma_{11} \\ \Delta\sigma_{22} \\ \Delta\sigma_{12} \end{Bmatrix} = \begin{bmatrix} E_1^\alpha & 0 & 0 \\ 0 & E_2^\alpha & 0 \\ 0 & 0 & G_{12}^\alpha \end{bmatrix} \begin{Bmatrix} \Delta\varepsilon_{11} \\ \Delta\varepsilon_{22} \\ \Delta\gamma_{12} \end{Bmatrix}. \tag{2}$$

The incremental stress-strain relations for the warp layer in the global coordinate system x-y can now be obtained using coordinate transformation as

$$\begin{Bmatrix} \Delta\sigma_{xx} \\ \Delta\sigma_{yy} \\ \Delta\sigma_{xy} \end{Bmatrix} = \begin{bmatrix} Q_{11}^\alpha & Q_{12}^\alpha & Q_{16}^\alpha \\ Q_{12}^\alpha & Q_{22}^\alpha & Q_{26}^\alpha \\ Q_{16}^\alpha & Q_{26}^\alpha & Q_{66}^\alpha \end{bmatrix} \begin{Bmatrix} \Delta\varepsilon_{xx} \\ \Delta\varepsilon_{yy} \\ \Delta\gamma_{xy} \end{Bmatrix} = \left[Q^\alpha\right] \begin{Bmatrix} \Delta\varepsilon_{xx} \\ \Delta\varepsilon_{yy} \\ \Delta\gamma_{xy} \end{Bmatrix}, \tag{3}$$

where the reduced stiffnesses for the warp layer, Q_{ij}^α, are given by

$$\begin{aligned} Q_{11}^\alpha &= E_1^\alpha \cos^4\alpha + 4G_{12}^\alpha \sin^2\alpha\cos^2\alpha + E_2^\alpha \sin^4\alpha, \\ Q_{12}^\alpha &= (E_1^\alpha + E_2^\alpha - 4G_{12}^\alpha)\sin^2\alpha\cos^2\alpha, \\ Q_{22}^\alpha &= E_1^\alpha \sin^4\alpha + 4G_{12}^\alpha \sin^2\alpha\cos^2\alpha + E_2^\alpha \cos^4\alpha, \\ Q_{16}^\alpha &= (E_1^\alpha - 2G_{12}^\alpha)\sin\alpha\cos^3\alpha - (E_2^\alpha - 2G_{12}^\alpha)\sin^3\alpha\cos\alpha, \\ Q_{26}^\alpha &= (E_1^\alpha - 2G_{12}^\alpha)\sin^3\alpha\cos\alpha - (E_2^\alpha - 2G_{12}^\alpha)\sin\alpha\cos^3\alpha, \\ Q_{66}^\alpha &= (E_1^\alpha + E_2^\alpha - 2G_{12}^\alpha)\sin^2\alpha\cos^2\alpha + G_{12}^\alpha(\sin^4\alpha + \cos^4\alpha). \end{aligned} \tag{4}$$

Similarly the incremental stress-strain relations in the global coordinate system for the weft layer are obtained as

$$\begin{Bmatrix} \Delta\sigma_{xx} \\ \Delta\sigma_{yy} \\ \Delta\sigma_{xy} \end{Bmatrix} = \begin{bmatrix} Q^{\beta}_{11} & Q^{\beta}_{12} & Q^{\beta}_{16} \\ Q^{\beta}_{12} & Q^{\beta}_{22} & Q^{\beta}_{26} \\ Q^{\beta}_{16} & Q^{\beta}_{26} & Q^{\beta}_{66} \end{bmatrix} \begin{Bmatrix} \Delta\varepsilon_{xx} \\ \Delta\varepsilon_{yy} \\ \Delta\gamma_{xy} \end{Bmatrix} = \left[Q^{\beta}\right] \begin{Bmatrix} \Delta\varepsilon_{xx} \\ \Delta\varepsilon_{yy} \\ \Delta\gamma_{xy} \end{Bmatrix}. \tag{5}$$

The superscript β denotes the weft layer and the reduced stiffnesses for the weft layer, Q^{β}_{ij}, are given by

$$\begin{aligned} Q^{\beta}_{11} &= E^{\beta}_1 \cos^4\beta + 4G^{\beta}_{12}\sin^2\beta\cos^2\beta + E^{\alpha}_2 \sin^4\beta, \\ Q^{\beta}_{12} &= (E^{\beta}_1 + E^{\beta}_2 - 4G^{\beta}_{12})\sin^2\beta\cos^2\beta, \\ Q^{\beta}_{22} &= E^{\beta}_1 \sin^4\beta + 4G^{\beta}_{12}\sin^2\beta\cos^2\beta + E^{\beta}_2 \cos^4\beta, \\ Q^{\beta}_{16} &= (E^{\beta}_1 - 2G^{\beta}_{12})\sin\beta\cos^3\beta - (E^{\beta}_2 - 2G^{\beta}_{12})\sin^3\beta\cos\beta, \\ Q^{\beta}_{26} &= (E^{\beta}_1 - 2G^{\beta}_{12})\sin^3\beta\cos\beta - (E^{\beta}_2 - 2G^{\beta}_{12})\sin\beta\cos^3\beta, \\ Q^{\beta}_{66} &= (E^{\beta}_1 + E^{\beta}_2 - 2G^{\beta}_{12})\sin^2\beta\cos^2\beta + G^{\beta}_{12}(\sin^4\beta + \cos^4\beta). \end{aligned} \tag{6}$$

The warp and weft layers exist in an interwoven state in the actual fabric and hence to simplify the formulation, we assume that both layers occupy the same space and have the same thickness (T) which is the thickness of one fabric layer. This thickness is set to be constant over the fabric undergoing large deformation. To be consistent, material properties for the warp and weft layers are defined using the thickness. Thus, the stiffness matrix for the fabric is obtained as

$$\left[Q\right] = \left[Q^{\alpha}\right] + \left[Q^{\beta}\right]. \tag{7}$$

Equation (7) provides the stiffness matrix for a single layer of fabric which is dependent on a total of six unknown material parameters – three each for warp and weft yarn directions. For each layer, the moduli E_1, E_2 and G_{12} are calibrated from the uniaxial and off-axis tension tests. These moduli must reflect the variation in yarn spacing under large deformations due to relative rotation of warp and weft yarns. True strain and true stress are used in the ABAQUS incremental formulation. In the following discussion, neat Kevlar K706 style fabric will be used as an example to illustrate the procedure for obtaining the material parameters. The same procedure is followed for other styles of neat and treated fabrics.

The uniaxial tension tests in the warp and weft directions display a bilinear trend. Hence, a simple bilinear function was used to approximate the tangent longitudinal moduli E^{α}_1 and E^{β}_1 in the warp and weft directions from these stress-strain curves. In the uniaxial tension tests, relative yarn rotations do not occur and thus the yarn spacing remains unchanged. However, when the fabric undergoes shear deformations, yarn rotations induce a change in the tangent longitudinal moduli. In order to capture this effect, the approximate bilinear functions for the tangent longitudinal moduli are factored by a nondimensional yarn spacing parameter which is defined as follows. Figure 10 shows the configuration of the yarns in the initial and deformed configurations. The yarn spacing parameters L_α and L_β for the warp and weft directions respectively are defined as the ratio between the yarn spacing in the deformed

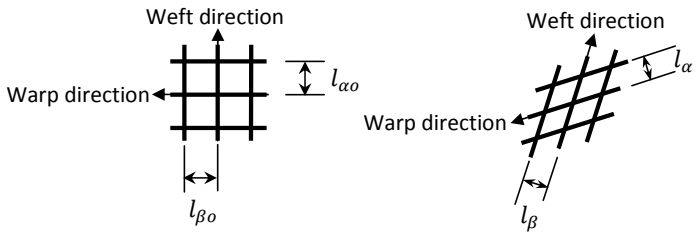

$$L_{\alpha o} = \frac{l_\alpha}{l_{\alpha o}} = 1 \qquad L_\alpha = \frac{l_\alpha}{l_{\alpha o}} = \left(1 + \varepsilon_{11}^{\beta}\right) \sin\theta$$

$$L_{\beta o} = \frac{l_\beta}{l_{\beta o}} = 1 \qquad L_\beta = \frac{l_\beta}{l_{\beta o}} = (1 + \varepsilon_{11}^{\alpha}) \sin\theta$$

Figure 10. Yarn spacing parameters: initial and deformed configurations.

configuration *(l_α and l_β)* to the initial yarn spacing *($l_{\alpha 0}$ and $l_{\beta 0}$)*.

$$L_\alpha = \frac{l_\alpha}{l_{\alpha 0}}, \quad L_\beta = \frac{l_\beta}{l_{\beta 0}}. \tag{8}$$

The nondimensional yarn spacing parameters are equal to 1 in the initial configuration. In the deformed configuration they are obtained from the geometry as a function of the yarn direction strains $\varepsilon_{11}^{\alpha}$ and ε_{11}^{β} and the angle between the yarns ($\theta = \alpha - \beta$) as

$$L_\alpha = \frac{l_\alpha}{l_{\alpha 0}} = (1 + \varepsilon_{11}^{\beta}) \sin\theta, \quad L_\beta = \frac{l_\beta}{l_{\beta 0}} = (1 + \varepsilon_{11}^{\alpha}) \sin\theta. \tag{9}$$

Initially, as the yarn direction strains are zero and the angle between the yarns is $\pi/2$, the values of L_α and L_β become 1, which is consistent with the definition of the yarn spacing parameters. Using the yarn spacing parameters, the tangent longitudinal moduli at each increment are approximated by

$$E_1^{\alpha} = \frac{1}{L_\alpha} \begin{cases} E_1^{\alpha 1} & \text{for } \varepsilon_{11}^{\alpha} \le \varepsilon_{11}^{\alpha 0}, \\ E_1^{\alpha 2} & \text{for } \varepsilon_{11}^{\alpha} > \varepsilon_{11}^{\alpha 0}, \end{cases} \qquad E_1^{\beta} = \frac{1}{L_\beta} \begin{cases} E_1^{\beta 1} & \text{for } \varepsilon_{11}^{\beta} \le \varepsilon_{11}^{\beta 0}, \\ E_1^{\beta 2} & \text{for } \varepsilon_{11}^{\beta} > \varepsilon_{11}^{\beta 0}, \end{cases} \tag{10}$$

where the superscript '0' indicates the bilinear transition strain. For neat K706 style fabric, the values of the various constant material parameters in (10) are obtained from linear curve fits to the uncrimping and elongation regimes of the warp and weft direction stress-strain curves as

$$\begin{aligned} E_1^{\alpha 1} &= 1.5\,\text{GPa}, \quad E_1^{\alpha 2} = 22.0\,\text{GPa}, \quad \varepsilon_{11}^{\alpha 0} = 0.025, \\ E_1^{\beta 1} &= 1.8\,\text{GPa}, \quad E_1^{\beta 2} = 23.0\,\text{GPa}, \quad \varepsilon_{11}^{\beta 0} = 0.016. \end{aligned} \tag{11}$$

When the yarns undergo rotations due to shear deformations, the yarn spacing reduces. This causes the yarn spacing parameter to decrease. Thus, the tangent longitudinal moduli which are inversely proportional to the yarn spacing parameters increase as the yarn spacing reduces. This reflects the phenomenon of increase in yarn direction moduli due to increase in friction between adjacent yarns as they become closely packed.

The transverse moduli and the shear modulus are estimated from the 45° off-axis tension tests. The mechanism by which the fabric resists shear loads transitions from one predominantly due to rotation of yarns to one due to the transverse compression of adjacent yarns as the relative angle between the yarns approaches the locking angle. Hence, the shear rigidity is very low during the initial phase of the deformation. Once the locking angle is reached, the yarns become closely packed and further deformation is resisted by compression of yarns in the transverse direction and the occurrence of out-of-plane wrinkling. We introduce this effect into the constitutive relations by assuming that the shear modulus (which is attributed to the initial yarn rotations) to be constant and that the highly nonlinear behavior at higher displacements are caused by variation in the transverse moduli. The load-displacement curves for the 45° off-axis tension test can be converted to an equivalent shear stress-shear angle curve using the kinematic relations for an equivalent picture frame test [Milani et al. 2010]. Comparisons show that both these curves have nearly the same slope at low values of displacement/ strain. Under these assumptions, the shear modulus is estimated from the initial slope of the load-displacement curves from off-axis tension tests. The individual shear moduli for the warp and weft layers are indistinguishable. Both G_{12}^{α} and G_{12}^{β} are assumed to be equal and to be the same as that of a single layer of fabric. For neat K706, the shear modulus is calculated from the initial slope of the curve as

$$G_{12}^{\alpha} = G_{12}^{\beta} = G_{12} = 0.4\,\text{MPa}. \tag{12}$$

The parameters E_2^{α} and E_2^{β} are obtained from the load-displacement curves using a nonlinear fitting function that depends on the yarn spacing parameters. When the cross yarns undergo large rotation, the parallel yarns are packed together. The stresses in transverse direction prevent the parallel yarns from being too close to each other under large shear deformation. The tangent transverse moduli E_2^{α} and E_2^{β} could be calculate from these transverse stresses. Since both E_2^{α} and E_2^{β} attribute to prevent the further yarn rotation, we assume they are the same nonlinear function in terms of nondimensional yarn spacing L_{α} and L_{β}. The form of the fitting function is such that as the yarn spacing parameters tend towards a limiting value (L_{lock}), after which further yarn rotations cannot occur, the transverse moduli increase rapidly. The function and the constants E_2^0 and L_{lock} are found by means of a trial and error procedure using numerical simulations as

$$E_2^{\alpha} = \frac{E_2^0}{L_{\alpha} - L_{\text{lock}}}, \quad E_2^{\beta} = \frac{E_2^0}{L_{\beta} - L_{\text{lock}}} \quad E_2^0 = 2.3\,\text{MPa}, \qquad \text{with } L_{\text{lock}} = 0.68. \tag{13}$$

Table 3 summarizes the material parameters estimated for five styles of neat and 24 wt% nanoparticle impregnated Kevlar fabrics. The mechanical properties of the five styles of fabrics are quite different. The material parameter G_{12} reflects the initial shear stiffness in the off-axis tension. Parameter E_2^0 provides the transverse stiffness which prevents the parallel yarns from being too close to each other. Both G_{12} and E_2^0 are directly related to the final shear rigidity under large deformation. Nanoparticles largely enhance the shear rigidity. Fabrics with nanoparticles have much larger values of both G_{12} and E_2^0.

5. Comparison of experimental and numerical results

The constitutive model was implemented as a user-defined material subroutine (UMAT) in ABAQUS/ Standard. The rectangular fabric specimen was modeled using four-node plane stress shell elements.

Style	nanopart. (wt%)	$E_1^{\alpha 1}$ (GPa)	$E_1^{\alpha 2}$ (GPa)	$\varepsilon_{11}^{\alpha 0}$	$E_1^{\beta 1}$ (GPa)	$E_1^{\beta 2}$ (GPa)	$\varepsilon_{11}^{\beta 0}$	G_{12} (MPa)	E_2^0 (MPa)	L_{lock}
K310	0	0.7	20.0	0.028	6.0	23.5	0.003	0.01	0.5	0.70
	24	1.8	20.0	0.030	6.0	23.5	0.003	0.6	3.2	0.75
K706	0	1.5	22.0	0.025	1.8	22.0	0.016	0.4	2.3	0.68
	24	3.0	22.0	0.027	3.0	22.0	0.017	1.5	7.5	0.73
K720	0	1.0	22.5	0.018	1.0	26.0	0.014	0.15	0.45	0.60
	24	3.0	22.5	0.020	2.5	26.0	0.015	1.5	5.0	0.75
K745	0	0.3	16.0	0.034	0.5	18.0	0.019	0.07	0.5	0.67
	24	2.0	16.0	0.037	1.5	18.0	0.020	1.7	11.0	0.77
K779	0	0.7	17.0	0.093	7.0	22.5	0.005	0.15	3.0	0.88
	24	1.7	17.0	0.099	14.0	22.5	0.010	9.0	9.5	0.93

Table 3. Material parameters for five styles of neat and 24 wt% nanoparticle impregnated Kevlar fabrics.

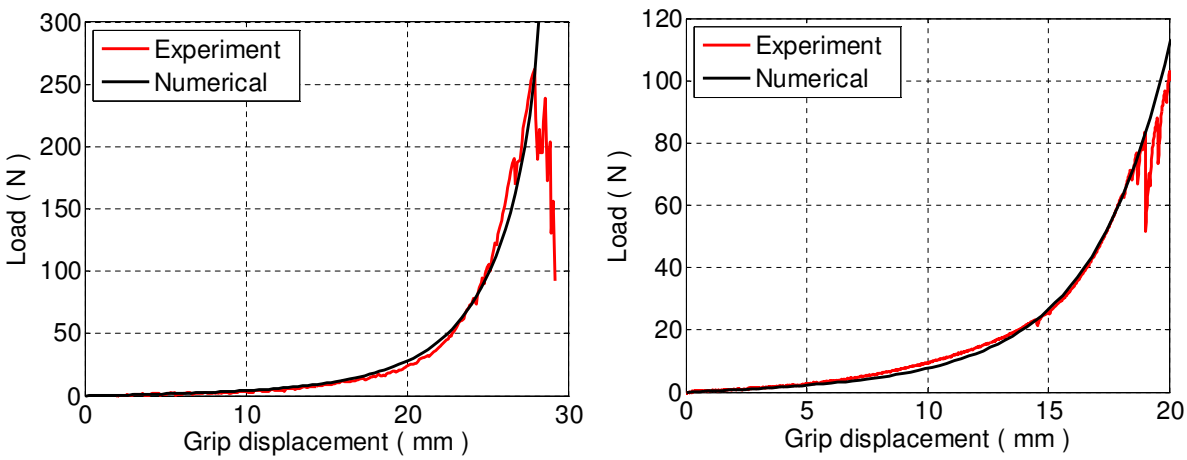

Figure 11. Experimental and numerical load-displacement curves for a 45° (left) and a 30° (right) off-axis tension test using neat K706 style fabric.

One edge was fixed and a prescribed displacement was applied to the opposite edge. Validation of the constitutive model is carried out by comparing the experimental result and the numerical simulation of the 30° off-axis tension test. Figure 11 shows the experimental load-displacement curves and the result of numerical simulations for 45° and 30° off-axis tension tests using neat K706. Numerical simulations fit the experimental data very well until the onset of failure. Figure 12 shows the snapshot of deformed specimen at grip displacement of 18 mm. Only the upper half of the specimen is shown. The middle line which was horizontal before loading tilts gradually when grip moves. The simulated tilting angle is almost the same as the experimental one. Overall, the simulated specimen shape agrees well with the image taken from the experiments.

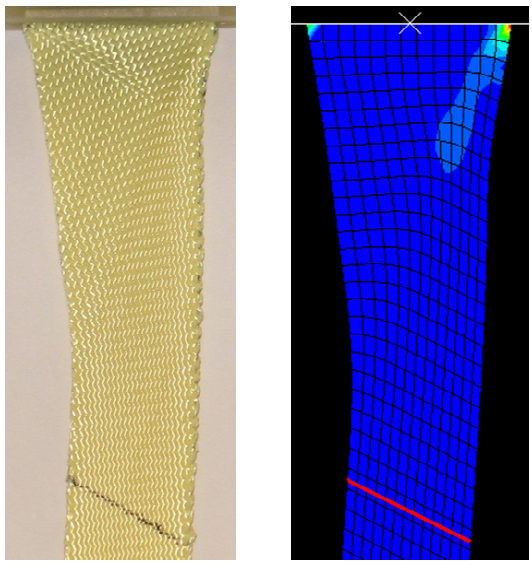

Figure 12. A snapshot of the deformation in a 30° off-axis tension test using neat K706 style fabric at a grip displacement of 18 mm.

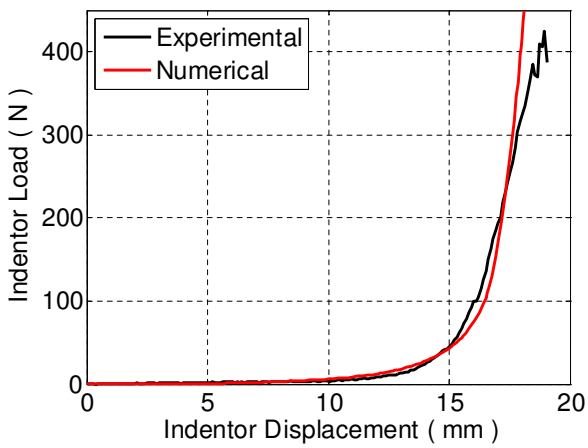

Figure 13. Experimental and numerical load displacement curves from a static indentation test on 45° neat K706 style fabric.

In the numerical simulation for the static indentation test, the fabric was meshed using four-node shell elements, the indentor was modeled as a rigid body and a frictionless contact definition was given between the indentor and the fabric. The indentor load was measured from the out-of-plane reaction force. Comparison of the experimental and numerical indentor load-displacement curves is presented in Figure 13. The numerical simulations fit the experimental data very well until failure of the fabric begins due to the slipping of yarns at the corners. Since this model does not account for damage, the simulation starts to deviate from the experimental results at large loads.

6. Conclusions

In-plane mechanical properties of five styles of Kevlar fabrics were investigated to show the difference between the neat fabric and the silica nanoparticle impregnated fabrics. The nanoparticles impart substantial increase to the in-plane shear rigidity. When off-axis load is applied, nanoparticle impregnated fabrics sustained higher failure loads. SEM images reveal that the nanoparticles are lodged in the interyarn and interfiber spaces in the fabric. This increases the friction between adjacent and cross yarns thereby augmenting the fabric's resistance to applied loads.

A two dimensional homogenized continuum constitutive model was developed to characterize the nonlinear anisotropic material properties of the neat and nanoparticle impregnated fabrics under large shear deformation. The material parameters required in this model were obtained from uniaxial tension and 45° off-axis tension tests. The constitutive model was interfaced with the commercial finite element code ABAQUS via a user-defined material subroutine (UMAT). Validation of the model was done by simulating a 30° off-axis tension test and a static indentation test. The simulated load-displacement curves were found to agree very well with the experimental data. This model can be used to predict the load deflection behavior of neat and nanoparticle impregnated plain woven Kevlar fabrics with good accuracy.

Acknowledgement

This work was supported by an ARO grant W911NF-05-2-0006. Dr. David Stepp was the program manager. We also wish to thank Dr. Eric Wetzel, who provided the Kevlar fabrics used in this study.

References

[Decker et al. 2007] M. J. Decker, C. J. Halbach, C. H. Nam, N. J. Wagner, and E. D. Wetzel, "Stab resistance of shear thickening fluid (STF)-treated fabrics", *Compos. Sci. Tech.* **67** (2007), 565–578.

[Grujicic et al. 2009] M. Grujicic, W. C. Bell, G. Arakere, T. He, and B. A. Cheeseman, "A meso-scale unit-cell based material model for the single-ply flexible-fabric armor", *Mater. Design* **30**:9 (2009), 3690–3704.

[Harrison et al. 2004] P. Harrison, M. J. Clifford, and A. C. Long, "Shear characterisation of viscous woven textile composites: a comparison between picture frame and bias extension experiments", *Compos. Sci. Technol.* **64**:10-11 (2004), 1453–1465.

[Kalman et al. 2009] D. P. Kalman, R. L. Merrill, N. J. Wagner, and E. D. Wetzel, "Effect of particle hardness on the penetration behavior of fabrics intercalated with dry particles and concentrated particle-fluid suspensions", *ACS Appl. Mat. Interf.* **1**:11 (2009), 2602–2612.

[King et al. 2005] M. J. King, P. Jearanaisilawong, and S. Socrate, "A continuum constitutive model for the mechanical behavior of woven fabrics", *Int. J. Solids Struct.* **42**:13 (2005), 3867–3896.

[Lebrun et al. 2003] G. Lebrun, M. N. Bureau, and J. Denault, "Evaluation of bias-extension and picture-frame test methods for the measurement of intraply shear properties of PP/glass commingled fabrics", *Compos. Struct.* **61**:4 (2003), 341–352.

[Lee et al. 2003] Y. S. Lee, E. D. Wetzel, and N. Wagner, "The ballistic impact characteristics of Kevlar woven fabrics impregnated with a colloidal shear thickening fluid", *J. Mater. Sci.* **38**:13 (2003), 2825–2833.

[Lin et al. 2009] H. Lin, M. J. Clifford, A. C. Long, and M. Sherburn, "Finite element modelling of fabric shear", *Model. Simul. Mater. Sci. Eng.* **17**:1 (2009), art. #15008.

[Lomov et al. 2006] S. V. Lomov, A. Willems, I. Verpoest, Y. Zhu, M. Barburski, and T. Stoilova, "Picture frame test of woven composite reinforcements with a full-field strain registration", *Textile Res. J.* **76**:3 (2006), 243–252.

[Milani et al. 2010] A. S. Milani, J. A. Nemes, G. Lebrun, and M. N. Bureau, "A comparative analysis of a modified picture frame test for characterization of woven fabrics", *Polym. Compos.* **31**:4 (2010), 561–568.

[Mohammed et al. 2000] U. Mohammed, C. Lekakou, L. Dong, and M. G. Bader, "Shear deformation and micromechanics of woven fabrics", *Compos. A Appl. Sci. Manuf.* **31**:4 (2000), 299–308.

[Peng et al. 2004] X. Q. Peng, J. Cao, J. Chen, P. Xue, D. S. Lussier, and L. Liu, "Experimental and numerical analysis on normalization of picture frame tests for composite materials", *Compos. Sci. Technol.* **64**:1 (2004), 11–21.

[Raftenberg and Mulkern 2002] M. N. Raftenberg and T. J. Mulkern, "Quasi-static uniaxial tension characteristics of plain-woven Kevlar KM2 fabric", technical report ARL-TR-2891, Army Research Laboratory, Aberdeen Proving Ground, MD, 2002, available at http://tinyurl.com/RaftenbergTR2891.

[Tan et al. 2005] V. B. C. Tan, T. E. Tay, and W. K. Teo, "Strengthening fabric armour with silica colloidal suspensions", *Int. J. Solids Struct.* **42**:5–6 (2005), 1561–1576.

Received 19 Feb 2009. Revised 13 Jan 2010. Accepted 28 Jan 2010.

ZHAOXU DONG: dong_zhaoxu@cat.com
Caterpillar Inc., 100 North East Adams Street, Peoria, IL 61629, United States

JAMES M. MANIMALA: jmanimal@purdue.edu
Purdue University, School of Aeronautics and Astronautics, 701 W. Stadium Ave, West Lafayette, IN 47907, United States

C. T. SUN: sun@purdue.edu
Purdue University, School of Aeronautics and Astronautics, 701 W. Stadium Ave, West Lafayette, IN 47907, United States

JOURNAL OF MECHANICS OF MATERIALS AND STRUCTURES
Vol. 5, No. 4, 2010

A GENERALIZED PLANE STRAIN MESHLESS LOCAL PETROV–GALERKIN METHOD FOR THE MICROMECHANICS OF THERMOMECHANICAL LOADING OF COMPOSITES

ISA AHMADI AND MOHAMAD AGHDAM

A generalized plane strain micromechanical model is developed to predict the behavior of a unidirectional fiber-reinforced composite subjected to combined thermal and mechanical loads. An appropriate meshless local Petrov–Galerkin formulation is presented for the solution of the governing partial differential equations of the problem. To reduce computation time, a unit step function is employed as test function. A direct method is presented for enforcement of the continuity of displacement and traction at the fiber-matrix interface to model the fully bonded interface. Results of this study revealed that the model provides highly accurate predictions with relatively small number of nodes. Numerical results for glass/epoxy and SiC/Ti composites subjected to thermomechanical loading show that predictions for both local and global responses of the composites are in good agreement with results of theoretical, experimental and finite element methods.

1. Introduction

During the past decade, the idea of using meshless methods for the solution of boundary value problems has received much attention and undergone significant progress. In meshless methods, no predefined mesh of elements is needed between the nodes for the construction of a trial or test function. One of the main objectives of such methods is to eliminate or alleviate difficulties inherent to meshing and remeshing of the domain, or the locking and distortion of elements.

Various meshless methods such as the diffuse element method [Nayroles et al. 1992], the element-free Galerkin (EFG) method [Belytschko et al. 1994], the reproducing kernel particle method [Liu et al. 1996], the meshless local boundary integral equation (LBIE) method [Zhu et al. 1998], and the meshless local Petrov–Galerkin (MLPG) method [Atluri and Zhu 1998] have been developed in the last two decades. In some of them, such as EFG, a background mesh is required for integration of the weak form of equations. By contrast, MLPG requires no mesh either for the interpolation of the solution variable or for the integration of the weak form of equations. Some applications of this promising, efficient and flexible method include solving Poisson's equation [Atluri and Zhu 1998], elastostatic and elastodynamic problems [Atluri and Zhu 2000; Long et al. 2006], plate bending [Gu and Liu 2001], fracture mechanics [Ching and Batra 2001], and Navier–Stokes flow [Lin and Atluri 2001; Atluri and Shen 2002].

On the other hand, various techniques both analytical [Gramoll et al. 1991; Arsenault and Taya 1987; Yeh and Krempl 1993; Uemura et al. 1979; Brayshaw and Pindera 1994; Tsai and Chi 2008]

Keywords: meshless local Petrov–Galerkin method, MLPG, generalized plane strain, micromechanics, metal-matrix composite, thermal residual stress.

and numerical have been used in the micromechanical analysis of heterogeneous materials. Though approaches based on the finite difference and boundary element methods can be found in the literature (see [Adams and Doner 1967] and [Eischen and Torquato 1993], respectively), most numerical approaches rely on the finite element method [Nimmer 1990; Nimmer et al. 1991; Wisnom 1990; Durodola and Derby 1994; Shaw and Miracle 1996; Zhang et al. 2004; Dvorak et al. 1973; Zahl and McMeeking 1991; Aghdam et al. 2000; Aghdam and Khojeh 2003; Gentz et al. 2004; Zhao et al. 2007; Shen 1998; Haktan Karadeniz and Kumlutas 2007], and have been used for predicting various elastic, elastoplastic and thermoelastic characteristics of composites.

Some of these models include the effect of thermal stress on the mechanical behavior of composite materials. In addition to [Durodola and Derby 1994; Shaw and Miracle 1996], we mention [Nimmer 1990; Nimmer et al. 1991; Wisnom 1990], where it was found that residual stresses at the interface of the fiber and matrix are compressive and therefore they are beneficial for the transverse behavior of the MMCs with weak interface. Shaw and Miracle [1996] used the finite element method to study the effects of interfacial region on the thermal residual stress and transverse behavior of a SiC/Ti metal-matrix composite. The influence of residual stresses on the yielding behavior of composite materials was studied in [Dvorak et al. 1973; Zahl and McMeeking 1991; Aghdam et al. 2000; Aghdam and Khojeh 2003], while [Gentz et al. 2004] and [Zhao et al. 2007] studied the effects of the residual stresses on the behavior of polymer-matrix composite. In addition, the overall coefficient of thermal expansion of composite materials was studied using micromechanical finite element [Shen 1998; Haktan Karadeniz and Kumlutas 2007], approximate closed-form models [Van Fo Fy 1965; Rogers et al. 1977; Chamis 1984], and experimental methods [Sideridis 1994].

More recently, Dang and Sankar [2007] employed the conventional MLPG method for the micromechanical analysis of unidirectional composites. They used the penalty parameter method to enforce the essential boundary conditions on the RVE. Their predictions show reasonably good agreement with finite element results. However, the conventional MLPG formulation with Gaussian weight functions and transformation technique in their paper seems to be time-consuming and computationally expensive due to a domain integration in the weak formulation.

In this study, a micromechanical model based on the generalized plane strain assumption is developed to study the behavior of unidirectional composites subjected to thermomechanical loading. An appropriate meshless local Petrov–Galerkin (MLPG) formulation is presented for the generalized plane strain case in the presence of thermal loading. This formulation is used to solve the governing equations of the system. A unit step function is considered as the test function, which leads to the elimination of domain integration in the absence of body forces and therefore, to the reduction in the computational cost. A direct interpolation method is introduced for the enforcement of the displacement continuity and traction reciprocity conditions at the fiber-matrix interface based on the fully bonded interface assumption. These continuity conditions are imposed directly on the discretized equation.

The method presented is used to predict the thermal residual stress in SiC/Ti metal-matrix composites resulting from the manufacturing process, and the effects of these stresses on the total stress distribution due to the mechanical loading of the SiC/Ti composite. Comparison of the predictions for the overall coefficient of thermal expansion and the displacement and stress components show excellent agreement with other experimental, finite element and approximate closed-form analyses. Numerical analysis suggests that the model can provide highly accurate results with a relatively small number of nodes.

2. Analysis

2.1. ***Micromechanical model.*** The micromechanical analysis of a unidirectional fiber-reinforced composite subjected to a combined normal and thermal loading can be modeled using a generalized plane strain assumption [Wisnom 1990] instead of a 3D elasticity model. In the generalized plane strain condition displacement occurs in all three directions, except that strain components are not functions of the x_3 coordinate (fiber direction) and the normal strain in the x_3-direction is constant (Figure 1). Therefore, the displacement fields within the domain based on the generalized plane strain assumption should be considered as

$$u_1 = u_1(x_1, x_2), \quad u_2 = u_2(x_1, x_2), \quad u_3 = \varepsilon_0 x_3, \tag{1}$$

where u_1, u_2 and u_3 are the displacements in x_1, x_2 and x_3 directions, respectively, and ε_0 is an unknown normal constant strain in x_3-direction to be determined. Using the displacement field (1), the strain-displacement relations based on the linear theory of elasticity can be obtained as

$$\varepsilon_{11} = \frac{\partial u_1}{\partial x_1}, \quad \varepsilon_{22} = \frac{\partial u_2}{\partial x_2}, \quad \varepsilon_{33} = \frac{\partial u_3}{\partial x_3} = \varepsilon_0, \quad \varepsilon_{12} = \frac{1}{2}\left(\frac{\partial u_1}{\partial x_2} + \frac{\partial u_2}{\partial x_1}\right), \quad \varepsilon_{13} = 0, \quad \varepsilon_{23} = 0. \tag{2}$$

Using (2), one can conclude that the out-of-plane shear stresses vanish: $\sigma_{13} = \sigma_{23} = 0$. The governing equilibrium equations of the problem in the x_1- and x_2-directions in the absence of shear stresses σ_{13} and σ_{23} can be considered as

$$\sigma_{ij,j} + b_i = 0 \quad \text{on } \Omega, \quad i, j = 1, 2, \tag{3}$$

in which $\sigma_{ij,j}$ is the partial derivative of the stress component σ_{ij} with respect to x_j, b_i is the body force in x_i-direction and Ω is the solution domain. Note that the equilibrium equation in the x_3 (fiber) direction in the absence of body force b_3 is automatically satisfied as $\sigma_{13} = \sigma_{23} = 0$ and the σ_3 stress are independent of the x_3 coordinate.

2.2. ***Solution domain.*** In most micromechanical models, a periodic arrangement of fibers is assumed in the composite and therefore, the smallest repeating area of the cross section of the composite known as the representative volume element (RVE) is considered as the solution domain. It is assumed further that the global behavior of the composite is the same as that of the RVE. Here a quarter of the fibers and corresponding matrix in a square array of fiber arrangement is selected as the RVE, as shown on the right in Figure 1.

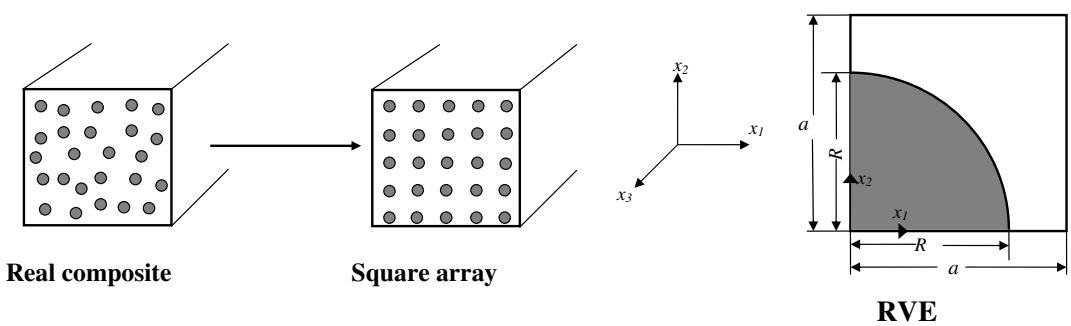

Figure 1. Left: real and idealized composite cross section (square array distribution). Right: the corresponding RVE.

2.3. ***Boundary and interface conditions.*** The boundary conditions must be set in such a way that the compatibility of the unit cell with neighboring cells in the infinite composite could be satisfied. For the thermomechanical loading of the composite in the absence of shear loading, the bottom edge of the RVE (x_1-axis) were not allowed to move in the x_2-direction and the left edge (x_2-axis) not allowed to move in the x_1-direction (Figure 1). The right edge can have an equal amount of the displacement in x_1-direction and the top edge can have an equal displacement in x_2-direction, so the nodes on right edge must be coupled in the x_2-direction. Similarly, the nodes on the top edge must be coupled in the x_1-direction. Therefore, appropriate boundary conditions on the various edges of the RVE can be considered as

$$\begin{aligned}
&\text{at } x_1 = 0: \quad u_1(0, x_2) = 0, \quad \sigma_{12} = 0, \\
&\text{at } x_1 = a: \quad u_1(a, x_2) = \bar{u}_1, \quad \sigma_{12} = 0, \quad \frac{1}{b}\int_{x_2=0}^{x_2=b} \sigma_1 dx_2 = \bar{\sigma}_1, \\
&\text{at } x_2 = 0: \quad u_2(x_1, 0) = 0, \quad \sigma_{12} = 0, \\
&\text{at } x_2 = b: \quad u_2(x_1, b) = \bar{u}_2, \quad \sigma_{12} = 0, \quad \frac{1}{a}\int_{x_1=0}^{x_1=a} \sigma_2 dx_1 = \bar{\sigma}_2, \quad \frac{1}{ab}\iint_{\Omega} \sigma_3 dx_1 dx_2 = \bar{\sigma}_3,
\end{aligned} \tag{4}$$

in which a is the length and b is the width of the RVE, $\bar{u}_i$ is the unknown constant displacement in the x_i-direction and $\bar{\sigma}_i$ is the applied transverse stress in the x_i-direction. The matrix is assumed to be perfectly bonded to the fibers throughout the analysis. This requires satisfaction of the continuity of displacements and reciprocity of traction at the fiber-matrix interface:

$$\boldsymbol{u}^f = \boldsymbol{u}^m, \quad \boldsymbol{t}^f + \boldsymbol{t}^m = 0, \tag{5}$$

where superscript f and m denote fiber and matrix, respectively, and $\boldsymbol{u}$ and $\boldsymbol{t}$ are the displacement and traction vectors on the interface. Solution of the governing equilibrium equation (3) together with the boundary conditions (4) in conjunction with the continuity of displacements and tractions at the interface (5) provides details of the distribution of various stress and strain components within the RVE.

3. Solution procedure

In this study, an appropriate Meshless Local Petrov–Galerkin (MLPG) formulation is presented for the generalized plane strain analysis of unidirectional composites subjected to thermomechanical loading. The MLPG solution procedure mainly includes three steps. 1- Approximation of the field variable $u(\boldsymbol{x})$ over randomly located nodes in the domain. 2- Converting the strong form of governing equations to the local symmetric weak form. 3- Numerical discretization of the weak form of the equations. In the first step the field variable must be approximated over the randomly distributed nodes and the trial functions must be constructed. One of the well-known methods for this purpose is the moving least squares (MLS) approximation technique [Atluri and Shen 2002] which is briefly described in the following section.

3.1. ***Moving least square (MLS) approximation.*** To approximate the distribution of the function $u(\boldsymbol{x})$ over a number of randomly located nodes within the domain by the MLS method, the unknown trial approximant $u^h(\boldsymbol{x})$ of the function $u(\boldsymbol{x})$ is defined as

$$u^h(\boldsymbol{x}) = \boldsymbol{p}^T(\boldsymbol{x})\boldsymbol{a}(\boldsymbol{x}), \quad \boldsymbol{x} \in \boldsymbol{\Omega}_{\boldsymbol{x}}, \tag{6}$$

where $\boldsymbol{p}^T(\boldsymbol{x}) = [p_1(\boldsymbol{x}), p_2(\boldsymbol{x}), \ldots, p_m(\boldsymbol{x})]$ is a complete monomial basis of order m and $\boldsymbol{a}(\boldsymbol{x})$ is a vector of unknown coefficients. For example, in a two-dimensional domain the complete monomial linear basis is $\boldsymbol{p}^T(\boldsymbol{x}) = [1, x_1, x_2]$, and the quadratic basis is $\boldsymbol{p}^T(\boldsymbol{x}) = [1, x_1, x_2, x_1^2, x_1x_2, x_2^2]$. In order to obtain the coefficients vector $\boldsymbol{a}(\boldsymbol{x})$, the weighted discrete norm

$$J(\boldsymbol{a}(\boldsymbol{x})) = \sum_{I=1}^{N} w_I(\boldsymbol{x})\big(\boldsymbol{p}^T(\boldsymbol{x}_I)\boldsymbol{a}(\boldsymbol{x}) - \hat{u}^I\big)^2 \tag{7}$$

should be minimized with respect to $\boldsymbol{a}(\boldsymbol{x})$. In (7) the $\hat{u}^I$ are fictitious nodal values of the field variable to be determined, w_I is a weigh function and N is the number of nodes in the neighborhood of $\boldsymbol{x}$ where the weight function vanishes: $w_I(\boldsymbol{x}) \neq 0$. In this study, quadratic spline functions are used:

$$w_I(\boldsymbol{x}) = \begin{cases} 1 - 6(d_I/r_I)^2 + 8(d_I/r_I)^3 - 3(d_I/r_I)^4 & \text{for } 0 \le d_I \le r_I, \\ 0 & \text{for } d_I \ge r_I, \end{cases} \tag{8}$$

where $d_I = |\boldsymbol{x} - \boldsymbol{x}_I|$ is the distance from the sampling point $\boldsymbol{x}$ to the node $\boldsymbol{x}_I$ and r_I is known as the radius of the domain of influence for the weight function $w_I(\boldsymbol{x})$ [Atluri and Shen 2002]. After obtaining $\boldsymbol{a}(\boldsymbol{x})$, one can determine from (6) the nodal interpolation form of $u^h(\boldsymbol{x})$:

$$u^h(\boldsymbol{x}) = \sum_{I=1}^{N} \phi^I(\boldsymbol{x})\hat{u}^I \quad \boldsymbol{x} \in \Omega_{\boldsymbol{x}}, \tag{9}$$

where $\phi^I(\boldsymbol{x})$ is the so-called shape function of the MLS approximation corresponding to node I and is defined as

$$\phi^I(\boldsymbol{x}) = \sum_{j=1}^{m} p_j(\boldsymbol{x})[\boldsymbol{A}^{-1}(\boldsymbol{x})\boldsymbol{B}(\boldsymbol{x})]_{jI}, \tag{10}$$

the matrices $\boldsymbol{A}(\boldsymbol{x})$ and $\boldsymbol{B}(\boldsymbol{x})$ being defined by

$$\boldsymbol{A}(\boldsymbol{x}) = \sum_{I=1}^{N} w_I(\boldsymbol{x})\boldsymbol{p}(\boldsymbol{x}_I)\boldsymbol{p}^T(\boldsymbol{x}_I), \tag{11}$$

$$\boldsymbol{B}(\boldsymbol{x}) = [w_1(\boldsymbol{x})\boldsymbol{p}(\boldsymbol{x}_1), w_2(\boldsymbol{x})\boldsymbol{p}(\boldsymbol{x}_2), \ldots, w_N(\boldsymbol{x})\boldsymbol{p}(\boldsymbol{x}_N)]. \tag{12}$$

Note that the shape functions derived from the MLS approximation are not orthonormal (that is, it need not be the case that $\phi^I(\boldsymbol{x}_J) = \delta_{IJ}$ and $u^h(\boldsymbol{x}_I) = \hat{u}^I$). Therefore, the enforcement of essential boundary conditions in the MLPG method has some difficulties and in the MLPG method, usually a penalty parameter or the Lagrange method is used for enforcement of the essential boundary conditions.

3.2. ***MLPG formulation.*** The MLPG method is based on the local weak form of the equations over the local subdomain Ω_s that is located inside the global domain Ω. The generalized local weak form (3) over the local subdomain of node I, Ω_s^I, can be written as

$$\int_{\Omega_s^I} (\sigma_{ij,j} + b_i)v_i \, d\Omega_s - \beta \int_{\Gamma_{su}^I} (u_i - \bar{u}_i)\, d\Gamma = 0, \tag{13}$$

where u_i and v_i are the trial and test (weight) functions, respectively, Γ^I_{su} is the part of the boundary of subdomain of node I i.e., $\partial\Omega^I_s$, over which the essential boundary conditions are specified and β is a large number which is known as penalty parameter and is employed in order to impose essential boundary conditions. Using the identity $\sigma_{ij,j}v_j = (\sigma_{ij}v_j)_{,j} - \sigma_{ij}v_{i,j}$ and applying the divergence theorem, the local symmetric weak form of (13) can be written as

$$\int_{\partial\Omega^I_s} \sigma_{ij}n_j v_i d\Gamma - \int_{\Omega^I_s} (\sigma_{ij}v_{i,j} - b_i v_i)\, d\Omega - \beta\int_{\Gamma^I_{su}} (u_i - \bar{u}_i)v_i d\Gamma = 0, \tag{14}$$

where n_j is the unit outward normal of the $\partial\Omega^I_s$. In general Ω^I_s could have arbitrary shape and $\partial\Omega^I_s$ consists of three parts: $\partial\Omega^I_s = L^I_s \cup \Gamma^I_{st} \cup \Gamma^I_{su}$, in which L^I_s, Γ^I_{st} and Γ^I_{su} are parts of the local boundary that are located totally inside the global domain, coincides with the global traction boundary and coincides with the global essential boundary, respectively. We can rewrite (14) in terms of L^I_s, Γ^I_{st}, and Γ^I_{su} as

$$\int_{\Omega^I_s} (\sigma_{ij}v_{i,j})\, d\Omega - \int_{L^I_s} t_i v_i d\Gamma - \int_{\Gamma^I_{su}} t_i v_i d\Gamma + \beta\int_{\Gamma^I_{su}} u_i v_i d\Gamma = \int_{\Gamma^I_{st}} \bar{t}_i v_i\, d\Gamma + \beta\int_{\Gamma^I_{su}} \bar{u}_i v_i\, d\Gamma + \int_{\Omega^I_s} b_i v_i d\Omega, \tag{15}$$

where $t_i = \sigma_{ij}n_j$ is the reaction vector on the boundary of the subdomain and $\bar{t}_i$ is the natural boundary condition on Γ^I_{st}. Unlike the conventional Galerkin method in which the trial and test functions are chosen from the same space, the Petrov–Galerkin method uses the trial and test functions from different spaces. In this study, in order to reduce the computational

time, the test functions v_i are chosen such that the domain integral on Ω^I_s is eliminated. This can be accomplished by using the unit step function as the test function in each subdomain as

$$v_i(\boldsymbol{x}) = \begin{cases} 1 & \text{for } \boldsymbol{x} \in \Omega^I_s, \\ 0 & \text{for } \boldsymbol{x} \notin \Omega^I_s. \end{cases} \tag{16}$$

It is clear that the partial derivatives of the unit step function are identically zero, and therefore, the corresponding domain integral in (15) is eliminated. The final form of the local symmetric weak form can be written as

$$-\int_{L^I_s} t_i d\Gamma - \int_{\Gamma^I_{su}} t_i d\Gamma + \beta\int_{\Gamma^I_{su}} u_i d\Gamma = \int_{\Gamma^I_{st}} \bar{t}_i d\Gamma + \beta\int_{\Gamma^I_{su}} \bar{u}_i d\Gamma + \int_{\Omega^I_s} b_i d\Omega. \tag{17}$$

Note that by ignoring the body forces, any domain integration is eliminated from (17).

3.3. ***Numerical discretization.*** Assuming a linear isotropic elastic behavior for both the fiber and matrix and the generalized plane strain condition, the compact form of the stress-strain relations in the presence of temperature change ΔT for each phase in the RVE can be written as

$$\left.\begin{aligned} \boldsymbol{\sigma}^i &= \boldsymbol{D}^i\boldsymbol{\varepsilon} + \hat{\boldsymbol{D}}^i\varepsilon_0 - \hat{\hat{\boldsymbol{D}}}^i\Delta T, \\ \sigma^i_{33} &= (\hat{\boldsymbol{D}}^i)^T\boldsymbol{\varepsilon} + (1-\nu^i)C^i\varepsilon_0 - \frac{E^i\alpha^i}{1-2\nu^i}\Delta T, \end{aligned}\right\} \qquad i = f, m, \tag{18}$$

where f and m denote the fiber and the matrix, $\boldsymbol{\sigma} = \{\sigma_{11}\ \ \sigma_{22}\ \ \sigma_{12}\}^T$ is the stress tensor, σ_{33} is the axial stress in the fiber direction, $\boldsymbol{\varepsilon} = \{\varepsilon_{11}\ \ \varepsilon_{22}\ \ 2\varepsilon_{12}\}^T$ is the strain tensor, ε_0 is the constant strain in the fiber

direction, $\boldsymbol{D}^i$, $\hat{\boldsymbol{D}}^i$, $\hat{\hat{\boldsymbol{D}}}^i$ are defined by

$$\boldsymbol{D}^i = C^i \begin{bmatrix} 1-\nu^i & \nu^i & 0 \\ \nu^i & 1-\nu^i & 0 \\ 0 & 0 & (1-2\nu^i)/2 \end{bmatrix}, \quad \hat{\boldsymbol{D}}^i = \nu^i C^i \begin{Bmatrix} 1 \\ 1 \\ 0 \end{Bmatrix}, \quad \hat{\hat{\boldsymbol{D}}}^i = \frac{E^i \alpha^i}{1-2\nu^i} \begin{Bmatrix} 1 \\ 1 \\ 0 \end{Bmatrix}. \tag{19}$$

Here E is the elastic modulus, ν is the Poisson's ratio, α is the coefficient of thermal expansion of the constituents, and

$$C^i = \frac{E^i}{(1-2\nu^i)(1+\nu^i)}.$$

Furthermore, the traction, $t_i = \sigma_{ij} n_j$ on the boundary of the support domain, $\partial\Omega_s^I$, in the matrix form can be obtained using (19) as

$$\boldsymbol{t} = \boldsymbol{N}\boldsymbol{\sigma} = \boldsymbol{N}\boldsymbol{D}\boldsymbol{\varepsilon} + \boldsymbol{N}\hat{\boldsymbol{D}}\varepsilon_0 - \boldsymbol{N}\hat{\hat{\boldsymbol{D}}}\Delta T. \tag{20}$$

By substituting (20) into (18) and using the MLS approximation (9), we obtain the discretized local weak form of governing equations (17):

$$\begin{aligned} -\sum_{J=1}^{N}\int_{L_s^I} \boldsymbol{N}\boldsymbol{D}\boldsymbol{B}^J \hat{\boldsymbol{u}}^J \, d\Gamma - \sum_{J=1}^{N}\int_{\Gamma_{su}^I} \boldsymbol{S}\boldsymbol{N}\boldsymbol{D}\boldsymbol{B}^J \hat{\boldsymbol{u}}^J \, d\Gamma + \beta \sum_{J=1}^{N}\int_{\Gamma_{su}^I} \boldsymbol{S}\boldsymbol{\Phi}^J \hat{\boldsymbol{u}}^J \, d\Gamma = \int_{\Omega_s^I} \boldsymbol{b}\, d\Omega + \int_{\Gamma_{st}^I} \bar{\boldsymbol{t}}\, d\Gamma \\ + \varepsilon_0 \left(\int_{L_s^I} \boldsymbol{N}\hat{\boldsymbol{D}}\, d\Gamma + \int_{\Gamma_{su}^I} \boldsymbol{N}\hat{\boldsymbol{D}}\, d\Gamma \right) - \Delta T \left(\int_{L_s^I} \boldsymbol{N}\hat{\hat{\boldsymbol{D}}}\, d\Gamma + \int_{\Gamma_{su}^I} \boldsymbol{N}\hat{\hat{\boldsymbol{D}}}\, d\Gamma \right) + \beta \int_{\Gamma_{su}^I} \bar{\boldsymbol{u}}\, d\Gamma, \end{aligned} \tag{21}$$

in which

$$\boldsymbol{B}^J = \begin{bmatrix} \phi^J_{,1} & 0 & \phi^J_{,2} \\ 0 & \phi^J_{,2} & \phi^J_{,1} \end{bmatrix}^T, \quad \boldsymbol{\Phi}^J = \begin{bmatrix} \phi^J & 0 \\ 0 & \phi^J \end{bmatrix}, \quad \boldsymbol{N} = \begin{bmatrix} n_1 & 0 & n_2 \\ 0 & n_2 & n_1 \end{bmatrix}, \quad \boldsymbol{S} = \begin{bmatrix} S_1 & 0 \\ 0 & S_2 \end{bmatrix}, \tag{22}$$

with (n_1, n_2) the outward unit normal vector to the boundary of the local subdomain $\partial\Omega_s^I$ and $\boldsymbol{S}$ the essential boundary conditions index (if u_i is prescribed on Γ_u, the index S_i is equal to 1; otherwise $S_i = 0$). Also, $\phi^J_{,i}$ is the partial derivative of $\phi^J(\boldsymbol{x})$ with respect to the x_i; details can be found in [Atluri and Shen 2002].

Equation (21) can be written in the standard form of linear algebraic equations in terms of $\hat{\boldsymbol{u}}^J$ as

$$\sum_{J=1}^{N} \boldsymbol{K}_{\boldsymbol{IJ}} \hat{\boldsymbol{u}}^J = \boldsymbol{f}_I, \tag{23}$$

where

$$\boldsymbol{K}_{\boldsymbol{IJ}} = -\int_{L_s^I} \boldsymbol{N}\boldsymbol{D}\boldsymbol{B}^J \, d\Gamma - \int_{\Gamma_{su}^I} \boldsymbol{S}\boldsymbol{N}\boldsymbol{D}\boldsymbol{B}^J \, d\Gamma + \beta \int_{\Gamma_{su}^I} \boldsymbol{S}\boldsymbol{\Phi}^J \, d\Gamma, \tag{24}$$

$$\begin{aligned} \boldsymbol{f}_I = \int_{\Gamma_{st}^I} \bar{\boldsymbol{t}}\, d\Gamma + \varepsilon_0 \left(\int_{\Gamma_s^I} \boldsymbol{N}\hat{\boldsymbol{D}}\, d\Gamma + \int_{\Gamma_{su}^I} \boldsymbol{N}\hat{\boldsymbol{D}}\, d\Gamma \right) \\ - \Delta T \left(\int_{\Gamma_s^I} \boldsymbol{N}\hat{\hat{\boldsymbol{D}}}\, d\Gamma + \int_{\Gamma_{su}^I} \boldsymbol{N}\hat{\hat{\boldsymbol{D}}}\, d\Gamma \right) + \beta \int_{\Gamma_{su}^I} \bar{\boldsymbol{u}}\, d\Gamma + \int_{\Omega_s^I} \boldsymbol{b}\, d\Omega. \end{aligned} \tag{25}$$

It is worth mentioning that the stiffness matrix $\boldsymbol{K}_{\boldsymbol{IJ}}$ in the present method is banded and asymmetric.

3.4. ***Material discontinuity.*** In order to treat the material discontinuity at the fiber and matrix interface, two sets of nodes are assigned on the interface at the same location with different material properties. One set is dedicated to the fiber denoted as I^f while the other set is related to the matrix denoted by I^m. Furthermore, a non-penetration rule is imposed to the influence domain of the nodes. This rule states that any point related to the matrix area cannot be influenced by the nodes in the fiber region and the fiber interface nodes, I^f and vise versa. This rule confines the influence domain of a node within the domain of the material of the same node. Finally, the displacement continuity and traction reciprocity conditions in (5) must be satisfied for the nodes on the interface as

$$\boldsymbol{u}^{I^f} = \boldsymbol{u}^{I^m}, \quad \boldsymbol{t}^{I^f} + \boldsymbol{t}^{I^m} = 0. \tag{26}$$

The discretized form of these equations for all interface nodes can be rewritten as

$$\sum_{J=1}^{N_f} (\boldsymbol{\Phi}^J(\boldsymbol{x}_{I^f})\hat{\boldsymbol{u}}^J)^f = \sum_{J=1}^{N_m} (\boldsymbol{\Phi}^J(\boldsymbol{x}_{I^m})\hat{\boldsymbol{u}}^J)^m, \tag{27}$$

$$\sum_{J=1}^{N_f} (\boldsymbol{NDB}^J\hat{\boldsymbol{u}}^J + \boldsymbol{N}\hat{\boldsymbol{D}}\boldsymbol{\varepsilon}_0 - \boldsymbol{N}\hat{\hat{\boldsymbol{D}}}\Delta T)^f = \sum_{J=1}^{N_m} (\boldsymbol{NDB}^J\hat{\boldsymbol{u}}^J + \boldsymbol{N}\hat{\boldsymbol{D}}\boldsymbol{\varepsilon}_0 - \boldsymbol{N}\hat{\hat{\boldsymbol{D}}}\Delta T)^m, \tag{28}$$

where N_f is the total nodes in the fiber and Nm is the total nodes in the matrix. In order to impose conditions (27) and (28) to the global stiffness and force matrix (23), the rows of the global stiffness and force matrix that are related to the interface nodes are replaced by the discretized form of the displacement and traction continuity equations (27) and (28). This leads to a direct implementation of the fiber-matrix interface conditions to the global system of equations.

4. Numerical results and discussion

The fabrication process of the composite materials, in particular metal-matrix composites (MMCs), takes place at high temperatures. Subsequently, when they are cooled down to room temperature, residual stresses are generated in the composite due to the mismatch between the coefficients of thermal expansion of the fiber and matrix. The generated residual stresses influence the overall thermomechanical properties of the composite. In the numerical results, the silicon carbide – titanium (SiC/Ti) metal-matrix composite

Composite system	Constituent	E (GPa)	ν	α ($10^{-6}/°$C)
SiC/Ti	SiC (fiber) Ti (matrix)	409 107	0.2 0.35	4.5 10
glass/epoxy	glass (fiber) epoxy (matrix)	72 3.5	0.2 0.35	5 52.5
[Shaw and Miracle 1996] [Nimmer et al. 1991]	Ti (fiber) SiC (matrix)	113.8 414	0.3 0.3	9.8 4.86

Table 1. Material properties of the fiber and matrix (E = Young's modulus; ν = Poisson's ratio; α = coefficient of thermal expansion).

and glass/epoxy polymer-matrix composite are studied. The composite constituents are assumed to be isotropic and homogeneous with the linear thermoelastic properties as shown in Table 1. To examine the efficiency and accuracy of the method, another analysis is carried out in the commercial finite element code ANSYS [2002].

In this session, the previously discussed micromechanical model with MLPG formulation is used to predict the process induced thermal residual stress in the SiC/Ti metal-matrix composite with 35% fiber volume fraction. The SiC/Ti composite is manufactured at the temperature of about 910°C that is assumed to be stress free temperature of this composite. At room temperature (25°C) the composite is subjected to a temperature change of about $\Delta T = -885$°C.

4.1. ***Pure thermal loading.*** The first step is to examine the rate of convergence of the method through a mesh sensitivity analysis. To this end, a 35% fiber volume fraction SiC/Ti composite system is subjected to a uniform thermal load of $\Delta T = -885$°C. Figure 2 shows the rate of convergence of the MLPG and ANSYS for the transverse displacement in the right side ($x_1 = a$) of the RVE in the x_1 direction. The results suggest that about 300 nodes are sufficient to provide final convergence in MLPG, while some 800 nodes are needed for convergence in FE analysis. Therefore, in order to maintain convergence, 350 and 1000 nodes, respectively, are used for all MLPG and FE results.

Thermal loading. The coefficient of thermal expansion (CTE) of the composite can be obtained by applying a pure thermal loading on the RVE. The CTE $\alpha_i = \varepsilon_i / \Delta T$ in the direction x_i is the quotient of the macroscopic total thermal strain ε_i in that direction by the applied thermal load ΔT. Figure 3 shows the longitudinal (α_3) and transverse ($\alpha_1 = \alpha_2$) CTE versus fiber volume fraction for a unidirectional glass/epoxy composite. Included in the figures are also predictions obtained by other approximate closed-form solutions [Van Fo Fy 1965; Rogers et al. 1977; Chamis 1984], FEM [Haktan Karadeniz and Kumlutas 2007] method and experimental measurements [Sideridis 1994]. It can be seen in the figures that predictions of the MLPG method are in the close agreement with the FEM and experiment for both longitudinal and transverse CTE. However, there are some discrepancies between the results of various approximate closed-form solutions in the transverse CTE of the glass/epoxy composite, mainly due to their various simplifying assumptions.

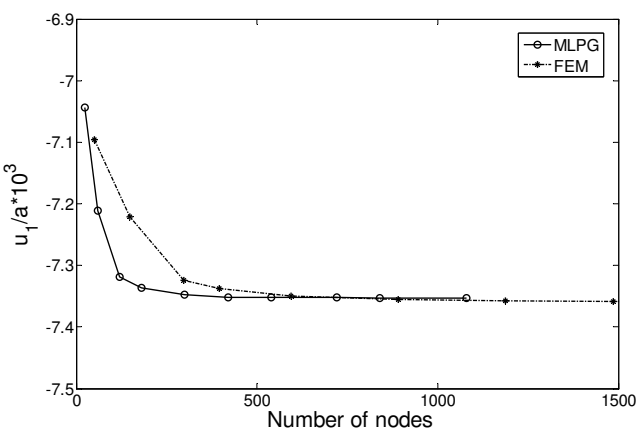

Figure 2. Convergence of u_1 displacement on the right side ($x_1 = a$) of the RVE.

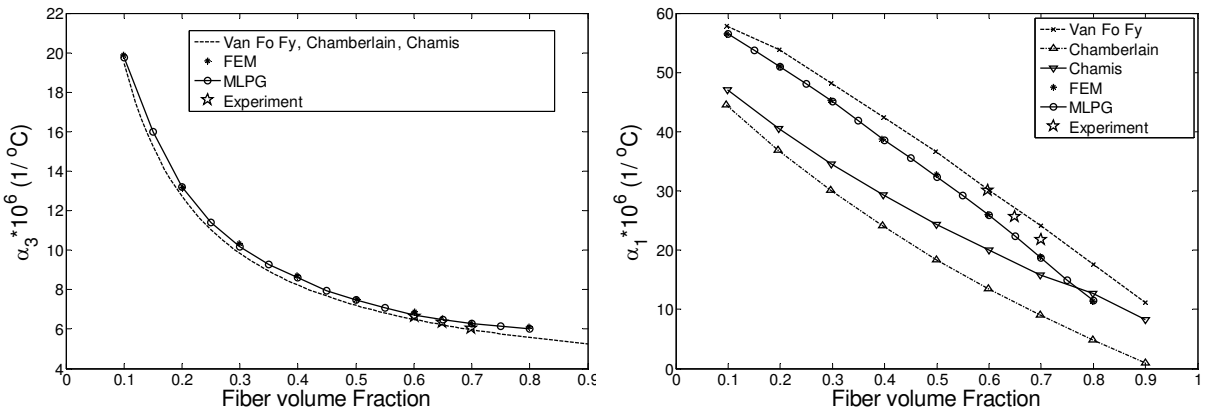

Figure 3. Longitudinal (left) and transverse (right) coefficients of thermal expansion of glass/epoxy composite. "FEM" and "Chamberlain" stand for the values in [Haktan Karadeniz and Kumlutas 2007] and "Experiment" for those in [Sideridis 1994].

Table 2 shows the CTE of SiC/Ti composite system predicted by MLPG, FE and approximate closed-form solutions [Van Fo Fy 1965; Rogers et al. 1977; Chamis 1984]. Again, very good agreement is seen between the results of MLPG and FE model while some differences exist in the predictions of approximate methods (loc. cit.), particularly in the transverse CTE.

We next consider the predicted manufacturing thermal residual stresses within the RVE of the SiC/Ti composite with 35% FVF induced by cooldown from 900°C to 25°C. Table 3 shows the stress components on the matrix side of the fiber-matrix interface at the point on the bottom edge of the RVE with coordinates $(R, 0)$. It also shows the results of ADINA finite element code presented in [Nimmer et al. 1991]. Discrepancies in the range from 5% to 10% are observed between the results there and ours. One possible reason for the discrepancies is that, in their FE analysis, Nimmer et al. regarded certain matrix properties as temperature-dependent, while we took them as temperature-independent in this study.

CTE	model	Fiber volume fraction				
		20%	35%	50%	60%	70%
$\alpha_1 = \alpha_2$	[Van Fo Fy 1965]	9.5400	8.7912	7.8989	7.2576	6.5916
	[Rogers et al. 1977]	8.3242	7.2080	6.1938	5.5678	4.9777
	[Chamis 1984]	9.7013	8.5327	7.2717	6.5074	5.8390
	[ANSYS 2002]	9.1705	8.3116	7.4112	6.7912	6.1264
	MLPG	9.1663	8.3058	7.4021	6.7815	6.0987
α_3	[Van Fo Fy 1965]	7.3124	6.2984	5.6405	5.3168	5.0545
	[ANSYS 2002]	7.4092	6.3981	5.7212	5.3812	5.1385
	MLPG	7.4006	6.3929	5.7164	5.3805	5.1322

Table 2. Coefficients of thermal expansion ($\times 10^6/°\text{C}$) of SiC/Ti metal-matrix composite, as predicted by approximate closed-form solutions (first three rows), FEM [ANSYS 2002] and the MLPG proposed here.

model	Radial stress σ_1 (MPa)	Hoop stress σ_2 (MPa)	Axial stress σ_3 (MPa)	Effective stress σ_{eff} (MPa)
MLPG	−329.8	559.7	395.3	819.8
FEM [Nimmer et al. 1991]	−314.2	509.8	371.90	760.5
discrepancy	4.96%	9.78%	6.29%	7.80%

Table 3. Thermal residual stress components on the matrix side of the interface at the point $(R, 0)$.

model	$\sigma_{1\,\max}$ at interface on x_1-axis	$\sigma_{2\,\max}$ in matrix near interface on diagonal line	σ_3 in fiber near interface on x_1-axis	$\sigma_{3\,\max}$ in matrix near interface on diagonal line	$\sigma_{3\,\min}$ in matrix near interface on x_1-axis
MLPG	−305.1	488.5	−779.8	354.2	310.4
FEM [Shaw and Miracle 1996]	−288	466	−782	354	316
discrepancy	5.93%	4.82%	−0.28%	0.056%	−1.77%

Table 4. Thermal residual stress (MPa) in SiC/Ti with 30% FVF system cool down from 800°C to 25°C.

Shaw and Miracle [1996] used ANSYS finite element code to study the SiC/Ti composite with 30% FVF cooled down from 800°C to 25°C. They used temperature-independent properties for fiber and matrix and considered a thin interfacial coating layer between the fiber and matrix. Table 4 compares their predictions for various thermal residual stresses with ours, showing reasonably good agreement.

Since the coefficient of thermal expansion of titanium is significantly higher than that of silicon carbide, it experiences greater contraction during cooldown, and relatively large radial compressive stresses build up at the fiber-matrix interface. The dimensionless displacements u_1/a at the bottom $(x_2 = 0)$ and top path $(x_2 = a)$ of the RVE induced during the cooling from 910°C to 25°C are shown in Figure 4. This

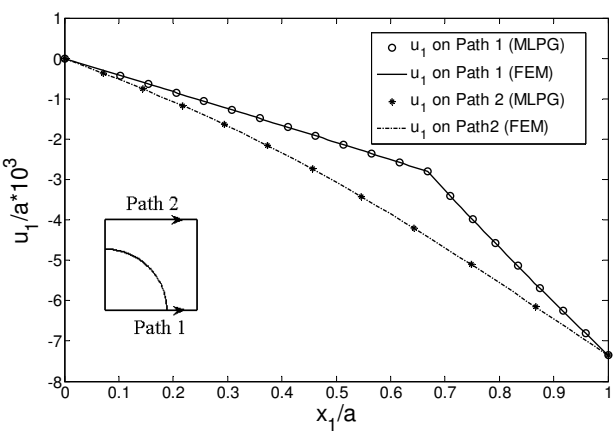

Figure 4. Displacement u_1 on the bottom path $(x_2 = 0)$ and top path $(x_2 = a)$ of the RVE in SiC/Ti composite after cooling; $\Delta T = -885$°C.

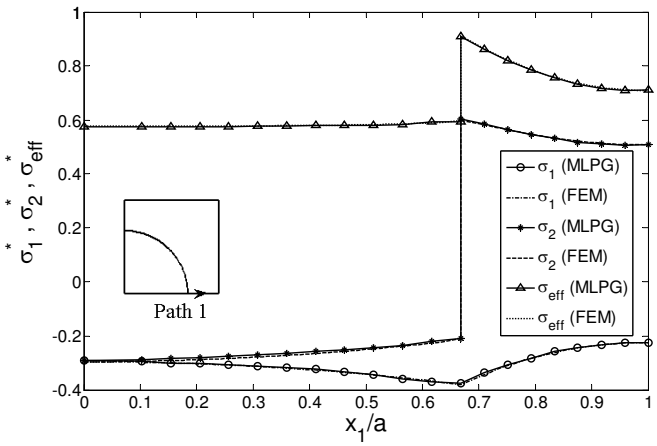

Figure 5. Distribution of thermal residual stresses σ_1^*, σ_2^* and σ_{eff}^* on the bottom path 1 of the RVE, $\Delta T = -885°\text{C}$.

figure includes the prediction of MLPG and ANSYS code. It is seen that the RVE contracts about 0.735% in transverse direction after cooling. On the bottom path, the slope of displacement in the matrix (Ti) is higher than that of fiber (SiC). It is clear that the MLPG method presented here is in appropriate agreement with FEM in the prediction of displacement distribution within the RVE. Both MLPG and FEM predict continuous displacement in the fiber-matrix interface. The contraction of the RVE in the fiber direction predicted by MLPG and FEM is 0.7350% and 0.7355%, respectively.

The distribution of dimensionless normal residual stresses σ_1^* and σ_2^* and effective von Mises stress σ_{eff}^* on the bottom path (x_1-axis) of the RVE is shown in Figure 5. In this study the dimensionless stress is defined as $\sigma^* = \sigma / Y_m$, where Y_m is the yield stress of Ti and taken $Y_m = 910\,\text{MPa}$. It is obvious that along the bottom path, the σ_1 stress is the radial stress and σ_2 stress is the hoop stress.

As expected, because the CTE of Ti is higher than of SiC, on the bottom path the σ_1^* stress is compressive in both fiber and matrix and is continuous at the fiber-matrix interface. On the bottom path, the σ_2^* stress is compressive in fiber, is tensile in the matrix, and is discontinuous at fiber matrix interface. As seen in Figure 5, although the effective stress induced through the cooling is large, it does not exceed the yield stress of the matrix and no yielding occurs during the cooling. The figure suggests excellent agreement between the MLPG predictions and the ANSYS results.

The distributions of the residual circumferential stress σ_θ^*, normal stress σ_n^* and shear stress $\sigma_{n\theta}^*$ at the fiber-matrix interface are shown in Figure 6. At the interface, σ_θ^* is compressive in the fiber and is tensile in the matrix. The tensile σ_θ stress in the matrix may cause micro cracks in the matrix normal to the interface. The radial stress is compressive on entire interface and reaches its greatest value, about $-337\,\text{MPa}$, at $\theta = 0$ and $\theta = 90°$. The compressive residual stress at the fiber-matrix interface has a beneficial effect on the transverse behavior of the MMC with a weak interface [Nimmer 1990; Nimmer et al. 1991; Wisnom 1990].

In order to illustrate the accuracy of our MLPG method over the entire domain, the spatial variation of residual von Mises effective stress (σ_{eff}) predicted by the MLPG model and an FEM model are visualized in Figure 7. It can be seen that the pattern of the stress distribution is completely similar in MLPG and

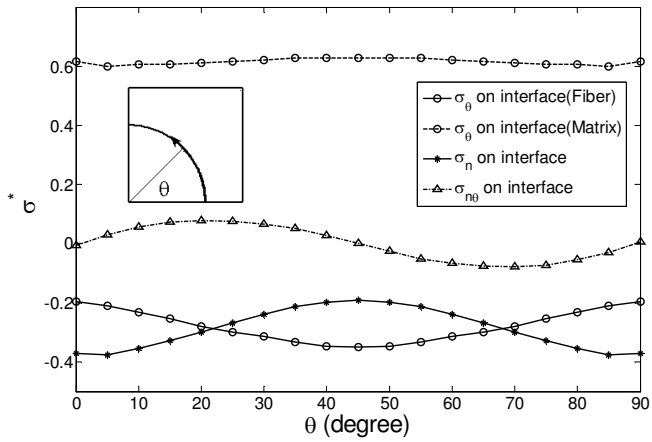

Figure 6. Distribution of dimensionless thermal residual stress σ_θ^*, σ_n^* and $\sigma_{n\theta}^*$ on the interface, $\Delta T = -885°\text{C}$.

FEM analysis. The effective stress in the fiber is uniform, about 527 MPa, and in the matrix varies from less than 300 MPa to more than 750 MPa. The largest value of the effective stress occurs at the fiber-matrix interface on the x_1-axis and x_2-axis. These locations are along the radial lines between closest neighbor fibers. The lowest effective stress is in top-right corner ($x_1 = x_2 = a$) of the RVE which is along the radial line between most distant neighbor fibers.

The radial residual stress σ_r^* is compressive in the fiber and the circumferential (hoop) stress σ_θ^* is compressive in the fiber and is tensile in the matrix. The axial stress σ_3^* in the fiber and matrix is fairly uniform and is compressive in the fiber and is tensile in the matrix. In the absence of axial load, the net force from the integration of local distribution of σ_3 over the entire face of the RVE is zero for any temperature distribution. The axial stress σ_3 on the fiber is almost uniform, with values between -793 and -782 MPa.

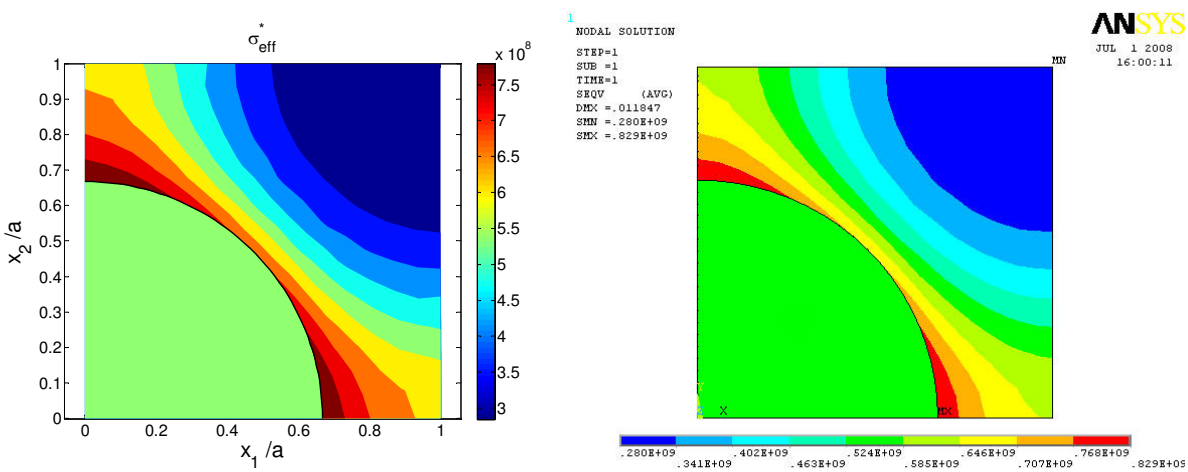

Figure 7. Distribution of von Mises effective stress σ_{eff} in the RVE, $\Delta T = -885°\text{C}$, as predicted by MLPG (left) and ANSYS (right).

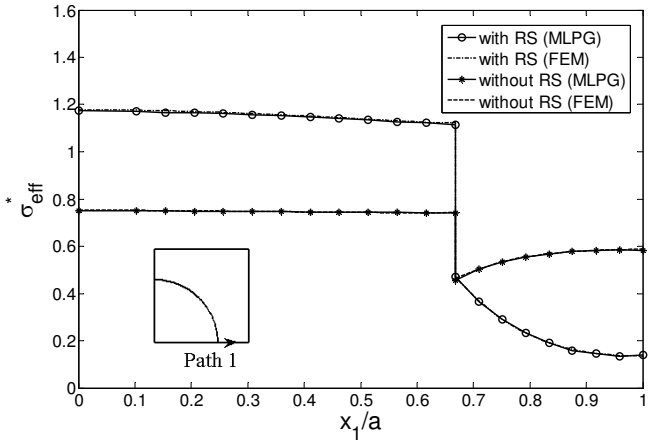

Figure 8. Dimensionless stress σ^*_{eff} on the bottom path for uniaxial tensile load $\bar{\sigma}_1 = +0.5Y_m$ with and without consideration of thermal residual stress.

4.2. ***Thermomechanical loading.*** In this section, the effect of thermal residual stress in the behavior of SiC/Ti system with 35% FVF under transverse mechanical normal loading is studied.

Transverse uniaxial loading. First, it is supposed that the SiC/Ti composite system is subjected to an external transverse tensile macro-stress $\bar{\sigma}_1 = 0.5Y_m = 455\,\text{MPa}$ in the x_1 direction. Figure 8 shows the distribution of σ^*_{eff} stress on the bottom path of the RVE with and without considering the thermal residual stress using the MLPG and the FE method. It is seen in the figure that in the presence of residual stress, the von Mises effective stress on the bottom path is increased in the fiber and is decreased in the matrix. Very close agreement is seen between the results of the present method and FEM analysis. It is concluded that our MLPG method has appropriate accuracy in the prediction of thermomechanical behavior of composite materials. The effect of the presence of thermal residual stress on the distribution of the dimensionless normal σ^*_n and shear stress $\sigma^*_{n\theta}$ at the fiber-matrix interface are shown in Figure 9.

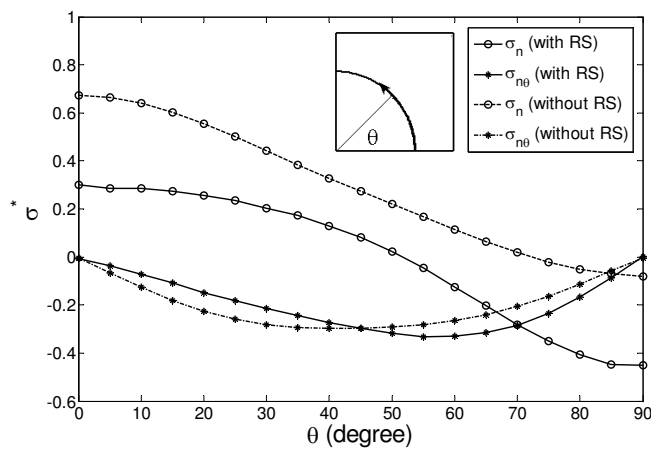

Figure 9. Dimensionless stress σ^*_n and $\sigma^*_{n\theta}$ on the interface for uniaxial tensile load $\bar{\sigma}_1 = +0.5Y_m$, considering thermal residual stress.

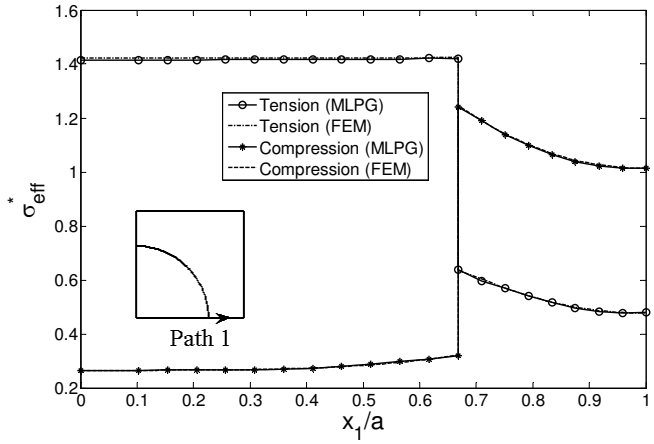

Figure 10. Dimensionless stress σ^*_{eff} on the bottom Path 1 of the RVE, biaxial tensile and compressive load $\bar{\sigma}_1 = \bar{\sigma}_2 = \pm 0.5 Y_m$ with considering thermal residual stress.

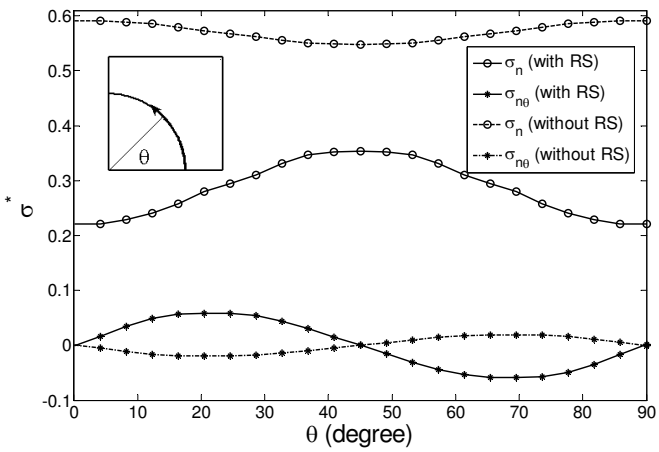

Figure 11. Dimensionless stress σ^*_n and $\sigma^*_{n\theta}$ on the interface for biaxial tensile load $\bar{\sigma}_1 = \bar{\sigma}_2 = +0.5 Y_m$, -Effect of thermal residual stress.

The maximum value of the normal to interface stress σ_n is decreased in the presence of thermal residual stress from 611.4 to 274.1 MPa. Therefore, thermal residual stresses have beneficial effect for metal-matrix composite with weak interface bonding [Nimmer 1990; Nimmer et al. 1991; Wisnom 1990].

Transverse biaxial loading. The behavior of the SiC/Ti composite with 35% FVF under biaxial transverse loading in presence of thermal residual stress is studied. For this case, the equal transverse normal tensile $\bar{\sigma}_1 = \bar{\sigma}_2 = +0.5 Y_m$ and compressive $\bar{\sigma}_1 = \bar{\sigma}_2 = -0.5 Y_m$ stresses are applied to the SiC/Ti composite system. Figure 10 shows the distribution of the dimensionless effective stress σ^*_{eff} on the bottom path of the RVE in the biaxial transverse tension and compression in the presence of thermal residual stress. It is seen that the von Mises effective stress in tension and compression does not have the same values. This will cause asymmetric yielding behavior for SiC/Ti MMC in the transverse tension and compression. In addition, it is seen that in the matrix the effective stress σ^*_{eff} for compressive transverse load is bigger

than for the same tensile load. Therefore, it can be concluded that the smaller compressive transverse load will cause yielding of SiC/Ti composite in comparison with the transverse tensile load.

The distributions of the dimensionless normal to fiber-matrix interface stress σ_n^* and shear stress on interface $\sigma_{n\theta}^*$ are shown in Figure 11. The stresses on the interface have symmetry respect to $\theta = 45°$. Thermal residual stresses change the location of maximum of σ_n from $\theta = 0$ and $\theta = 90°$ to $\theta = 45°$. In the presence of thermal residual stress the σ_n stress on x_1- and x_2-axis ($\theta = 0$ and $\theta = 90°$) decreases from 538.3 to 200.7 MPa and at the location $\theta = 45$ is decreased from 499.1 to 321.9 MPa.

5. Conclusion

An appropriate meshless local Petrov–Galerkin method is presented for micromechanical modeling of the unidirectional composites subjected to various thermomechanical loadings. Generalized plane strain assumption in the context of theory of elasticity is used to obtain the governing partial differential equations of the problem. A direct method is introduced for the treatment of material discontinuity at the fiber-matrix interface in which both the displacement continuity and traction reciprocity are satisfied. This MLPG method together with the MLS approximation is employed to obtain a solution for the governing equations over the selected RVE with appropriate boundary conditions. The computational time is substantially reduced by employing the unit step function as the test function. The accuracy and convergence rate of the method for micromechanical analysis of unidirectional composite is investigated. The mesh sensitivity analysis revealed that in comparison with the finite element analysis, the method presented provides highly accurate results with relatively small number of nodes. Comparison of the coefficient of thermal expansion, displacement and stress components distribution with experimental, numerical and analytical methods shows good agreement.

References

[Adams and Doner 1967] D. F. Adams and D. R. Doner, "Transverse normal loading of a unidirectional composite", *J. Compos. Mater.* **1**:2 (1967), 152–164.

[Aghdam and Khojeh 2003] M. M. Aghdam and A. Khojeh, "More on the effects of thermal residual and hydrostatic stresses on yielding behavior of unidirectional composites", *Compos. Struct.* **62**:3–4 (2003), 285–290.

[Aghdam et al. 2000] M. M. Aghdam, D. J. Smith, and M. J. Pavier, "Finite element micromechanical modelling of yield and collapse behaviour of metal matrix composites", *J. Mech. Phys. Solids* **48**:3 (2000), 499–528.

[ANSYS 2002] *ANSYS documentation*, ANSYS, Inc., Canonsburg, PA, 2002, Available at http://www.ansys.com/services/ss-documentation-manuals.asp.

[Arsenault and Taya 1987] R. J. Arsenault and M. Taya, "Thermal residual stresses in metal matrix composite", *Acta Metall.* **35**:3 (1987), 651–659.

[Atluri and Shen 2002] S. N. Atluri and S. Shen, *The meshless local Petrov–Galerkin (MLPG) method*, Tech Science Press, Encino, CA, 2002.

[Atluri and Zhu 1998] S. N. Atluri and T. Zhu, "A new meshless local Petrov–Galerkin (MLPG) approach in computational mechanics", *Comput. Mech.* **22**:2 (1998), 117–127.

[Atluri and Zhu 2000] S. N. Atluri and T. Zhu, "The meshless local Petrov–Galerkin (MLPG) approach for solving problems in elasto-statics", *Comput. Mech.* **25**:2–3 (2000), 169–179.

[Belytschko et al. 1994] T. Belytschko, Y. Y. Lu, and L. Gu, "Element-free Galerkin methods", *Int. J. Numer. Methods Eng.* **37**:2 (1994), 229–256.

[Brayshaw and Pindera 1994] J. B. Brayshaw and M.-J. Pindera, "The effect of matrix constitutive model on residual thermal stresses in MMC", *J. Eng. Mater. Technol. (ASME)* **116**:4 (1994), 505–511.

[Chamis 1984] C. C. Chamis, "Simplified composite micromechanics equations for hygral, thermal and mechanical properties", *SAMPE Q.* **15**:3 (1984), 14–23.

[Ching and Batra 2001] H.-K. Ching and R. C. Batra, "Determination of crack tip fields in linear elastostatics by the meshless local Petrov–Galerkin (MLPG) method", *Comput. Model. Eng. Sci.* **2**:2 (2001), 273–290.

[Dang and Sankar 2007] T. D. Dang and B. V. Sankar, "Meshless local Petrov–Galerkin for problems in composite micromechanics", *AIAA J.* **45**:4 (2007), 912–921.

[Durodola and Derby 1994] J. F. Durodola and B. Derby, "An analysis of thermal residual stresses in Ti-6-4 alloy reinforced with SiC and Al_2O_3 fibres", *Acta Metall. Mater.* **42**:5 (1994), 1525–1234.

[Dvorak et al. 1973] G. J. Dvorak, M. S. M. Rao, and J. Q. Tarn, "Yielding in unidirectional composites under external loads and temperature changes", *J. Compos. Mater.* **7**:2 (1973), 194–216.

[Eischen and Torquato 1993] J. W. Eischen and S. Torquato, "Determining elastic behavior of composites by the boundary element method", *J. Appl. Phys.* **74**:1 (1993), 159–170.

[Gentz et al. 2004] M. Gentz, B. Benedikt, J. K. Sutter, and M. Kumosa, "Residual stresses in unidirectional graphite fiber/polyimide composites as a function of aging", *Compos. Sci. Technol.* **64**:10–11 (2004), 1671–1677.

[Gramoll et al. 1991] K. C. Gramoll, K. P. Walker, and A. D. Freed, "An overview of self-consistent methods for fiber reinforced composites", NASA Technical Memorandum 103713, Lewis Research Center, Cleveland, OH, 1991, Available at http://tinyurl.com/NASA-TM-103713.

[Gu and Liu 2001] Y. T. Gu and G. R. Liu, "A meshless local Petrov–Galerkin (MLPG) formulation for static and free vibration analyses of thin plates", *Comput. Model. Eng. Sci.* **2**:4 (2001), 463–476.

[Haktan Karadeniz and Kumlutas 2007] Z. Haktan Karadeniz and D. Kumlutas, "A numerical study on the coefficients of thermal expansion of fiber reinforced composite materials", *Compos. Struct.* **78**:1 (2007), 1–10.

[Lin and Atluri 2001] H. Lin and S. N. Atluri, "The meshless local Petrov–Galerkin (MLPG) method for solving incompressible Navier–Stokes equations", *Comput. Model. Eng. Sci.* **2**:2 (2001), 117–142.

[Liu et al. 1996] W. K. Liu, Y. Chen, C. T. Chang, and T. Belytschko, "Advances in multiple scale kernel particle methods", *Comput. Mech.* **18**:2 (1996), 73–111.

[Long et al. 2006] S. Y. Long, K. Y. Liu, and D. A. Hu, "A new meshless method based on MLPG for elastic dynamic problems", *Eng. Anal. Bound. Elem.* **30**:1 (2006), 43–48.

[Nayroles et al. 1992] B. Nayroles, G. Touzot, and P. Villon, "Generalizing the finite element method: diffuse approximation and diffuse elements", *Comput. Mech.* **10**:5 (1992), 307–318.

[Nimmer 1990] R. P. Nimmer, "Fiber-matrix interface effects in the presence of thermally induced residual stress", *J. Compos. Tech. Res.* **12**:2 (1990), 65–75.

[Nimmer et al. 1991] R. P. Nimmer, R. J. Bankert, E. S. Russell, G. A. Smith, and P. K. Wright, "Micromechanical modeling of fiber/matrix interface effects in transversely loaded SiC/Ti-6-4 metal matrix composites", *J. Compos. Tech. Res.* **13**:1 (1991), 3–13.

[Rogers et al. 1977] K. F. Rogers, L. N. Phillips, D. M. Kingston-Lee, B. Yates, M. J. Overy, J. P. Sargent, and B. A. McCalla, "The thermal expansion of carbon fibre-reinforced plastics, 1: The influence of fibre type and orientation", *J. Mater. Sci.* **12**:4 (1977), 718–734.

[Shaw and Miracle 1996] L. L. Shaw and D. B. Miracle, "Effects of an interfacial region on the transverse behavior of metal-matrix composites: a finite element analysis", *Acta Mater.* **44**:5 (1996), 2043–2055.

[Shen 1998] Y.-L. Shen, "Thermal expansion of metal-ceramic composites: a three-dimensional analysis", *Mater. Sci. Eng. A* **252**:2 (1998), 269–275.

[Sideridis 1994] E. Sideridis, "Thermal expansion coefficients of fiber composites defined by the concept of the interphase", *Compos. Sci. Technol.* **51**:3 (1994), 301–317.

[Tsai and Chi 2008] J.-L. Tsai and Y.-K. Chi, "Investigating thermal residual stress effect on mechanical behaviors of fiber composites with different fiber arrays", *Compos. B Eng.* **39**:4 (2008), 714–721.

[Uemura et al. 1979] M. Uemura, H. Iyama, and Y. Yamaguchi, "Thermal residual stresses in filament-wound carbon-fiber-reinforced composites", *J. Therm. Stresses* **2**:3–4 (1979), 393–412.

[Van Fo Fy 1965] G. A. Van Fo Fy, "Elastic constants and thermal expansion of certain bodies with inhomogeneous regular structure", *Dokl. Akad. Nauk SSSR* **166** (1965), 817. In Russian; translated in *Sov. Phys. Dokl.* **11** (1966), 176.

[Wisnom 1990] M. R. Wisnom, "Factors affecting the transverse tensile strength of unidirectional continuous silicon carbide fibre reinforced 6061 aluminum", *J. Compos. Mater.* **24**:7 (1990), 707–726.

[Yeh and Krempl 1993] N.-M. Yeh and E. Krempl, "The influence of cool-down temperature histories on the residual stresses in fibrous metal-matrix composites", *J. Compos. Mater.* **27**:10 (1993), 973–995.

[Zahl and McMeeking 1991] D. B. Zahl and M. R. McMeeking, "The influence of residual stress on the yielding of metal matrix composites", *Acta Metall. Mater.* **39**:6 (1991), 1117–1122.

[Zhang et al. 2004] Y. Zhang, Z. Xia, and F. Ellyin, "Evolution and influence of residual stresses/strains of fiber reinforced laminates", *Compos. Sci. Technol.* **64**:10–11 (2004), 1613–1621.

[Zhao et al. 2007] L. G. Zhao, N. A. Warrior, and A. C. Long, "A thermo-viscoelastic analysis of process-induced residual stress in fibre-reinforced polymer-matrix composites", *Mater. Sci. Eng. A* **452–453** (2007), 483–498.

[Zhu et al. 1998] T. Zhu, J.-D. Zhang, and S. N. Atluri, "A local boundary integral equation (LBIE) method in computational mechanics, and a meshless discretization approach", *Comput. Mech.* **21**:3 (1998), 223–235.

Received 26 Apr 2009. Revised 30 Nov 2009. Accepted 7 Dec 2009.

ISA AHMADI: i_ahmadi@aut.ac.ir
Department of Mechanical Engineering, Amirkabir University of Technology, Tehran 15914, Iran

MOHAMAD AGHDAM: aghdam@aut.ac.ir
Thermoelasticity Center of Excellency, Department of Mechanical Engineering, Amirkabir University of Technology, Tehran 15914, Iran

JOURNAL OF MECHANICS OF MATERIALS AND STRUCTURES
Vol. 5, No. 4, 2010

EFFECTIVE MEDIUM THEORIES FOR WAVE PROPAGATION IN TWO-DIMENSIONAL RANDOM INHOMOGENEOUS MEDIA

JIN-YEON KIM

Two effective medium models for two-dimensional scalar wave propagation in random inhomogeneous media are examined in a single theoretical framework. It is shown how the hypotheses and self-consistency conditions in these models are mathematically formulated. As a special case, a two-phase composite in which circular cylindrical inclusions are embedded in a continuous matrix is considered. Numerical calculations are performed for such composites with different combinations of constituent properties in the frequency range up to $ka = 10$, where geometric optic behavior starts appearing. The models mutually deviate when the motion of inclusions is relatively large, such as at the resonance scattering of the inclusions. Otherwise, deviations in the low-frequency regime ($ka < 1$) are negligible and those at high frequencies are also strikingly small. The same facts are observed for two composites having very different constituent properties and in the high-frequency limit.

1. Introduction

Theoretical prediction of the effective properties of inhomogeneous materials is of fundamental importance in materials research since virtually every material is inhomogeneous at smaller scales. For the prediction of the dynamic effective properties of such materials, analysis of the interaction of propagating waves with inhomogeneities, that is, the multiple scattering of waves, is needed. However, except for some simple cases in which multiple scattering effects are sufficiently small, the complete treatment of such a problem is quite difficult for the mathematical and physical reasons described in [Frisch 1968], and thus an approximate solution is sought.

There are two typical approaches to this approximation: the direct and indirect. In the direct approach, the multiple scattering solution for a set of scatterers is first found and then the solution is averaged (the effective field) for all possible configurations of the scatterer distribution. This approach, however, ends up with an infinite hierarchy of integral equations in which each order contains more statistical information than those preceding [Lax 1952]. This infinite hierarchy shows that an exact solution of the problem is prohibitively veiled. To truncate the infinite hierarchy, the rigorous perturbation method [Karal and Keller 1964] can be used, but this approach is limited to the case of weak scattering [Frisch 1968]. In the case of strong scattering, the quasicrystalline approximation (QCA) of [Lax 1952] is often used as an explicit closure approximation while the alternatives are methods based on the stochastic variational principles [Willis 1981; Weaver 1985]. The QCA is relevant to the cases where the total field can be approximated by the sum of single and double scattering fields and thus often fails in a dense scatterer system [Kim 2010].

Keywords: effective medium theory, wave propagation, composite materials, multiple scattering.

One of the indirect approaches, the so-called effective medium theory (EMT), also known as the self-consistent theory, is a group of approximation methods that are formulated in a few steps of thought experiment. One distinctive point in this theory is that multiple scattering is seen to occur in the effective medium [Kim et al. 1995; Choy 1999]. In most effective medium type formulations, the single scattering approximation is adopted and thus the correlations between scatterers are neglected. However, by solving the associated scattering problem in the effective medium, the average multiple scattering effect is taken into account in an implicit way. In spite of the fact that this hypothesis is not theoretically justifiable, the EMT has been successfully applied to predicting the effective properties (not the effective fields) of inhomogeneous materials. A few variants have been set forward which are based on slightly different hypotheses. One is the coherent potential approximation in solid-state physics [Soven 1967; Velicky et al. 1968], which has been regarded as a reliable theory in predicting alloy properties. A quasistatic version for predicting mechanical properties of composites has been proposed by Berryman [1979; 1980]. A dynamic generalization of this theory has been made for two and three-dimensional problems [Kim et al. 1995; Kim 1996]. As shown in [Kim et al. 1995], this theory was very successful in predicting the effective wave speed and attenuation in random particulate composites for wide ranges of frequency and volume fraction. A second variant is the dynamic extension [Sabina and Willis 1988; Bussink et al. 1995; Kanaun and Levin 2003; Kanaun et al. 2004] of the static self-consistent theories of [Budiansky 1965; Hill 1965]. The major difference between these two theories lies in how the roles of constituents are treated, which will be discussed later in this paper. While the direct approach faces a dead end in that the QCA incorporated with an exact pair-correlation function [Varadan et al. 1985] often fails to predict correct effective dynamic properties [Kim 2010] and an analysis of higher order scattering is extremely difficult, opportunities seem to exist in the indirect approaches that offer a tractable scheme on which a more rigorous formalism can be easily built [Martin 2006].

In this paper, a comparative theoretical and numerical study is conducted for the effective medium models of Kim [1996] and Kanaun and Levin [2003], which are called here EMT-1 and EMT-2, respectively. Following [Kanaun and Levin 2003], a theoretical formalism is elaborated and a clear physical meaning is given in each step of the derivations. Horizontally polarized shear (SH) waves propagating in a two-phase composite, in which circular cylindrical inclusions are randomly distributed in a continuous matrix, are considered. Numerical calculations are performed for composites with different combinations of constituent properties in a wide frequency range. Although SH wave propagation in a two-dimensional composite with circular inclusions is considered here for the computational simplicity, similar conclusions are expected for other types of waves and inclusions.

2. Preliminaries

Let us consider an infinite elastic medium that contains a large number (N) of two-dimensional elastic inclusions. The inclusions occupy a region Ω that consists of discrete subregions Ω_i, so that $\Omega = \sum_{i=1}^{N} \Omega_i$. Let μ_1 and ρ_1 be the shear modulus and the mass density of the host medium and μ_2 and ρ_2 be those of the inclusions. The shear modulus μ and mass density ρ of the entire medium may be written:

$$\mu(\boldsymbol{r}) = \mu_1 + \Delta\mu\Theta(\boldsymbol{r}), \qquad \rho(\boldsymbol{r}) = \rho_1 + \Delta\rho\Theta(\boldsymbol{r}), \tag{1}$$

where $\boldsymbol{r}$ is the position vector, $\Delta\mu = (\mu_2 - \mu_1)$, $\Delta\rho = (\rho_2 - \rho_1)$, and $\Theta(\boldsymbol{r})$ is a step function, $\Theta(\boldsymbol{r}) = 1$ if $\boldsymbol{r} \in \Omega$ and $\Theta(\boldsymbol{r}) = 0$ if $\boldsymbol{r} \notin \Omega$. Now suppose that a time-harmonic source, $S(\boldsymbol{r}, t) = s(\boldsymbol{r})e^{-i\omega t}$, occupying

the region Ω_s in the host medium, is generating an antiplane body force. The antiplane time-harmonic displacement field $u(\boldsymbol{r})e^{-i\omega t}$ in this medium satisfies the following equation of motion:

$$\nabla \cdot [\mu(\boldsymbol{r})\nabla u(\boldsymbol{r})] + \rho(\boldsymbol{r})\omega^2 u(\boldsymbol{r}) = s(\boldsymbol{r}). \tag{2}$$

The Green's function for the homogeneous matrix that satisfies the boundary condition at infinity is the solution of the following equation:

$$\mu_1 \nabla^2 G(\boldsymbol{r}-\boldsymbol{r}') + \rho_1 \omega^2 G(\boldsymbol{r}-\boldsymbol{r}') = -\delta(\boldsymbol{r}-\boldsymbol{r}'), \tag{3}$$

$$G(\boldsymbol{r}-\boldsymbol{r}') = \frac{i}{4\mu_1} H_0(k_1|\boldsymbol{r}-\boldsymbol{r}'|), \tag{4}$$

where δ is the Dirac delta function in the two-dimensional space, $H_0(x)$ is the Hankel function of the first kind and order zero, and $k_1 = \omega/c_1$ is the wavenumber associated with the shear wave speed c_1. A two-dimensional Fourier transform pair is defined

$$f(\boldsymbol{k}) = (2\pi)^{-2} \int f(\boldsymbol{r}) e^{i\boldsymbol{k}\cdot\boldsymbol{r}} d\boldsymbol{r}, \qquad f(\boldsymbol{r}) = \int f(\boldsymbol{k}) e^{-i\boldsymbol{k}\cdot\boldsymbol{r}} d\boldsymbol{k}, \tag{5}$$

where $\boldsymbol{k}$ denotes the wave vector with components (k_x, k_y), $d\boldsymbol{r} = dxdy$, and $d\boldsymbol{k} = dk_x dk_y$. Forward Fourier transformation of Equation (3) yields the following relation between the operator $A(\boldsymbol{k}_1)$ and the Green's function in the wavenumber domain: $(\mu_1 k_1^2 - \rho_1\omega^2)G(\boldsymbol{k}_1) = A(\boldsymbol{k}_1)G(\boldsymbol{k}_1) = 1$, where $\boldsymbol{k}_1$ is the wave vector associated with the wavenumber k_1.

Substituting (1) into (2), one obtains $\mu_1\nabla^2 u + \rho_1\omega^2 u = s - [\nabla\cdot(\Delta\mu\nabla u) + \Delta\rho\omega^2 u]\Theta$. Using the Green's function in (3), one gets the integral equation for the total field

$$u(\boldsymbol{r}) = u^{\text{in}}(\boldsymbol{r}) + \int_\Omega \Delta\mu(\boldsymbol{r}')\nabla G(\boldsymbol{r}-\boldsymbol{r}')\cdot\boldsymbol{\varepsilon}(\boldsymbol{r}') + \Delta\rho(\boldsymbol{r}')\omega^2 G(\boldsymbol{r}-\boldsymbol{r}')u(\boldsymbol{r}')\,d\boldsymbol{r}', \tag{6}$$

where the first term, given as $u^{\text{in}}(\boldsymbol{r}) = \int_{\Omega_s} G(\boldsymbol{r}-\boldsymbol{r}')s(\boldsymbol{r}')\,d\boldsymbol{r}'$, is the incident wave, the second term represents the scattered waves, and $\boldsymbol{\varepsilon} = \nabla u$ is the strain vector field in the inclusion. The prime sign in the integral in (6) is used to denote the field quantities in the inclusions and the derivatives in the integral are accordingly differentiation with respect to the primed variables. Assuming that the source is located at infinity (far from the region of interest), the incident wave is regarded as a plane wave:

$$u^{\text{in}}(\boldsymbol{r}) = U e^{i\boldsymbol{k}_1^i\cdot\boldsymbol{r}}, \tag{7}$$

where $\boldsymbol{k}_1^i/k_1$ is the unit vector in the direction of incidence and the Fourier transform of (7) is

$$u^{\text{in}}(\boldsymbol{k}_1) = (2\pi)^{-2} U\delta(\boldsymbol{k}_1 - \boldsymbol{k}_1^i). \tag{8}$$

Since the plane wave satisfies the wave equation without a source in a finite domain, the following holds: $A(\boldsymbol{k}_1)u^{\text{in}}(\boldsymbol{k}_1) = 0$. Using the far-field asymptotic expression of the Green's function, the far-field scattering pattern is obtained as an integral of the displacement and strain in the inclusion:

$$u^{\text{sc}} \sim \sqrt{\frac{2}{\pi k_1 r}} e^{i(k_1 r - \pi/4)} f(\boldsymbol{k}_1), \qquad f(\boldsymbol{k}_1) = -\frac{1}{8}\int_\Omega [\Delta\mu i\boldsymbol{k}_1\cdot\nabla u(\boldsymbol{r}') - \Delta\rho\omega^2 u(\boldsymbol{r}')]\exp(-i\boldsymbol{k}_1\cdot\boldsymbol{r}')\,d\boldsymbol{r}'. \tag{9}$$

Due to the generalized optical theorem for the scattering in an absorbing medium [Kim 2003a; 2003b; Kim and Lee 2009; 2010], the total cross section is

$$\gamma = -\frac{4}{k_1'}\,\mathrm{Re}[f(\boldsymbol{k}_1^i)], \tag{10}$$

where $f(\boldsymbol{k}_1^i)$ is the forward scattering amplitude and k_1' is the real part of the complex wavenumber k_1. Equation (10) states that the total power loss during the process of scattering is proportional to the forward scattering amplitude.

3. The models

EMTs commonly require the following three steps: first, finding the approximate average displacement and strain fields in a representative inclusion by solving the single scattering problem in the effective medium with yet-unknown properties; second, embedding the inclusions with these average fields in a homogeneous medium (the original or the effective medium) in which averaging over composition and geometry is to be performed; finally, obtaining expressions for the effective properties applying a self-consistency condition. The second step is often called the self-consistent embedding and the self-consistency condition requires the equivalence of the average field to a plane wave that is assumed to propagate in the effective medium. Different EMTs use different averaging schemes in which the roles of the constituent materials are treated differently.

In order to obtain the approximate average fields, both the EMT-1 and EMT-2 start with:

Hypothesis 1. Every inclusion in the composite behaves as an isolated inclusion embedded in a homogeneous medium having the effective properties of the composite. The field acting on this inclusion is a plane wave propagating in the effective medium [Kim et al. 1995; Kanaun and Levin 2003].

By this hypothesis, the original multiple scattering problem defined in the host medium is reduced to a single scattering problem defined in the effective medium. The integral equation (6) for the scattering by a single representative inclusion in the effective medium is written

$$\bar{u}(\boldsymbol{r}) = \bar{u}^{\mathrm{in}}(\boldsymbol{r}) + \int_{\Omega_i} \overline{\Delta\mu}_2 \nabla\bar{G}(\boldsymbol{r}-\boldsymbol{r}')\cdot\boldsymbol{\varepsilon}(\boldsymbol{r}') + \overline{\Delta\rho}_2\omega^2\bar{G}(\boldsymbol{r}-\boldsymbol{r}')u(\boldsymbol{r}')\,d\boldsymbol{r}', \tag{11}$$

where the overbar ($\bar{}$) is used to denote material properties and physical quantities in the effective medium. For example, the incident wave is $\bar{u}^{\mathrm{in}}(\boldsymbol{r}) = Ue^{i\bar{\boldsymbol{k}}^i\cdot\boldsymbol{r}}$, where $\bar{\boldsymbol{k}}^i$ is the wave vector of the incident wave in the effective medium, $\bar{k} = |\bar{\boldsymbol{k}}^i|$ is the wavenumber associated with the effective shear wave speed $\bar{c}$, $\overline{\Delta\mu}_2 = (\mu_2 - \bar{\mu})$, and $\overline{\Delta\rho}_2 = (\rho_2 - \bar{\rho})$. The region Ω_i is now the area occupied by the single representative inclusion. Its location is not prescribed yet since it is a random variable and later the scattered field obtained from (11) is averaged over all possible locations. Averages are also performed over the shape and orientation of the inclusions. If the effective medium is presumed to be isotropic and homogeneous, the location of Ω_i is permitted to be everywhere in the medium, which states the translational invariance.

To realize this averaging process, let us consider a plane wave incident on the representative inclusion located at $\boldsymbol{r}_i$ in the global coordinate system, and place the origin of a local coordinate system (x_1, y_1) at the mass center of the inclusion. Then, the displacement and strain fields described in the global coordinate system are related to those fields in the local coordinate system ($\hat{\bar{u}}(\boldsymbol{r}_1)$ and $\hat{\bar{\boldsymbol{\varepsilon}}}(\boldsymbol{r}_1)$) in response

to the incident wave with unit magnitude ($\hat{\bar{u}}^{\text{in}}(\boldsymbol{r}_1) = Ue^{i\bar{\boldsymbol{k}}^i\cdot\boldsymbol{r}_1}$):

$$\bar{u}(\boldsymbol{r}) = \hat{\bar{u}}(\boldsymbol{r}_1)e^{-i\bar{\boldsymbol{k}}^i\cdot\boldsymbol{r}_1}\bar{u}^{\text{in}}(\boldsymbol{r}) \equiv \bar{\Lambda}_u(\boldsymbol{r}_1)\bar{u}^{\text{in}}(\boldsymbol{r}), \qquad \boldsymbol{r}\in\Omega_i, \tag{12}$$

$$\bar{\boldsymbol{\varepsilon}}(\boldsymbol{r}) = \hat{\bar{\boldsymbol{\varepsilon}}}(\boldsymbol{r}_1)e^{-i\bar{\boldsymbol{k}}^i\cdot\boldsymbol{r}_1}\bar{u}^{\text{in}}(\boldsymbol{r}) = \nabla\hat{\bar{u}}(\boldsymbol{r}_1)e^{-i\bar{\boldsymbol{k}}^i\cdot\boldsymbol{r}_1}\bar{u}^{\text{in}}(\boldsymbol{r}) \equiv \bar{\boldsymbol{\Lambda}}_\varepsilon(\boldsymbol{r}_1)\bar{u}^{\text{in}}(\boldsymbol{r}), \qquad \boldsymbol{r}\in\Omega_i, \tag{13}$$

where $\boldsymbol{r}_1 = \boldsymbol{r} - \boldsymbol{r}_i$ is the position vector in the local coordinate system. The discrete random functions $\bar{\Lambda}_u$ and $\bar{\boldsymbol{\Lambda}}_\varepsilon$ appear as the transition operators that relate the displacement and strain fields in the remote inclusion to the incident wave. Note that these operators are independent of the locations $\boldsymbol{r}_i$ of the remote inclusion.

Now consider scattering of a set of imaginary inclusions whose internal fields are given by (12) and (13) and whose properties and positions are those of the inclusions (μ_2 and ρ_2, and $\boldsymbol{r}_i$). These inclusions are embedded in the *original* host medium in which a plane incident wave is propagating. The integral in (6) can be written

$$u(\boldsymbol{r}) = u^{\text{in}}(\boldsymbol{r}) + \int_\Omega [\Delta\mu\nabla G(\boldsymbol{r}-\boldsymbol{r}')\cdot\bar{\boldsymbol{\Lambda}}_\varepsilon(\boldsymbol{r}_1) + \Delta\rho\omega^2 G(\boldsymbol{r}-\boldsymbol{r}')\bar{\Lambda}_u(\boldsymbol{r}_1)]\bar{u}^{\text{in}}(\boldsymbol{r}')\,d\boldsymbol{r}'. \tag{14}$$

Taking an ensemble average on (14) for all possible sets of $\{\boldsymbol{r}_1, \boldsymbol{r}_2, \ldots, \boldsymbol{r}_N\}$, one obtains

$$\langle u(\boldsymbol{r})\rangle = u^{\text{in}}(\boldsymbol{r}) + \int_\Omega [\Delta\mu\nabla G(\boldsymbol{r}-\boldsymbol{r}')\cdot\langle\bar{\boldsymbol{\Lambda}}_\varepsilon\rangle + \Delta\rho\omega^2 G(\boldsymbol{r}-\boldsymbol{r}')\langle\bar{\Lambda}_u\rangle]\bar{u}^{\text{in}}(\boldsymbol{r}')\,d\boldsymbol{r}'. \tag{15}$$

Note that the averages over shape and orientation do not appear since the inclusions are assumed to be identical cylinders with the same volume (Ω_i). Due to the translation invariance the averages of the transition operators are taken over a representative inclusion Ω_i

$$\langle\bar{\Lambda}_u\rangle = \frac{1}{\Omega_t}\int_{\Omega_t}\bar{\Lambda}_u\,d\boldsymbol{r} = \frac{N}{\Omega_t}\int_{\Omega_i}\hat{\bar{u}}(\boldsymbol{r}_1)e^{-i\bar{\boldsymbol{k}}^i\cdot\boldsymbol{r}_1}d\boldsymbol{r}_1 = v_2\langle\bar{\Lambda}_u(\bar{\boldsymbol{k}})\rangle_{\Omega_i}, \tag{16}$$

$$\langle\bar{\boldsymbol{\Lambda}}_\varepsilon\rangle = \frac{1}{\Omega_t}\int_{\Omega_t}\bar{\boldsymbol{\Lambda}}_\varepsilon\,d\boldsymbol{r} = \frac{N}{\Omega_t}\int_{\Omega_i}\nabla\hat{\bar{u}}(\boldsymbol{r}_1)e^{-i\bar{\boldsymbol{k}}^i\cdot\boldsymbol{r}_1}d\boldsymbol{r}_1 = v_2\langle\bar{\boldsymbol{\Lambda}}_\varepsilon(\bar{\boldsymbol{k}})\rangle_{\Omega_i}, \tag{17}$$

where v_2 is the volume fraction of the inclusion phase, Ω_t represents the entire domain covering the matrix and all inclusions, and $\langle\ \rangle_{\Omega_i}$ denotes volume averaging over Ω_i. Substituting (16) and (17) into (15) yields

$$\langle u(\boldsymbol{r})\rangle = u^{\text{in}}(\boldsymbol{r}) + v_2\int_\Omega [\Delta\mu\nabla G(\boldsymbol{r}-\boldsymbol{r}')\cdot\langle\bar{\boldsymbol{\Lambda}}_\varepsilon(\bar{\boldsymbol{k}})\rangle_{\Omega_i} + \Delta\rho\omega^2 G(\boldsymbol{r}-\boldsymbol{r}')\langle\bar{\Lambda}_u(\bar{\boldsymbol{k}})\rangle_{\Omega_i}]\bar{u}^{\text{in}}(\boldsymbol{r}')\,d\boldsymbol{r}'. \tag{18}$$

For self-consistency, a second hypothesis is introduced:

Hypothesis 2. The average field (the average displacement in (18)) is equal to the incident plane wave propagating in the effective medium.

That is,

$$\bar{u}^{\text{in}}(\boldsymbol{r}) = \langle u(\boldsymbol{r})\rangle, \tag{19}$$

which leads to

$$\langle u(\boldsymbol{r})\rangle = u^{\text{in}}(\boldsymbol{r}) + v_2\int_\Omega [\Delta\mu\nabla G(\boldsymbol{r}-\boldsymbol{r}')\cdot\langle\bar{\boldsymbol{\Lambda}}_\varepsilon(\bar{\boldsymbol{k}})\rangle_{\Omega_i} + \Delta\rho\omega^2 G(\boldsymbol{r}-\boldsymbol{r}')\langle\bar{\Lambda}_u(\bar{\boldsymbol{k}})\rangle_{\Omega_i}]\langle u(\boldsymbol{r}')\rangle\,d\boldsymbol{r}', \tag{20}$$

since (20) is a convolution integral, Fourier transformation of (20) yields

$$\langle u(\boldsymbol{k}_1)\rangle = u^{\text{in}}(\boldsymbol{k}_1) + v_2[\Delta\mu i\boldsymbol{k}_1 \cdot \langle \bar{\boldsymbol{\Lambda}}_\varepsilon(\bar{\boldsymbol{k}})\rangle_{\Omega_i} + \Delta\rho\omega^2\langle \bar{\Lambda}_u(\bar{\boldsymbol{k}})\rangle_{\Omega_i}]G(\boldsymbol{k}_1)\langle u(\boldsymbol{k}_1)\rangle. \tag{21}$$

Applying the operator $A(\boldsymbol{k}_1)$ on (21), it turns out that the average displacement spectrum in (21) is the solution of the operator equation

$$\bar{A}(\boldsymbol{k}_1)\langle u(\boldsymbol{k}_1)\rangle = 0, \quad \bar{A}(\boldsymbol{k}_1) = A(\boldsymbol{k}_1) - v_2\Delta\mu i\boldsymbol{k}_1 \cdot \langle \bar{\boldsymbol{\Lambda}}_\varepsilon(\bar{\boldsymbol{k}})\rangle_{\Omega_i} - v_2\Delta\rho\omega^2\langle \bar{\Lambda}_u(\bar{\boldsymbol{k}})\rangle_{\Omega_i}, \tag{22}$$

the operator for the effective medium. Due to (19), the Fourier transform of the average field is replaced with that of the plane incident wave in the effective medium, $\langle u(\boldsymbol{k}_1)\rangle = \bar{u}^{\text{in}}(\bar{\boldsymbol{k}})$, requiring a necessary condition, $\boldsymbol{k}_1 = \bar{\boldsymbol{k}}$. Then, the expressions for the effective operator and the effective shear modulus and mass density in the EMT-2 formulation are

$$\bar{A}(\bar{\boldsymbol{k}}) = A(\bar{\boldsymbol{k}}) - v_2\Delta\mu i\bar{\boldsymbol{k}} \cdot \langle \bar{\boldsymbol{\Lambda}}_\varepsilon(\bar{\boldsymbol{k}})\rangle_{\Omega_i} - v_2\Delta\rho\omega^2\langle \bar{\Lambda}_u(\bar{\boldsymbol{k}})\rangle_{\Omega_i}, \tag{23}$$

$$\bar{\mu} = \mu_0 - v_2\Delta\mu i\bar{\boldsymbol{k}} \cdot \frac{\langle \bar{\boldsymbol{\Lambda}}_\varepsilon(\bar{\boldsymbol{k}})\rangle_{\Omega_i}}{\bar{k}^2}, \quad \bar{\rho} = \rho_0 + v_2\Delta\rho\langle \bar{\Lambda}_u(\bar{\boldsymbol{k}})\rangle_{\Omega_i}. \tag{24}$$

These are the formulae derived in [Kanaun and Levin 2003]. Note that the signs in the expressions for $\bar{A}$ and $\bar{\mu}$ are different from Equations (3.16) and (3.17) of that reference due to the different time-dependence: $e^{-i\omega t}$ in this paper versus $e^{i\omega t}$ in their paper.

In the EMT-1, an additional hypothesis is introduced:

Hypothesis 3. In the effective medium not only the discrete inclusions but also the surrounding medium acts as a scatterer because its properties differ from those of the effective medium, and these two scattering processes are independent.

The integral equations for the fields in a representative volume for the matrix (Ω_m) and in a representative inclusion (Ω_i) are

$$\bar{u}(\boldsymbol{r}) = \bar{u}^{\text{in}}(\boldsymbol{r}) + \int_{\Omega_m} \Delta\bar{\mu}_1\nabla\bar{G}(\boldsymbol{r}-\boldsymbol{r}') \cdot \boldsymbol{\varepsilon}_1(\boldsymbol{r}') + \Delta\bar{\rho}_1\omega^2\bar{G}(\boldsymbol{r}-\boldsymbol{r}')u_1(\boldsymbol{r}')\,d\boldsymbol{r}', \tag{25}$$

$$\bar{u}(\boldsymbol{r}) = \bar{u}^{\text{in}}(\boldsymbol{r}) + \int_{\Omega_i} \Delta\bar{\mu}_2\nabla\bar{G}(\boldsymbol{r}-\boldsymbol{r}') \cdot \boldsymbol{\varepsilon}_2(\boldsymbol{r}') + \Delta\bar{\rho}_2\omega^2\bar{G}(\boldsymbol{r}-\boldsymbol{r}')u_2(\boldsymbol{r}')\,d\boldsymbol{r}', \tag{26}$$

where subscripts 1 and m and 2 and i denote the matrix and the inclusions, respectively, and $\Delta\bar{\mu}_p = (\mu_p - \bar{\mu})$ and $\Delta\bar{\rho}_p = (\rho_p - \bar{\rho})$ for $p = 1, 2$. The displacement and strain fields in the representative volumes (Ω_m and Ω_i) may be obtained in the same way as in (12) and (13).

In the EMT-1, a schizoid medium, a medium that has estimates of the yet-unknown effective properties $\hat{\mu}$ and $\hat{\rho}$, is used for self-consistent embedding, in which the inclusions and the matrix are embedded and insonified by a plane wave. Then, (14) is written

$$\hat{u}(\boldsymbol{r}) = \hat{u}^{\text{in}}(\boldsymbol{r}) + \sum_{p=1,2}\int_{\Omega_p} [\Delta\hat{\mu}_p\nabla\hat{G}(\boldsymbol{r}-\boldsymbol{r}') \cdot \bar{\boldsymbol{\Lambda}}^p_\varepsilon(\boldsymbol{r}_1) + \Delta\hat{\rho}_p\omega^2\hat{G}(\boldsymbol{r}-\boldsymbol{r}')\bar{\Lambda}^p_u(\boldsymbol{r}_1)]\hat{u}(\boldsymbol{r}')\,d\boldsymbol{r}', \tag{27}$$

where variables with a caret are those of the estimate of the effective medium and $\Delta\hat{\mu}_p = (\mu_p - \hat{\mu})$ and $\Delta\hat{\rho}_p = (\rho_p - \hat{\rho})$ for $p = 1, 2$. Following the steps described above, (27) is averaged over the entire

domain:

$$\langle\hat{u}(\boldsymbol{r})\rangle=\hat{u}^{\text{in}}(\boldsymbol{r})+\sum_{p=1,2}v_p\int_{\Omega_p}[\Delta\hat{\mu}_p\nabla\hat{G}(\boldsymbol{r}-\boldsymbol{r}')\cdot\langle\bar{\boldsymbol{\Lambda}}_{\varepsilon}^{p}(\bar{\boldsymbol{k}})\rangle_{\Omega_p}+\Delta\hat{\rho}_p\omega^2\hat{G}(\boldsymbol{r}-\boldsymbol{r}')\langle\bar{\Lambda}_{u}^{p}(\bar{\boldsymbol{k}})\rangle_{\Omega_p}]\langle\hat{u}(\boldsymbol{r}')\rangle\,d\boldsymbol{r}'. \quad (28)$$

Fourier transformation of (28) yields

$$\langle\hat{u}(\hat{\boldsymbol{k}})\rangle=\hat{u}^{\text{in}}(\hat{\boldsymbol{k}})+\sum_{p=1,2}v_p[\Delta\hat{\mu}_p i\hat{\boldsymbol{k}}\cdot\langle\bar{\boldsymbol{\Lambda}}_{\varepsilon}^{p}(\bar{\boldsymbol{k}})\rangle_{\Omega_p}+\Delta\hat{\rho}_p\omega^2\langle\bar{\Lambda}_{u}^{p}(\bar{\boldsymbol{k}})\rangle_{\Omega_p}]\hat{G}(\hat{\boldsymbol{k}})\langle\hat{u}(\hat{\boldsymbol{k}})\rangle. \quad (29)$$

Upon applying the operator $\hat{A}(\hat{\boldsymbol{k}})$ on (29), the equation takes the form

$$\left[\hat{A}(\hat{\boldsymbol{k}})-\sum_{p=1,2}v_p\big(\Delta\hat{\mu}_p i\hat{\boldsymbol{k}}\cdot\langle\bar{\boldsymbol{\Lambda}}_{\varepsilon}^{p}(\bar{\boldsymbol{k}})\rangle_{\Omega_p}+\Delta\hat{\rho}_p\omega^2\langle\bar{\Lambda}_{u}^{p}(\bar{\boldsymbol{k}})\rangle_{\Omega_p}\big)\right]\langle\hat{u}(\hat{\boldsymbol{k}})\rangle=0, \quad (30)$$

where $\hat{A}(\hat{\boldsymbol{k}})$ is the estimate of the effective operator. By the definition of the effective operator,

$$\bar{A}(\hat{\boldsymbol{k}})\equiv\hat{A}(\hat{\boldsymbol{k}})-\sum_{p=1,2}v_p\big(\Delta\hat{\mu}_p i\hat{\boldsymbol{k}}\cdot\langle\bar{\boldsymbol{\Lambda}}_{\varepsilon}^{p}(\bar{\boldsymbol{k}})\rangle_{\Omega_p}+\Delta\hat{\rho}_p\omega^2\langle\bar{\Lambda}_{u}^{p}(\bar{\boldsymbol{k}})\rangle_{\Omega_p}\big). \quad (31)$$

Then, the formulae for the effective shear modulus and mass density are

$$\bar{\mu}=\hat{\mu}-\sum_{p=1,2}v_p\Delta\hat{\mu}_p i\hat{\boldsymbol{k}}\cdot\frac{\langle\boldsymbol{\Lambda}_{\varepsilon}^{p}(\bar{\boldsymbol{k}})\rangle_{\Omega_p}}{\hat{k}^2},\qquad\bar{\rho}=\hat{\rho}-\sum_{p=1,2}v_p\Delta\hat{\rho}_p\langle\Lambda_{u}^{p}(\bar{\boldsymbol{k}})\rangle_{\Omega_p}. \quad (32)$$

Finally, the self-consistency is that the estimates of the effective shear modulus and density in (32) are the true effective shear modulus and density, that is, $\hat{\mu}=\bar{\mu}$ and $\hat{\rho}=\bar{\rho}$. This statement is, in fact, identical to the hypothesis that the plane wave in the effective medium is coincident with the mean field. Then, two conditions that should be satisfied by the effective medium are

$$\sum_{p=1,2}v_p\overline{\Delta\mu}_p i\bar{\boldsymbol{k}}\cdot\langle\boldsymbol{\Lambda}_{\varepsilon}^{p}(\bar{\boldsymbol{k}})\rangle_{\Omega_p}=0,\qquad\sum_{p=1,2}v_p\overline{\Delta\rho}_p\langle\Lambda_{u}^{p}(\bar{\boldsymbol{k}})\rangle_{\Omega_p}=0. \quad (33)$$

Kim [1996] obtained the same expressions based more on physical intuition. Adding together the two equations in (33), one gets

$$\sum_{p=1,2}v_p\langle\bar{f}_p(\bar{\boldsymbol{k}}^i)\rangle_{\Omega_p}=0. \quad (34)$$

This implies that the effective medium in the EMT-1 is defined as the one in which the spatial and volume-fraction averaged forward scattering amplitude vanishes. In other words, since the scattered energy is proportional to the forward scattering amplitude (10), the effective medium is the medium in which there is no scattering on the average of the mean field by the constituents. This endows a full physical meaning to the effective medium and its properties in the EMT-1 formulation. One can find the origin of this idea in the solid-state physics problems [Soven 1967; Velicky et al. 1968]; it has also been used in electromagnetic problems [Stroud and Pan 1978; Niklasson et al. 1981].

It is noted that the EMT-1 is a possible dynamic generalization of the theory of Berryman [1979; 1980] and the EMT-2 of [Budiansky 1965; Hill 1965]. It is shown in the Appendix that the EMT-1 yields the same static effective density and shear modulus as the EMT-2 [Kanaun and Levin 2003], and their effective shear moduli are of course identical to those of [Budiansky 1965; Hill 1965; Sabina and Willis

1988]. It is interesting to note that even though these static theories ([Budiansky 1965; Hill 1965] versus [Berryman 1979; 1980]) treat the role of the matrix differently, they yield identical equations for the effective properties.

A parameter which remains unspecified so far in the EMT-1 is the shape and size of the representative volume for the matrix (Ω_m). It is shown also in the Appendix that a natural and meaningful choice is to use the same shape and size of the inclusions, that is, $\Omega_m = \Omega_i$. In the numerical calculations in the next section, Ω_m is taken to be a circular cylinder with the radius a.

4. Results and discussion

Numerical calculations are performed for two-phase composites having different combinations of constituent properties. The mechanical properties of the constituent materials are listed in Table 1 and the composites considered and their characteristics are given in Table 2. As shown in the third column of Table 2, these four composites are all distinctive in their ratios of densities and shear moduli. These distinctive combinations are selected to see how the two model predictions are different for composites with different dynamic characteristics. The effective wave speed and coherent attenuation are calculated for frequencies up to $k_1 a = 10$ for these composites and for different volume concentrations up to 60% of the inclusion phase.

In Figures 1–4, the results from the EMT-1 and EMT-2 are compared. The effective wave speed is normalized with the shear wave speed in the matrix and the coherent attenuation is also presented in a normalized form, $4\pi \mathrm{Im}[\bar{k}]/\mathrm{Re}[\bar{k}]$, which is called the specific attenuation capacity. It is quite surprising that both the wave speed and attenuation predicted by the two models generally agree very well for all composites considered. They are almost identical at frequencies where $k_1 a < 1$ and are also very close to each other at high frequencies. This is quite contrary to the expectation [Kanaun et al. 2004] that these two models would predict substantially different results in the wave speed and coherent attenuation since the matrix phase is treated quite differently in these two models, as a continuous phase in the EMT-2 as opposed to an equivalent inclusion in the EMT-1. Relatively large deviations are seen at the frequencies where the attenuation has a peak due to the rigid-body resonance of the inclusions (see Figures 2 and 3) and at some high frequencies where numerous elastic resonances occur (see Figure 4). Excessive motion will be set up in the inclusions at the resonance frequencies and the motion in the matrix will accordingly be large. Therefore, the relatively large deviations at and near resonance frequencies are due to the amplification effect of the resonance scattering.

To confirm what has been observed in Figures 1–4, these theories are further compared for two composites with extremely different constituent properties, one with hard and heavy inclusions ($\mu_2/\mu_1 = 100$

Material	Density (kg/m^3)	Shear modulus (GPa)	Wave speed (m/s)
Aluminum	2720	38.7	3772
Steel	7800	80.9	3220
Graphite	1310	21.0	4004
Titanium	4510	41.4	3030
SiC (SCS-6)	3200	182.0	7542

Table 1. Elastic properties of constituent materials.

Materials	ρ_2/ρ_1	μ_2/μ_1	Remarks
Steel/aluminum	2.9	2.1	$\rho_2 > \rho_1, \mu_2 > \mu_1$
Graphite/aluminum	0.48	0.54	$\rho_2 < \rho_1, \mu_2 < \mu_1$
SiC/titanum	0.71	4.4	$\rho_2 < \rho_1, \mu_2 > \mu_1$
Steel/SiC	2.44	0.45	$\rho_2 > \rho_1, \mu_2 < \mu_1$

Table 2. Ratios of density and shear moduli.

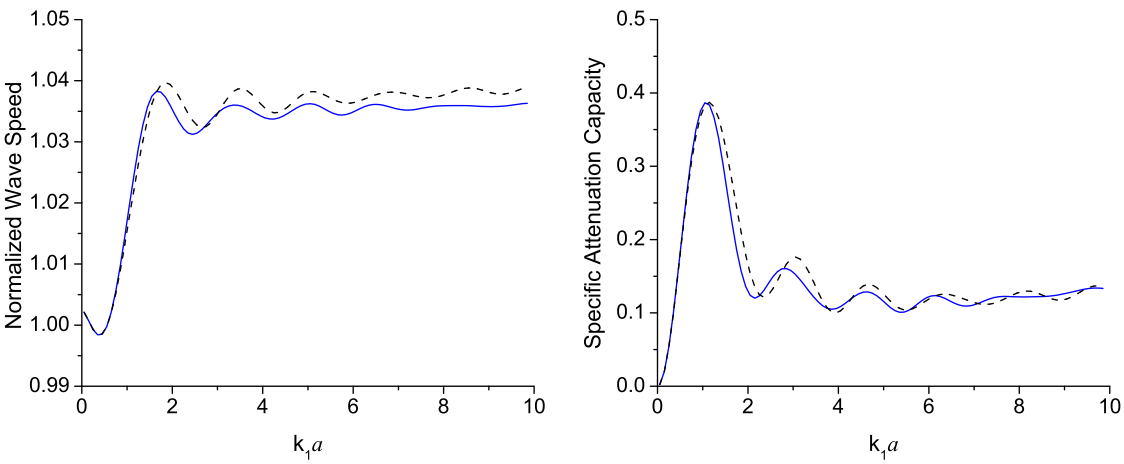

Figure 1. Average wave speed and coherent attenuation in a graphite/aluminum composite with 60% graphite fibers. The continuous line represents the EMT-1, and the dashed line the EMT-2.

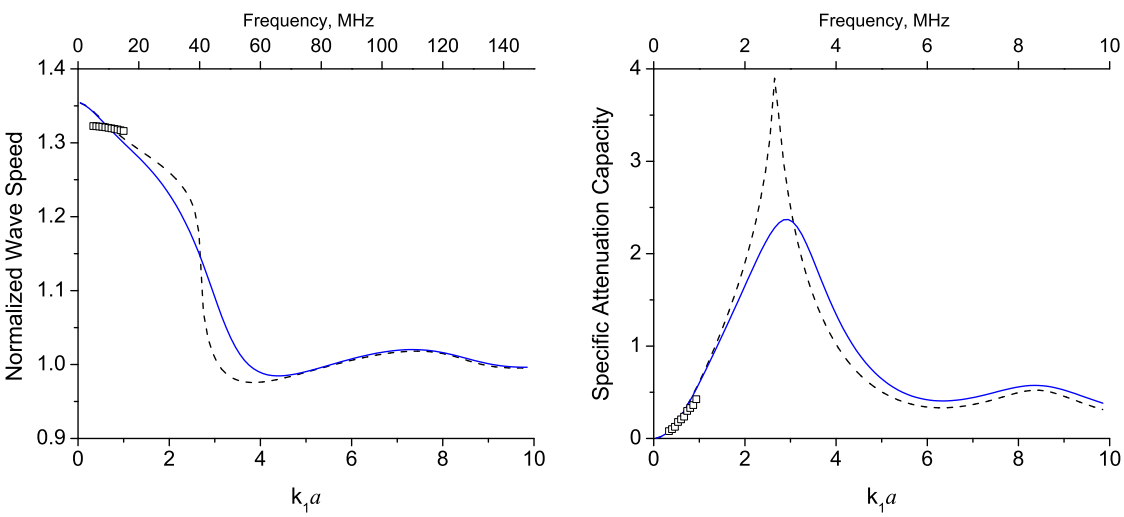

Figure 2. Average wave speed and coherent attenuation in a SiC/Ti composite with 35% SiC fibers. The continuous line represents the EMT-1, the dashed line the EMT-2, and the open squares are from an ultrasonic measurement in the frequency range 5–15 MHz.

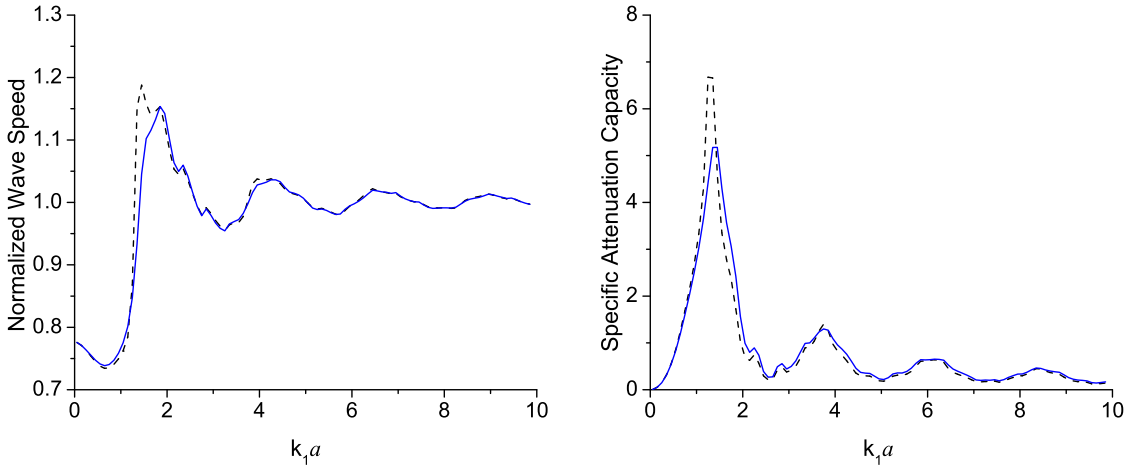

Figure 3. Average wave speed and coherent attenuation in a steel/SiC composite with 35% steel fibers. The continuous line represents the EMT-1, and the dashed line the EMT-2.

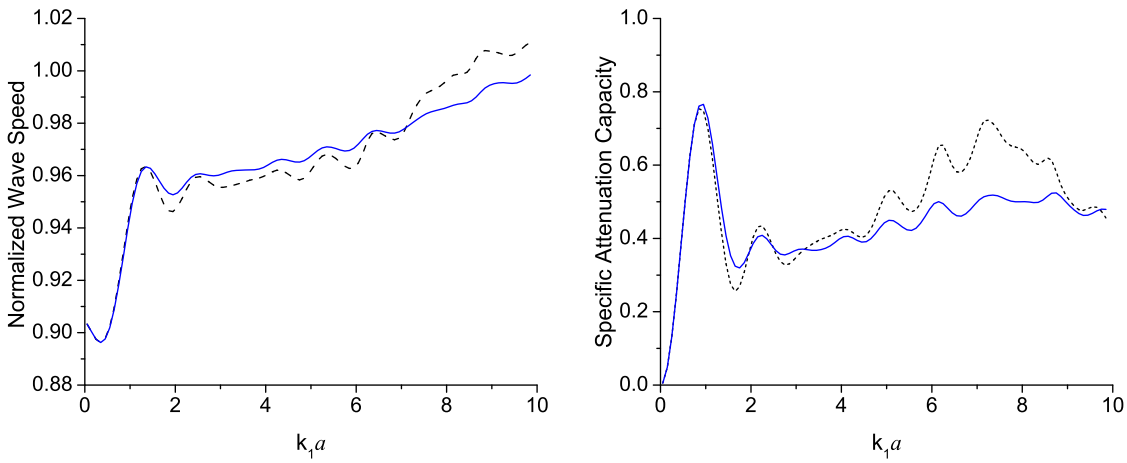

Figure 4. Average wave speed and coherent attenuation in a steel/aluminum composite with 25% steel fibers. The continuous line represents the EMT-1, and the dashed line the EMT-2.

and $\rho_2/\rho_1 = 10$) in Figure 5, and another with soft and light inclusions ($\mu_2/\mu_1 = 0.01$ and $\rho_2/\rho_1 = 0.1$) in Figure 6. Note that these are the numerical examples presented in [Kanaun and Levin 2003]. The frequency range in the numerical simulations is extended to $k_1a = 50$ to see if any large deviation occurs at frequencies above $k_1a = 10$. First of all, just as in Figures 1–4, the results from the two theories agree excellently for both cases, which strongly reinforces the conclusion made from the results in Figures 1–4, that the way the EMT-2 treats the matrix phase does not make any substantial difference. Secondly, both the wave speed and attenuation of the EMT-1 converge monotonically to their frequency-independent geometric optic limits: the wave speed of the matrix c_1 and a constant attenuation, respectively. The attenuation factors (of the EMT-1) divided by the inclusion volume fraction ($\mathrm{Im}[\bar{k}a]/v_2$) calculated at $k_1a = 50$ and for different volume fractions turn out to be nearly a constant — the attenuation predicted

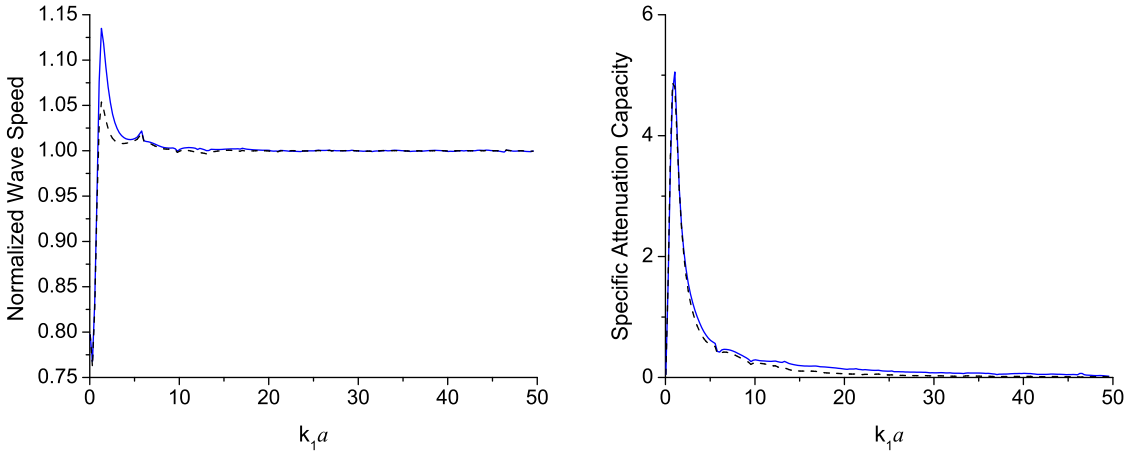

Figure 5. Average wave speed and coherent attenuation in a composite with 30% hard and heavy inclusions ($\mu_2/\mu_1 = 100$ and $\rho_2/\rho_1 = 10$). The continuous line represents the EMT-1, and the dashed line the EMT-2.

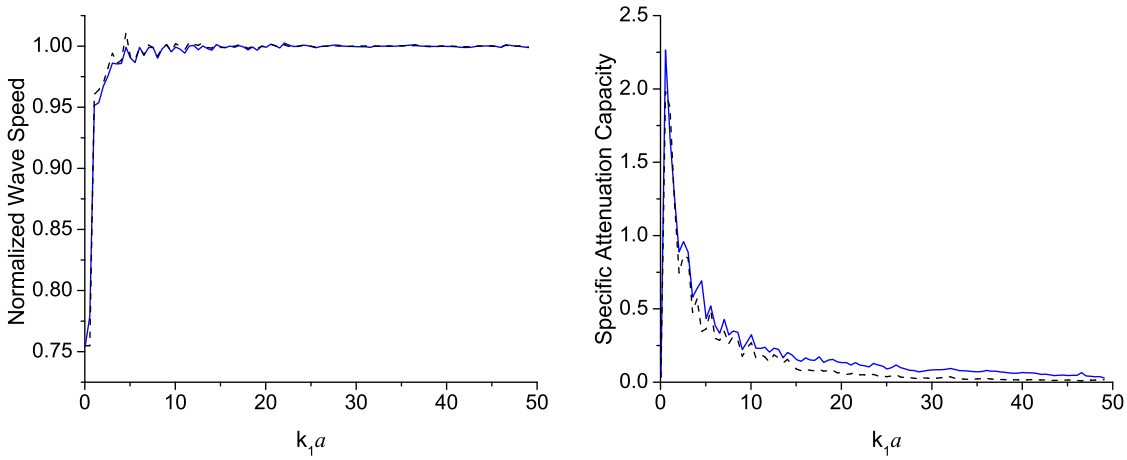

Figure 6. Average wave speed and coherent attenuation in a composite with 30% soft and light inclusions ($\mu_2/\mu_1 = 0.01$ and $\rho_2/\rho_1 = 0.1$). The continuous line represents the EMT-1, and the dashed line the EMT-2.

by the EMT-1 depends only on the volume fraction in the high-frequency limit. These are some expected properties of composites in the high-frequency limit [Kanaun and Levin 2003]. However, it is noted that these high-frequency limit values predicted by the EMT-1 could be inaccurate.

Finally, it should be pointed out that the comparisons given in Figures 5 and 6 are merely to demonstrate the equivalence of the two models. In this high-frequency range, the multiple scattering is so strong that waves quickly lose their mutual coherence, turning to a noise-like random field (called a diffuse field [Sheng 1995]) in a few wavelengths of propagation, and only the mean energy density of this random field is physically meaningful. Therefore, the calculated wave speed and attenuation of coherent waves in this high-frequency range (above $k_1 a = 10$) are purely mathematical with no connection to measurable physics. Furthermore, at these high frequencies, the intrinsic material absorption of constituents will

be dominant over the coherent attenuation. All these figures show that major changes in the effective properties occur at frequencies below $k_1a = 10$ and thus it is believed that this is the frequency range where a micromechanical theory is useful, not the high-frequency limit in which the effective properties have no relation to the randomness of the composite. Note also that typical ultrasonic measurements are usually limited to far below $k_1a = 10$. Again, therefore, the calculation and discussion of the effective properties of coherent waves in this high-frequency region are nonsensical. For all these reasons, regardless whether the EMT-1 is correct or incorrect in the high-frequency limit, it would be more sensible to limit the useful and physically meaningful frequency range of the EMT-1 to below $k_1a = 10$.

In Figure 2, the wave speed and attenuation calculated for the SiC/Ti composite are compared with the experimental data (the open squares) in the range 5–15 MHz which corresponds to $k_1a = 0.35$–1.05 [Kim 2010]. In this frequency range, the predictions from the two theories are indistinguishable, and the experimental wave speed shows a nearly constant wave speed ($\bar{c}/c_1 = 1.322$–1.316). This is close to the lower bound static wave speed, $\bar{c}/c_1 = 1.32$, which is the result of the well-isolated fiber arrangement in this composite (see, for example, the micrograph in [Huang and Rokhlin 1995]). Therefore, as mentioned earlier, the EMTs that implicitly assume an aggregated (or granular) microstructure [Yonezawa and Cohen 1983] are not suitable for predicting the effective wave speed of this composite. The low-frequency wave speed in this composite can be better predicted by a model that assumes an isolated arrangement of fibers [Kim 2004]. Every micromechanical model assumes a certain form of the microstructure and as a natural result every model has its utility for the microstructure that it assumes. A blind comparison between theories and experimental data, without considering the microstructure of the sample under examination, will lead to a meaningless conclusion. The attenuation factors predicted by the EMTs are in good agreement with the experimental results.

5. Conclusion

Two effective medium models [Kim 1996; Kanaun and Levin 2003] are formulated in a consistent mathematical procedure. The major difference between these two models lies in how the continuous matrix phase is treated. In spite of the apparently significant difference in these formulations (especially in their averaging schemes), the numerical results show minor discrepancies for all four distinctive composites and in frequencies up to $k_1a = 10$. This leads to the important conclusion that in the effective medium formulation the self-consistent embedding and the use of the fields in the inclusion obtained by solving the scattering problem in the effective medium are the core operations in which the effective properties are actually determined. Therefore, how the matrix phase is treated must be of minor importance and so could be details as to the representative volume for the matrix. This conclusion is fully supported by two composites with extremely different constituents properties. Deviations appear at the frequencies of inclusion resonances possibly due to their excessive motion. Both models are very efficient computationally compared to other models [Varadan et al. 1985] and take about the same computational cost. In summary, the recent formulation (the EMT-2) of [Kanaun and Levin 2003] does not seem to make an appreciable difference versus the earlier formulation (the EMT-1) of [Kim 1996]. This is analogous to the coincidence between different EMTs in the static limit. The same facts found for electromagnetic waves will be reported elsewhere. As to the question of which model is preferable, it is, of course, up to the reader's discretion to choose one between the two.

Appendix: The EMT-1 in the long wavelength limit

Let us first consider scattering of a plane SH wave ($u^{\text{in}} = \exp(ik_1x)$) by a single elastic circular inclusion having a radius a embedded in an infinite elastic matrix. The scattered and refracted fields may be expressed by an infinite series of normal modes as [Eringen and Suhubi 1975]

$$u^{\text{sc}} = \sum_{n=0}^{\infty} A_n H_n(k_1 r)\cos n\theta, \tag{A.1}$$

$$u^{\text{re}} = \sum_{n=0}^{\infty} B_n J_n(k_2 r)\cos n\theta, \tag{A.2}$$

where $J_n(z)$ is the Bessel function of order n and $H_n(z)$ the Hankel function of the first kind of order n. Imposing the boundary conditions (continuities of axial displacement and axial shear stress), the scattering coefficients are obtained:

$$A_n = -i^n \varepsilon_n \frac{p J_n'(\xi_1) J_n(\xi_2) - J_n(\xi_1) J_n'(\xi_2)}{p H_n'(\xi_1) J_n(\xi_2) - H_n(\xi_1) J_n'(\xi_2)}, \tag{A.3}$$

where ε_n is the Neumann factor, $p = \mu_1 k_1/\mu_2 k_2$, $\xi_1 = k_1 a$, and $\xi_2 = k_2 a$. In the long wavelength limit ($\xi_1, \xi_2 \to 0$), the scattering coefficients are

$$A_0 = -\frac{i\pi}{4}\left(\frac{\rho_2}{\rho_1} - 1\right)\xi_1^2 + O(\xi_1^4), \tag{A.4}$$

$$A_n = \frac{i\pi}{4^n n!(n-1)!}\left(\frac{\mu_2 - \mu_1}{\mu_2 + \mu_1}\right)\xi_1^{2n} + O(\xi_1^{2n+1}\ln\xi_1), \qquad n \geq 1. \tag{A.5}$$

Hence, the first two terms in Equation (A.1) with A_0 and A_1 are the leading terms in this limit. The forward scattering amplitude is approximated as

$$f_p(\boldsymbol{k}_1^i) \approx A_0 - iA_1. \tag{A.6}$$

There are two ways to derive the quasistatic effective properties: one using (33) and the other using (34). The second way, which is simpler and is essentially the method of Berryman [1979; 1980], is adopted. Consider scattering by the representative volumes for the matrix (Ω_m) and inclusion (Ω_i). It is first assumed that these volumes are circular and have radii of a_1 and a_2. Using (A.4)–(A.6) together with (34), the following two formulae are obtained:

$$\sum_{p=1,2} v_p \left(\frac{\mu_p - \bar{\mu}}{\mu_p + \bar{\mu}}\right)(\bar{k}a_p)^2 = 0, \qquad \sum_{p=1,2} v_p \left(\frac{\rho_p}{\bar{\rho}} - 1\right)(\bar{k}a_p)^2 = 0. \tag{A.7}$$

Note that the overbar indicates that the scattering occurs in the effective medium. It is obvious that in order for these formulae to be meaningful and consistent, the size of the matrix inclusion should be equal to that of the original inclusions, so $a_1 = a_2$. This means that in the EMT-1 the size of the original inclusion should be taken as the unit volume for all constituents in the composite. Then, one obtains the

effective static properties:

$$\sum_{p=1,2} v_p \left(\frac{\mu_p - \bar{\mu}}{\mu_p + \bar{\mu}} \right) = 0, \qquad \sum_{p=1,2} v_p \left(\frac{\rho_p}{\bar{\rho}} - 1 \right) = 0. \tag{A.8}$$

References

[Berryman 1979] J. G. Berryman, "Theory of elastic properties of composite materials", *Appl. Phys. Lett.* **35**:11 (1979), 856–858.

[Berryman 1980] J. G. Berryman, "Long-wavelength propagation in composite elastic media, I: Spherical inclusions", *J. Acoust. Soc. Am.* **68**:6 (1980), 1809–1819.

[Budiansky 1965] B. Budiansky, "On the elastic moduli of some heterogeneous materials", *J. Mech. Phys. Solids* **13**:4 (1965), 223–227.

[Bussink et al. 1995] P. G. J. Bussink, P. L. Iske, J. Oortwijn, and G. L. M. M. Verbist, "Self-consistent analysis of elastic wave propagation in two-dimensional matrix-inclusion composites", *J. Mech. Phys. Solids* **43**:10 (1995), 1673–1690.

[Choy 1999] T. C. Choy, *Effective medium theory*, Oxford University Press, Oxford, 1999.

[Eringen and Suhubi 1975] A. C. Eringen and E. S. Suhubi, *Elastodynamics*, vol. 2, Academic Press, New York, 1975.

[Frisch 1968] U. Frisch, "Wave propagation in random media", pp. 75–198 in *Probabilistic methods in applied mathematics*, vol. 1, edited by A. T. Bharuch-Reid, Academic Press, New York, 1968.

[Hill 1965] R. A. Hill, "A self-consistent mechanics of composite materials", *J. Mech. Phys. Solids* **13**:4 (1965), 213–222.

[Huang and Rokhlin 1995] W. Huang and S. I. Rokhlin, "Frequency dependences of ultrasonic wave velocity and attenuation in fiber composites: theory and experiments", pp. 1233–1240 in *Review of progress in quantitative nondestructive evaluation* (Snowmass Village, CO, 1994), vol. 14, edited by D. O. Thompson and D. E. Chimenti, Plenum Press, New York, 1995.

[Kanaun and Levin 2003] S. K. Kanaun and V. M. Levin, "Effective medium method in the problem of axial elastic shear wave propagation through fiber composites", *Int. J. Solids Struct.* **40**:18 (2003), 4859–4878.

[Kanaun et al. 2004] S. K. Kanaun, V. M. Levin, and F. J. Sabina, "Propagation of elastic waves in composites with random set of spherical inclusions (effective medium approach)", *Wave Motion* **40**:1 (2004), 69–88.

[Karal and Keller 1964] F. C. Karal and J. B. Keller, "Elastic, electromagnetic, and other waves in a random medium", *J. Math. Phys.* **5**:4 (1964), 537–547.

[Kim 1996] J.-Y. Kim, "Dynamic self-consistent analysis for elastic wave propagation in fiber reinforced composites", *J. Acoust. Soc. Am.* **100**:4 (1996), 2002–2010.

[Kim 2003a] J.-Y. Kim, "Extinction and propagation of elastic waves in inhomogeneous materials", *Mech. Mater.* **35**:9 (2003), 877–884.

[Kim 2003b] J.-Y. Kim, "Extinction of elastic wave energy due to scattering in a viscoelastic medium", *Int. J. Solids Struct.* **40**:17 (2003), 4319–4329.

[Kim 2004] J.-Y. Kim, "On the generalized self-consistent model for elastic wave propagation in composite materials", *Int. J. Solids Struct.* **41**:16–17 (2004), 4349–4360.

[Kim 2010] J.-Y. Kim, "Models for wave propagation in two-dimensional random composites: A comparative study", *J. Acoust. Soc. Am.* **127**:4 (2010), 2201–2209.

[Kim and Lee 2009] J.-Y. Kim and J.-S. Lee, "Extinction cross-section for elastic wave scattering in energy-absorbing media: revisited", *Acta Mech.* **207**:3–4 (2009), 153–161.

[Kim and Lee 2010] J.-Y. Kim and J.-S. Lee, "Erratum to: Extinction cross-section for elastic wave scattering in energy-absorbing media: revisited", *Acta Mech.* **211**:3–4 (2010), 357–359.

[Kim et al. 1995] J.-Y. Kim, J.-G. Ih, and B.-H. Lee, "Dispersion of elastic waves in random particulate composites", *J. Acoust. Soc. Am.* **97**:3 (1995), 1380–1388.

[Lax 1952] M. Lax, "Multiple scattering of waves, II: The effective field in dense systems", *Phys. Rev.* **85**:4 (1952), 621–629.

[Martin 2006] P. A. Martin, *Multiple scattering: Interaction of time-harmonic waves with N obstacles*, Cambridge University Press, New York, 2006.

[Niklasson et al. 1981] G. A. Niklasson, C. G. Granqvist, and O. Hunderi, "Effective medium models for the optical properties of inhomogeneous materials", *Appl. Opt.* **20**:1 (1981), 26–30.

[Sabina and Willis 1988] F. J. Sabina and J. R. Willis, "A simple self-consistent analysis of wave propagation in particulate composites", *Wave Motion* **10**:2 (1988), 127–142.

[Sheng 1995] P. Sheng, *Introduction to wave scattering, localization, and mesoscopic phenomena*, Academic Press, San Diego, CA, 1995.

[Soven 1967] P. Soven, "Coherent-potential model of substitutional disordered alloys", *Phys. Rev.* **156**:3 (1967), 809–813.

[Stroud and Pan 1978] D. Stroud and F. P. Pan, "Self-consistent approach to electromagnetic wave propagation in composite media: Application to model granular metals", *Phys. Rev. B* **17**:4 (1978), 1602–1610.

[Varadan et al. 1985] V. K. Varadan, V. V. Varadan, and Y. Ma, "Multiple scattering of elastic waves by cylinders of arbitrary cross section, II: Pair-correlated cylinders", *J. Acoust. Soc. Am.* **78**:5 (1985), 1874–1878.

[Velicky et al. 1968] B. Velicky, S. Kirkpatrick, and H. Ehrenreich, "Single-site approximations in the electronic theory of simple binary alloys", *Phys. Rev.* **175**:3 (1968), 747–766.

[Weaver 1985] R. L. Weaver, "A variational principle for waves in discrete random media", *Wave Motion* **7**:2 (1985), 105–121.

[Willis 1981] J. R. Willis, "Variational principles for dynamic problems for inhomogeneous elastic media", *Wave Motion* **3**:1 (1981), 1–11.

[Yonezawa and Cohen 1983] F. Yonezawa and M. H. Cohen, "Granular effective medium approximation", *J. Appl. Phys.* **54**:6 (1983), 2895–2899.

Received 30 May 2009. Revised 7 Dec 2009. Accepted 7 Dec 2009.

JIN-YEON KIM: jinyeon.kim@me.gatech.edu
School of Civil and Environmental Engineering, Georgia Institute of Technology, Atlanta, GA 30332, United States

JOURNAL OF MECHANICS OF MATERIALS AND STRUCTURES
Vol. 5, No. 4, 2010

A NUMERICAL MODEL FOR MASONRY-LIKE STRUCTURES

MAURIZIO ANGELILLO, LUCA CARDAMONE AND ANTONIO FORTUNATO

Masonry has historically been one of the most widely used construction materials. Despite this, there is a lack of computational tools for the analysis of masonry structures compared with what is available for steel and concrete structures. One of the main reasons is likely to be found in the peculiar mechanical behavior of masonry, which shows a small and unpredictable resistance in tension and a nonlinear inelastic behavior in compression. In this paper we put forward a constitutive model for masonry based on the extension to associate path-dependent plasticity of the classical normal, elastic, no-tension model. This new model allows the onset of fracture and irreversible crushing of the material and accounts for a wider variety of stress states within the structure, highlighting the progress of pseudorigid kinematics. The elastoplastic problem is decomposed into a sequence of nonlinear elastic problems formulated in variational form, which are solved by searching for the minimum of a suitable functional via descent methods. The model is implemented in variational finite element code and validated against analytical solutions and experimental tests. Applications to realistic cases are presented showing the capability of the model to reproduce nontrivial cracking and crushing patterns.

1. Introduction

Masonry structures, if not dry, are formed by individual blocks bound together by mortar joints. The complexity of the mechanical response of masonry materials depends not only on the narrow limits of applicability of simple theories, but above all on the inherent difficulties in the accurate characterization of their material behavior: besides the quality of the units and of the mortar, the quality of workmanship and the pattern the blocks are put in can strongly affect the mechanical properties of the overall construction in a practically unpredictable way. Although it is perfectly legitimate and appropriate to study and propose sophisticated models based on detailed knowledge of the microstructure [Luciano and Sacco 1997; Sab 2003] the range of applicability of such models is restricted to special situations. The material behavior of real masonry is strongly dependent on elastic nonlinearity, anisotropy, and friction, but considerations of simplicity and the inherent difficulties in actually knowing the material microstructure in old masonry suggest that we should not insist on very detailed descriptions of the stress-strain behavior [Lucchesi et al. 1996]. Concerning elastic nonlinearity and anisotropy there are no difficulties, at least in principle, to including such behaviors in the present model. But a reasonable model for masonry with a wide scope should be necessarily simplified and confined to the overall description of the mechanical behavior of large masonry masses.

Masonry material is brittle and characterized by a very small and unpredictable value of toughness; cracks are physiological in masonry, and are likely to open up in the material solely under the effect of working loads. As a first approximation of this behavior, a no-tension material model has been proposed.

Keywords: masonry, descent methods, energy minimization, unilateral materials, plasticity.

This crude model, which describes the material as elastic in compression but incapable of sustaining tensile stresses, was first introduced explicitly in [Heyman 1995]; however, the idea of a no-tension material underlies, more or less consciously, the design of all masonry structures, and has done so since antiquity [Benvenuto 1991], particularly in the case of vaulted structures and arches. Based on the no-tension model, the safety of the structure is a problem of geometry rather than of material strength, in keeping with the spirit of the rules of proportions used by ancient architects in masonry design. The approach of Heyman was aimed at collapse analysis of masonry structures. Analyzing the structure before collapse requires a description of strain more detailed than that considered by Heyman.

The unilateral constraint on stress produces a latent part of strain (anelastic strain) representing a local measure of cracking. A proper constraint principle has to be introduced to define the restrictions on the anelastic strain. The most popular choice is the normal elastic no-tension model (NENT) introduced in the 1980s (see [Romano and Romano 1979; Di Pasquale 1984; Castellano 1988; Angelillo 1993; Angelillo and Rosso 1995] for more general assumptions on fracture strains) and studied rigorously from the mathematical point of view in [Giaquinta and Giusti 1985]. A lucid and complete synthesis of the NENT model is presented in [Del Piero 1989].

Essentially the constitutive restrictions defining NENT materials are as follows:

- The stress tensor is assumed to be negative semidefinite and depend linearly upon the elastic part of the strain.
- The total strain is the sum of its elastic and anelastic parts.
- The anelastic strain is assumed to be normal to the boundary of the elastic stress domain and turns out to be positive semidefinite.

The NENT model gives a rather primitive description of the actual masonry behavior and can furnish only a gross overall description of the stress and fracture distribution in the material. Yet, in spite of its simplicity, it poses serious numerical problems even in the most elementary cases. A long series of papers on numerical techniques for the analysis of no-tension problems (see for example [Romano and Sacco 1984; Alfano et al. 2000] and references therein) has not, so far, produced computer codes simple enough to be included in structural analysis commercial packages. Besides, in many cases of practical interest, the structural crisis is due to simultaneous crack opening and crushing, that is, to the attainment of the limit strength in compression: the shear strength of a masonry wall depends sensibly on the crushing strength. A strength criterion in compression has to be added to the NENT model to account for such phenomena.

Here we consider a material model for masonry, called a masonry-like (ML) model, obtained by adding to the NENT restrictions a Drucker–Prager type yield criterion in compression and considering a flow rule for the corresponding anelastic strain rates of the associated type. The extension of the NENT model to limited compressive strength was considered in [Lucchesi et al. 1996; Marfia and Sacco 2005]. Both numerical approaches require the computation of the tangent stiffness matrix in order to determine the solution of the equilibrium problem. The ML material with bounded compressive strength proposed in [Lucchesi et al. 1996] is basically an elastic (i.e., conservative) NENT model with nonlinear behavior in compression, and therefore does not account for irreversible crushing and energy dissipation in the material. The model proposed in [Marfia and Sacco 2005] accounts for irreversible crushing of the material using a complex return mapping algorithm to compute the plastic strains.

The main contributions of the present paper consist in the development of an alternative numerical procedure based on descent minimization to solve the equilibrium problem at each loading step and a direct computation of the plastic strain increment, providing a simple and efficient tool for handling no-tension materials such as NENT and ML materials. The numerical method we propose, based on the NENT and ML material models, is aimed at description of the stress, fracture, irreversible crushing strain, and energy dissipation in plane masonry structures under working conditions, that is, away from collapse. This kind of analysis could be relevant in the diagnosis of structural disarrangement, where investigation is usually pursued long before signs of incipient collapse. The structure safety margins with respect to collapse can be evaluated beforehand by employing the tools of limit analysis [Como and Grimaldi 1985; Como 1992]. The presently proposed method of analysis can be applied to study collapse situations as limit cases, as illustrated by some of the examples presented in the applications.

In the first part of the paper we test the ability of our numerical approach to represent the behavior of structures made of normal elastic no-tension (NENT) material, that is, without the additional hypothesis of limited strength in compression. As proved in [Del Piero 1989] the NENT material is hyperelastic, the material response is path independent, and the equilibrium solutions can be characterized as minimizers of the total potential energy functional. Our research group in the last ten years has developed considerable numerical and computational experience in minimization problems for complex energy functionals [Angelillo et al. 2006; 2008]. The numerical technique we employ, based on descent methods (steepest descent, conjugate gradient), is unusual in structural mechanics. The convenience of descent methods, favored in recent years due to the increase of available computational power, is recovered in the case of nonsmooth energy shapes. In the specific case of masonry the method is particularly indicated since the problem becomes unconstrained and the potential energy is a convex function of its arguments. Several numerical tests we performed on simple problems, for which the exact solutions are known, show the competitiveness of the descent approach with respect to more classical techniques. Some of these benchmark problems are reported in Section 3. Comparisons with numerical solutions obtained by other developing codes [Lucchesi et al. 2008a] and commercial programs (ABAQUS) indicate [Angelillo et al. 2010] that the descent method seems to be the right choice to overcome the difficulties which are inherent to the no-tension constraint.

In the second part of this paper we consider ML materials, that is, we add to the NENT model a crushing strength criterion, considering an elastoplastic associate behavior. At first glance it seems that the proposed numerical technique, based on energy minimization (extremely convenient for unilateral materials) should be abandoned. The elastoplastic behavior is indeed inherently path-dependent: the stress state at time t depends, in general, on the whole strain history in the interval $[0, \bar{t})$ rather than on the strain at time t. Then the equilibrium problem for such a material is essentially an evolutive problem whose solution cannot be obtained by simply minimizing an energy functional. The proposed technique can still be applied to this evolutive problem considering the exact evolution as the limit of a sequence of minimum problems. This is done by discretizing the time interval into steps and updating the energy in a suitable way. The evolutive problem is then approximated as a sequence of a discrete number of minimizing movements. The evolutive solution is obtained as the limit of the discrete evolution by letting the time step go to zero (see [De Giorgi 1996] for the general formulation, and [Dal Maso et al. 2006; Mielke and Ortiz 2008] for the convergence proofs in the general case of rate independent materials and in the specific case of perfect elastoplasticity). Finally, we present some numerical results for ML structures.

2. Methods

2A. *The equilibrium problem for NENT materials.*

2A1. *Minimum problem.* Many problems in mathematics and physics can be formulated in terms of a minimum search: a functional describing the energy of the system and depending on an unknown function has to be minimized over the set of all admissible functions.

The form of energy to be minimized in the case of NENT materials is

$$\mathscr{E}(\boldsymbol{u}) = -\int_{\partial\Omega_N} \boldsymbol{p}\cdot\boldsymbol{u}\,ds - \int_\Omega \boldsymbol{b}\cdot\boldsymbol{u}\,da + \int_\Omega \varphi\big(\boldsymbol{e}(\boldsymbol{u})\big)\,da, \tag{2-1}$$

where $\boldsymbol{p}$ and $\boldsymbol{b}$ are the given loads, $\boldsymbol{e}(\boldsymbol{u})$ is the infinitesimal strain associated to $\boldsymbol{u}$:

$$\boldsymbol{e}(\boldsymbol{u}) = \tfrac{1}{2}(\nabla\boldsymbol{u} + \nabla\boldsymbol{u}^{\mathrm{T}}), \tag{2-2}$$

and $\varphi\big(\boldsymbol{e}(\boldsymbol{u})\big)$ is the elastic energy density. Then the stress $\boldsymbol{T}$ is related to $\boldsymbol{e}$ through the relation

$$\boldsymbol{T} = \frac{\partial\varphi}{\partial\boldsymbol{e}}. \tag{2-3}$$

The minimizer of $\mathscr{E}(\boldsymbol{u})$ is searched for as $\boldsymbol{u}\in\mathcal{S}$ (a Banach space) and $\boldsymbol{u}=\bar{\boldsymbol{u}}$ on $\partial\Omega_D$, where $\bar{\boldsymbol{u}}$ is the given displacement. The nature of such a Banach space and other results concerning the principle of minimum potential energy and the minimum of complementary energy are discussed in Appendix A.

2A2. *The boundary value problem in two dimensions.* As shown in [Del Piero 1989], an energy form $\varphi\big(\boldsymbol{e}(\boldsymbol{u})\big)$ can be introduced such that the minimum problem for the functional (2-1) provides the existence of the solution for the following boundary value problem in the two-dimensional case:

Given a bounded open set Ω of $\mathbb{R}^2$ and given

$$\boldsymbol{p}:\partial\Omega_N\to V^2,\quad \boldsymbol{b}:\Omega\to V^2,\quad \bar{\boldsymbol{u}}:\partial\Omega_D\to V^2, \tag{2-4}$$

find the fields

$$\boldsymbol{u}:\Omega\to V^2 \quad\text{and}\quad \boldsymbol{T}:\Omega\to \mathrm{Sym} \tag{2-5}$$

such that

$$\boldsymbol{T}\in \mathrm{N\,Sym}\ \text{ for } \boldsymbol{x}\in\Omega,\qquad \boldsymbol{e}(\boldsymbol{u})=\boldsymbol{\varepsilon}+\boldsymbol{\lambda},\qquad \boldsymbol{\varepsilon}=\mathbb{A}[\boldsymbol{T}],\qquad \boldsymbol{\lambda}\in \mathrm{P\,Sym}\ \text{ for } \boldsymbol{x}\in\Omega,\qquad \boldsymbol{T}\cdot\boldsymbol{\lambda}=0, \tag{2-6}$$

where N Sym and P Sym are the closed cones of negative semidefinite and positive semidefinite symmetric second order tensors and $\mathbb{A}$ is the positive definite fourth-order tensor of the elastic compliances, such that

$$\operatorname{div}\boldsymbol{T}+\boldsymbol{b}=\boldsymbol{0}\ \text{ in }\Omega,\qquad \boldsymbol{T}\boldsymbol{n}=\boldsymbol{p}\ \text{ on }\partial\Omega_N,\qquad \boldsymbol{u}=\bar{\boldsymbol{u}}\ \text{ on }\partial\Omega_D, \tag{2-7}$$

$\boldsymbol{n}$ being the unit outward normal to Ω.

The mechanical interpretation of conditions (2-6) and (2-7) is as follows. Conditions (2-6) are the restrictions characterizing NENT materials. They state that the stress $\boldsymbol{T}$ is negative semidefinite, that is,

$$\boldsymbol{T}\cdot\boldsymbol{m}\otimes\boldsymbol{m}\le 0\ \text{ for } \boldsymbol{m}\in V^2 \qquad \text{(no-tension assumption)}. \tag{2-8}$$

The total strain $\boldsymbol{e}$ is the sum of two parts: an elastic part $\boldsymbol{\varepsilon}$ related to the stress $\boldsymbol{T}$ through the linear operator $\mathbb{A}$ and a latent anelastic part $\boldsymbol{\lambda}$ which is positive semidefinite and orthogonal to $\boldsymbol{T}$. Conditions

(2-7) correspond to the equilibrium balance at the interior and on the part $\partial\Omega_N$ of the boundary, with the given force fields $\boldsymbol{b}$ and $\boldsymbol{p}$, and to the compatibility of the displacement field with the displacement given on the part $\partial\Omega_D$ of the boundary.

Notice that the condition on the displacement should actually be unilateral, since the material can open up freely. A way to keep the same displacement boundary conditions of classical elasticity is to consider the domain Ω closed on $\partial\Omega_D$, that is, to add to the domain a one-dimensional skin that must comply with the constraint on displacement, and to allow for concentrated deformations on $\partial\Omega_D$.

2A3. *Fundamental partition of a no-tension body.* The no-tension hypothesis restricts the stress to belonging to the cone of negative semidefinite symmetric tensors N Sym. This restriction is equivalent to restricting the principal stresses to be nonpositive. In the two-dimensional case the no-tension assumption is also equivalent to imposing the following restrictions on the invariants of $\boldsymbol{T}$:

$$\operatorname{tr}\boldsymbol{T} \le 0 \quad \text{and} \quad \det\boldsymbol{T} \ge 0. \tag{2-9}$$

These inequalities lead naturally to the following partition of the domain Ω:

$$\begin{aligned} \Omega_1 &= \{\boldsymbol{x} \in \Omega : \operatorname{tr}\boldsymbol{T} < 0, \det\boldsymbol{T} > 0\},\\ \Omega_2 &= \{\boldsymbol{x} \in \Omega : \operatorname{tr}\boldsymbol{T} < 0, \det\boldsymbol{T} = 0\},\\ \Omega_3 &= \{\boldsymbol{x} \in \Omega : \operatorname{tr}\boldsymbol{T} = 0, \det\boldsymbol{T} = 0\}. \end{aligned} \tag{2-10}$$

In Ω_1 the material subject to biaxial compression and behaves as a classical bilateral elastic material; in Ω_3 it is completely inert while in Ω_2 it is under uniaxial compression. Notice that in Ω_2 the equilibrium equations and the condition $\det\boldsymbol{T} = 0$ form a system of three equations in the three unknown independent components of $\boldsymbol{T}$. The differential problem is parabolic and the stress is determined by equilibrium regardless of the material response. In Ω_1 fractures are not possible, that is, $\boldsymbol{\lambda} = \boldsymbol{0}$. In Ω_3, where $\boldsymbol{T} = \boldsymbol{0}$ any positive semidefinite fracture field is possible. Also in Ω_2 the material can be fractured. The necessity of fractures is naturally produced by the problem being statically determined: the elastic strain associated with the statically determined stress is generally not compatible and fracture strains are required to restore compatibility.

The normality condition requires that in Ω_2 the fractures must open up orthogonally to the isostatic lines of compression. In an orthogonal curvilinear frame with natural bases $\{\boldsymbol{a}_1, \boldsymbol{a}_2\}$ coincident with the eigenvectors of $\boldsymbol{T}$, $\boldsymbol{T}$ admits the representation

$$\boldsymbol{T} = \sigma \frac{\boldsymbol{a}_1 \otimes \boldsymbol{a}_1}{\boldsymbol{a}_1 \cdot \boldsymbol{a}_1}, \tag{2-11}$$

with σ the only nonzero, negative eigenvalue of $\boldsymbol{T}$. Normality implies the following form for the fracture strain $\boldsymbol{\lambda}$:

$$\boldsymbol{\lambda} = \lambda \frac{\boldsymbol{a}_2 \otimes \boldsymbol{a}_2}{\boldsymbol{a}_2 \cdot \boldsymbol{a}_2}, \tag{2-12}$$

where λ is the only nonzero, nonnegative eigenvalue of $\boldsymbol{\lambda}$. Then regardless of the elastic anisotropy of a NENT material the principal directions of stress and anelastic strain are always coincident all over Ω.

2A4. *The strain energy density in two dimensions.* In the one-dimensional case the behavior of NENT materials is summarized by the stress-strain graph of Figure 1. Notice that the stress-strain relation is completely reversible both in traction and compression.

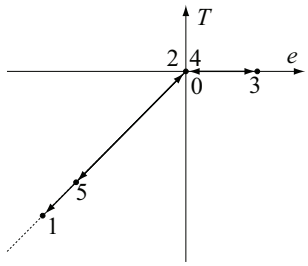

Figure 1. Stress-strain plot for a no-tension material in one dimension. A strain cycle is considered: $0 \to 1 \to 2$ (shortening cycle), $2 \to 3 \to 4$ (lengthening cycle), and $4 \to 5$ (further shortening). During shortening $T = Ee$ and $\lambda = 0$ (E being the Young's modulus), and during lengthening $T = 0$ and $\lambda = e$.

While in the one-dimensional case the existence of a strain energy density is assured, to obtain hyperelasticity in the two-dimensional case there is a price to pay: the assumption of normality must be made on the total latent strain $\boldsymbol{\lambda}$ (conditions $(2\text{-}6)_4$ and $(2\text{-}6)_5$). Such an assumption implies that on a discontinuity line Γ for the displacement, that is, the support of concentrated fractures, the jump of displacement must be orthogonal to Γ. Therefore sliding is forbidden on fracture lines.

It is shown in [Del Piero 1989] that for NENT materials the major symmetry of $\mathbb{A}$ is necessary and sufficient to get existence of an energy function. In the isotropic case (plane stress) the energy density φ is easily expressed in terms of the eigenvalues e_1 and e_2 ($e_1 \le e_2$) of $\boldsymbol{e}$:

$$\varphi(\boldsymbol{e}) = \begin{cases} 0 & \text{if } e_1 \ge 0, \\ \frac{1}{2} E e_1^2 & \text{if } e_1 < 0 \text{ and } e_2 \ge -\nu e_1, \\ \dfrac{E}{2(1-\nu^2)}(e_1^2 + e_2^2 + 2\nu e_1 e_2) & \text{if } e_1 < 0 \text{ and } e_2 < -\nu e_1, \end{cases} \tag{2-13}$$

where E is the Young's modulus and ν the Poisson's ratio. Notice that the stress $\boldsymbol{T}$, derived from φ by using (2-3), satisfies identically the no-tension restriction, that is, there is no need to impose it as a constraint. A representation of φ in the space of principal total strains is given in Figure 2.

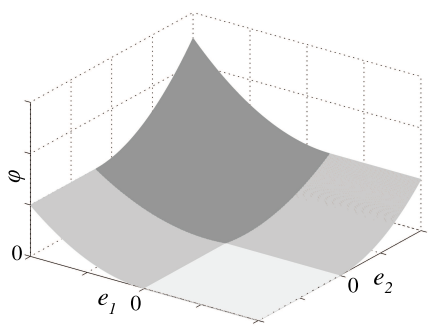

Figure 2. Strain energy density function for isotropic NENT material in two dimensions. In dark gray the parabolic sector corresponding to the biaxial compression is shown. In gray are the cylindrical regions of uniaxial compression, and in light gray the flat region of potential biaxial fractures.

For hyperelastic materials equilibrium states of the body can be sought as minimizers of the total potential energy (2-1):

$$\min_{\boldsymbol{u}\in\mathcal{K}} \mathscr{E}(\boldsymbol{u}), \tag{2-14}$$

$\mathcal{K}$ being the set

$$\mathcal{K} = \{\boldsymbol{u} \in \mathcal{S}(\Omega) : \boldsymbol{u} = \overline{\boldsymbol{u}} \text{ on } \partial\Omega_N\} \tag{2-15}$$

for $\mathcal{S}(\Omega)$ a convenient Banach space (see Appendix A).

2A5. *Numerical minimization strategy.* The numerical method we adopt to search for the minimum of the potential energy (2-1) is based on the direct minimization of such a functional through a descent method (steepest descent, conjugate gradient). The search is carried out in the subset of $\mathcal{K}$ defined by the C^0 displacement fields obtained by employing a standard finite element approximation based on a triangular finite element discretization Π_h of the domain Ω, where h is the mesh size. This kind of discretization excludes discontinuities in $\boldsymbol{u}$, that is, real cracks. The reason for considering such a simplification is twofold: Firstly, the authors believe that fractures in NENT material will appear smeared within the domain if the loads are not collapse loads in the sense specified in Appendix A. Secondly, in limit cases in which the loads approach the collapse limit the fracture strain may accumulate in narrow bands indicating the occurrence of real cracks in the limit.

The functional $\mathscr{E}$ is then approximated with the function $\mathfrak{E}(\{u_h\})$ of the nodal displacements $\{u_h\}$:

$$\mathfrak{E}(\{u_h\}) = -\sum_r L_r \boldsymbol{p}(\boldsymbol{x}_r)\cdot\boldsymbol{u}_r - \sum_m \boldsymbol{F}_m\cdot\boldsymbol{u}_m - \sum_n A_n\boldsymbol{b}(\boldsymbol{x}_n)\cdot\boldsymbol{u}_n + \sum_q A_q\varphi(\boldsymbol{x}_q), \tag{2-16}$$

where $\boldsymbol{u}_r$ is the displacement at the midpoint $\boldsymbol{x}_r$ of the r-th edge of length L_r on $\partial\Omega_n$, $\boldsymbol{u}_m$ the displacement of the m-th mesh node where the concentrated force $\boldsymbol{F}_m$ is applied, $\boldsymbol{u}_n$ the displacement of the Gauss point $\boldsymbol{x}_n$ of the n-th mesh triangle with area A_n, and $\boldsymbol{x}_q$ the Gauss point of the q-th mesh triangle of area A_q where the strain energy density φ is evaluated for integration. In (2-16) all the displacements $\boldsymbol{u}_j$, as well as the strain energy density $\varphi(\boldsymbol{x}_q)$ in the q-th triangle, are clearly explicit functions of the nodal displacements $\{u_h\}$ via the linear shape functions of a standard triangular mesh.

The iterative procedure adopted to minimize the function (2-16) is based on a step-by-step minimization method. Let us indicate with $\{u_h\}_j$ the nodal displacements at the j-th minimization step. The force acting on the mesh nodes is given by the negative gradient of the energy $\boldsymbol{F}(\{u_h\}_j) = -\nabla\mathfrak{E}(\{u_h\}_j)$. The descent method implemented computes the velocity $\boldsymbol{p}_j$ employing the nodal forces at the current and previous step as

$$\boldsymbol{p}_j = \eta_j\boldsymbol{p}_{j-1} + \boldsymbol{F}(\{u_h\}_j), \tag{2-17}$$

where the scalar η_j is

$$\eta_j = \max\left\{\frac{\boldsymbol{F}(\{u_h\}_j)\cdot\big(\boldsymbol{F}(\{u_h\}_j) - \boldsymbol{F}(\{u_h\}_{j-1})\big)}{\boldsymbol{F}(\{u_h\}_{j-1})\cdot\boldsymbol{F}(\{u_h\}_{j-1})}, 0\right\}, \tag{2-18}$$

in the Polak–Ribière version of the conjugate gradient method, and

$$\eta_j = \frac{\boldsymbol{F}(\{u_h\}_j)\cdot\boldsymbol{F}(\{u_h\}_j)}{\boldsymbol{F}(\{u_h\}_{j-1})\cdot\boldsymbol{F}(\{u_h\}_{j-1})}, \tag{2-19}$$

if the Fletcher–Reeves variant of the method is employed. (The Polak–Ribière method is usually adopted in the applications reported herein.)

If the nodes of the mesh are constrained, the velocity $\boldsymbol{p}_j$ is projected onto the tangent space of the constraints equation to obtain the compatible velocity $\boldsymbol{p}_j^*$. The velocity $\boldsymbol{p}_j^*$ gives the direction for the minimization motion while obeying all the constraints imposed on the nodes. The nodal displacement $\{u_h\}_j$ is computed as

$$\{u_h\}_j = \{u_h\}_{j-1} + \kappa_j \boldsymbol{p}_j^*, \tag{2-20}$$

where κ_j is the amplitude of the minimization step in the direction of $\boldsymbol{p}_j^*$ and is computed via line search method[1] to minimize the energy $\mathfrak{E}(\{u_h\})$ in the direction of the velocity $\boldsymbol{p}_j^*$. The iteration stops when a suitable norm of the energy gradient $\|\nabla\mathfrak{E}(\{u_h\}_j)\|$ becomes sufficiently small (see [Angelillo et al. 2008] for decrease conditions).

Descent methods appear very efficient in approximating the solutions of elastic problems with unilateral constraints on stress since the problem is reduced to the unconstrained minimization of a convex function. So far, there are no other computer programs of comparable simplicity for the stress analysis of no-tension materials. Numerical code for the approximation of the elastostatic problems of no-tension materials has been recently proposed in [Alfano et al. 2000; Lucchesi et al. 2008a], but such computer programs are still at a preliminary research stage.

The ability of descent methods to approximate the solution of boundary value problems for NENT materials is tested in this paper in two ways. The numerical solutions are compared first with some simple exact solutions, then with some experimental results. Finally the numerical solutions obtained with our code for more complex boundary value problems concerning masonry façades are presented.

2B. ***The equilibrium problem for ML materials.*** The crushing behavior of masonry is modeled as perfectly plastic. The initial-boundary value problem describing the quasistatic evolution of a no-tension elastoplastic body occupying a bounded domain Ω with boundary $\partial\Omega$ is then considered. Plastic behavior is described in terms of strain rates and the problem is not merely a boundary value one. The evolution is assumed to be quasistatic, that is, to occur so slowly that inertial and viscous effects may be ignored.

2B1. *The initial-boundary value problem in two dimensions.* Again we assume small strains and restrict ourselves to two-dimensional problems. The plastic behavior of the material is assumed to be represented within the classical framework of a convex elastic domain coupled with the normality law. The yield surface is assumed to be fixed in the stress space (no hardening or softening).

We consider given time dependent data such as fields $\boldsymbol{b}(\boldsymbol{x}, t)$ (body forces per unit volume), $\boldsymbol{p}(\boldsymbol{x}, t)$ (surface tractions per unit area), and $\bar{\boldsymbol{u}}(\boldsymbol{x}, t)$ (surface displacements):

$$\begin{aligned} \boldsymbol{b}: &\quad (\boldsymbol{x}, t) \in \Omega \times [0, \bar{t}) \to V^2, \\ \boldsymbol{p}: &\quad (\boldsymbol{x}, t) \in \partial\Omega_N \times [0, \bar{t}) \to V^2, \\ \bar{\boldsymbol{u}}: &\quad (\boldsymbol{x}, t) \in \partial\Omega_D \times [0, \bar{t}) \to V^2, \end{aligned} \tag{2-21}$$

with $[0, \bar{t})$ the time interval we consider and $\bar{t}$ the final instant of the simulation. Usually it is assumed that

$$\boldsymbol{b}(\boldsymbol{x}, 0) = \boldsymbol{0}, \quad \boldsymbol{p}(\boldsymbol{x}, 0) = \boldsymbol{0}, \quad \bar{\boldsymbol{u}}(\boldsymbol{x}, 0) = \boldsymbol{0}. \tag{2-22}$$

[1]The line search method calculates the energy for several values of the scale factor κ_j (doubling or halving each time) until the minimum energy is passed. The optimum scale is then calculated by quadratic interpolation.

Under the small strain hypothesis, the total deformation is again described by (2-2), and the additive decomposition of the total strain can be considered as

$$\boldsymbol{e} = \boldsymbol{\varepsilon}^e + \boldsymbol{\varepsilon}^p, \tag{2-23}$$

where $\boldsymbol{\varepsilon}^p$ is the plastic strain. Notice that now $\boldsymbol{\varepsilon}^e$ represents the total elastic deformation:

$$\boldsymbol{\varepsilon}^e = \boldsymbol{\varepsilon} + \boldsymbol{\lambda}, \tag{2-24}$$

the sum of

$$\boldsymbol{\varepsilon} = \mathbb{A}[\boldsymbol{T}], \tag{2-25}$$

where $\mathbb{A}$ is the compliance tensor, and

$$\boldsymbol{\lambda} \in \mathrm{P\,Sym}, \quad \boldsymbol{T} \cdot \boldsymbol{\lambda} = 0. \tag{2-26}$$

Assuming that the system is initially at rest in the natural state the initial conditions are

$$\boldsymbol{u}(\boldsymbol{x}, 0) = \boldsymbol{0} \quad \text{and} \quad \boldsymbol{T}(\boldsymbol{x}, 0) = \boldsymbol{0}. \tag{2-27}$$

The constitutive equations are defined on introducing the free energy $\varphi(\boldsymbol{\varepsilon}^e)$ and on specifying the flow law governing the evolution of the plastic strain. In particular $\varphi(\boldsymbol{\varepsilon}^e)$ is taken of the form (2-13):

$$\varphi(\boldsymbol{\varepsilon}^e) = \begin{cases} 0 & \text{if } \varepsilon_1^e \geq 0, \\ \frac{1}{2} E (\varepsilon_1^e)^2 & \text{if } \varepsilon_1^e < 0 \text{ and } \varepsilon_2^e \geq -\nu \varepsilon_1^e, \\ \dfrac{E}{2(1-\nu^2)} \big((\varepsilon_1^e)^2 + (\varepsilon_2^e)^2 + 2\nu \varepsilon_1^e \varepsilon_2^e \big) & \text{if } \varepsilon_1^e < 0 \text{ and } \varepsilon_2^e < -\nu \varepsilon_1^e, \end{cases} \tag{2-28}$$

ε_1^e and ε_2^e being the eigenvalues of $\boldsymbol{\varepsilon}^e$. The stress $\boldsymbol{T}$ is then assumed to be given by

$$\boldsymbol{T} = \frac{\partial \varphi(\boldsymbol{\varepsilon}^e)}{\partial \boldsymbol{\varepsilon}^e}. \tag{2-29}$$

We further assume that the stress cannot be arbitrarily large but is confined to belong to a bounded convex set K of Sym containing the origin. The interior of $K \cap \mathrm{N\,Sym}$ is the elastic region while its boundary is the yield surface. Notice that $K \cap \mathrm{N\,Sym}$ is convex but need not to be smooth. The boundary of K may be represented by the level set of a function f, called the crushing function, so that

$$K = \{\boldsymbol{T} \in \mathrm{Sym} : f(\boldsymbol{T}) \leq 0\}. \tag{2-30}$$

For the time rate $\dot{\boldsymbol{\varepsilon}}^p$ of the plastic strain we consider the associative flow law

$$(\boldsymbol{T}' - \boldsymbol{T}) \cdot \dot{\boldsymbol{\varepsilon}}^p \leq 0 \ \text{ for } \boldsymbol{T}' \in K. \tag{2-31}$$

For simplicity we consider

$$f(\boldsymbol{T}) = \varphi\big(\boldsymbol{\varepsilon}^e(\boldsymbol{T})\big) - \frac{\sigma_0^2}{2E}, \tag{2-32}$$

where $\varphi\big(\boldsymbol{\varepsilon}^e(\boldsymbol{T})\big) = \varphi(\mathbb{A}[\boldsymbol{T}] + \boldsymbol{\lambda}) = \varphi(\mathbb{A}[\boldsymbol{T}])$ is the strain energy density of the NENT material, expressed here as a function of the stress $\boldsymbol{T}$, and σ_0 is the crushing stress in axial compression, that is, the boundary of K is a level set of the free energy of the NENT material. Figure 3 depicts a section of the elastic domain on the plane $T_{12} = 0$.

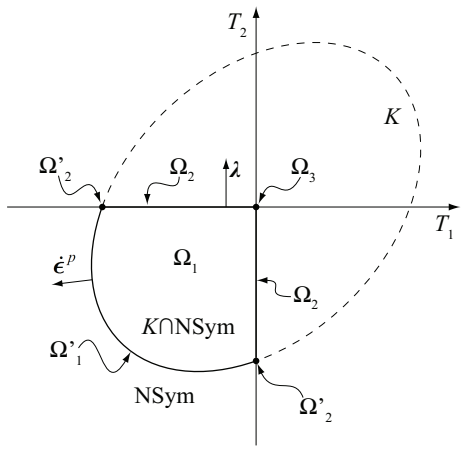

Figure 3. Elastic domain in the plane $T_{12} = 0$. The regions Ω'_i are the plastic duals of the regions Ω_i defined in (2-10), i.e., in Ω'_1 the material is yielding in biaxial compression while in Ω'_2 it is yielding in uniaxial compression. A point $\boldsymbol{x} \in \Omega$ lies in Ω_1 if and only if $\boldsymbol{T}(\boldsymbol{x}) \in (\mathrm{N}\,\mathring{\mathrm{Sym}} \cap K)$, and it lies in the union $\Omega'_1 \cup \Omega_2 \cup \Omega'_2 \cup \Omega_3$ if and only if $\boldsymbol{T}(\boldsymbol{x}) \in \partial(\mathrm{N}\,\mathrm{Sym} \cap K)$.

2B2. *Energy formulation, internal variables.* We choose to describe the problem in terms of the total strain and of the recorded history of mechanical behavior, by introducing as an internal variable the total plastic strain $\boldsymbol{\varepsilon}^p$. If we consider that the form of $\varphi(\boldsymbol{e}, \boldsymbol{\varepsilon}^p)$ is prescribed and that $\boldsymbol{T} = \partial\varphi/\partial\boldsymbol{\varepsilon}^e$, the instantaneous values of $\boldsymbol{T}$ are known if $\boldsymbol{e}$ is given and the entire process of plastic strain is known. Obviously $\boldsymbol{\varepsilon}^p(t) = \int_0^t \dot{\boldsymbol{\varepsilon}}^p(\tau)\,d\tau$ and $\dot{\boldsymbol{\varepsilon}}^p$ is described by the flow rule (2-31). In the one-dimensional case the stress-deformation behavior, the admissible region in the (e, ε^p) space and the form of φ, represented by a three-dimensionalgraph in the space $(e, \varepsilon^p, \varphi)$, are depicted in Figure 4, where a typical loading path

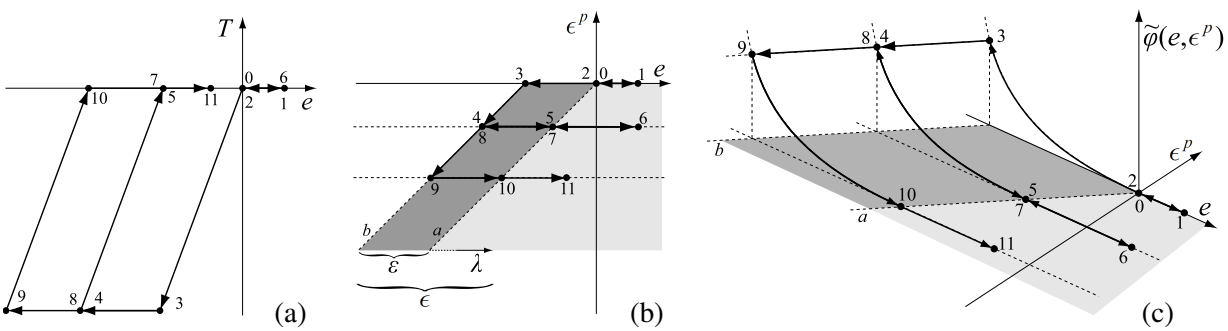

Figure 4. Example of loading-unloading paths of an ML material in one dimension depicted in (a) the (e, T) plane, (b) the (e, ε^p) plane, and (c) the $(e, \varepsilon^p, \varphi)$ space: $0 \to 1 \to 2$ (lengthening cycle), $2 \to 3 \to 4 \to 5$ (shortening cycle in elastoplastic regime), $5 \to 6 \to 7$ (lengthening cycle), $7 \to 8 \to 9 \to 10$ (shortening cycle), and $10 \to 11$ (further lengthening). The material is fractured in the light gray area and compressed in the dark gray area, while plastic strain increases during the compressions $3 \to 4$ and $8 \to 9$.

is reported. Notice that, based on the ML model, fracture strains are reversible and are perfectly recoiled upon load inversion. Crushing strains, by contrast, cannot be healed and, being totally irreversible, can either stay or grow. In other words, smeared fractures cannot cancel crushing strains; the two mechanisms are completely independent.

2B3. *Numerical minimization strategy.* The time interval $[0, \bar{t})$ is discretized into k subintervals by means of the instants $0 = t_0 \le \cdots \le t_i \cdots \le t_k = \bar{t}$. The idea is to solve, at each time step t_i, the minimum problem of a suitably defined, updated functional characteristic of an evolving no-tension material with a nonlinear elastic behavior in compression, to approximate the solution path $\zeta(t) = \big(\boldsymbol{u}(t), \boldsymbol{\varepsilon}^p(t)\big)$ which solves the initial-boundary value problem defined above.

To model perfect plasticity in compression, we assume a linearly-growing extension of the strain energy function (2-13) above the yield surface defined by (2-32). Namely, at time step t_i, the functional form implemented in the finite element code is

$$\tilde{\varphi}_i(\boldsymbol{\varepsilon}_i^e) = \begin{cases} 0 & \text{if } (\varepsilon_i^e)_1 \ge 0,\ (\varepsilon_i^e)_2 \ge 0, \\ \frac{1}{2} E (\varepsilon_i^e)_1^2 & \text{if } (\varepsilon_i^e)_1 < 0,\ (\varepsilon_i^e)_2 \ge -\nu(\varepsilon_i^e)_1,\ f(\boldsymbol{\varepsilon}_i^e) \le 0, \\ \alpha\sqrt{\frac{1}{2} E (\varepsilon_i^e)_1^2} + \beta & \text{if } (\varepsilon_i^e)_1 < 0,\ (\varepsilon_i^e)_2 \ge -\nu(\varepsilon_i^e)_1,\ f(\boldsymbol{\varepsilon}_i^e) > 0, \\ \dfrac{E}{2(1-\nu)}\big((\varepsilon_i^e)_1^2 + (\varepsilon_i^e)_2^2 + 2\nu(\varepsilon_i^e)_1(\varepsilon_i^e)_2\big) & \text{if } (\varepsilon_i^e)_1 < 0,\ (\varepsilon_i^e)_2 < -\nu(\varepsilon_i^e)_1,\ f(\boldsymbol{\varepsilon}_i^e) \le 0, \\ \alpha\sqrt{\dfrac{E}{2(1-\nu^2)}\big((\varepsilon_i^e)_1^2 + (\varepsilon_i^e)_2^2 + 2\nu(\varepsilon_i^e)_1(\varepsilon_i^e)_2\big)} + \beta & \text{if } (\varepsilon_i^e)_1 < 0,\ (\varepsilon_i^e)_2 < -\nu(\varepsilon_i^e)_1,\ f(\boldsymbol{\varepsilon}_i^e) > 0, \end{cases} \tag{2-33}$$

where the elastic strain at time t_i is given by the difference between the total strain $\boldsymbol{e}_i$ at the same time step and the plastic strain inherited from the previous solution step $\boldsymbol{\varepsilon}_{i-1}^p$, i.e., $\boldsymbol{\varepsilon}_i^e = \boldsymbol{e}_i - \boldsymbol{\varepsilon}_{i-1}^p$, and $(\varepsilon_i^e)_j$ $(j = 1, 2)$ are the principal values of $\boldsymbol{\varepsilon}_i^e$. The constants $\alpha = \sqrt{2/E}\sigma_0$ and $\beta = -\sigma_0^2/(2E)$ are introduced to preserve the C^1 regularity of $\tilde{\varphi}_i$. A representation of $\tilde{\varphi}_i$ in the space of principal elastic strains is given in Figure 5. The numerical method finds the minimum of the total potential energy defined at time t_i as

$$\mathscr{E}_i(\boldsymbol{u}_i) = -\int_{\partial\Omega_N^i} \boldsymbol{p}_i \cdot \boldsymbol{u}_i \, ds - \int_\Omega \boldsymbol{b}_i \cdot \boldsymbol{u}_i \, da + \int_\Omega \tilde{\varphi}_i\big(\boldsymbol{e}_i(\boldsymbol{u}_i)\big) da, \tag{2-34}$$

via finite element discretization of the domain Ω and descent minimization. The solution at the previous load step is used as the initial condition for the minimization of the function

$$\mathfrak{E}_i(\{u_h\}_i) = -\sum_r L_r \boldsymbol{p}_i(\boldsymbol{x}_r) \cdot \boldsymbol{u}_r - \sum_m \boldsymbol{F}_m \cdot \boldsymbol{u}_m - \sum_n A_n \boldsymbol{b}_i(\boldsymbol{x}_n) \cdot \boldsymbol{u}_n + \sum_q A_q \tilde{\varphi}_i(\boldsymbol{x}_q), \tag{2-35}$$

representing the finite element approximation of the total potential energy (2-34) as in the case of (2-16) for the NENT material. The minimization is performed via the descent method described in Section 2A5.

A plastic strain update is then performed at each Gauss point: Equation (2-32) defines a surface whose position vector is $\boldsymbol{s}$, of coordinates $\{s_j\}$, in the space of principal elastic strains $\boldsymbol{\varepsilon}_i^e$. It is useful to give a parametric description $\boldsymbol{s}(\boldsymbol{\gamma})$ of the yielding surface in the space of principal elastic strain, with $\boldsymbol{\gamma}$ being a suitable set of parameters. The return mapping algorithm, according to the principle of minimum

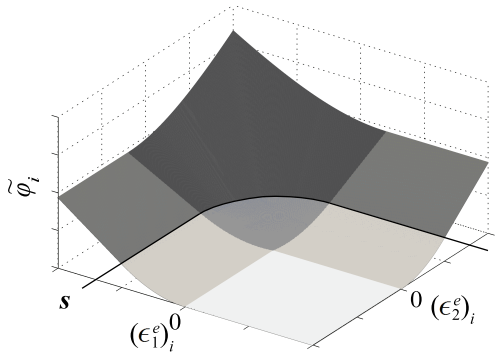

Figure 5. Strain energy density function for an isotropic ML material in two dimensions. It is evident here that, above the yielding curve s, the energy consists of an extension of the energy φ, depicted in Figure 2, characterized by a linear growth.

dissipation imposed by the assumption of associated plasticity [Ortiz and Simo 1986], consists in finding the set of parameters $\boldsymbol{\gamma}^0$ of minimum distance, in the energy norm, of the current elastic strain $\boldsymbol{\varepsilon}_i^e$ from the surface $\boldsymbol{s}(\boldsymbol{\gamma})$:

$$\min_{\boldsymbol{\gamma}} \varphi\big(\boldsymbol{s}(\boldsymbol{\gamma}) - \boldsymbol{\varepsilon}_i^e\big). \tag{2-36}$$

In the two-dimensional case considered here, the yielding surface is merely a curve in the plane of the principal elastic strains $(\varepsilon_i^e)_j$ $(j = 1, 2)$, as depicted in Figure 5, and can be described by a single parameter γ. The minimum problem (2-36) can be easily formulated as

$$\frac{d}{d\gamma}\varphi\big(\boldsymbol{s}(\gamma) - \boldsymbol{\varepsilon}_i^e\big) = 0. \tag{2-37}$$

Equation (2-37) is solved for γ, at each Gauss point, via the Newton–Raphson method.

The tensor of plastic strain rate $\dot{\boldsymbol{\varepsilon}}^p$ at time t_i is coaxial to the elastic strain tensor $\boldsymbol{\varepsilon}_i^e$, therefore the principal components $(\Delta\varepsilon_i^p)_j$ (with $j = 1, 2$) of the plastic strain increment $\Delta\boldsymbol{\varepsilon}_i^p$ (i.e., the discrete version of $\dot{\boldsymbol{\varepsilon}}^p$) are simply computed as

$$(\Delta\varepsilon_i^p)_j = (\varepsilon_i^e)_j - s_j(\gamma^0). \tag{2-38}$$

Once the plastic strain has been updated in the global reference frame, i.e., $\boldsymbol{\varepsilon}_i^p = \boldsymbol{\varepsilon}_{i-1}^p + \Delta\boldsymbol{\varepsilon}_i^p$ (a backward Euler finite difference scheme), the energy density dissipation at the given Gauss point, at time step i, can be computed as

$$\mathcal{D}_i = \tilde{\varphi}_i(\boldsymbol{e}_i, \boldsymbol{\varepsilon}_{i-1}^p) - \tilde{\varphi}_i(\boldsymbol{e}_i, \boldsymbol{\varepsilon}_i^p) = \tilde{\varphi}_i(\boldsymbol{e}_i, \boldsymbol{\varepsilon}_{i-1}^p) - \tfrac{1}{2}\boldsymbol{T}_i\mathbb{A}[\boldsymbol{T}_i], \tag{2-39}$$

where it is clear from the first expression that the plastic strain increments dissipate energy. The stress tensor $\boldsymbol{T}_i$ in the second expression is computed via (2-29).

3. Comparing numerical with analytical/semianalytical solutions for NENT materials

3A. ***Flexure of a NENT panel.*** The first problem we consider is the flexure of a rectangular strip. The geometry and the boundary conditions are depicted in Figure 6 to which we refer for notation.

A simple solution of the problem exists if the material is isotropic and $\nu = 0$. The displacement field $\boldsymbol{u} = u\hat{\boldsymbol{\imath}} + v\hat{\boldsymbol{\jmath}}$, $\hat{\boldsymbol{\imath}}$ and $\hat{\boldsymbol{\jmath}}$ being the unit vectors in the x and y directions respectively, with

$$u = \frac{\Phi}{H}(H - 2x)y, \quad v = \frac{\Phi}{H}x(x - H), \tag{3-1}$$

solves all the field and boundary equations for an isotropic NENT material with $\nu = 0$. Indeed the corresponding total strain is

$$\boldsymbol{e} = -\frac{2\Phi}{H}y\hat{\boldsymbol{\imath}} \otimes \hat{\boldsymbol{\imath}}, \tag{3-2}$$

which is easily decomposed into the elastic and fracture parts:

$$\boldsymbol{\varepsilon} = \begin{cases} \boldsymbol{e} & \text{if } y > 0, \\ \boldsymbol{0} & \text{if } y \le 0, \end{cases} \qquad \boldsymbol{\lambda} = \begin{cases} \boldsymbol{0} & \text{if } y > 0, \\ \boldsymbol{e} & \text{if } y \le 0. \end{cases} \tag{3-3}$$

The corresponding stress field is

$$\boldsymbol{T} = \begin{cases} -E\dfrac{2\Phi}{H}y\hat{\boldsymbol{\imath}} \otimes \hat{\boldsymbol{\imath}} & \text{if } y > 0, \\ \boldsymbol{0} & \text{if } y \le 0. \end{cases} \tag{3-4}$$

This stress field is obviously balanced with the prescribed loads $\boldsymbol{b} = \boldsymbol{0}$ at the interior and with the surface tractions $\boldsymbol{p} = \boldsymbol{0}$ given at the boundary $|x| = B/2$. Based on this solution for the stress the domain Ω is split into two zones of type Ω_2, Ω_3 as depicted in Figure 6. This example can give some evidence of the nonuniqueness of the solution and particularly the possibility of different fracture fields under the same boundary conditions.

Indeed another solution to the same problem is defined by the displacement field $\boldsymbol{u} = u\hat{\boldsymbol{\imath}} + v\hat{\boldsymbol{\jmath}}$ with

$$u = \begin{cases} \Phi(y/H)(H - 2x) & \text{if } y > 0, \\ \Phi y & \text{if } y < 0 \text{ and } x < H/2, \\ -\Phi y & \text{if } y < 0 \text{ and } x > H/2, \end{cases} \tag{3-5}$$

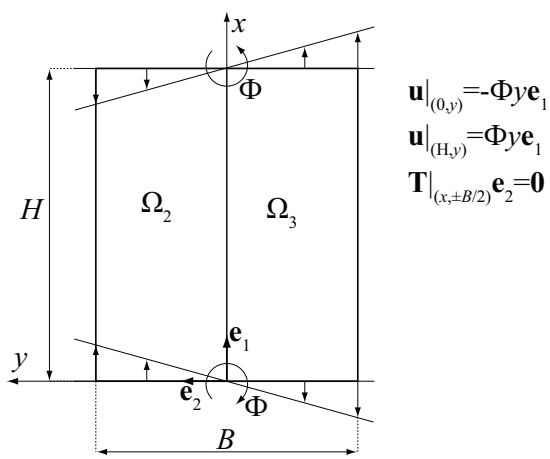

Figure 6. Flexure of a NENT panel: coordinates, nomenclature, boundary conditions, and partition of the domain.

and

$$v = \begin{cases} \Phi(x/H)(x-H) & \text{if } y > 0, \\ -\Phi x & \text{if } y < 0 \text{ and } x < H/2, \\ \Phi(x-H) & \text{if } y < 0 \text{ and } x > H/2. \end{cases} \tag{3-6}$$

The corresponding total strain is composed of absolutely continuous and singular parts: $\boldsymbol{e} = \boldsymbol{e}^a + \boldsymbol{e}^s$ with

$$\boldsymbol{e}^a = \begin{cases} -2\Phi(y/H)\hat{\boldsymbol{\imath}} \otimes \hat{\boldsymbol{\imath}} & \text{if } y > 0, \\ \mathbf{0} & \text{if } y \le 0, \end{cases} \tag{3-7}$$

and

$$\boldsymbol{e}^s = \begin{cases} (\Phi/H)x^2\delta(y)\hat{\boldsymbol{\jmath}} \otimes \hat{\boldsymbol{\jmath}} & \text{if } x \le H/2, \\ (\Phi/H)(x-H)^2\delta(y)\hat{\boldsymbol{\jmath}} \otimes \hat{\boldsymbol{\jmath}} & \text{if } x > H/2, \\ -2\Phi y\delta(x-H/2)\hat{\boldsymbol{\imath}} \otimes \hat{\boldsymbol{\imath}} & \text{if } y \le 0, \\ \mathbf{0} & \text{otherwise.} \end{cases} \tag{3-8}$$

Here $\delta(\xi)$ denotes the line Dirac delta at $\xi = 0$. The total strain is decomposed in its elastic and fracture parts as follows:

$$\boldsymbol{\lambda} = \boldsymbol{e}^s, \quad \boldsymbol{\varepsilon} = \boldsymbol{e}^a. \tag{3-9}$$

Therefore the stress $\boldsymbol{T}$ is the same as that of the first solution and determines the same partition of the domain Ω as described in Figure 6.

The fracture strain is singular and corresponds to the cracks exhibited by the deformed configuration depicted in Figure 7, left. Graphs of the λ_{11} and λ_{22} components of $\boldsymbol{\lambda}$ are reported in Figure 7, middle.

In the absence of any energy price to pay to open up fractures the two solutions reported are perfectly equivalent and the body can choose any of the two. It could be of some interest to look at the result of a flexure test performed on an ML material (a composite of lime, gypsum, and pozzolana with a ratio between tensile and compressive strength of 1/30) shown in Figure 7, right.

In the numerical simulations we assumed $\nu = 0$, $E = 660\,\text{MPa}$, $\Phi = 0.001$, $H = B = 2\,\text{m}$, and thickness equal to 0.5 m. Figure 8, left, is a contour plot of the maximum eigenvalue of the fracture strain. Fractures are nonzero in the region indicated by Ω_3 in Figure 6, and their distribution suggests that the numerical solution is close to the rigid-block scheme of Figure 8, right, which can be an energetically-equivalent alternative to the two solutions introduced above.

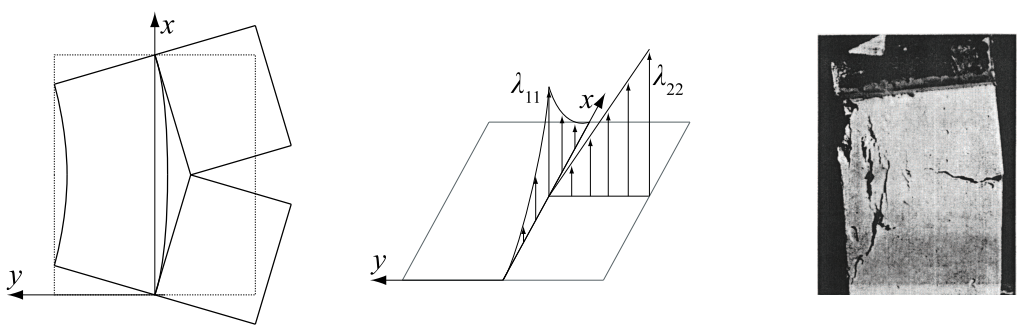

Figure 7. Flexure of a NENT panel. Left: deformed configuration corresponding to the solution described in (3-5)–(3-9). Middle: plot of the singular part of the strain described by $(3\text{-}8)_2$. Right: flexure test on a masonry panel (courtesy of G. Castellano).

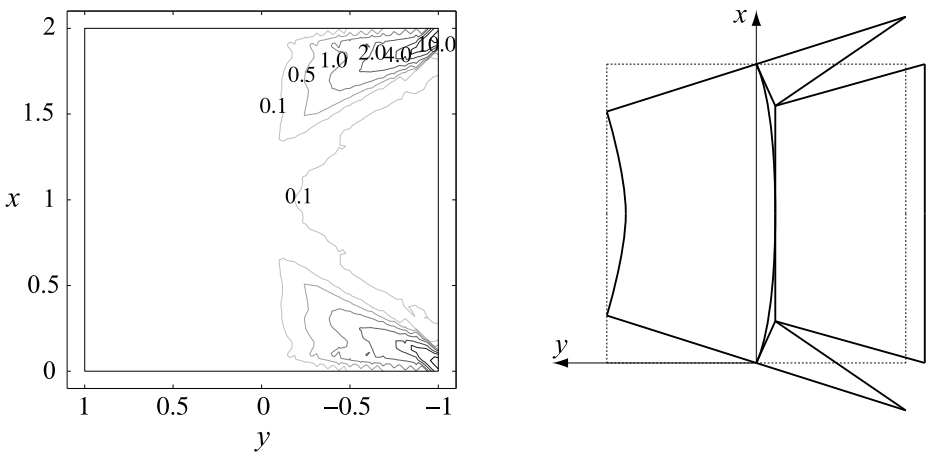

Figure 8. Flexure of a NENT panel. Left: maximum fracture strain $[10^{-3}]$. Right: rigid-block kinematic close to the numerical solution.

We performed a numerical convergence study on the stress for the flexure problem of a NENT panel by considering a sequence of discretizations of decreasing mesh size h. The result is reported in Figure 9. The top row of Figure 10 shows the different discretizations of the domain Ω employed in the convergence analysis. The related level plots of the maximum stress compared to the exact solution described by (3-4) are depicted in the bottom row of Figure 10, to show graphically the rate of convergence.

In Figure 9 we plot the correlation between the approximation error for the stress

$$e_h = \frac{\|\boldsymbol{T}_h - \boldsymbol{T}_0\|_{L^2}}{\|\boldsymbol{T}_h\|_{L^2}} \tag{3-10}$$

and the dimensionless mesh size h/D, where $D = \sqrt{H^2 + B^2}$ is the diameter of Ω, $\boldsymbol{T}_h$ is the stress field computed with a mesh of size h and $\boldsymbol{T}_0$ is the exact solution. A linear convergence of the method is obtained.

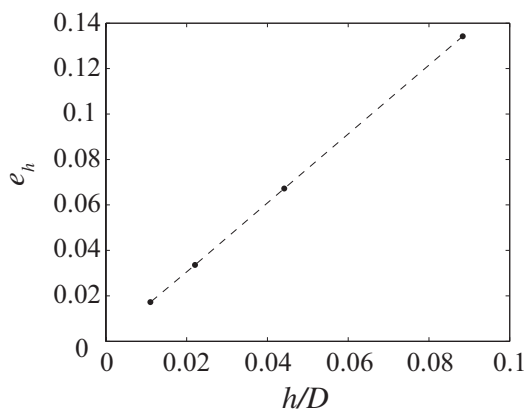

Figure 9. Flexure of a NENT panel: convergence diagram.

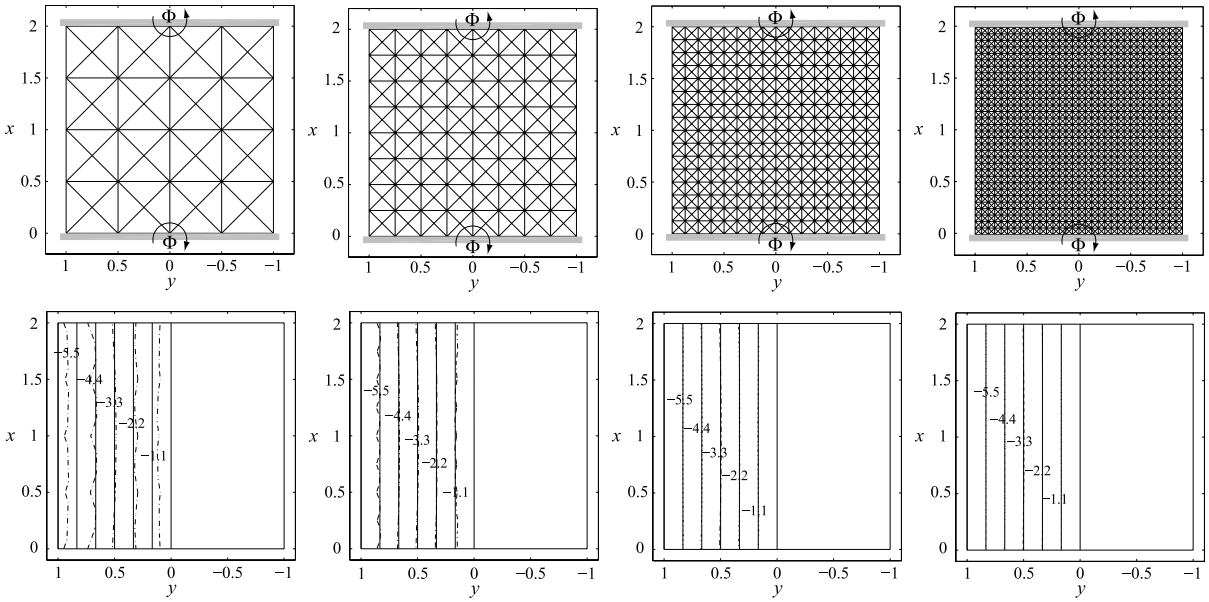

Figure 10. Flexure of a NENT panel. Top: meshes employed for the simulations in the convergence analysis. Bottom: progressive convergence of the computed maximum stress contour plot (dash-dotted curves) [10^5 Pa] to the exact solution (solid curves).

3B. ***Shear of a NENT panel.*** The simple rectangular panel depicted in Figure 11 subject to a given relative horizontal translation of the bases (of value $2U$) and zero traction condition on the lateral sides is considered. The material parameters and the geometry are the same adopted in the previous section. The value $U = 1$ mm is considered.

In Figures 11 and 12 the numerical solution is compared to a semianalytical solution obtained by minimizing the complementary energy $\mathscr{E}_c$ (see Appendix B), restricting the search to uniaxial stress

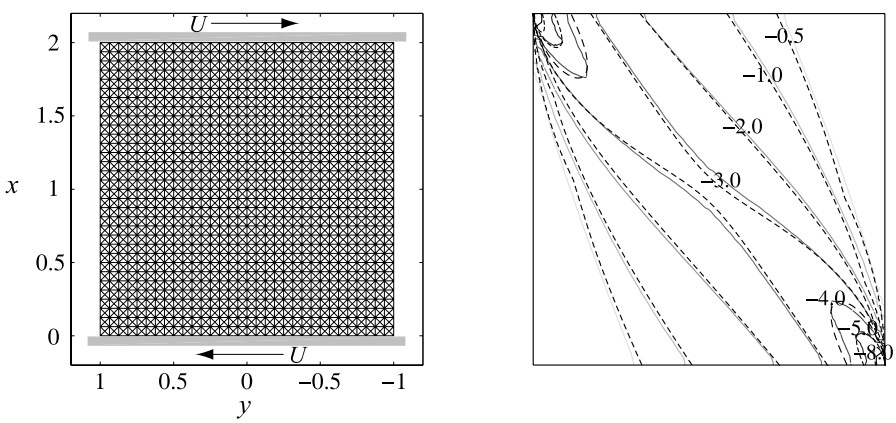

Figure 11. Shear of a NENT panel. Left: mesh and boundary conditions. Right: comparison of the maximum compressive stress [10^5 Pa] obtained via finite element solution (solid curves) with the semianalytical method of [Fortunato 2010] (dashed curves).

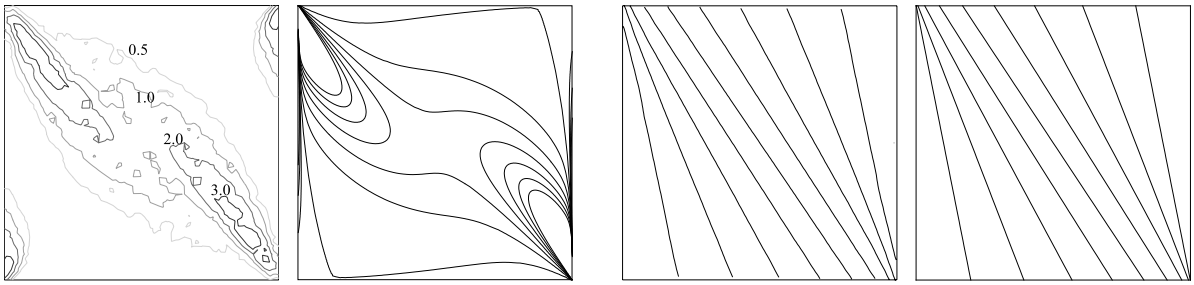

Figure 12. Shear of a NENT panel: maximum principal value of the fracture strain $[10^{-3}]$ (left two panes) and isostatic curves (right two panes), computed via finite elements (FE) and via the semianalytical approach (SA).

states, that is, assuming that $\Omega = \Omega_2 \cup \Omega_3$. The general case of arbitrary prescribed relative displacements between the two bases is considered and solved in [Fortunato 2010]. To make the present paper self contained we present in Appendix B the derivation of this semianalytical solution in the special case considered here. The distribution of the maximum compressive stress, the fracture strain, and the form of the isostatic lines computed numerically are in good agreement with the results of the semianalytical method of [Fortunato 2010], as summarized in Figures 11 and 12.

4. Comparing numerical solutions with analytical solutions and experiments for ML materials

4A. ***Flexure of an ML panel.*** The numerical experiment performed in Section 3A for a NENT panel is repeated here for an ML panel assuming $\Phi = 0.006$ and the maximum compressive strength $\sigma_0 = 19.8\,\text{MPa}$. The value of $\Phi = 2\sigma_0 H/BE$ is selected in such a way that the strip $y > B/4$ is forced into the yielding regime. The exact stress solution is

$$\boldsymbol{T}_0 = \begin{cases} -\sigma_0 \hat{\boldsymbol{\imath}} \otimes \hat{\boldsymbol{\imath}} & \text{if } y \geq B/4, \\ -4\sigma_0 (y/B) \hat{\boldsymbol{\imath}} \otimes \hat{\boldsymbol{\imath}} & \text{if } 0 < y < B/4, \\ \mathbf{0} & \text{if } y \leq 0. \end{cases} \tag{4-1}$$

Again a sequence of discretizations of decreasing mesh size is considered. Figure 13a shows the computed isostatic curves. For the finest mesh they are very close to being vertical lines as expected. In Figure 13b we compare the level plot of the computed maximum compressive stress relative to the finest mesh (the solid lines) with the exact solution given by (4-1) (the dash-dotted lines). The solution shows good accuracy. The maximum fracture strain is reported in Figure 13c, and it can be noticed that the fracture distribution in the strip $y < 0$ (region Ω_3 in Figure 6) is similar to the one observed in the NENT material (see Figure 8a). The distribution of fracture strain in the Ω_2 region resembles closely the vertical fractures that appear in the experiment shown in Figure 13d. We point out here that, in this problem, the distribution of plastic strains is not unique since they only need to satisfy the integral relation

$$\int_0^H \lambda_{11}(x, y)\, dx = -\frac{2\Phi}{H} y + \frac{\sigma_0}{E} \qquad \text{for } y \geq \frac{B}{4}. \tag{4-2}$$

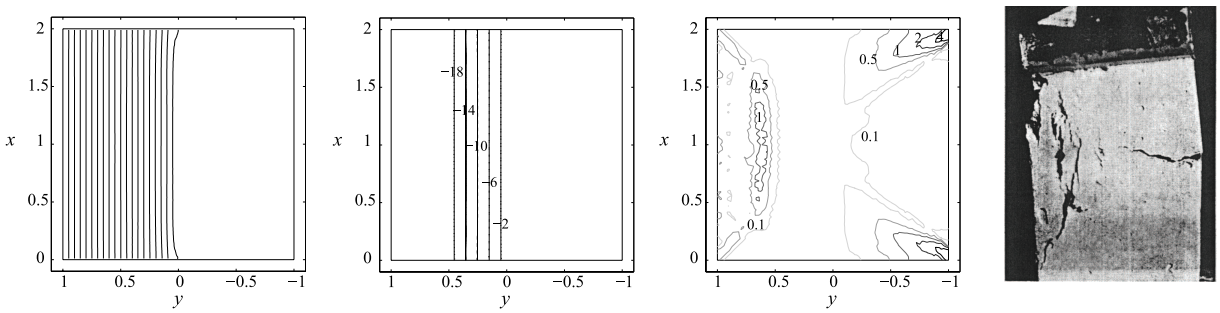

Figure 13. Flexure of an ML panel: (a) isostatic curves, (b) contour plot of the computed maximum compression (the dash-dotted curves) compared to the exact solution [10^5 Pa], (c) contour plot of the maximum principal value of the fracture strain [10^{-3}] compared to (d) flexure test on a masonry panel (courtesy of G. Castellano).

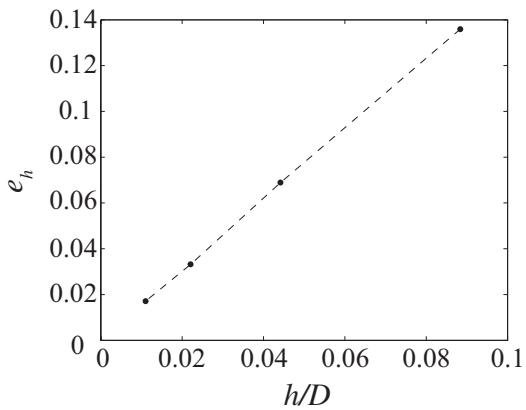

Figure 14. Flexure of an ML panel: convergence diagram.

Figure 14 shows the convergence diagram for the problem of flexure of an ML panel. The definitions of the normalized mesh size h/D and of the error e_h are the same introduced in Section 3A and the method converges again linearly to the exact solution given by (4-1).

4B. ***Shear of an ML panel.*** The value of the displacement at the boundary U considered in Section 3B is small enough to confine yielding in the material close to the corners of an ML panel that behaves essentially as a NENT panel. In this section we follow the evolution of the shear problem as the value of U increases and the crushing of the material progresses.

In Figure 15 we report three stages of the evolving solution. As the boundary displacement increases, a diagonal band, uniaxially and uniformly compressed at the limit stress $\sigma_0 = 1.98$ MPa, forms progressively and the isostatic lines become parallel.

The contour plots in Figure 16 show the maximum fracture strain, which concentrates on two subdiagonal lines, and the maximum plastic strain, which concentrates near the constrained boundary. The concentration of the plastic strain is expected, due to the perfect plasticity of the material.

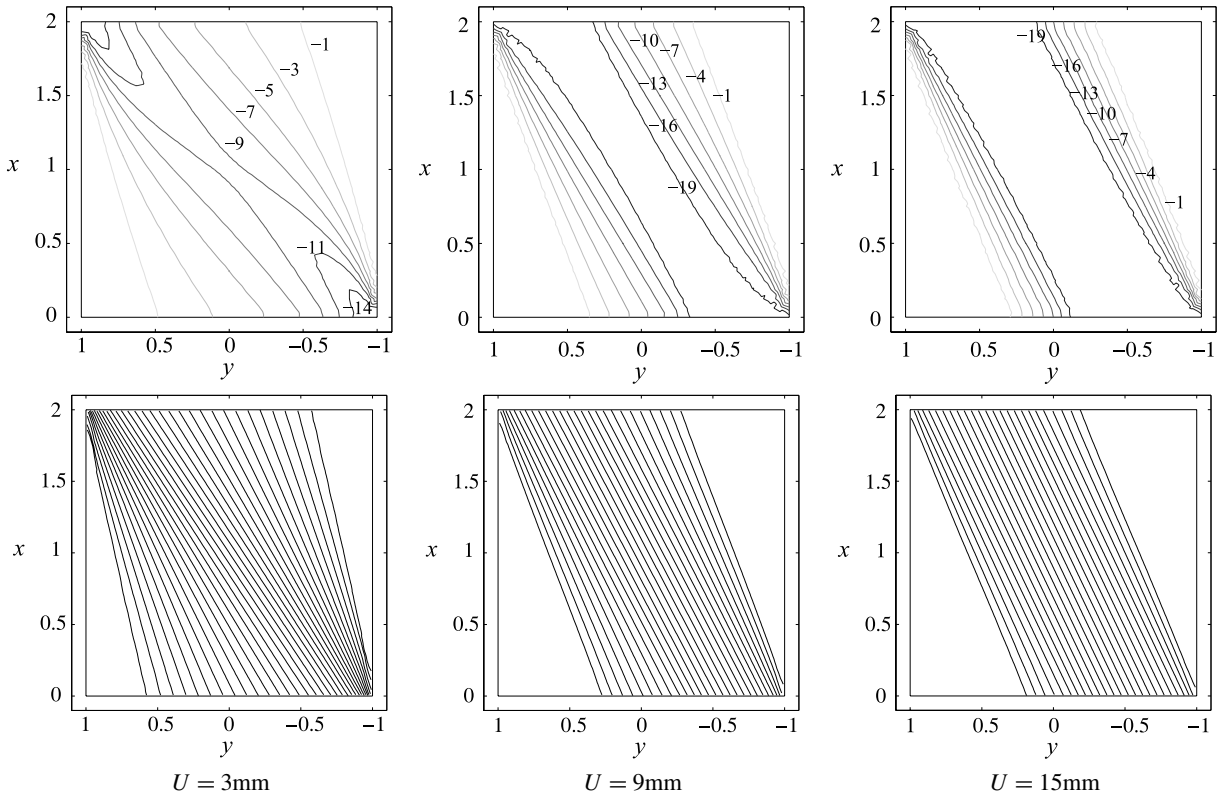

Figure 15. Shear of an ML panel: evolution as boundary displacement increases ($U =$ 3 mm, 9 mm, 15 mm). Top: minimum principal stress [10^5 Pa]. Bottom: isostatic lines.

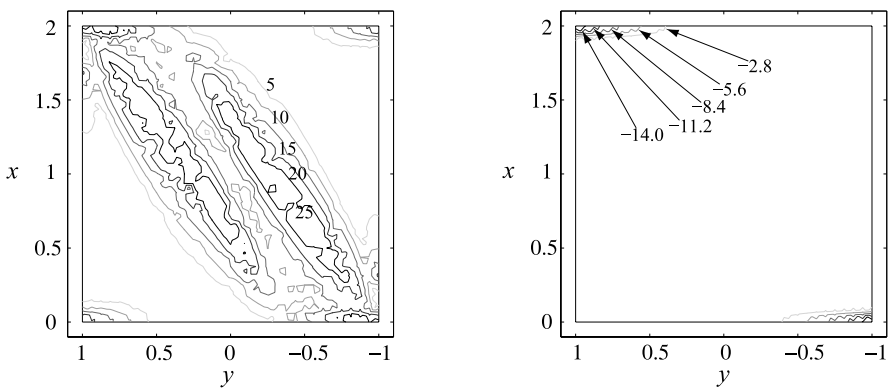

Figure 16. Shear of an ML panel: contour plots of the maximum principal value of the fracture strain [10^{-3}] (left) and the plastic strain [10^{-2}] (right).

Figure 17, left, represents the behavior of the energy as a function of the discrete increment of the boundary displacement U: at each time step i in the process the energy level denoted by • represents the computed solution, the point denoted by ∘ is the energy level corresponding to the increment of the

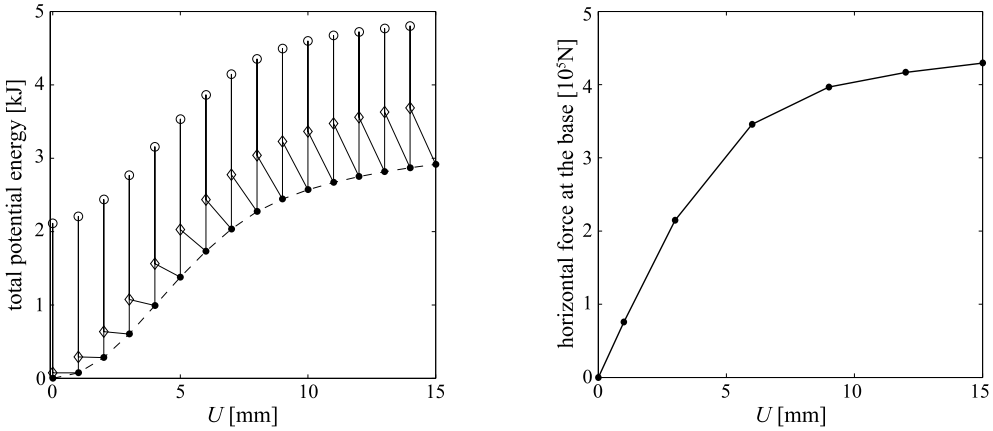

Figure 17. Shear of an ML panel. Left: energy history in the computational process. Right: evolution of the computed reaction at the base.

boundary condition at the step $i+1$ and the point denoted by $\diamond$ corresponds to the energy level after the convergence of the minimization procedure. Therefore the branch $\bullet_i \to \circ_i$ represents the effect of updating the load from the value at time i to the one at time $i+1$, $\circ_i \to \diamond_i$ the effect of the numerical minimization of $\mathscr{E}_{i+1}$, and $\diamond_i \to \bullet_{i+1}$ the effect of the numerical update of the plastic strain that gives the solution at time $i+1$. The energy drop in the branch $\diamond_i \to \bullet_{i+1}$ represents energy dissipation that can be computed integrating over the domain Ω, with the dissipation density $\mathscr{D}_i$ given by (2-39). The dashed line is the envelope of the solution points representing the numerical approximation of the time history of the total potential energy. In Figure 17, right, the evolution of the horizontal component of the computed reaction at the base (the horizontal force) as the displacement U_i increases is depicted. The shear force plateaus as expected for a structure close to collapse.

4C. ***Validation against experimental tests.*** In this section we validate the ML material model against independent sets of experimental results from [Benedetti and Steli 2008] and [Eucentre 2008], performed on different types of masonry. Figure 18 depicts the clamped-clamped load scheme used in the simulations. It reproduces the setup used in both the experimental sets: a masonry panel of width B, height H, and thickness D is clamped to the ground at the bottom and to a steel beam at the top (the gray strip in Figure 18). A uniform load is distributed at the top part of the steel beam and the horizontal load is applied in incremental steps by imposing the horizontal displacement U of the left extreme of the steel beam. Table 1 on page 604 lists the geometrical and material parameters for the experiments simulated. Neither [Benedetti and Steli 2008] and [Eucentre 2008] report measurements of the Poisson's ratio, and because of that we take $\nu = 0$ in the simulations. Nevertheless, parametric studies, not reported here, show that the simulated force-displacement curves manifest very low sensitivity to the Poisson's ratio.

The graphs in the top row of Figure 19 compare the numerical simulations and the experimental results for specimens 1A-08 and 2C-03 of [Benedetti and Steli 2008], made of crushed stone and injected crushed stone masonry. The model reproduces quantitatively the substantial features of the measured force-displacement curves, with a slight overestimation of the force for higher levels of the horizontal displacement U.

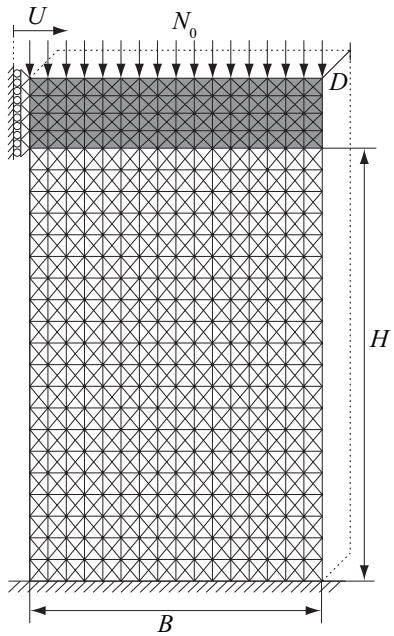

Figure 18. Load scheme of the simulation reproducing the experimental setup used in [Benedetti and Steli 2008; Eucentre 2008].

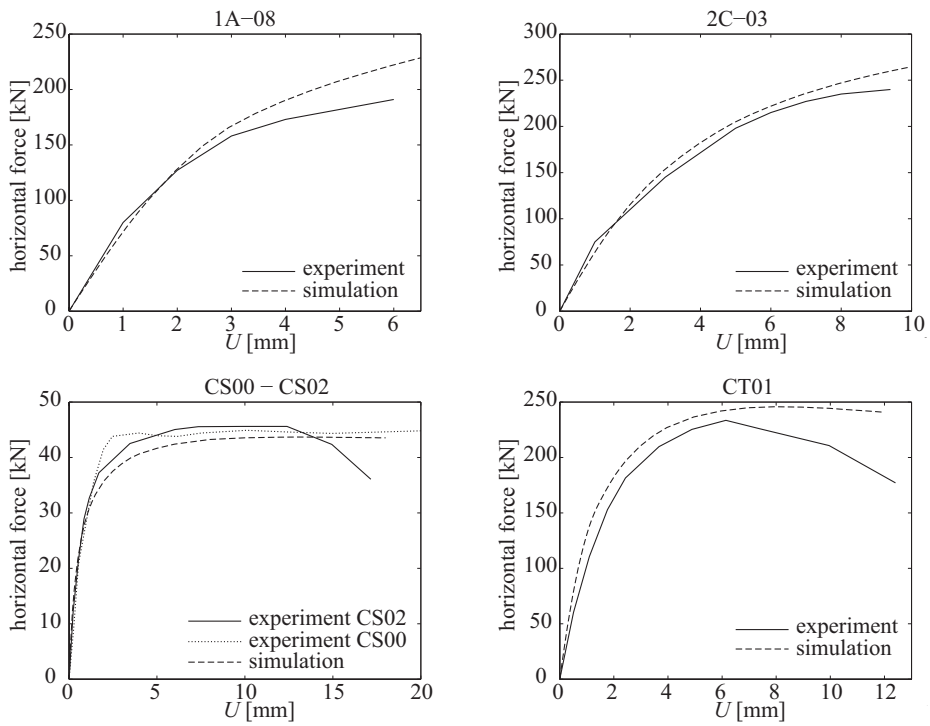

Figure 19. Comparison of numerical simulations with experimental results from [Benedetti and Steli 2008] (top row) and [Eucentre 2008] (bottom row).

Experiment	Material	B [m]	H [m]	D [m]	E [MPa]	ν	σ_0 [MPa]	N_0 [MPa]
1A-08	Crushed stone	1.25	1.85	0.50	1290	0.0	3.69	0.57
2C-03	Injected crushed stone	1.25	1.82	0.50	1118	0.0	6.00	0.55
CS00-CS02	Stone	1.25	2.50	0.32	3000	0.0	3.30	0.20
CT01	Stone	2.50	2.50	0.32	3000	0.0	3.30	0.50

Table 1. Structural and material parameters used in the simulations of the experimental tests. The load scheme is reported in Figure 18. Experiments 1A-08 and 2C-03 [Benedetti and Steli 2008], and experiments CS00-CS02 and CT01 [Eucentre 2008].

The graphs in the bottom row of Figure 19 report the comparison between experimental data and numerical simulations for specimens CS00, CS02, and CT01 in [Eucentre 2008], all made of stone masonry. Specimen CS00 differs from the other two because the mortar has been reinforced with 20% sand in mass fraction. This might explain the flatness of the force-displacement curve for experiment CS00 which is very well captured by the model. The marked reduction of the horizontal force at higher levels of the displacement U might be due to softening effects induced in the masonry by the unreinforced mortar, an effect that is not captured by the ML model as presented here (see [Cardamone 2008] for a generalization of the model to softening and hardening behavior).

4D. ***Masonry façade.*** In this section we apply the ML material model to simulate the response of a simple two-story façade to working loads, seismic loads, and differential foundation subsiding. The geometry of the façade, the applied loads, and the boundary conditions are summarized in Figure 20. The façade is provided, above the openings, with 25 cm-thick wood beams and is assumed to be made of tuff and mortar of good quality. Wood is modeled as elastic with Young's modulus $E_w = 11$ GPa,

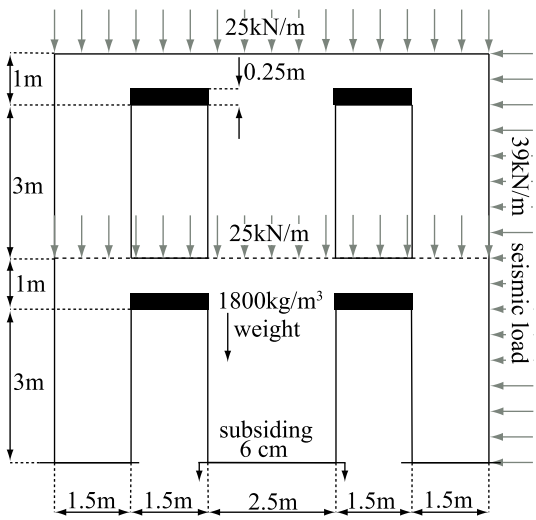

Figure 20. Masonry façade under working loads: geometry and load cases. Horizontal loads are considered in Section 4D2 and Figure 22, and foundation subsiding in Section 4D3 and Figure 24.

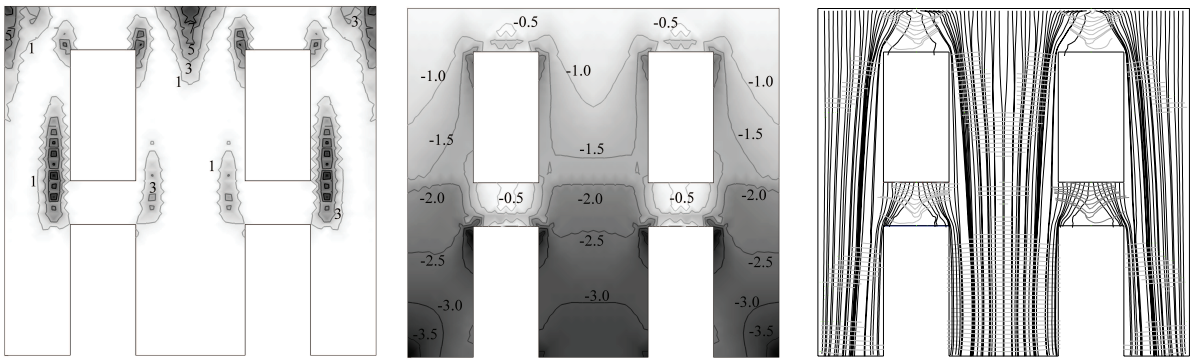

Figure 21. Masonry façade under working loads. Left: contour plot of the maximum fracture strain [10^{-4}]. Middle: contour plot of the maximum compressive stress [10^5 Pa]. Right: isostatic lines of maximum and minimum stress (black and gray curves respectively).

Poisson's ratio $\nu_w = 0.35$, and density $\rho_w = 800\,\text{kg/m}^3$. For the tuff wall we assume Young's modulus $E = 660\,\text{MPa}$, Poisson's ratio $\nu = 0.2$, density $\rho = 1800\,\text{kg/m}^3$, and compression limit $\sigma_0 = 1.98\,\text{MPa}$. The whole structure is assumed to be 0.5 m thick.

4D1. *Working loads.* Working loads are represented by the weight of masonry and the force transmitted by the floors (25 kN/m); the results of the simulation are reported in Figure 21. The structure sustains the working loads without crushing. The value of the maximum stress at the base of the wall is about 0.35 MPa. The partition of the domain Ω can be inferred from Figure 21, right: $\boldsymbol{x} \in \Omega_1$ if both families of isostatics are defined, $\boldsymbol{x} \in \Omega_2$ if only the maximum compression isostatic is depicted, while $\boldsymbol{x} \in \Omega_3$ if the isostatics are not defined. In this load case we see that $\Omega_3 = \varnothing$ and $\Omega = \Omega_1 \cup \Omega_2$.

4D2. *Horizontal loads.* We simulated the response of the façade to a uniform force density of 39 kN/m distributed on the left side of the structure and superimposed on the structure subject to the working loads (see Figure 20). The total horizontal load is equivalent to 70% of the weight of the structure and is applied in ten steps. This kind of loading can be adopted to simulate seismic loads if horizontal ties or connections are present. Crushing strain accumulates in very localized regions near the corners (see Figure 22a). The formation of a compressed diagonal truss element is evident from Figures 22c and 22d. The force-displacement curve, depicted in Figure 23, shows that the structure is approaching collapse for the maximum horizontal load applied.

4D3. *Differential foundation subsiding.* A 6 cm subsiding is imposed, in fifteen steps, to the base of the central wall of the structure under working loads only. The structure shows peculiar kinematics, with the central wall following the foundation subsiding and the lateral walls rotating outward around the extremal points of the bases, where the plastic strain concentrates. The computed vertical component of the reaction of the central wall drops from about $3.9 \cdot 10^5$ N to $2.4 \cdot 10^5$ N after the subsiding. This computation suggests the redistribution of the vertical loads from the central to the lateral walls, redistribution that is also evident from the isostatics depicted in Figure 24d compared to the ones in Figure 21, right.

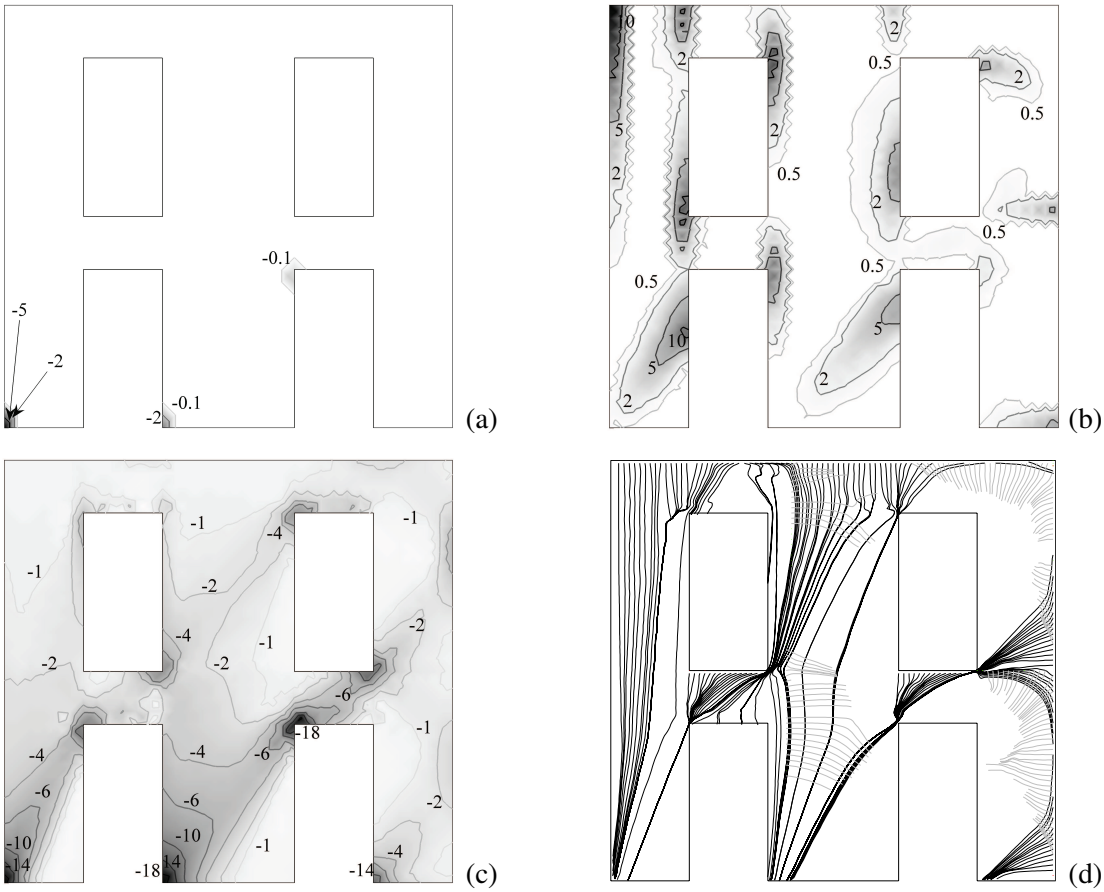

Figure 22. Masonry façade under working and horizontal loads: (a) contour plot of the maximum plastic strain [10^{-4}], (b) contour plot of the maximum fracture strain [10^{-3}], (c) contour plot of the maximum compressive stress [10^5 Pa], and (d) isostatic lines of maximum and minimum stress (black and gray curves respectively).

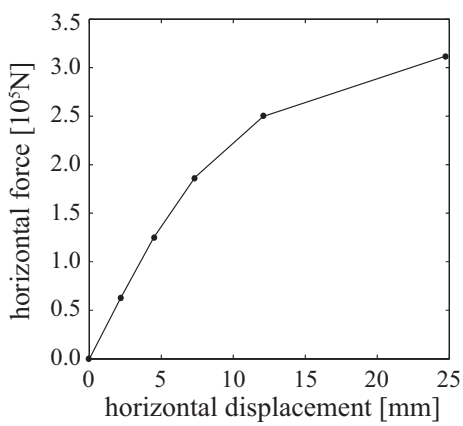

Figure 23. Masonry façade under working and horizontal loads (Figure 20): applied horizontal force versus leftward horizontal displacement of the midpoint of the top edge.

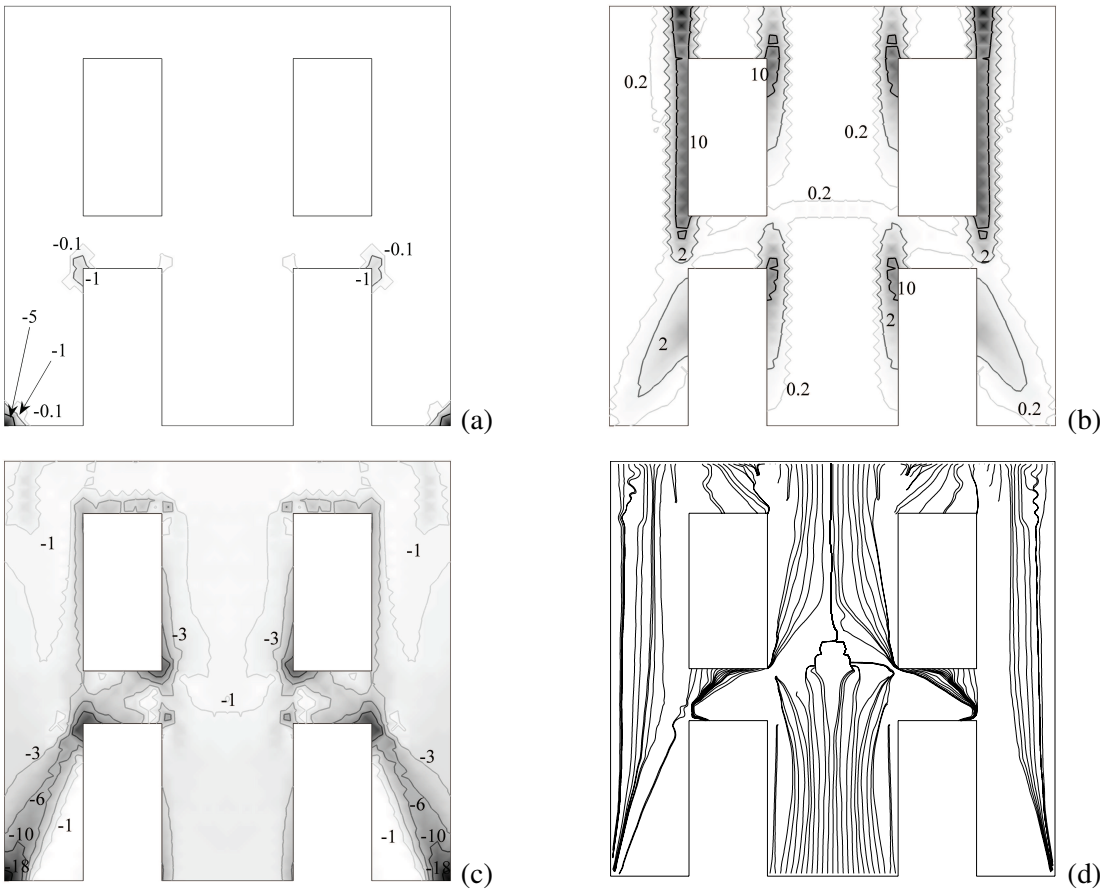

Figure 24. Masonry façade under working loads and foundation subsiding: (a) contour plot of the maximum plastic strain [10^{-3}], (b) contour plot of the maximum fracture strain [10^{-2}], (c) contour plot of the maximum compressive stress [10^5 Pa], and (d) isostatic lines of maximum and minimum stress (black and gray curves respectively).

5. Conclusions

In the present paper we present a numerical FE model of masonry structures based on the normal elastic no-tension (NENT) and masonry-like material models.

The NENT material model is used extensively in the technical literature to model masonry materials. The attribute normal refers to a law of normality imposed on the total anelastic strain (fracture) to the cone N Sym of the admissible stress. It is essentially this assumption that makes the behavior of the material hyperelastic, allowing for a characterization of equilibrium states as minimizers of the total potential energy $\mathscr{E}(\boldsymbol{u})$.

A long debate on the physical feasibility of the normality assumption has agitated the research community working on masonry structures for decades. Is a fact that such an assumption is violated and manifestly false for macroscopically large fractures. The idea is that the normality assumption is close to reality at the onset of the cracking phenomenon and holds as long as fractures are small in size. Besides,

in real masonry structures, fractures appear and evolve in a completely different way: real macroscopic fractures open up through dissipation of a surface energy in an original coherent material. Often such fractures are preceded by microscopic cracks and voids through which the material is damaged and degraded, such cracks finally coalescing in a single macroscopic fracture.

Instead the model material is by assumption originally incapable of sustaining tensile stress. The law of normality on the latent strain has the effect, in rough terms, of giving some sort of fictitious coherence to the material, avoiding the sudden collapse of vertical walls under the action of feeble lateral forces.

Variational approximations based on the NENT model are supported by existence theorems only under rather restrictive assumptions on the loads. Many of the situations encountered in the applications (such as parts of the boundary subject to zero traction) are not covered by the known theorems. The function space in which the minimum problem can be formulated is rather wide and allows for discontinuous displacements.

The numerical model for the analysis of structures composed of NENT material that we propose is based on C^0 finite element triangulations. We apply it to several benchmark problems for which the known existence proofs do not work, detecting numerical convergence in all the cases considered and in particular linear convergence (the same expected in linear elasticity) and square root convergence for the cases of collapse loads and with strain singularities in the solution (not shown). The results we obtain encourage the adoption of continuous finite elements for the analysis of NENT materials.

As shown by the numerical examples we present, the stress level in masonry buildings can increase noticeably due to horizontal loads, differential subsidings, or geometrical modifications of the structure. As a matter of fact, in many cases of interest the collapse of a masonry structure is produced by simultaneous fracturing and crushing. The masonry-like (ML) model consists in the addition to the NENT model of a strength criterion for crushing consisting in a Prager–Drucker elastic-perfectly plastic yield criterion of the associated type.

The numerical strategy we adopt to solve the quasistatic evolution problem for ML materials is again based on energy minimization. The loading process is discretized into steps and the incremental solution at each step is obtained by minimizing a form of the energy updated step by step.

The desired convergence of the approximate trajectory to the exact one is proved in [Dal Maso et al. 2006] in the simpler case of elastic-perfectly plastic behavior.

In the numerical experiments we present, linear convergence is detected in the flexure problem. A number of more realistic examples solved with our FE code show how masonry structures are able to release high levels of stored elastic energy through sliding dissipation.

It has to be pointed out that the apparent sliding-type plasticity of our model simplifies more realistic dissipation phenomena due to friction. In the examples the release of elastic energy is not complete since unlimited ductility and softening effects are not taken into account.

Appendix A

As it is evident from Figure 2, the strain energy function φ characterizing NENT materials is not coercive. Mathematicians (see [Alfano et al. 2000; Angelillo et al. 2002] and references therein) restore coercivity of the total potential energy by considering the following load condition on the applied forces:

Supersafe load condition. The load $(\boldsymbol{p}, \boldsymbol{b})$ is said to be *supersafe* if there exists at least one stress field $\boldsymbol{T} \in \mathcal{H}$ such that $\boldsymbol{T} + \beta \boldsymbol{I} \in \mathrm{N\,Sym}$ for some constant $\beta > 0$.

Here $\mathcal{H}$ is the set of statically admissible stress fields

$$\mathcal{H} = \{\boldsymbol{T} \in \mathcal{M}(\Omega) : \operatorname{div} \boldsymbol{T} + \boldsymbol{b} = \boldsymbol{0},\ \boldsymbol{T}\boldsymbol{n} = \boldsymbol{p} \text{ on } \partial\Omega_N,\ \boldsymbol{T} \in \mathrm{N\,Sym}\}, \tag{A-1}$$

where $\mathcal{M}(\Omega)$ is a convenient Banach space. In other words the load is supersafe if there exists a stress field $\boldsymbol{T}$ that is strictly admissible over the open set Ω in a uniform way, that is, independently of $\boldsymbol{x}$. We prefer to give the name "safe load" to a load system $(\boldsymbol{p}, \boldsymbol{b})$ such that there exists a stress field that is strictly admissible over Ω, not necessarily in a uniform way, and add the attribute *super* to the load system that gives coercivity. If the load is safe then the potential energy associated with the external forces can be rewritten in the form

$$\int_{\partial\Omega_N} \boldsymbol{p} \cdot \boldsymbol{u}\, ds + \int_\Omega \boldsymbol{b} \cdot \boldsymbol{u}\, da = \int_\Omega \boldsymbol{T} \cdot (\boldsymbol{\varepsilon} + \boldsymbol{\lambda})\, da, \tag{A-2}$$

and the total potential energy becomes

$$\mathcal{E} = -\int_\Omega \boldsymbol{T} \cdot (\boldsymbol{\varepsilon} + \boldsymbol{\lambda})\, da + \frac{1}{2} \int_\Omega \boldsymbol{\varepsilon} \cdot \mathbb{A}^{-1}[\boldsymbol{\varepsilon}]. \tag{A-3}$$

Using the supersafe load assumption one can write

$$-\int_\Omega \boldsymbol{T} \cdot \boldsymbol{\lambda}\, da \geq \beta \int_\Omega |\boldsymbol{\lambda}|\, da; \tag{A-4}$$

then the energy has linear growth with respect to the norm of the space $BD(\Omega)$, that is, the space of functions $\boldsymbol{u}$ whose corresponding infinitesimal deformation is a bounded measure. For full information on this function space we refer to [Temam and Strang 1980]. Here we notice only that since the infinitesimal strain $\boldsymbol{e}$ is a bounded measure then $\boldsymbol{u}$ can be discontinuous and $\boldsymbol{e}$ can be decomposed into its absolutely continuous and singular parts with respect to two-dimensional Lebesgue measure:

$$\boldsymbol{e}(\boldsymbol{u}) = \boldsymbol{e}^a(\boldsymbol{u}) + \boldsymbol{e}^s(\boldsymbol{u}). \tag{A-5}$$

Recalling the decomposition of $\boldsymbol{e}$ into its elastic and fracture parts, since the potential energy depends quadratically on the elastic part of the deformation, only the fracture part $\boldsymbol{\lambda}$ can be singular, that is, only fracture discontinuities are admitted.

Theorem 6.8 of [Giaquinta and Giusti 1985, p. 381] shows the existence of the solution for the minimum problem (2-14) in $BD(\Omega)$ under the supersafe load condition and some supplementary technical conditions, in the special case of traction problems and isotropic elastic behavior. Since the energy is not strictly convex the solution is in general nonunique.

Also a dual energy principle based on the complementary energy can be considered. The stress state $\boldsymbol{T}^{\mathrm{o}}$ that corresponds to the solution of the boundary value problem for NENT materials can be characterized as the minimizer of the energy functional

$$\mathcal{E}_c(\boldsymbol{T}) = -\int_{\partial\Omega_D} \boldsymbol{T}\boldsymbol{n} \cdot \bar{\boldsymbol{u}}\, ds + \frac{1}{2} \int_\Omega \boldsymbol{T} \cdot \mathbb{A}[\boldsymbol{T}], \tag{A-6}$$

over the set $\mathcal{H}$ of statically admissible stress fields [Giaquinta and Giusti 1985]. $\mathcal{M}(\Omega)$ in (A-1) can be considered as the Hilbert space $L^2(\Omega)$. In other words $\mathcal{H}$ is represented by the symmetric second order tensors $\boldsymbol{T}$ of $L^2(\Omega)$ such that $\boldsymbol{T}$ is negative semidefinite and balanced with $\boldsymbol{p}$ and $\boldsymbol{b}$. Obviously on considering $\boldsymbol{T}$ in $L^2(\Omega)$ the balance conditions must be considered in a generalized sense:

$$\int_\Omega \boldsymbol{T}\cdot\delta\boldsymbol{\varepsilon}\,da = \int_\Omega \boldsymbol{b}\cdot\delta\boldsymbol{u}\,da + \int_{\partial\Omega_N} \boldsymbol{p}\cdot\delta\boldsymbol{u} \quad \text{for } \delta\boldsymbol{u}\in\delta K, \tag{A-7}$$

where

$$\delta K = \{\delta\boldsymbol{u}\in H^1(\Omega) : \delta\boldsymbol{\varepsilon} = \tfrac{1}{2}(\nabla\delta\boldsymbol{u} + \nabla\delta\boldsymbol{u}^{\mathrm{T}}),\ \delta\boldsymbol{u} = \boldsymbol{0} \text{ on } \partial\Omega_D\}. \tag{A-8}$$

The choice of $L^2(\Omega)$ as the function space for the stress field is natural considering the quadratic term which represents the stress energy in $\mathscr{E}_c(\boldsymbol{T})$. Since the complementary energy functional is strictly convex over the convex set $\mathcal{H}$ the existence and the uniqueness of the minimizer $\boldsymbol{T}^{\mathrm{o}}$ of such a functional is guaranteed whenever $\mathcal{H}$ is not void (that is, there exists at least one stress field $\boldsymbol{T}$ such that $\boldsymbol{T}$ is negative semidefinite and balanced with $\boldsymbol{p}$, $\boldsymbol{b}$).

Therefore, though the solution $\boldsymbol{u}^{\mathrm{o}}$ may be nonunique, the elastic part $\boldsymbol{\varepsilon}^{\mathrm{o}}$ of the strain solution is unique. Nonuniqueness is restricted to the anelastic part of the deformation $\boldsymbol{\lambda}^{\mathrm{o}}$ and to special arrangements of the boundary conditions.

This circumstance makes the displacement and stress approach to the equilibrium of NENT materials nonsymmetric, in the sense that existence of the minimizer $\boldsymbol{T}^{\mathrm{o}}$ for $\mathscr{E}_c(\boldsymbol{T})$ is not sufficient for the existence of the minimizer $\boldsymbol{u}^{\mathrm{o}}$ of $\mathscr{E}(\boldsymbol{u})$. The existence of $\boldsymbol{T}^{\mathrm{o}}$ requires only the existence of an admissible stress field; the existence of $\boldsymbol{u}^{\mathrm{o}}$, with the known theorems, requires instead the existence of a uniformly strictly admissible stress field.

There are indeed counterexamples to the existence of $\boldsymbol{u}^{\mathrm{o}}$ in the case where the loads are admissible but do not satisfy the safe load condition. It has to be pointed out that the existence results obtained by mathematicians through the direct method of the calculus of variation are, from the engineering point of view, rather frustrating. Most of the buildings or masonry structures for which the stress and fracture fields are sought are under loads that are not supersafe since some part of the boundary is loaded with zero tractions.

To the authors knowledge there are no examples of nonexistence in the case in which the loads do not satisfy the supersafe load condition but there exists a balanced and strictly admissible stress field $\boldsymbol{T}$ (safe load). The only known counterexamples refer to the case in which the loads do not satisfy the supersafe load condition and there exists a balanced and admissible, but not strictly admissible, stress field $\boldsymbol{T}$. In the known counterexamples there are parts of the domain Ω that can be taken away without paying any energy price, that is, actually $|\boldsymbol{u}|_{BD}\to\infty$ and $\mathscr{E}=0$; then we can say that the loads are collapse loads, in the sense that the deformation can increase indefinitely at constant load.

Another example of a collapse load is represented by the rocking mechanism of a wall. A homogeneous rectangular wall carrying its own weight is subject to increasing uniform horizontal forces pushing on the left edge of the wall. When the resultant of the vertical and horizontal forces passes through the bottom right vertex of the rectangle there exists a collapse mechanism for which $|\boldsymbol{u}|_{BD}\to\infty$ and $\mathscr{E}=0$; then we can say that the loads are collapse loads, again in the sense that the deformation can increase indefinitely at constant load. In this second example balanced and admissible stress fields can be found that are not in $L^2(\Omega)$, $\boldsymbol{T}$ being only a bounded measure, e.g., a line Dirac delta.

Recently Lucchesi et al. [2008b] considered a number of examples referring to stress states that are bounded measures and statically admissible stress fields for safe loads and sometimes for collapse loads. The consideration of such concentrated stress fields is outside the scope of the present work, which is restricted to stress fields represented by symmetric second order tensors $\boldsymbol{T}$ belonging to $L^2(\Omega)$ such that $\boldsymbol{T}$ is negative semidefinite and balanced with $\boldsymbol{p}, \boldsymbol{b}$, and explicitly forbids the case of collapse loads. It has to be pointed out that numerical methods based on concentrated stress or strain have been recently proposed in the literature for the approximate solution of elastic problems (see for example [Davini and Pitacco 2000; Angelillo et al. 2002]) and could be extended to NENT or ML materials through relaxation of the energy $\mathscr{E}$.

Appendix B

In [Fortunato 2010], using the assumptions of the so-called TFT [Mansfield 1969], some analytical-numerical solutions are presented relative to rectangular panels made of NENT material undergoing arbitrary relative rigid displacements of the bases. This appendix summarizes the contents of that paper for the special case described in Section 3B.

Consider a rectangular ML panel, traction free on the lateral sides and subject to prescribed rigid body displacements of the top and bottom bases (Figure 25, left and middle). We introduce a Cartesian frame of reference $(O; x_1 = x, x_2 = y)$, with associated base vectors ($\hat{\boldsymbol{\imath}}$ and $\hat{\boldsymbol{\jmath}}$), and define $\{u_A, v_A, \varphi_A\}$ as the translation and rotation parameters of the block $\mathscr{R}_A$ relative to pole A^0, $\{u_B, v_B, \varphi_B\}$ as the translation and rotation parameters of the block $\mathscr{R}_B$ relative to pole B^0, and $\{U, V, \Phi\}$ as the relative rigid displacement parameters between the top and bottom bases. The displacements of the top and bottom bases, modulo an ineffective rigid body translation, can be expressed in terms of the relative translation parameters. In the special case described in Section 3B we have

$$\boldsymbol{u}^a = U\hat{\boldsymbol{\imath}}, \quad \boldsymbol{u}^b = -U\hat{\boldsymbol{\imath}}. \tag{B-1}$$

Based on the complementary energy principle stated in Appendix A the equilibrium solution can be searched for by minimizing the energy (A-6) over the set $\mathscr{H}$ defined in (A-1). In particular we seek the solution in the restricted set $\tilde{\mathscr{H}}$ obtained by considering stress fields $\boldsymbol{T} \in \mathscr{H}$ such that $\boldsymbol{T}$ is of rank one (the tension field assumption). The minimizer $\tilde{\boldsymbol{T}}$ of the complementary energy $\mathscr{E}_c$ over the restricted set $\tilde{\mathscr{H}}$ is generally an approximate solution of the BVP. For $\boldsymbol{T} \in \tilde{\mathscr{H}}$ one has $\Omega = \Omega_2 \cup \Omega_3$, that is, $\Omega_1 = \varnothing$. Once the free boundary between Ω_2 and Ω_3 is localized, the solution of the equilibrium problem is reduced to the search for the stress field solution in Ω_2. In equilibrium and in the absence of body forces, in Ω_2 one of the two families of principal stress curves is made of straight lines that are called *compression rays* [Fortunato 2010]. The compression rays carry the nonzero stress and do not overlap. Since the lateral sides of the panel are stress free the compression rays intersect the boundary along the bases. Therefore the definition of the behavior of a single panel, under the above assumptions, is reduced to finding in Ω_2 the optimal compression ray distribution, the optimal choice being determined by energy convenience.

It is shown in [Fortunato 2010] that it is possible to locate the interfaces between the regions Ω_2 and Ω_3, in terms of the parameters $\{U, V, \Phi\}$, through geometrical arguments only. Such an interface is straight and along it the strain is zero, that is, the interface is an unextended ray. In the case of *pure shear* $\{U, 0, 0\}$ we have $\Omega = \Omega_2$ and $\Omega_3 = \varnothing$.

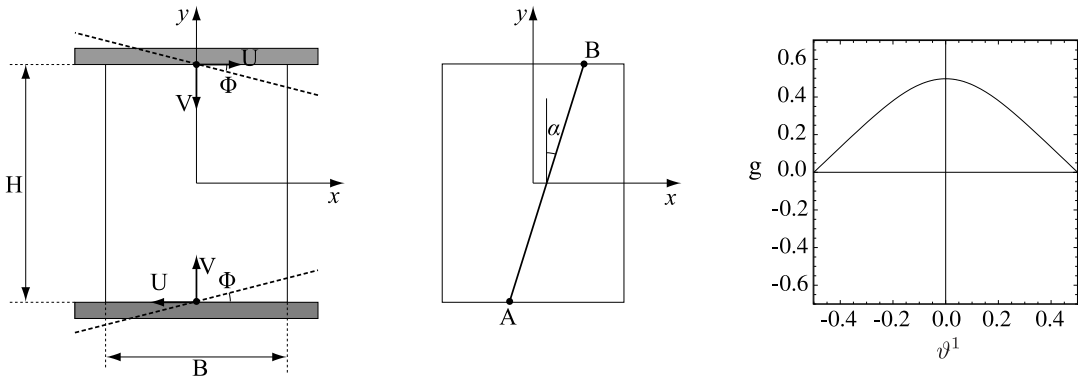

Figure 25. Left: panel geometry and relative displacements. Middle: typical ray geometry. Right: minimizer g° for the problem described in Section 3B.

Given a rectangular panel of base B_0 and height H_0 we consider a *normalized* panel, that is, a rectangular panel whose bases are of unit length and whose height is $H = H_0/B_0$. We introduce the slope function g of a ray, that intersects the bottom and top bases at the abscissae x_A and x_B and the horizontal axis at $\vartheta^1 = (x_A + x_B)/2$, as follows:

$$\left[-\tfrac{1}{2}, \tfrac{1}{2}\right] \ni \vartheta^1 \mapsto g(\vartheta^1) := \tan\big(\alpha(\vartheta^1)\big), \tag{B-2}$$

where α is the angle between such a ray and the y axis as shown in Figure 25, middle. In order that the rays belong entirely to Ω, these geometrical constraints on g must be satisfied:

$$-\frac{1-2\vartheta^1}{H} \le g(\vartheta^1) \le \frac{1-2\vartheta^1}{H}, \quad \vartheta^1 > 0, \tag{B-3}$$

$$-\frac{1+2\vartheta^1}{H} \le g(\vartheta^1) \le \frac{1+2\vartheta^1}{H}, \quad \vartheta^1 \le 0, \tag{B-4}$$

In Ω_2 it is convenient to introduce a system of curvilinear coordinates $(\vartheta^1, \vartheta^2)$ with one of the curvilinear lines, say ϑ^2, along the compression rays. In terms of the Cartesian coordinates $(x_1 \equiv x, x_2 \equiv y)$, with associated base vectors $(\hat{\boldsymbol{\imath}}, \hat{\boldsymbol{\jmath}})$, the curvilinear coordinates $(\vartheta^1, \vartheta^2)$ are defined by

$$x_1 = \vartheta^1 + g\vartheta^2, \quad x_2 = \vartheta^2, \tag{B-5}$$

where g, a function of ϑ^1 alone, is the slope of the rays defined in (B-2). Since in Ω_2 the stress is uniaxial along the direction of the compression ray, it admits the representation

$$\boldsymbol{T} = T^{22}\boldsymbol{a}_2 \otimes \boldsymbol{a}_2, \tag{B-6}$$

where $\boldsymbol{a}_2$ is one of the natural base vectors associated with the curvilinear coordinates system defined by (B-5).

The local equilibrium equations in Ω_2, in the absence of body forces and in terms of the curvilinear coordinates ϑ^1 and ϑ^2, gives

$$T^{22}{}_{,2} + T^{22}\frac{g'}{1+g'\vartheta^2} = 0. \tag{B-7}$$

Therefore $\boldsymbol{T} \in \tilde{\mathcal{H}}$ if the only nonvanishing component of stress has the form

$$T^{22} = \frac{f}{1+g'\vartheta^2}, \tag{B-8}$$

f being an arbitrary function of ϑ^1.

Assuming that the material has linear elastic isotropic behavior in compression and denoting by E and ν the Young's modulus and Poisson's ratio of the material, respectively, the complementary energy $\mathscr{E}_c$ can be written as

$$\mathscr{E}_c(f,g) = \int_{-1/2}^{1/2} f 2U\, d\vartheta^1 + \frac{1}{2}\int_{-1/2}^{1/2}\int_{H/2}^{H/2} \frac{1}{E} f^2 \frac{(1+g^2)^2}{1+g'\vartheta^2}\, d\vartheta^1 d\vartheta^2. \tag{B-9}$$

$\mathscr{E}_c$ is a functional of the scalar functions f and g. These functions can be found by minimizing $\mathscr{E}_c$ with respect to f and g. We find f first. By taking the variation of $\mathscr{E}_c$ with respect to f one obtains the condition

$$\int_{-1/2}^{1/2} 2U\, d\vartheta^1 = -\int_{-1/2}^{1/2}\int_{H/2}^{H/2} \frac{1}{E} f^2 \frac{(1+g^2)^2}{1+g'\vartheta^2}\, d\vartheta^1 d\vartheta^2, \tag{B-10}$$

that can be solved for f integrating the right hand side of (B-10) with respect to ϑ^2:

$$f = \frac{Eg'}{(1+g^2)^2}\,\frac{2Ug}{\ln(1-g'H/2) - \ln(1+g'H/2)}. \tag{B-11}$$

Substituting (B-11) into (B-9) and integrating with respect to ϑ^2, the complementary energy can be rewritten as

$$\mathscr{E}_c(g) = -2E\int_{-1/2}^{1/2} \frac{U^2 g'^2}{(1+g^2)^2 \ln\dfrac{1+g'H/2}{1-g'H/2}}\, d\vartheta^1. \tag{B-12}$$

Then minimizing $\mathscr{E}_c$ in $\tilde{\mathcal{H}}$ corresponds to maximizing the stress energy with respect to g.

We seek the minimum of the complementary energy functional among all functions g that satisfy the boundary conditions

$$g\left(-\tfrac{1}{2}\right) = 0 \quad \text{and} \quad g\left(\tfrac{1}{2}\right) = 0 \tag{B-13}$$

by finding the zeros of the *derivative* (the Euler equation) associated with (B-12):

$$\frac{8gU^2\left(6\gamma_1 g'^2(1-g^2)(9g'^2-16) + 96g\gamma_2(\gamma_3-\gamma_1)g''\right)}{\gamma_1^3\gamma_2^3(9g'^2-16)^2} = 0, \tag{B-14}$$

where

$$\gamma_1 := \ln\frac{1+g'H/2}{1-g''H/2}, \quad \gamma_2 := 1+g^2, \quad \gamma_3 := Hg'.$$

The minimizer of $\mathscr{E}_c$, that is, the solution of the Euler equation, is actually unique and is denoted by g°. Observe that (B-14) can be simply solved numerically if the conditions are of *Cauchy* type. For the problem at hand boundary conditions are given, therefore to solve numerically (B-14) a *shooting*-type technique is adopted.

The solution g° for a rectangular panel of normalized lengths subject to given *shear* displacements $\{U, 0, 0\}$ is shown in Figure 25.

References

[Alfano et al. 2000] G. Alfano, L. Rosati, and N. Valoroso, "A numerical strategy for finite element analysis of no-tension materials", *Int. J. Numer. Methods Eng.* **48**:3 (2000), 317–350.

[Angelillo 1993] M. Angelillo, "Constitutive relations for no-tension materials", *Meccanica* (*Milano*) **28**:3 (1993), 195–202.

[Angelillo and Rosso 1995] M. Angelillo and F. Rosso, "On statically admissible stress fields for a plane masonry-like structure", *Quart. Appl. Math.* **53**:4 (1995), 731–751.

[Angelillo et al. 2002] M. Angelillo, A. Fortunato, and F. Fraternali, "A lumped stress method for plane elastic problems and the discrete-continuum approximation", *Int. J. Solids Struct.* **39**:25 (2002), 6211–6240.

[Angelillo et al. 2006] M. Angelillo, E. Babilio, and A. Fortunato, "Folding of thin walled tubes as a free gradient discontinuity problem", *J. Elasticity* **82**:3 (2006), 243–271.

[Angelillo et al. 2008] M. Angelillo, E. Babilio, L. Cardamone, and A. Fortunato, "A numerical model for variational fracture based on discontinuous finite elements", in *Proceedings of the 3rd Canadian Conference on Nonlinear Solid Mechanics* (*CanCNSM*) (Toronto, 2008), 2008.

[Angelillo et al. 2010] M. Angelillo, L. Cardamone, A. Fortunato, and M. Lippiello, "Descent strategies for finite element analysis of normal no-tension materials", preprint, 2010. Submitted to *Meccanica*.

[Benedetti and Steli 2008] A. Benedetti and E. Steli, "Analytical models for shear-displacement curves of unreinforced and FRP reinforced masonry panels", *Constr. Build. Mater.* **22**:3 (2008), 175–185.

[Benvenuto 1991] E. Benvenuto, *An introduction to the history of structural mechanics, II: Vaulted structures and elastic systems*, Springer, New York, 1991.

[Cardamone 2008] L. Cardamone, "Unilateral, elastoplastic behavior of masonry-like materials: some considerations on reinforcements application", in *Conference proceedings: 7th International PhD Symposium in Civil Engineering* (Stuttgart, 2008), edited by R. Eligehausen et al., Fédération Internationale du Béton/Institute of Construction Materials, Lausanne/Stuttgart, 2008.

[Castellano 1988] G. Castellano, "Un modello cinematico per i materiali non resistente a trazione", pp. 241–256 in *Cinquantenario della Facoltà di Architettura di Napoli: Franco Jossa e la sua opera*, edited by U. Carputi, Istituto di Costruzioni, Facoltà di Architettura, Napoli, 1988.

[Como 1992] M. Como, "Equilibrium and collapse analysis of masonry bodies", *Meccanica* (*Milano*) **27**:3 (1992), 185–194.

[Como and Grimaldi 1985] M. Como and A. Grimaldi, "A unilateral model for the limit analysis of masonry walls", pp. 25–45 in *Unilateral problems in structural analysis*, edited by G. Del Piero and F. Maceri, CISM Courses and Lectures **288**, Springer, Vienna, 1985.

[Dal Maso et al. 2006] G. Dal Maso, A. DeSimone, and M. G. Mora, "Quasistatic evolution problems for linearly elastic-perfectly plastic materials", *Arch. Ration. Mech. An.* **180**:2 (2006), 237–291.

[Davini and Pitacco 2000] C. Davini and I. Pitacco, "An unconstrained mixed method for the biharmonic problem", *SIAM J. Numer. Anal.* **38**:3 (2000), 820–836.

[De Giorgi 1996] E. De Giorgi, "Congetture riguardanti alcuni problemi di evoluzione", *Duke Math. J.* **81**:2 (1996), 255–268.

[Del Piero 1989] G. Del Piero, "Constitutive equation and compatibility of the external loads for linear elastic masonry-like materials", *Meccanica* (*Milano*) **24**:3 (1989), 150–162.

[Di Pasquale 1984] S. Di Pasquale, "Questioni concernenti la meccanica dei mezzi non reagenti a trazione", pp. 227–238 in *Atti del VII Congresso Nazionale AIMETA, 5: Meccanica delle strutture* (Trieste, 1984), Associazione Italiana de Meccanica Teorica ed Applicata, Milano, 1984.

[Eucentre 2008] Eucentre, "Prove murature", 2008, Available at http://www.eucentre.it/provemurature.

[Fortunato 2010] A. Fortunato, "Elastic solutions for masonry-like panels", *J. Elasticity* **98**:1 (2010), 87–110.

[Giaquinta and Giusti 1985] M. Giaquinta and E. Giusti, "Researches on the equilibrium of masonry structures", *Arch. Ration. Mech. An.* **88**:4 (1985), 359–392.

[Heyman 1995] J. Heyman, *The stone skeleton: structural engineering of masonry architecture*, Cambridge University Press, 1995.

[Lucchesi et al. 1996] M. Lucchesi, C. Padovani, and N. Zani, "Masonry-like solids with bounded compressive strength", *Int. J. Solids Struct.* **33**:14 (1996), 1961–1994.

[Lucchesi et al. 2008a] M. Lucchesi, C. Padovani, G. Pasquinelli, and N. Zani, *Masonry constructions: mechanical models and numerical applications*, Lecture Notes in Applied and Computational Mechanics **39**, Springer, Berlin, 2008.

[Lucchesi et al. 2008b] M. Lucchesi, M. Šilhavý, and N. Zani, "Integration of measures and admissible stress fields for masonry bodies", *J. Mech. Mater. Struct.* **3**:4 (2008), 675–696.

[Luciano and Sacco 1997] R. Luciano and E. Sacco, "Homogenization technique and damage model for old masonry material", *Int. J. Solids Struct.* **34**:24 (1997), 3191–3208.

[Mansfield 1969] E. H. Mansfield, "Tension field theory", pp. 305–320 in *Applied mechanics: proceedings of the 12th International Congress of Applied Mechanics* (Stanford, CA, 1968), edited by M. Hetényi and W. G. Vincenti, Springer, Berlin, 1969.

[Marfia and Sacco 2005] S. Marfia and E. Sacco, "Numerical procedure for elasto-plastic no-tension model", *Int. J. Comput. Methods Eng. Sci. Mech.* **6**:3 (2005), 187–199.

[Mielke and Ortiz 2008] A. Mielke and M. Ortiz, "A class of minimum principles for characterizing the trajectories and the relaxation of dissipative systems", *ESAIM Control Optim. Calc. Var.* **14**:3 (2008), 494–516.

[Ortiz and Simo 1986] M. Ortiz and J. C. Simo, "An analysis of a new class of integration algorithms for elastoplastic constitutive relations", *Int. J. Numer. Methods Eng.* **23**:3 (1986), 353–366.

[Romano and Romano 1979] G. Romano and M. Romano, "Sulla soluzione di problemi strutturali in presenza di legami costitutivi unilaterali", *Rend. Accad. Naz. Lincei* **67** (1979), 104–113.

[Romano and Sacco 1984] G. Romano and E. Sacco, "Sul calcolo di strutture non resistenti a trazione", pp. 221–233 in *Atti del VII Congresso Nazionale AIMETA* (Trieste, 1984), Associazione Italiana de Meccanica Teorica ed Applicata, Milano, 1984.

[Sab 2003] K. Sab, "Yield design of thin periodic plates by a homogenization technique and an application to masonry walls", *C. R. Mécanique* **331**:9 (2003), 641–646.

[Temam and Strang 1980] R. Temam and G. Strang, "Functions of bounded deformation", *Arch. Ration. Mech. An.* **75**:1 (1980), 7–21.

Received 16 Jun 2009. Revised 26 Jan 2010. Accepted 31 Jan 2010.

MAURIZIO ANGELILLO: mangelil@unisa.it
University of Salerno, Via Ponte Don Melillo, 84084 Fisciano, Italy

LUCA CARDAMONE: lcardamo@unisa.it
University of Salerno, Via Ponte Don Melillo, 84084 Fisciano, Italy

ANTONIO FORTUNATO: a.fortunato@unisa.it
University of Salerno, Via Ponte Don Melillo, 84084 Fisciano, Italy

JOURNAL OF MECHANICS OF MATERIALS AND STRUCTURES
Vol. 5, No. 4, 2010

A COUPLED HONEYCOMB COMPOSITE SANDWICH BRIDGE-VEHICLE INTERACTION MODEL

MIJIA YANG AND A. T. PAPAGIANNAKIS

This paper presents a coupled, dynamic vehicle and honeycomb composite sandwich bridge deck interaction model. The composite sandwich deck consists of E-glass fibers and polyester resin. Its core consists of corrugated cells in a sinusoidal configuration along the travel direction. First, analytical predictions of the effective flexural and transverse shear stiffness properties of the sandwich deck were obtained in the longitudinal and transverse directions. These were based on the modeling of equivalent properties for the face laminates and core elements. Using the first order shear sandwich theory, the dynamic response of the sandwich deck was analyzed under moving dynamic loads. A dynamic vehicle simulation model was used for the latter, assuming that the deck response is the only source of excitation (i.e., its roughness was assumed to be negligible). Subsequently, the dynamic load factors of the sandwich bridge deck were calculated for different traveling velocities. The results suggest that the dynamic load factors vary with the traveling speed and increase significantly with decreasing deck stiffness. Considering multiple degrees of freedom for the vehicle further amplifies the dynamic loading factor and increases the vibration generated by vehicles.

Introduction

Sandwich elements are commonly used in aerospace and automobile structures since they offer great energy absorption and higher moment of inertia without imposing a significant weight penalty. Recently, growing civil engineering infrastructure rehabilitation needs suggest that innovative deck materials such as fiber-reinforced polymer (FRP) composite sandwich structures may be suitable for bridge decks [Plunkett 1997; Davalos et al. 2001]. These structures typically consist of a corrugated or closed- cell core encased between two face sheets. Such systems are lightweight while providing high strength. Keller [2001] also conducted a series of laboratory and field experiments of FRP bridges and verified that the sandwich elements, if well designed, can be implemented as bridge decks.

However, the performance of sandwich decks for different core configurations and loading cases is not fully understood. Davalos et al. [2001] conducted a performance evaluation of the FRP sandwich panels with a sinusoidal honeycomb core. Xu et al. [2001] proposed an analytical method to estimate the core transverse shear stiffness. Librescu and Hause [2000] reported their research in the modeling of the advanced sandwich structures, especially the study of stability behavior of sandwich panels. Analysis of modern sandwich panels was done in [Frostig 2003; Frostig and Thomsen 2004] using both classical and high-order models. This work studied in-plane and out-of-plane displacement patterns and stress distributions in the sandwich panels under various boundaries and loading conditions.

Keywords: Vehicle-bridge interaction, dynamic loading factor, sandwich structures, stiffness.

There is considerably less literature on the dynamic response of sandwich structures, especially under forced vibrations. Most recently, dynamic response models of higher-order sandwich panels with flexible core were developed in [Yang and Qiao 2005a]. These were used to study free vibration, impact behavior, and stress wave propagation in a sandwich beam. However, in order to safely design and implement sandwich panels as bridge decks, the dynamic response and its dynamic load factor of a sandwich deck under moving forces need to be studied.

This paper describes a comprehensive approach to predicting the dynamic response of thick sandwich bridge deck. In addition, it compares their dynamic loading factors to those of conventional concrete decks. First, the analytical stiffness properties of the face sheets and the core of the sandwich structures are estimated using the micro/macromechanics method [Davalos et al. 1996]. The stiffness properties of whole sandwich panel are then evaluated by modeling the sandwich panel as a three-layer laminated structure, and the estimated stiffness properties are subsequently used for predicting the dynamic responses of FRP sandwich bridge decks. A semi-analytical relationship between the mechanical properties and the dynamic response of the sandwich deck is finally developed. Based on this relationship, the dynamic loading factor impacted by traveling vehicles is evaluated and used in analyzing composite sandwich bridge decks.

1. Effective flexural and shear stiffness of sandwich decks

The first step in designing a composite sandwich deck is the estimation of the equivalent stiffness properties of the face sheets, the core elements, and the sandwich deck. The configuration of the face laminate, sinusoidal core, and sandwich panels are summarized in Figure 1.

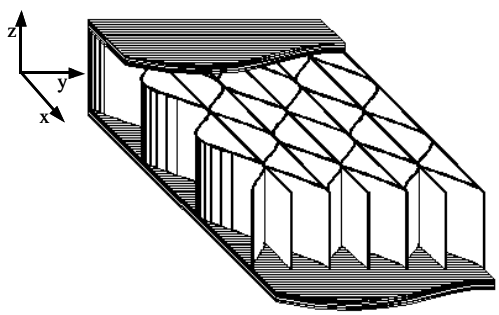

Figure 1. Configuration of sandwich panel.

1.1. ***Modeling of face laminates.*** The engineering properties of laminated panels can be predicted by a combined micro/macromechanics approach [Davalos et al. 1996]. The prediction of the ply properties using the micromechanics approach is well defined [Chamis 1984]. The stiffness properties of each layer can be computed from existing micromechanics models, such as rule of mixtures (ROM) [Jones 1999], periodic microstructure (PM) [Luciano and Barbero 1994] and composite cylinders (CC) [Hashin and Rosen 1964], wherein each layer is modeled as a homogeneous, linearly elastic, and generally orthotropic material. As in [Davalos et al. 2001], a typical face laminate may include the following four types of fiber layers:

Ply name	Orientation	E_1(GPa)	E_2(GPa)	G_{12}(GPa)	G_{23}(GPa)	ν_{12}	ν_{23}
bond layer	random	9.72	9.72	3.50	2.12	0.394	0.401
CM3205	0° or 90°	27.72	8.00	3.08	2.88	0.295	0.390
	random	11.79	11.79	4.21	2.36	0.402	0.400
UM1810	0°	30.06	8.55	3.30	3.08	0.293	0.386
	random	15.93	15.93	5.65	2.96	0.409	0.388
core mat	random	11.79	11.79	4.21	2.97	0.402	0.388

Table 1. Ply stiffness properties obtained from micromechanics model.

(1) Chopped strand mat (ChopSM), which is made of short fibers randomly oriented, resulting in nearly isotropic in-plane properties.

(2) Continuous strand mat (ContSM) which consists of continuous randomly oriented fibers; this product is commonly used as backing material for non-woven fabrics and can be modeled as an isotropic layer.

(3) Bidirectional stitched fabrics (SF) with balanced off-angle unidirectional fibers (e.g., 0°/90° or ±45°).

(4) Unidirectional layer of fiber bundles or rovings.

The stiffness of each ply can be predicted from micromechanics models. In this study, a micromechanics model for composites with periodic microstructure [Luciano and Barbero 1994] is used to obtain the elastic constants for each individual layer (Table 1).

After the elastic properties of each ply are obtained from micromechanics, the equivalent stiffness properties of the face laminate are computed from classical lamination theory [Jones 1999]. A set of equivalent laminate stiffness properties can be defined for approximately balanced symmetric face laminates [Davalos et al. 1996] and are given in Table 2. These elastic constants (e.g., E_x^f, E_y^f, G_{xy}^f, and ν_{xy}^f) represent the stiffness of an equivalent orthotropic plate that behaves like the actual laminate under out-of-plane and in-plane loads.

1.2. ***Modeling of honeycomb core.*** Unlike traditional honeycomb sandwich structures, the shape of the corrugated cell wall in the sandwich is defined by a sinusoidal function (Figure 1).

An example of a honeycomb core manufactured by Kansas Structural Composites, Inc. (KSCI, Russell, Kansas) is shown in Figure 2, and the dimensions of the sinusoidal core are $h = 25.4$ mm (1.0 in) and $b = 50.8$ mm (2.0 in). In the coordinate system shown in Figure 2, the wave function of a corrugated

E_x^f	E_y^f	ν_{xy}^f	G_{xy}^f	G_{xz}^f	G_{yz}^f
19.62 GPa 2.85×10^6 psi	12.76 GPa 1.85×10^6 psi	0.302	3.76 GPa 0.55×10^6 psi	3.75 GPa 0.54×10^6 psi	3.68 GPa 0.53×10^6 psi

Table 2. Material properties of face laminates.

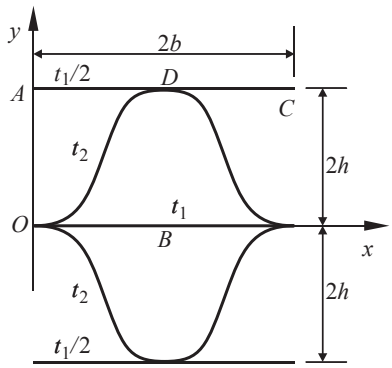

Figure 2. A unit cell of sinusoidal core.

core wall can be described as

$$y = h\left(1 - \cos\frac{\pi x}{b}\right). \tag{1}$$

The microstructure of core walls, either flat or corrugated, includes a continuous strand mat (ContSM) consisting of continuous randomly oriented fibers. This layer can be modeled as an isotropic layer and its properties, predicted by the micromechanics model [Luciano and Barbero 1994], are given in Table 1.

An improved mechanics approach recently developed by [Qiao and Wang 2005] is used to evaluate the effective in-plane Young's moduli of sinusoidal cores. For the transverse shear moduli, the formulas for general core configuration obtained from homogenization theory [Xu et al. 2001] are applied for the case of sinusoidal core.

To obtain the core effective transverse Young's modulus (E_y^e), a macroscopic stress σ_y is applied to the unit cell in the y direction (Figure 2). Due to the symmetry of the unit cell, only a quarter of it is considered, as shown in Figure 3, left. The free body diagram of a half-wave curved core wall is presented in Figure 3, right, where P, F, and M_0 are the resultant forces and a moment of curved wall from macroscopic stress σ_y. Based on the equilibrium condition, the internal forces and moment (M, N, and V in Figure 3, right) of the curved wall beam element are

$$M = -P(b - x) + Fh\left(1 + \cos\frac{\pi x}{b}\right) + M_0, \tag{2}$$

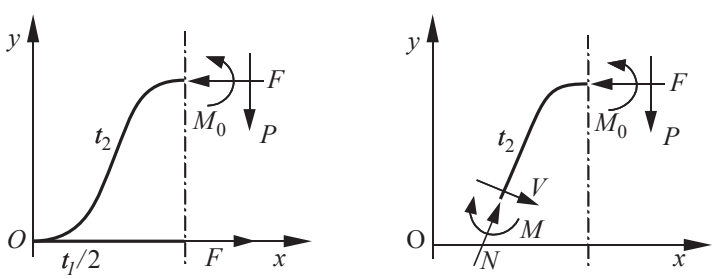

Figure 3. Modeling of the core effective transverse Young's modulus, E_y^e: loading configuration (left) and internal force analysis (right).

$$N = \frac{Fb + Ph\pi \sin(\pi x/b)}{b\sqrt{1 + (h\pi/b)^2 \sin^2(\pi x/b)}}, \tag{3}$$

$$V = \frac{Fh\pi \sin(\pi x/b) - Pb}{b\sqrt{1 + (h\pi/b)^2 \sin^2(\pi x/b)}}. \tag{4}$$

The elastic strain energy of the curved wall in Figure 3 is expressed as

$$U = \int_0^S \left(\frac{\alpha_M M^2}{2} + \frac{\alpha_N N^2}{2} + \frac{\alpha_V V^2}{2} \right) ds, \tag{5}$$

where

$$\alpha_M = \frac{12}{E_1 t_2^3}, \quad \alpha_N = \frac{1}{E_1 t_2}, \quad \alpha_V = \frac{1}{\kappa G_{13} t_2}. \tag{6}$$

Castigliano's theorem gives

$$\frac{\partial U}{\partial M_0} = 0, \quad \frac{\partial U}{\partial P} = \Delta_y, \quad \frac{\partial U}{\partial F} = \Delta_x. \tag{7}$$

It is noted that

$$\Delta_x = -\frac{2Fb}{E_1 t_1}. \tag{8}$$

Combining (7) and (8) gives the expression of Δ_y in term of P. Therefore, the core effective transverse Young's modulus (E_y^e) is obtained as

$$E_y^e = \frac{\sigma_y}{\varepsilon_y} = \frac{P/b}{\Delta_y/2h} = \frac{2Ph}{b\Delta_y}. \tag{9}$$

Similarly, a macroscopic stress σ_x is applied to the unit cell to compute the core effective longitudinal Young's modulus in the x direction (Figure 4). Again, due to the symmetry of the unit cell, only a quarter of it is modeled (Figure 4, left). Its internal forces and moment can be obtained with the aid of Figure 4, right.

The strain energy of the quarter representative volumetric element (RVE) is given as

$$U = \int_0^S \left(\frac{\alpha_M M^2}{2} + \frac{\alpha_N N^2}{2} + \frac{\alpha_V V^2}{2} \right) ds + \frac{F_1^2 b}{E_1 t_1} + \frac{F_3^2 b}{E_1 t_1}, \tag{10}$$

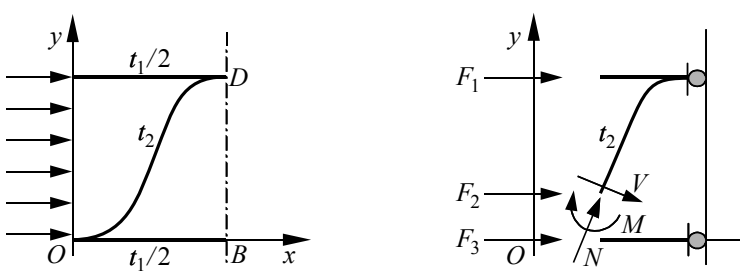

Figure 4. Modeling of the core effective longitudinal Young's modulus, E_x^e: loading configuration (left) and internal force analysis (right).

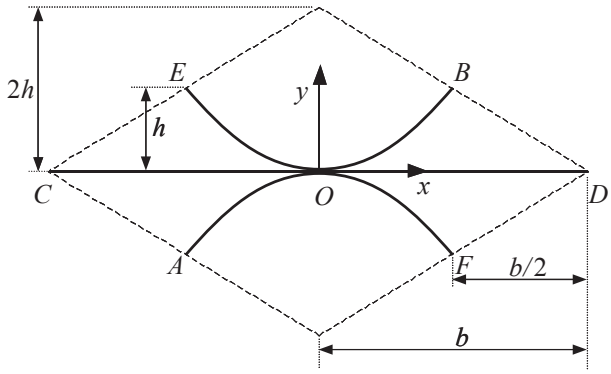

Figure 5. Unit cell of sinusoidal core for out-of-plane shear moduli.

where M is the internal moment and N, and V are the internal forces of the half curve waved wall and are calculated by using (2)–(4) with $P = 0$.

Again, invoking Castigliano's theorem results in

$$\frac{\partial U}{\partial M_0} = 0, \quad \frac{\partial U}{\partial F_1} = \Delta_x, \quad \frac{\partial U}{\partial F_2} = \Delta_x, \quad \frac{\partial U}{\partial F_3} = \Delta_x, \tag{11}$$

where F_1, F_2, and F_3 correspond to the forces on the top flat, curved, and bottom flat walls, respectively (see Figure 4, right), and can be expressed in term of Δ_x. Hence, the core effective longitudinal Young's modulus (E_x^e) is obtained as

$$E_x^e = \frac{(F_1 + F_2 + F_3)}{\Delta_x}. \tag{12}$$

The solutions for the core effective transverse shear moduli (G_{yz}^e and G_{xz}^e) are obtained based on a homogenization method [Xu et al. 2001] and are given as

$$G_{xz}^e = \left(\frac{t_1}{2h} + \frac{bt_2}{2hS}\right) G_{12}^s, \quad G_{yz}^e = \frac{2ht_2}{bS} G_{12}^s, \tag{13}$$

where G_{12}^s is the shear modulus of solid walls (Table 1), and S is the length for the curved segment, $S = \int_A^B ds$ (Figure 5).

Based on the above formulas for both the Young moduli and transverse shear moduli, the equivalent material properties of the sinusoidal core in the longitudinal and transverse directions are provided in Table 3.

1.3. ***Effective stiffness properties of honeycomb sandwich beams.*** Next we find the stiffness coefficients of a sandwich panel by modeling the sandwich as a three-layer laminated plate (top and bottom face sheets

E_x^c	E_y^c	G_{xz}^c	G_{yz}^c
0.531 GPa	0.0449 GPa	0.292 GPa	0.119 GPa
7.702×10^4 psi	0.651×10^4 psi	4.235×10^4 psi	1.726×10^4 psi

Table 3. Equivalent material properties of sinusoidal honeycomb core.

and core). Then the constitutive relations for the sandwich deck including the transverse shear deformation are obtained. The in-plane stress-strain relation of a general orthotropic lamina is expressed as

$$\{\sigma\} = [\bar{Q}]\{\varepsilon\}, \tag{14}$$

where, $\{\sigma\} = \{\sigma_x, \sigma_y, \sigma_{xy}\}$, $\{\varepsilon\} = \{\varepsilon_x, \varepsilon_y, \varepsilon_{xy}\}$, and $[\bar{Q}]$ is the matrix of reduced stiffness coefficient $\bar{Q}_{ij}$. Integration of (14) through the thickness of the beam results in the relation between the resultant forces and moments and the strains and curvatures:

$$\begin{Bmatrix} \{N\} \\ \{M\} \end{Bmatrix} = \begin{bmatrix} [A] & [B] \\ [B] & [D] \end{bmatrix} \begin{Bmatrix} \{\varepsilon\} \\ \{\kappa\} \end{Bmatrix}, \tag{15}$$

where $[A]$ is the 3×3 extensional stiffness sub-matrix, $[B]$ is the 3×3 bending-extension coupling stiffness sub-matrix, $[D]$ is the 3×3 bending stiffness sub-matrix [Jones 1999]. The sandwich beam is symmetric with respect to the middle surface; hence the bending-extension coupling coefficients are zero. The compliance equations are obtained by inverting the matrices in (15):

$$\begin{Bmatrix} \{\varepsilon\} \\ \{\kappa\} \end{Bmatrix} = \begin{bmatrix} [\alpha] & [0] \\ [0] & [\delta] \end{bmatrix} \begin{Bmatrix} \{N\} \\ \{M\} \end{Bmatrix}. \tag{16}$$

To obtain the beam stiffness coefficients from (16), in accordance with Whitney's assumption [1987], only N_x and M_x are retained. Hence, the compliance coefficients for the sandwich beam can be simplified to

$$\begin{Bmatrix} \varepsilon_x^0 \\ \kappa_x \end{Bmatrix} = \begin{bmatrix} \alpha_{11} & 0 \\ 0 & \delta_{11} \end{bmatrix} \begin{Bmatrix} N_x \\ M_x \end{Bmatrix}. \tag{17}$$

Inverting (17) leads to the expression for the force resultant of the sandwich beam as

$$\begin{Bmatrix} N_x \\ M_x \end{Bmatrix} = \begin{bmatrix} \bar{A} & 0 \\ 0 & \bar{D} \end{bmatrix} \begin{Bmatrix} \varepsilon_x^0 \\ \kappa_x \end{Bmatrix}, \tag{18}$$

where $\bar{A}$ and $\bar{D}$ are the extensional and bending stiffnesses of the sandwich beam, and they are defined as $\bar{A} = 1/\alpha_{11} = (A_{11}A_{22} - A_{12}^2)/A_{22}$ and $\bar{D} = 1/\delta_{11} = (D_{11}D_{22} - D_{12}^2)/D_{22}$.

Subsequently, the transverse shear stress resultant is derived by considering the constitutive relations for transverse shear stresses in an orthotropic lamina:

$$\begin{Bmatrix} \sigma_{xz} \\ \sigma_{yz} \end{Bmatrix} = \begin{bmatrix} \bar{Q}_{55} & 0 \\ 0 & \bar{Q}_{44} \end{bmatrix} \begin{Bmatrix} \gamma_{xz} \\ \gamma_{yz} \end{Bmatrix}. \tag{19}$$

Following a similar procedure for the extensional and bending stiffnesses and considering only the resultant component in the x-direction (Q_x) and assuming a constant transverse shear strain through the beam thickness, the constitutive relation for the transverse shear resultant is

$$Q_x = kF\gamma_{xz}, \tag{20}$$

where k is the shear correction factor and F is the transverse shear stiffness.

Thus, from (18) and (20), the constitutive relations of the sandwich beam are expressed as

$$\begin{Bmatrix} N_x \\ M_x \\ Q_x \end{Bmatrix} = \begin{bmatrix} \bar{A} & 0 & 0 \\ 0 & \bar{D} & 0 \\ 0 & 0 & kF \end{bmatrix} \begin{Bmatrix} \varepsilon_x^0 \\ \kappa_x \\ \gamma_{xz} \end{Bmatrix}. \tag{21}$$

In the following, the shear correction factor of a three-layer sandwich beam is derived using the energy equivalence principle. Using two-dimensional equilibrium equations, the shear strain energy is calculated and equated to the shear strain energy obtained from the constitutive relations of (20).

Using the equilibrium equation for the stresses on the xz plane in the absence of body forces and after integrating through the thickness of the section, the shear stress expression becomes

$$\sigma_{xz} = -\int_{-h/2}^{z} \sigma_{x,x} dz. \tag{22}$$

Substitution of (14) into (22), use of the expression of strains and curvatures in (16), and consideration of the equilibrium equation of a beam (i.e., $N_{x,x} = 0$ and $M_{x,x} = -Q_x$) yields

$$\sigma_{xz} = -\int_{-h/2}^{z} Q_x z(\bar{Q}_{11}\delta_{11} + \bar{Q}_{12}\delta_{12}) dz. \tag{23}$$

Equation (23) expresses the variation of the transverse shear stress through the thickness of the section. Employing the constitutive relation for the transverse shear given in (19) and assuming σ_{yz} as negligible, the shear strain energy per unit length is obtained as follows:

$$U = \frac{1}{2}\int_{-h/2}^{h/2} \frac{(\sigma_{xz})^2}{\bar{Q}_{55}} dz. \tag{24}$$

Then

$$U = \frac{1}{2}\int_{-h/2}^{h/2} \frac{Q_x^2}{\bar{Q}_{55}} \left(\int_{-h/2}^{z} z(\bar{Q}_{11}\delta_{11} + \bar{Q}_{12}\delta_{12}) dz \right)^2 dz. \tag{25}$$

Similarly, the constitutive relation of (20), which assumes that the average transverse shear strain is constant through the thickness, results in the shear strain energy per unit length as

$$U = \frac{1}{2}\frac{Q_x^2}{kF}. \tag{26}$$

Equating both strain energies given by (25) and (26), the expression of the effective transverse shear stiffness of the sandwich beams including the shear correction factor is given by

$$kF = (kGA)_{xz} = \left[\int_{-h/2}^{h/2} \frac{1}{\bar{Q}_{55}} \left(\int_{-h/2}^{z} z(\bar{Q}_{11}\delta_{11} + \bar{Q}_{12}\delta_{12}) dz \right)^2 dz \right]^{-1}. \tag{27}$$

For the sandwich beam application, which consists of three layers (two face sheet layers and one core layer), the effective transverse shear stiffness of the sandwich beam is computed, based on (27), as

$$(kGA)_{xz} = b\Bigg[\, 2\int_{-h/2}^{-hc/2} \frac{1}{\bar{Q}_{55f}}\Big(\int_{-h/2}^{z} z(\bar{Q}_{11f}\delta_{11} + \bar{Q}_{12f}\delta_{12})dz\Big)^2 dz + \int_{-hc/2}^{hc/2} \frac{1}{\bar{Q}_{55c}}\Big(\int_{-h/2}^{z} z(\bar{Q}_{11f}\delta_{11} + \bar{Q}_{12f}\delta_{12})dz + \int_{-h/2}^{z} z(\bar{Q}_{11c}\delta_{11} + \bar{Q}_{12c}\delta_{12})dz\Big)^2 dz\Bigg]^{-1}, \quad (28)$$

and the bending stiffness is computed using (18) as

$$(EI)_x = b\bar{D} = b\frac{(D_{11}D_{22} - D_{12}^2)}{D_{22}}, \quad (29)$$

where h is the thickness of the sandwich; h_c is the thickness of the core; b is the width of the beam; the subscripts f and c stand for the face sheet and the core, respectively; and the other parameters are as explained earlier. Based on (14) and (15) and the equivalent properties of face laminates and cores given in Tables 2 and 3, the beam stiffness properties along the longitudinal and transverse directions are reported in Table 4. These properties, which are shown as plate stiffness in Table 5, are later used for the dynamic response analysis and dynamic impact factor calculations.

Beam	width b	depth d	EI	kGA
Longitudinal	0.334 m	0.105 m	0.4965×10^6 N-m^2	12.323×10^6 N
	13.125 in	4.125 in	172.883×10^6 lb-in^2	2.7706×10^6 lb
Transverse	0.203 m	0.105 m	0.1900×10^6 N-m^2	3.0945×10^6 N
	8.000 in	4.125 in	66.2012×10^6 lb-in^2	0.695×10^6 lb

Table 4. Analytical bending and transverse shear stiffness coefficients of sandwich beams.

A_{11}	A_{12}	A_{22}	A_{66}	D_{11}	D_{12}	D_{22}	D_{66}	A_{44}	A_{55}
in units of 10^9 N/m				in units of 10^6 Nm				in units of 10^6 N/m	
1.62	0.31	1.02	0.0206	1.65	0.31	1.03	0.0508	22.9	55.3

Table 5. Axial, bending and shear stiffnesses of the sandwich panel.

2. Dynamics of sandwich bridge decks

The bridge-vehicle interaction involves dynamics of bridge decks and vehicles. Ignoring the roughness of the deck, the governing equations for sandwich bridge deck dynamics consider the total bending deflection (including shear deformation), w, and the bending slope, ψ_x, ψ_y, and they can be written as follows [Dobyns 1981; Ip and Tse 2001]:

$$\begin{aligned} A_{11}\frac{\partial^2 u_0}{\partial x^2} + A_{66}\frac{\partial^2 u_0}{\partial y^2} + (A_{12} + A_{66})\frac{\partial^2 v_0}{\partial x \partial y} &= \bar{\rho}\frac{\partial^2 u_0}{\partial t^2}, \\ (A_{12} + A_{66})\frac{\partial^2 u_0}{\partial x \partial y} + A_{66}\frac{\partial^2 v_0}{\partial x^2} + A_{22}\frac{\partial^2 v_0}{\partial y^2} &= \bar{\rho}\frac{\partial^2 v_0}{\partial t^2}, \end{aligned} \quad (30a)$$

$$D_{11}\frac{\partial^2\psi_x}{\partial x^2}+D_{66}\frac{\partial^2\psi_x}{\partial y^2}+(D_{12}+D_{66})\frac{\partial^2\psi_y}{\partial x\partial y}-kA_{55}(\psi_x+\frac{\partial w}{\partial x})=I\frac{\partial^2\psi_x}{\partial t^2},$$
$$(D_{12}+D_{66})\frac{\partial^2\psi_x}{\partial x\partial y}+D_{66}\frac{\partial^2\psi_y}{\partial x^2}+D_{22}\frac{\partial^2\psi_y}{\partial y^2}-kA_{44}\left(\psi_y+\frac{\partial w}{\partial y}\right)=I\frac{\partial^2\psi_y}{\partial t^2}, \tag{30b}$$

$$k\left[A_{55}\left(\frac{\partial\psi_x}{\partial x}+\frac{\partial^2 w}{\partial x^2}\right)+A_{44}\left(\frac{\partial\psi_y}{\partial y}+\frac{\partial^2 w}{\partial y^2}\right)\right]+q=\bar{\rho}\frac{\partial^2 w}{\partial t^2}, \tag{30c}$$

where A_{ij} ($i, j = 1, 2,$ or 6) are the extensional stiffness of the face sheet; A_{44} and A_{55} are the transverse shear stiffnesses of the face sheet, and k is the shear correction factor; D_{ij} ($i, j = 1, 2,$ or 6) is the bending stiffness of face sheet; u_0, v_0, and w are the mid-surface displacements of the face sheet in the x, y, and z directions, respectively; ψ_x and ψ_y are the rotations of the face sheet; and $\bar{\rho}=\int_{-h_t/2}^{h_t/2}\rho dz$ and $I=\int_{-h_t/2}^{h_t/2}\rho z^2 dz$ (r is the individual layer density in the face sheet laminate).

The loading function resulting from a group of moving loads can be written as

$$q=\sum_{l=1}^{N_p}p_l(t)\delta(x-x_l(t))\delta(y-y_l(t)), \tag{31}$$

where $\{p_l(t), l = 1, 2, \ldots, N_p\}$ are the moving loads which are moving as a group at a fixed spacing; $x_l(t)$, $y_l(t)$ is the position of the moving load $p_l(t)$; $\delta(x)$ is the Dirac function.

By modal superposition, the displacement of the orthotropic plate can be written as

$$\begin{aligned}
u_0(x,y,t)&=\sum_{m=1}^{M}\sum_{n=1}^{N}A_{mn}(t)\cos\frac{m\pi x}{a}\sin\frac{n\pi y}{b},\\
v_0(x,y,t)&=\sum_{m=1}^{M}\sum_{n=1}^{N}B_{mn}(t)\sin\frac{m\pi x}{a}\cos\frac{n\pi y}{b},\\
w(x,y,t)&=\sum_{m=1}^{M}\sum_{n=1}^{N}C_{mn}(t)\sin\frac{m\pi x}{a}\sin\frac{n\pi y}{b},\\
\psi_x(x,y,t)&=\sum_{m=1}^{M}\sum_{n=1}^{N}D_{mn}(t)\cos\frac{m\pi x}{a}\sin\frac{n\pi y}{b},\\
\psi_y(x,y,t)&=\sum_{m=1}^{M}\sum_{n=1}^{N}E_{mn}(t)\sin\frac{m\pi x}{a}\cos\frac{n\pi y}{b},
\end{aligned} \tag{32}$$

where $A_{mn}(t)$, $B_{mn}(t)$, $C_{mn}(t)$, $D_{mn}(t)$ and $E_{mn}(t)$ are the time-dependent unknown coefficients to be determined; and M and N are the number of the terms used in the series.

The impact load from the truck can also be represented as

$$q(x,y,t)=\sum_{m=1}^{M}\sum_{n=1}^{N}Q_{mn}(t)\sin\left(\frac{m\pi x}{a}\right)\sin\left(\frac{n\pi y}{b}\right). \tag{33}$$

(See Figure 6.)

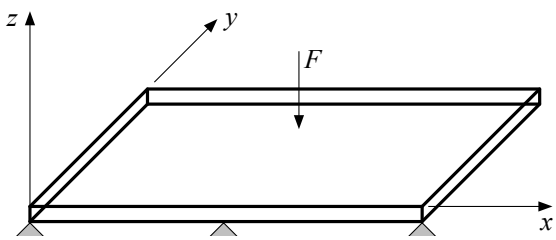

Figure 6. Model of a continuous bridge deck.

In this study, the effects of rotational inertia are neglected ($I = 0$). By considering (30) and (32), an independent set of five equations for each pair (m, n) of Fourier coefficients is obtained,

$$\begin{bmatrix} L_{11} & L_{12} & 0 & 0 & 0 \\ L_{12} & L_{22} & 0 & 0 & 0 \\ 0 & 0 & L_{33} & L_{34} & L_{35} \\ 0 & 0 & L_{34} & L_{44} & L_{45} \\ 0 & 0 & L_{35} & L_{45} & L_{55} \end{bmatrix} \begin{Bmatrix} A_{mn}(t) \\ B_{mn}(t) \\ C_{mn}(t) \\ D_{mn}(t) \\ E_{mn}(t) \end{Bmatrix} = \begin{Bmatrix} 0 \\ 0 \\ Q_{mn}(t) - \rho h \ddot{C}_{mn}(t) \\ 0 \\ 0 \end{Bmatrix}, \tag{34}$$

where the coefficients in the matrix are expressed as

$$\begin{aligned} L_{11} &= A_{11}\left(\frac{m\pi}{a}\right)^2 + A_{66}\left(\frac{n\pi}{b}\right)^2, \\ L_{12} &= (A_{11} + A_{66})\frac{m\pi}{a}\frac{n\pi}{b}, \\ L_{22} &= A_{22}\left(\frac{n\pi}{b}\right)^2 + A_{66}\left(\frac{m\pi}{a}\right)^2, \\ L_{33} &= kA_{55}\left(\frac{m\pi}{a}\right)^2 + kA_{44}\left(\frac{n\pi}{b}\right)^2, \\ L_{34} &= kA_{55}\frac{m\pi}{a}, \quad L_{35} = kA_{44}\frac{n\pi}{b}, \\ L_{44} &= D_{11}\left(\frac{m\pi}{a}\right)^2 + D_{66}\left(\frac{n\pi}{b}\right)^2 + kA_{55}, \\ L_{45} &= (D_{11} + D_{66})\frac{m\pi}{a}\frac{n\pi}{b}, \\ L_{55} &= D_{66}\left(\frac{m\pi}{a}\right)^2 + D_{22}\left(\frac{n\pi}{b}\right)^2 + kA_{44}. \end{aligned} \tag{35}$$

Following [Yang and Qiao 2005b], one can reduce (34) to a single differential equation by the transformation

$$A_{mn}(t) = K_{A1}C_{mn}(t), \quad B_{mn}(t) = K_{B1}C_{mn}(t), \quad D_{mn}(t) = K_{A2}C_{mn}(t), \quad E_{mn}(t) = K_{B2}C_{mn}(t), \tag{36}$$

where K_{A1}, K_{B1}, K_{A2}, K_{B2} are the system constants that transform (34) into a single differential equation,

$$\ddot{C}_{mn}(t) + \frac{L_{34}K_{A2} + L_{35}K_{B2} + L_{33}}{\rho h}C_{mn}(t) = \frac{Q_{mn}(t)}{\rho h}. \tag{37}$$

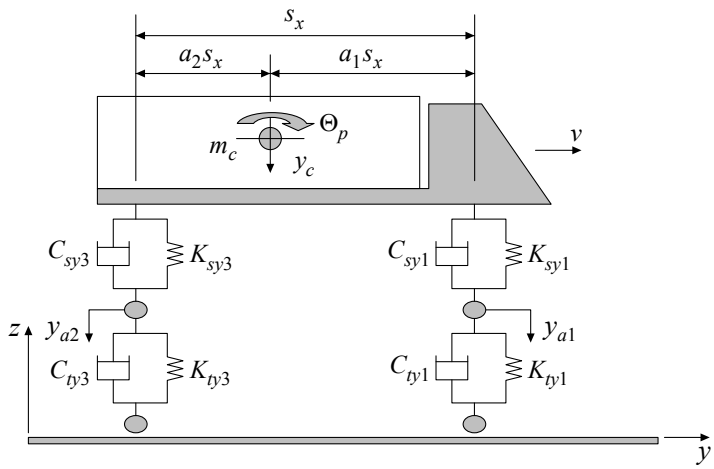

Figure 7. Idealization of two-axle vehicle.

3. Dynamics of vehicles

The mathematical model for the H20-44 truck is shown in Figure 7. The model is similar to that employed in [Zhu and Law 2002].

The vehicle body is assigned three degrees of freedom, corresponding to the vertical displacement (bounce or y), rotation about the transverse axis (pitch or θ_p), and the rotation about the longitudinal axis (roll or θ_r). Each wheel/axle set is described with two additional degrees of freedom in the vertical and roll directions ($y_{a1}, y_{a2}, \theta_{a1}, \theta_{a2}$). Therefore, the total number of independent degrees of freedom is seven. The equations of motion of the vehicle are derived using Lagrange's formulation as follows:

$$M_V \ddot{Y} + C_V \dot{Y} + K_V Y = F_V^{\text{int}}, \tag{38}$$

where F_V^{int} is the interaction force vector applied on the vehicle, M_V, C_V and K_V are, respectively, the mass, damping and stiffness matrices of the vehicle system and Y is the vector of the vehicle degrees of freedom.

4. The vehicle-bridge interaction

The vehicle-bridge interaction forces for a single vehicle can be written as

$$\begin{aligned}
F_{t1} &= K_{ty1}\big(y_{a1} - \tfrac{1}{2}S_{d1}\theta_{a1} - w_1 - d_1\big) + C_{ty1}\big(\dot{y}_{a1} - \tfrac{1}{2}S_{d1}\dot{\theta}_{a1} - \dot{w}_1 - \dot{d}_1\big),\\
F_{t2} &= K_{ty2}\big(y_{a1} + \tfrac{1}{2}S_{d1}\theta_{a1} - w_2 - d_2\big) + C_{ty2}\big(\dot{y}_{a1} + \tfrac{1}{2}S_{d1}\dot{\theta}_{a1} - \dot{w}_2 - \dot{d}_2\big),\\
F_{t3} &= K_{ty3}\big(y_{a2} - \tfrac{1}{2}S_{d2}\theta_{a2} - w_3 - d_3\big) + C_{ty3}\big(\dot{y}_{a2} - \tfrac{1}{2}S_{d2}\dot{\theta}_{a2} - \dot{w}_3 - \dot{d}_3\big),\\
F_{t4} &= K_{ty4}\big(y_{a2} + \tfrac{1}{2}S_{d2}\theta_{a2} - w_4 - d_4\big) + C_{ty4}\big(\dot{y}_{a2} + \tfrac{1}{2}S_{d2}\dot{\theta}_{a2} - \dot{w}_4 - \dot{d}_4\big),
\end{aligned} \tag{39}$$

where $\{K_{tyi}, i = 1, 2, 3, 4\}$ are the stiffnesses of the tires; $\{C_{tyi}, i = 1, 2, 3, 4\}$ are the friction coefficients of the tires; S_{d1}, S_{d2} are the wheel spacings of the front and rear axles respectively, and

$$w_i = w(x_i(t), y_i(t), t), \tag{40}$$

$$d_i = d(x_i(t), y_i(t), t), \tag{41}$$

where $d(x, y)$ is the surface roughness of the bridge deck (here we assume $d(x, y) = 0$, that is, the surface is smooth), and $(x_i(t), y_i(t))$ is the location of the i-th tire at time t. As the vehicle moves along one lane, we have

$$y_1(t) = y_0 + S_{d1}/2, \quad y_2(t) = y_0 - S_{d1}/2, \quad y_3(t) = y_0 + S_{d2}/2, \quad y_4(t) = y_0 - S_{d2}/2, \tag{42}$$

where y_0 is the transverse coordinate of the centerline of the vehicle.

5. Dynamic responses and dynamic loading factor of different bridge decks

5.1. ***Vehicle approximated with one degree of freedom.*** Based on the simply supported boundary conditions we have assumed, the bridge-vehicle interaction model is formulated using (37)–(39) and solved using Newmark-β method [Zhu and Law 2002]. The vehicle body is rigid and subjected to bounce, pitch, and roll motions. The parameters of the vehicle-bridge system for a typical concrete deck are as follows:

l	b	h	E	ν	ρ	m_c	K_{ty}
26.4 m	10.7 m	0.95 m	14.54×10^{10} N/m^2	0.3	2375 kg/m^3	18600 kg	7.85×10^5 N/m

Table 6. Calculation parameters for the concrete deck-vehicle system (where l is the span length, b the bridge width, h the deck thickness, ρ, E and ν the density, Young's modulus and Poisson's ratio of the deck material, m_c the mass of the vehicle, and K_{ty} the contact stiffness of tire with the bridge).

The vehicle simulation started from the location of (0, 5.35) and the deflection generated at the center point of the simply supported plate is calculated as shown in Figure 8. The number of Fourier series terms used are 50×50, which grantees its convergence as shown in the sandwich deck case.

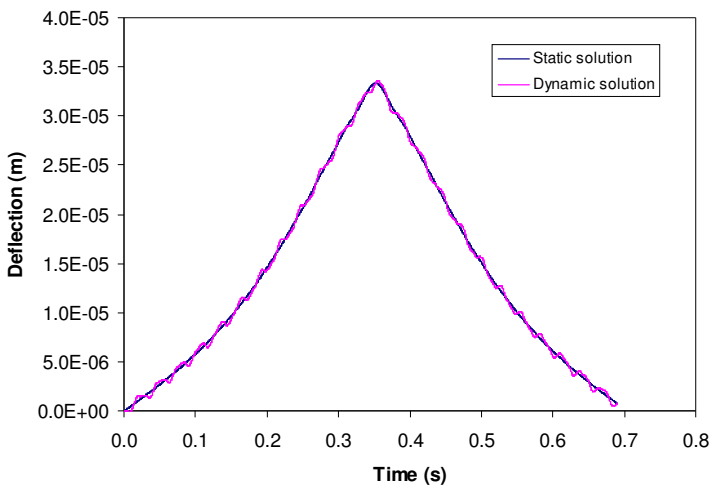

Figure 8. Comparison of the static and dynamic deflection generated by a passing vehicle.

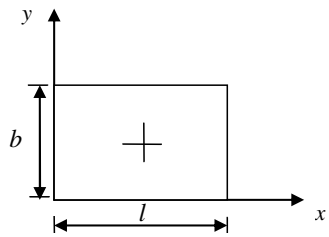

Figure 9. Reference node on the bridge deck.

First the dynamic simulated results are compared with the static results. From Figure 8, we see that the model captures the static and dynamic effect very well. And the peak result is also very close to the numerical result 3.29×10^{-5} m calculated by ABAQUS when the load is applied at the center point.

5.2. ***Vehicle approximated with seven degrees of freedom.*** The bridge is still simplified as a simply supported plate. However the vehicle body is approximated as a seven-degree-freedom rigid body and subjected to bounce, pitch and roll motions. The parameters of the vehicle-bridge system are listed in Tables 7 and 8.

The dynamic displacement responses of the symbol + on the bridge deck (Figure 9) under the moving vehicle at speed of 32.5 m/s and 37.5 m/s are shown in Figure 10.

Figure 10 suggests that higher traveling velocities will shorten the time to reach the maximal deflection. Comparing the seven-degree vehicle model with the one-degree vehicle model, it is evident that the seven-degree vehicle model introduces larger vibrations compared to the one-degree model and accurately captures the wheel loads. The wheel loads for $v = 37.5$ m/s are shown in Figure 11. For the given vehicle, the load on the front wheels will be higher, since the gravity center of the vehicle is closer to the front wheels.

l	b	h	E	ν	ρ	S_x	a_1	a_2	S_{d1}	S_{d2}
26.4 m	10.7 m	0.95 m	14.54×10^{10} N/m^2	0.3	2375 kg/m^3	4.73	0.67	0.33	2.05	2.05

m_c	m_{a1}	m_{a2}	I_c	I_t	I_{a1}	I_{a2}	S_{y1}	S_{y2}
17000 kg	600 kg	1000 kg	9×10^4 kg m^2	1.3×10^4 kg m^2	550 kg m^2	600 kg m^2	1.41 m	1.41 m

Table 7. Geometric parameters (top row) and mass and inertial parameters (bottom row) for the composite sandwich deck-vehicle system.

K_{sy1}	K_{sy2}	K_{sy3}	K_{sy4}
1.16×10^5 N/m	1.16×10^5 N/m	3.73×10^5 N/m	3.73×10^5 N/m

C_{sy1}	C_{sy2}	C_{sy3}	C_{sy4}	C_{ty1}	C_{sy2}	C_{ty3}	C_{ty4}
2.5×10^4	2.5×10^4	3.5×10^4	3.5×10^4	100	100	200	200

Table 8. Spring stiffness in N/m (top row) and damping parameters in Ns/m (bottom rwo) for the HS20-44 truck.

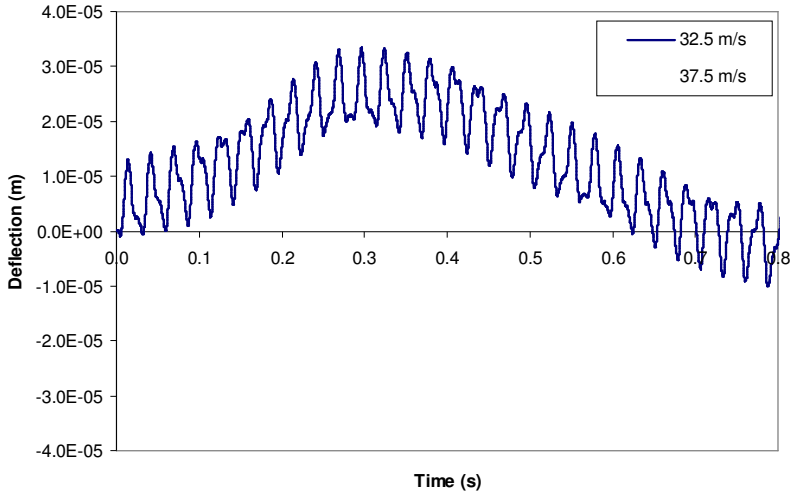

Figure 10. Dynamic displacement time history of the marked position on the composite bridge deck.

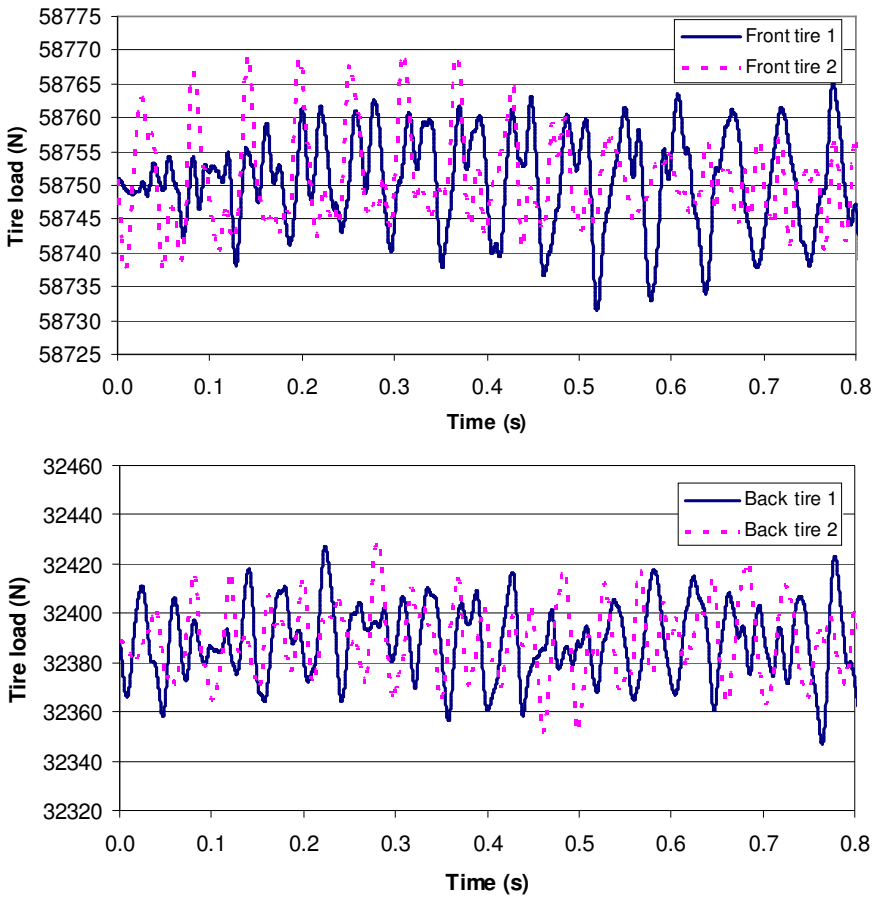

Figure 11. Front wheel (top) and back wheel (bottom) loads of the vehicle.

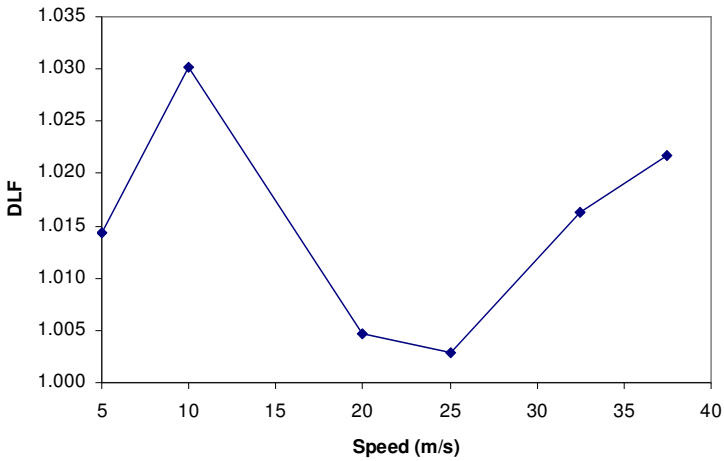

Figure 12. Dynamic load factors of the bridge under given vehicle.

Different dynamic responses will cause different effects on bridge response and need to be considered in design. In order to consider the vehicle-bridge interaction, dynamic loading factor is introduced in many design codes, such as ASSHTO 2002 and ACI 318-05. The dynamic loading factor is defined as the ratio of the maximal dynamic deflection to the maximal static deflection. It is shown in Figure 12 for the center point of the bridge deck considered, taking into account only bridge displacement and ignoring surface roughness.

5.3. ***Effect of deck stiffness.*** Using the given sandwich deck as shown in Table 5, the bridge-truck simulation is conducted at a speed $v = 37.5$ m/s. Since the sandwich panel has relatively low stiffness, it is worth verifying the convergence of the solution as a function of the number of terms used. As shown in Figure 13, when the number of terms in each direction reaches 40, the solution convergences. Using 50 terms of series in each direction, the center point deflection of the sandwich deck under the given vehicle is shown on Figure 14 with its static maximal deflection as 0.385 m, while the maximal wheel deflection is 0.576 m. From this figure and Figure 15, it is evident that the dynamic load factor (DLF) is 1.50 for the given composite sandwich deck, which is much larger than the design dynamic load factor

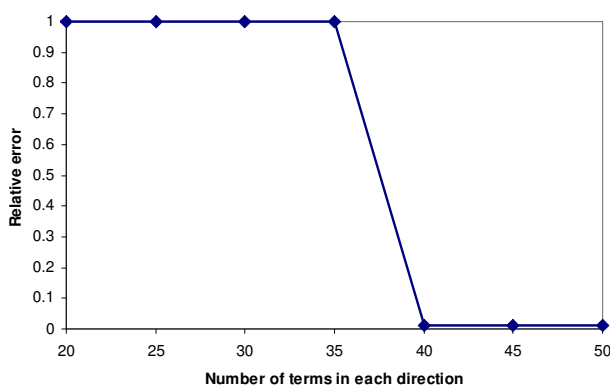

Figure 13. Convergence of the solution.

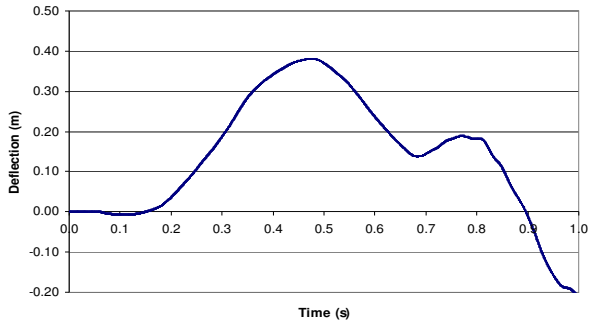

Figure 14. Center deflection history of the sandwich deck panel under the given vehicle.

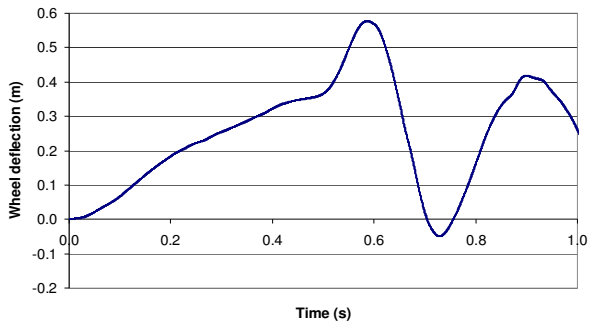

Figure 15. Front wheel deflection of the vehicle considering the sandwich bridge deck and vehicle interaction.

(1.25) for concrete type bridge decks. The reason behind the large deflection and dynamic load factor is that the lower stiffness of the sandwich plays a large role in the bridge-vehicle interaction and needs more attention. Since the maximum dynamic load factor is 1.5, it means that in a linear analysis as used in many codes the maximum stresses in the bridge deck are also 1.5 times those calculated by only considering static loading (neglecting its dynamic effect). Therefore, it is absolutely vital to use dynamic equations when analyzing or designing bridge decks made of composite materials. At the same time, due to large deflections of the composite deck, wheel loads (Figure 16) on the deck are also increased about three times compared to the concrete bridge deck as shown earlier in Figure 11.

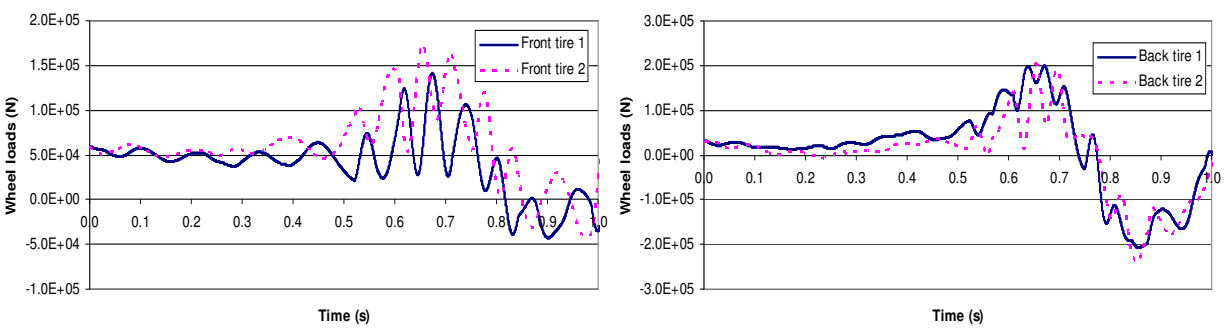

Figure 16. Front wheel (left) and back wheel (right) load of the vehicle.

6. Conclusions

A coupled generalized composite sandwich bridge-vehicle interaction model was introduced capable of capturing the interaction between vehicles and bridge deck systems. The results demonstrate that the proposed dynamic bridge-vehicle interaction procedure using modified Timoshenko plate models can be used to evaluate the dynamic response and the dynamic loading factors of sandwich bridge deck systems. The results suggest that the dynamic load factors vary with traveling speed and increase significantly with decreasing deck stiffness. The proposed model also predicts the increased vibration generated by vehicles. The vehicle simulation model has multi-degrees of freedom and provides estimates of the amplified dynamic loading factor. The procedure described here has potential practical application in the design of sandwich bridge decks.

Acknowledgements

The authors thank Prof. Pizhong Qiao at the Washington State University for his technical support.

References

[Chamis 1984] C. C. Chamis, "Simplified composites micromechanics equations for strength, fracture toughness, and environmental effects", technical report TM-83696, NASA, Houston, 1984, available at http://ntrs.nasa.gov/details.jsp?R=725506.

[Davalos et al. 1996] J. F. Davalos, H. A. Salim, P. Z. Qiao, R. Lopez-Anido, and E. J. Barbero, "Analysis and design of pultruded FRP shapes under bending", *Compos. B Eng. J.* **27**:3–4 (1996), 295–305.

[Davalos et al. 2001] J. F. Davalos, P. Qiao, X. F. Xu, J. Robinson, and K. E. Barth, "Modeling and characterization of fiber-reinforcement plastic honeycomb sandwich panels for highway bridge applications", *Compos. Struct.* **52**:3–4 (2001), 441–452.

[Dobyns 1981] A. L. Dobyns, "Analysis of simply-supported orthotropic plates subject to static and dynamic loads", *AIAA J.* **19**:5 (1981), 642–650.

[Frostig 2003] Y. Frostig, "Classical and high-order computational models in the analysis of modern sandwich panels", *Compos. B Eng. J.* **34**:1 (2003), 83–100.

[Frostig and Thomsen 2004] Y. Frostig and O. T. Thomsen, "High-order free vibration of sandwich panels with a flexible core", *Int. J. Solids Struct.* **41**:7 (2004), 1697–1724.

[Hashin and Rosen 1964] Z. Hashin and B. W. Rosen, "The elastic modulieling of fiber-reinforced materials", *J. Appl. Mech.* **31**:1 (1964), 223–232.

[Ip and Tse 2001] K. H. Ip and P. C. Tse, "Determination of dynamic flexural and shear moduli of thick composite beam using natural frequencies", *J. Compos. Mater.* **35**:17 (2001), 1553–1569.

[Jones 1999] R. M. Jones, *Mechanics of composite materials*, 2nd ed., Taylor & Francis, Philadelphia, 1999.

[Keller 2001] T. Keller, "Recent all-composite and hybrid fibre-reinforced polymer bridges and building", *Progress Struct. Eng. Mater.* **3**:2 (2001), 132–140.

[Librescu and Hause 2000] L. Librescu and T. Hause, "Recent developments in the modeling and behavior of advanced sandwich constructions: a survey", *Compos. Struct.* **48**:1 (2000), 1–17.

[Luciano and Barbero 1994] R. Luciano and E. J. Barbero, "Formulas for the stiffness of composites with periodic microstructure", *Int. J. Solids Struct.* **31**:21 (1994), 2933–2944.

[Plunkett 1997] J. D. Plunkett, "Fiber-reinforcement polymer honeycomb short span bridge for rapid installation", IDEA Project Report, NCHRP, Washington, DC, 1997.

[Qiao and Wang 2005] P. Z. Qiao and J. L. Wang, "On the mechanics of composite sinusoidal honeycomb cores", *J. Aerospace Eng., ASCE* **18**:1 (2005), 42–50.

[Whitney 1987] J. M. Whitney, *Structural analysis of laminated anisotropic plates*, Technomic, Lancaster, PA, 1987.

[Xu et al. 2001] X. F. Xu, P. Qiao, and J. F. Davalos, "Transverse shear stiffness of composite honeycomb core with general configuration", *J. Eng. Mech.* **127**:11 (2001), 1144–1151.

[Yang and Qiao 2005a] M. J. Yang and P. Qiao, "Higher-order impact modeling of sandwich beams with flexible core", *Int. J. Solids Struct.* **42**:20 (2005), 5460–5490.

[Yang and Qiao 2005b] M. J. Yang and P. Qiao, "Nonlinear impact analysis of fully backed composite sandwich structures", *Compos. Sci. Technol.* **65**:3–4 (2005), 551–562.

[Zhu and Law 2002] X. Q. Zhu and S. S. Law, "Dynamic load on continuous multi-lane bridge deck from moving vehicles", *J. Sound Vib.* **251**:4 (2002), 697–716.

Received 19 Jun 2009. Revised 10 Jan 2010. Accepted 11 Jan 2010.

MIJIA YANG: mijia.yang@utsa.edu
Department of Civil and Environmental Engineering, The University of Texas, San Antonio, TX 78249, United States

A. T. PAPAGIANNAKIS: AT.papagiannakis@utsa.edu
Department of Civil and Environmental Engineering, The University of Texas, San Antonio, TX 78249, United States

JOURNAL OF MECHANICS OF MATERIALS AND STRUCTURES
Vol. 5, No. 4, 2010

SPECTRAL ELEMENT APPROACH TO WAVE PROPAGATION IN UNCERTAIN BEAM STRUCTURES

V. AJITH AND S. GOPALAKRISHNAN

This paper presents a study on the uncertainty in material parameters of wave propagation responses in metallic beam structures. Special effort is made to quantify the effect of uncertainty in the wave propagation responses at high frequencies. Both the modulus of elasticity and the density are considered uncertain. The analysis is performed using a Monte Carlo simulation (MCS) under the spectral finite element method (SEM). The randomness in the material properties is characterized by three different distributions, the normal, Weibull and extreme value distributions. Their effect on wave propagation in beams is investigated. The numerical study shows that the CPU time taken for MCS under SEM is about 48 times less than for MCS under a conventional one-dimensional finite element environment for 50 kHz loading. The numerical results presented investigate effects of material uncertainties on high frequency modes. A study is performed on the usage of different beam theories and their uncertain responses due to dynamic impulse load. These studies show that even for a small coefficient of variation, significant changes in the above parameters are noticed. A number of interesting results are presented, showing the true effects of uncertainty response due to dynamic impulse load.

1. Introduction

In the last few years, we have witnessed great improvement in the area of new material research. As a result there is a rapid growth in the use of lighter materials in aerospace and other major industries. These materials show significant variation in material properties and as a result, create a variety of structural problems in which the uncertainties in these properties play a major part in design. Uncertainties may exist in the characteristics of the structure itself and in the environment to which the structure is exposed [Vinckenroy and De Wilde 1995]. The lack of knowledge of material properties and their behaviors can be categorized as the first type of uncertainty. The other type of uncertainty is due to the change in the load and support condition with the change in environmental variables such as temperature and pressure. Another important aspect, when considering the sources of uncertainties, is the modeling technique. In this context, when the variability is large, we can find in the literature that the probabilistic models are more advantageous than the deterministic ones. In probabilistic methods, uncertainty in the parameters is considered and is represented by a random variable or random field. Development in the field of computers has revolutionized the status of research in this area [Li and Chen 2006]. In many cases of structural design, with the availability of computational tools such as Monte Carlo simulations, uncertainty analysis is incorporated in the design phase of the structures.

Keywords: MCS, SEM, normal distribution, Weibull distribution, extreme value distribution, wavenumber, group speeds.
Work supported by the Boeing Aircraft Company (Chicago, IL). The authors are thankful to Mr. Edward White of Boeing for valuable suggestions.

One of the major divisions in the field of probabilistic methods in mechanics is between statistical and nonstatistical approaches [Liu et al. 1986a]. Direct Monte Carlo simulation (MCS), which involves sampling and estimation, is an example of a frequently used statistical approach; the theory of MCS is explained in [James 1980; Decker 1991; Schueller 2001]. Techniques like the random perturbation method, orthogonal polynomial expansion methods, and numerical integration come under the category of nonstatistical schemes [Li and Chen 2006]. Nonstatistical methods do not need prior knowledge about the multivariate distribution of the stochastic parameters. Because of their simplicity and low computational effort, perturbation techniques are used along with the stochastic finite element method (PSFEM) in many problems in static and dynamic elastic analysis, composite ply failure problems, inelastic deformation studies, analysis of free vibration of composite cantilevers, and nonlinear dynamics [Kleiber and Hien 1992]. The simplicity and low computational cost makes PSFEM advantageous. However, in this approach, because of the use of Taylor series expansion for the approximation of the structural response, accurate results are expected only for the case of low variability of the parameters and for nearly linear problems. The method of orthogonal expansion is also used widely for a variety of structural problems [Ghanem and Spanos 2003]. In this method, the accuracy is highly influenced by the variability of parameters and the linearity of the problem. From the literature [Liu et al. 1986a; Liu et al. 1986b; Li and Chen 2006], we see the inability of the nonstatistical approaches to handle large variances of the random variables when compared with their mean values. Usually, the maximum bound set for the coefficient of variation (COV) is 10%. However, some researchers [Ang and Tang 1975; Liu et al. 1986b] have shown that acceptable results can be obtained even if the COV is as high as 20%. The Monte Carlo method is a versatile approach, which can be applied easily to any complex problem whose deterministic solution is known [Shinozuka 1972; Spanos and Zeldin 1998; Lepage 2006]. This method is commonly used for the prediction of the eigenvalues of structures [Lepage 2006]. The Monte Carlo method can be coupled with the finite element method with only slight modification in the parent code. Here the results converge to the correct solution as the number of simulations becomes large and hence the method becomes computationally expensive. Monte Carlo solutions are usually used as reference solutions on account of the absence of inherent assumptions [Cecchi and Sab 2009]. In some literature the Monte Carlo method is used along with other methods to reduce computational time. A compatible blend of the Neumann expansion with MCS has been found to work efficiently for computation of stochastic structural response [Bhattacharyya and Chakraborty 2002]. There are also many methods of sampling available in the literature to improve the accuracy and the efficiency of Monte Carlo methods [Lepage 2006; Stefanou 2009].

In the area of structural health monitoring, wave propagation responses, which are very sensitive to small stiffness changes, are used effectively to detect small defects, such as delamination, cracks, et cetera, in structures [Nag et al. 2003; Ostachowicz 2005; Gopalakrishnan et al. 2008]. However, structures made from common structural materials exhibit large variation in material properties. The response to dynamic loading shows significant changes in responses compared to the deterministic value. The presence of damage causes stiffness reduction, which causes a shift in the natural frequencies, especially at high frequencies [Pardoen 1989]. Variation in the material properties also shifts the natural frequencies and the modal amplitudes. Without a proper uncertain dynamic analysis, these shifts in natural frequencies can be misunderstood as being caused by the presence of structural damage. The deterministic wave propagation analysis in such cases will give results which may be misleading. Hence, a detailed study on the effect of variation in the different structural parameters on the structural response, for a high

frequency impact load, is required to bring greater clarity to the interpretation of the obtained results. However, to the author's best knowledge not much work has been done in the area of uncertainties in wave propagation in structures. Also, high frequency response analysis using the conventional finite element method is computationally expensive since the maximum possible size of the finite element depends on the wavelength of the propagating wave [Horr and Safi 2003; Gopalakrishnan et al. 2008]. Consequently, some of the current literature on the high frequency analysis of structural response uses the spectral finite element method (SEM) [Gopalakrishnan et al. 2008], which combines the accuracy of conventional spectral methods and the geometric flexibility of finite element methods. Unlike the spectral methods in PSFEM, the solution from SEM is exact in most of the deterministic case [Doyle 1997; Gopalakrishnan et al. 2008]. Also SEM, due to its ability to model the inertial distribution of the structure accurately, requires a very small system size to model and obtain deterministic responses, especially for high frequency content loads. The speed of wave analysis using SEM depends on the total time window required to avoid the problems due to enforced periodicity; the time window can be adjusted by changing the time sampling rate or the number of FFT points. The increase in the group speed with frequency reduces the total time window needed for the analysis, which further reduces the computational time. However, in conventional FEM, the requirement that the size of the element be comparable with the wavelength makes the problem size so large that it becomes computationally prohibitive, especially in the context of uncertainty analysis. Large computational times are the major restricting factor for researchers in performing high frequency wave propagation analysis in an uncertain environment. In this context the reduction in computational time of SEM and the large increase in its computational efficiency over conventional FEM with increase in frequency is a very relevant fact, and still an unexplored area of research. Incorporating MCS under SEM is straightforward. Due to its very small size, incorporation of MCS under SEM, unlike conventional FEM, can no longer be considered a luxury from the computational viewpoint. MCS under SEM can be part of the design. The versatility of the Monte Carlo approach and the time aspect of SEM are the major factors which paved the way for the union of these two approaches. This will help researchers to save an immense amount of computational time, especially in the field of uncertain wave propagation analysis.

The paper is organized as follows. In Section 2, a brief description of conventional SEM is given, which is followed by the brief description of MCS and the implementation of SEM under MCS. Section 3 details numerical examples. First we conduct a study on the effects of uncertainties on the time domain responses. Then the computational superiority of SEM under MCS, as opposed to conventional FEM under MCS, is established. Then uncertainty analysis is performed for the frequency response functions. In Section 4A we analyze the variation of time of arrival of first reflection with uncertainty, which is followed by a study of the effect of loading frequency (for a tone-burst signal) on the uncertain responses and a detailed study on spectrum relations. It is well known that the inclusion of higher-order effects dramatically changes the deterministic response in an elementary beam and rod. Hence, a small subsection is included on the effects of different beam and rod theories on the uncertain responses. In all cases, both the Young's modulus and density of structure are considered as uncertain, with their statistical distributions assumed as normal, Weibull, and extreme value distributions. In addition, in most cases both axial and bending responses are considered to study the effects of uncertainties, where the load histories considered are broad-band triangular loading and narrow-band, modulated tone-burst loading. We present some interesting results on the input and output distributions of these parameters.

2. The spectral finite element method

In the spectral element approach, the actual response is synthesized by a prudent combination of many infinitely long wave trains of different periods (or frequencies). Thus the governing equations are first converted to the frequency domain using discrete Fourier transforms and solved. The last step of the analysis involves performing an inverse Fourier transform to reconstruct the signal to obtain the time domain responses. In SEM, the stiffness matrix is established in the frequency domain, which is the main difference between it and conventional FEM. Also in contrast to conventional FEM, the spectral elements can span all the way from one joint. Hence, SEM yields system sizes many orders smaller than for conventional FEM. More details of this approach are given in [Gopalakrishnan et al. 2008]. In this section, we briefly discuss the formulation of spectral rod and beam element formulation. In the case of beams, we provide the formulation of both Euler–Bernoulli and Timoshenko beam, although only the Timoshenko beam model is used in all simulations.

For a rod [Gopalakrishnan et al. 2008], the governing partial differential equation is

$$EA\frac{\partial^2 u}{\partial x^2} - \rho A\frac{\partial^2 u}{\partial t^2} = 0, \tag{2-1}$$

where $u(x,t)$ is the axial displacement, ρ the density, E the Young's modulus, and A the cross sectional area. In SEM the common procedure is to convert this governing partial differential equation to the frequency domain and to solve the ordinary differential equations so obtained. This is a discrete Fourier transform (DFT) based analysis of wave propagation, where the DFT is performed by a FFT algorithm, popularly known as a Cooley–Tukey algorithm [Doyle 1997; Gopalakrishnan et al. 2008]. The DFT of u is given as a solution in exponential form:

$$u(x,t) = \sum_{n=1}^{N} \hat{u}_n(x,\omega_n)e^{i\omega_n t}, \tag{2-2}$$

where $\hat{u}_n(x,\omega_n)$ is the transform of $u(x,t)$, N is the number of FFT points, and ω_n is the frequency at the n-th sampling point.

Substitution of (2-2) in (2-1) converts the governing PDE to an ODE:

$$\frac{\partial^2 \hat{u}_n}{\partial x^2} + k_n^2 \hat{u}_n = 0, \tag{2-3}$$

where k_n is the wavenumber, which is given by

$$k_n = \omega_n\sqrt{\frac{\rho A}{EA}}. \tag{2-4}$$

The nature of the wavenumber depends on the frequency, and tells about the type of wave generated by the medium. In the present case, the wavenumber varies linearly with the frequency and hence the waves are nondispersive, that is, they retain their shape as they propagate. The group speed of propagation is obtained from

$$C_g = \frac{d\omega}{dk} = \sqrt{\frac{E}{\rho}}. \tag{2-5}$$

The solution of (2-3) is given by

$$u(x,t) = \sum_{n=1}^{N} [Ae^{-ik_n x} + Be^{+ik_n(L-x)}]e^{i\omega_n t}. \tag{2-6}$$

SEM uses (2-6) as an interpolating function for finite element formulation. The procedure for element formulation, assembly, and solution is similar to that for finite elements and hence is not reported here.

In the case of beams we derive the spectral solution for Euler–Bernoulli beams. The governing equation is given by

$$EI\frac{\partial^4 w}{\partial x^4} = \rho A\frac{\partial^2 w}{\partial t^2}, \tag{2-7}$$

where $w(x,t)$ is the transverse displacement, EI is the flexural rigidity, ρ is the density, and A is the cross sectional area. Transforming (2-7) into the frequency domain using a DFT, we get

$$w(x,t) = \sum_{n=1}^{N} \hat{w}_n(x,\omega_n)e^{i\omega_n t}, \qquad \frac{d^4\hat{w}_n}{dx^4} + k_n^4 = 0, \quad k_n^2 = \sqrt{\frac{\omega_n^2\rho A}{EI}}. \tag{2-8}$$

$\hat{w}(x,\omega_n)$ is the transform of $w(x,t)$. We see that the wavenumber is a nonlinear function of frequency and hence the waves are highly dispersive. Hence the group speed C_g in the case of beams, unlike the case of rods, is a function of frequency, which is a characteristic of the most dispersive waves:

$$C_g = \frac{d\omega}{dk} = 2\sqrt{\omega_n}\left(\frac{EI}{\rho A}\right)^{1/4}. \tag{2-9}$$

Similarly, in Timoshenko beam theory the value of the wavenumber can be calculated from the transformed homogeneous differential equation in the frequency domain [Gopalakrishnan et al. 2008]:

$$GAK\left(\frac{d^2\hat{w}}{dx^2} - \frac{d\hat{\phi}}{dx}\right) + \rho A\omega_n^2\hat{w} = 0, \qquad EI\frac{d^2\hat{\phi}}{dx^2} + GAK\left(\frac{d^2\hat{w}}{dx^2} - \hat{\phi}\right) + \rho I\omega_n^2\hat{\phi} = 0, \tag{2-10}$$

and the boundary conditions

$$(\hat{w}) \text{ or } \left(\hat{V} = GAK\left(\frac{\partial\hat{w}}{\partial x} - \hat{\phi}\right)\right), \qquad (\hat{\phi}) \text{ or } \left(\hat{M} = EI\frac{\partial\hat{\phi}}{\partial x}\right), \tag{2-11}$$

where $\hat{w}(x,\omega_n)$ is the transform of transverse displacement, $\hat{\phi}(x,\omega_n)$ is the transform of slope, G is the modulus of rigidity, A is the cross sectional area, I is the moment of inertia, ω_n is the frequency at the n-th sampling point, ρ is the density, E is the Young's modulus, $\hat{V}(x,\omega_n)$ is the transform of shear force, $\hat{M}(x,\omega_n)$ is the transform of the bending moment, and K is the shear correction factor (K is assumed to have value 0.86 as in [Gopalakrishnan et al. 2008]. Thus from the homogeneous differential equations and the boundary condition we arrive at the characteristic equation for wavenumber computation:

$$[GAKEI]k^4 - [GAK\rho I\omega_n^2 + EI\rho A\omega_n^2]k^2 + [\rho I\omega_n^2 - GAK]\rho A\omega_n^2 = 0. \tag{2-12}$$

Since the equation is of fourth order, we have four solutions for the wavenumber. The second wavenumber, which is associated with shear deformation, is evanescent to start with and becomes propagating at some high frequencies. The frequency at which this happens is called the cutoff frequency,

which is obtained by setting the last term in (2-12) to zero:

$$\omega_c = \sqrt{\frac{GAK}{\rho I}}. \tag{2-13}$$

Elementary beam equations can be obtained by setting GAK to infinity and ρI to zero. Then the complete solution can be written in the form

$$v(x,t) = \sum \left(R_1 e^{-ik_1 x} + R_2 e^{-ik_2 x} - R_1 e^{-ik_1(L-x)} - R_2 e^{-ik_2(L-x)}\right) e^{i\omega_n t}, \tag{2-14}$$

$$\phi(x,t) = \sum \left(A e^{-ik_1 x} + B e^{-ik_2 x} + C e^{-ik_1(L-x)} + D e^{-ik_2(L-x)}\right) e^{i\omega_n t}. \tag{2-15}$$

A, B, C, and D are coefficients determined from the boundary conditions and the R_i are the amplitude ratios given in [Gopalakrishnan et al. 2008]:

$$R_i = \frac{ik_i GAK}{GAKk_i^2 - \rho A\omega_n^2}. \tag{2-16}$$

Note that the Euler–Bernoulli beam predicts unrealistic speeds at higher frequencies. When the beams are thick, the effects of shear are significant, converting the evanescent mode of the Euler–Bernoulli beam to a shear propagating at high frequency. If this mode is not represented properly, then it will lead to erroneous description of the dynamics of the beam. Hence all simulations in the paper are carried out using the Timoshenko beam model.

In the case of the higher-order rod model, in addition to axial deformation, we add the lateral motion through a term associated with the Poisson's contraction. This theory, called Mindlin–Hermann theory, was first formulated for circular cross sections in Mindlin and Herrmann [1952] and later extended to rectangular cross sections in Martin et al. [1994], for metallic structures. The details of the element formulation, wavenumber, and the group speed computation are given in [Martin et al. 1994]. Here, for the sake of completeness, we provide the characteristic equation for computation of the wavenumber:

$$\begin{aligned}\left(2G(1+\bar{\nu})K_1 GI\right)k^4 - \left((2GA)^2(1+2\bar{\nu}) - 2GA(1+\bar{\nu})K_2\rho I\omega_n^2 - K_1 GI\rho A\omega_n^2\right)k^2 \\ + \left(\rho I K_2 \rho I\omega_n^4 - 2GA(1+\bar{\nu})K_2\rho I\omega_n^2\right) = 0,\end{aligned} \tag{2-17}$$

where $\bar{\nu}$ is the effective Poisson's ratio,

$$\bar{\nu} = \frac{\nu}{1-\nu} \tag{2-18}$$

for plane stress problems and

$$\bar{\nu} = \frac{\nu}{1-\nu^2} \tag{2-19}$$

for plane strain problems, where ν is the Poisson's ratio. K_1 and K_2 are correction factors intended to compensate for the approximate form of the displacement field. In this study K_1 and K_2 are assumed to have values 1.2 and 1.75 as in [Martin et al. 1994].

Unlike the elementary rod, the wavenumber is highly dispersive, especially at high frequencies. The lateral contraction mode becomes propagating only at high frequencies. The cutoff frequency occurs at

$$\omega_c = \sqrt{\frac{2GA(1+\bar{\nu})}{\rho I K_2}}. \tag{2-20}$$

3. MCS under SEM

MCS is capable of giving accurate solutions for any problems whose deterministic solution is known, since it statistically converges to the correct solution provided that a large number of simulations are employed. In direct MCS, the procedure starts with the generation of sampling of the input parameters according to their probability distributions and correlations. For each input sample, a deterministic spectral finite element analysis is performed, giving an output sample. Finally, a response sampling is obtained, from which the mean and the standard deviation of the response can be obtained.

The estimator of the response $\bar{y}$ is defined in [Lepage 2006]:

$$\bar{y} = \frac{1}{n}\sum_{i=1}^{n} y_i, \tag{3-1}$$

where n is the number of samples and y_i is the response corresponding to the i-th input sample.

$$E[\bar{y}] = \mu_y \tag{3-2}$$

and

$$\operatorname{var}(\bar{y}) = E[(\bar{y} - E[\bar{y}])^2] = \frac{\sigma_y^2}{n}, \tag{3-3}$$

where $E[\bar{y}]$ and $\operatorname{var}(\bar{y})$ are the expected value (first moment) and variance (second moment) of the random variable and $\mu_y = E[y]$ and $\sigma_y^2 = E[(y - \mu_y)^2]$ denote the unknown mean and variance of the response. In most of the uncertainty analysis the scatter of the distribution is measured in terms of a parameter, the coefficient of variation (COV), which is the ratio of the square root of the variance of the samples to the mean of the samples. The square root of the variance is also called the standard deviation. In this study, we use the COV as a measure of the scatter of the distribution, is COV. COV of an output parameter can also be used to measure the sensitivity of the input parameter by computing the ratio of output COV to input COV. Many such studies are carried out in this paper by considering wave parameters such as wavenumber, speed, cutoff frequency, et cetera, as output parameters and then investigating sensitivity to the material properties.

In wave propagation analysis, this y can be the transform of the time response of axial and transverse velocity, frequency response functions (FRF), wavenumber, group speed, et cetera. Each value of y_i is obtained using deterministic spectral finite element code or by conventional finite element code (for the comparative study) each time.

4. Numerical results and discussions

There are many factors that govern the wave propagation response in a structure. Some of the key factors are the wavenumber, the group speeds, and the natural frequency of vibration and phase information. All the factors depend on the material properties of the medium in which these waves propagate. Since the material properties in this study are considered uncertain, one can expect substantial changes in the wave responses as compared to the deterministic responses. Hence, the aim of this section is to bring in the effects of uncertainty in the material properties on the wavenumbers, group speeds, and natural frequency of the system. The uncertain responses are shown in the form of time histories of velocities, the FRF, or the probability density distribution, in order to bring out clearly the effect of uncertainty in

these parameters. Both broad-band and modulated high frequency tone-burst loading is considered in this study. In particular, the effect of loading frequency on the uncertain response is investigated.

Last but not least, the effect of using higher-order theories on the uncertain response is investigated. It is quite well known [Gopalakrishnan et al. 2008] that higher-order effects in rods and beams manifest themselves in such a manner that introduces the cutoff frequency in the higher-order wave modes, which propagates beyond the cutoff frequency. The cutoff frequency depends on the material properties and geometric properties and occurs at high frequencies. If this cutoff frequency occurs at a frequency which is beyond the point of interest, one can still use the elementary beam model for the analysis. Uncertainty in material properties, geometric properties, or both, can affect its value. Hence, a detailed uncertainty analysis is required, which is undertaken in this section. Here, each result is obtained by the method of MCS coupled with SEM, as discussed in the previous section. In this work the uncertainty is modeled by representing the uncertain parameters by a random variable and by different probability distribution functions to compare the pattern of distribution of the output parameters. Here, the input random variables are created using MATLAB expressions for creating random variables. The spectral elements used for the metallic beams and rods are similar to the type found in [Gopalakrishnan et al. 2008].

First a study of the effect of axial and transverse response of the metallic beam is performed, comparing between conventional FEM and SEM, for a normal distribution and for different COVs of the Young's modulus and the density. Then, variation in the frequency responses, speed, and wavenumber are also analyzed to investigate the variation of these output parameters as discussed previously.

4A. ***Effect of uncertainty on velocity time histories.*** In this study, we consider a cantilever metallic beam 1 m in length with a rectangular cross section of 10 mm$\times$10 mm. The beam is modeled using a single Timoshenko beam and elementary rod in the SEM case, while 200 one-dimensional beam and rod elements are used in the case of conventional FEM. The deterministic values of the Young's modulus and density are 70 GPa and 2700 kg/m^3 respectively. The objective here is twofold: first we will compare the axial and flexural responses predicted by conventional FEM and SEM to validate the latter; second, we will quantify the responses' changes due to material uncertainties. For the FEM and SEM comparison, we assume only the Young's modulus as uncertain, with a normal distribution. Ten thousand randomly generated samples of the Young's modulus are used in the simulation. In most of the uncertainty analysis, the mean of a parameter obtained from the simulated data should converge to a constant value. This requires a large number of samples; from our study we found that 10,000 samples are required to satisfy this condition. For comparison of the SEM and FEM solutions, two different inputs are used: Figure 1a shows a broad-band loading situation, whose FFT gives a frequency content of 20 kHz. This pulse is used in the case of axial wave propagation. Flexural waves are highly dispersive in nature. This is due to the dependence of the group speeds of the waves on the frequency. One of the ways to make a signal travel nondispersively in a beam is to use a tone-burst modulated pulse, shown in Figure 1b, modulated at a 5 kHz frequency. The FFT of the pulse, shown in the inset of the figure, has significant energy only at 5 kHz, and hence the waves travel at a speed corresponding to 5 kHz. We use this pulse for flexural wave propagation. First we consider the Young's modulus as a random variable and MCS is performed both under conventional FEM and SEM environments using 10,000 samples. Here, in each figure, "min" and "max" signify the minimum and maximum values of the time of arrival of the first reflection obtained through MCS and "det" the value when the material properties are deterministic. Figures 2a and 2b

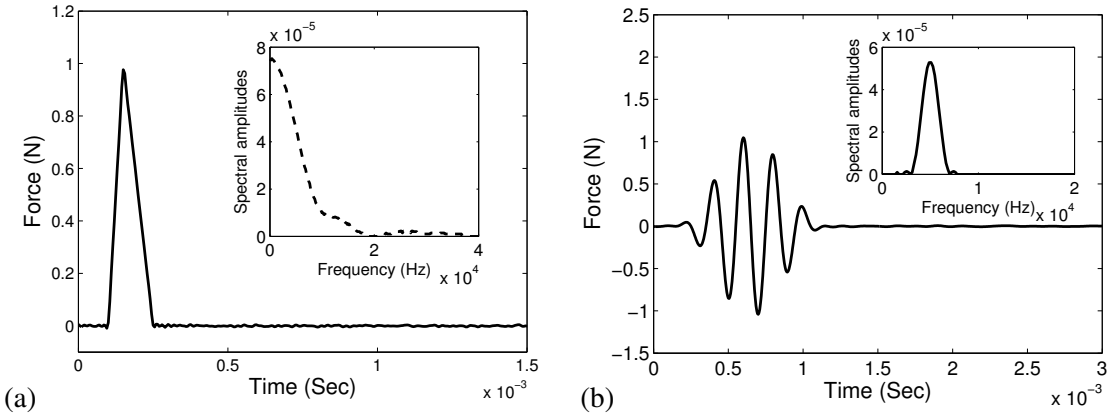

Figure 1. Input force used in simulation: (a) broad-band pulse and (b) narrow band modulated (at 5 kHz) pulse.

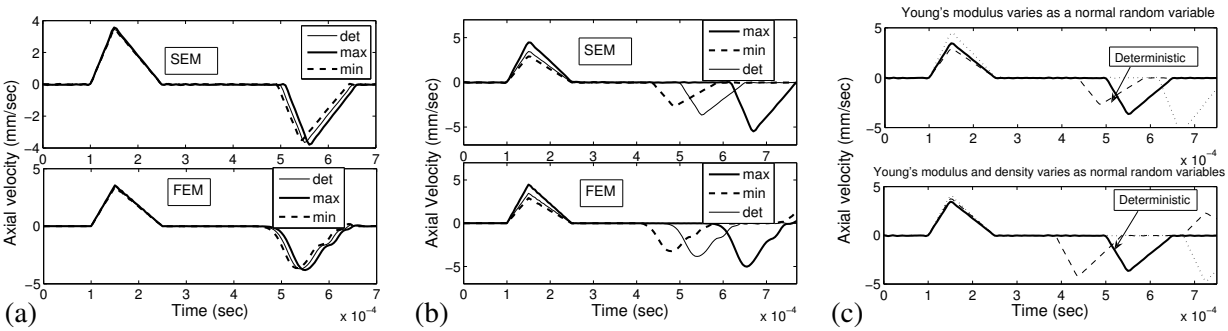

Figure 2. Axial velocity responses: (a) uncertain Young's modulus with COV 1%, (b) uncertain Young's modulus with COV 10%, and (c) uncertain Young's modulus and density with COV 10%.

show the axial velocity histories obtained with input parameters COV 1% and 10% respectively. Two things are quite apparent from the figure. First the predictions made by MCS under FEM and SEM match very well. The second is that if the COV is small, the uncertain response does not deviate much compared to the deterministic response. Since the group speed of the medium depends on the material properties, uncertainty in material properties can cause changes in the predicted group speeds, which can be quantified by looking at the time of arrival of the first reflection. From Figure 2b, it is clear that the total scatter in the time of arrival of the first reflection is 15%, compared to its value in the deterministic case, for a COV of 10%, which in terms of speed will be around 2000 m/s. There is a significant increase in group speed introduced by uncertainties in material properties.

Figures 3a and 3b show the flexural responses obtained through MCS under FEM and SEM as a function of COV. As in the case of axial waves, the FEM and SEM predictions match well. Unlike in the case of axial wave propagation, for larger COVs the scatters induced in the flexural group speeds are not that significant. Next, both Young's modulus and density are made uncertain and we assume a normal distribution for both these parameters. Figures 2c and 3d show, respectively, the axial and transverse velocity histories for the case of 10% COV, obtained through SEM. From these figures, it

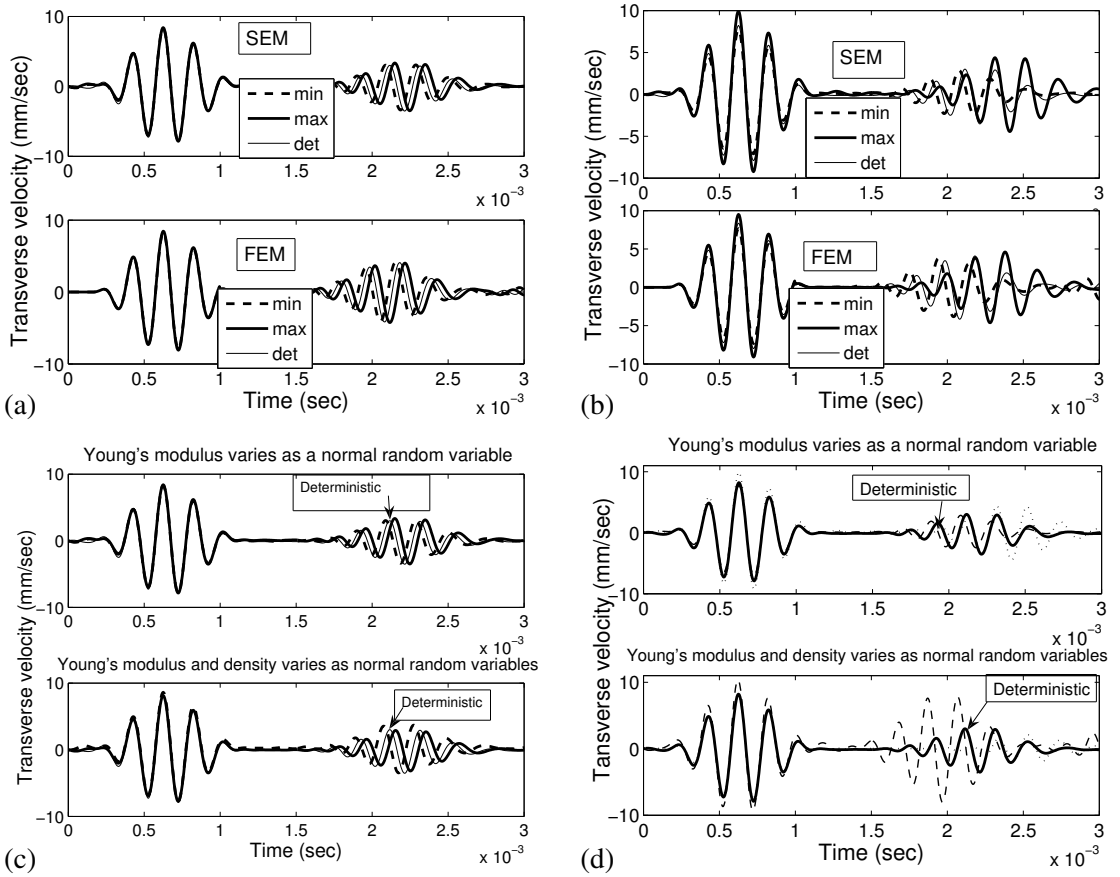

Figure 3. Transverse velocity responses: (a) uncertain Young's modulus with COV 1%, (b) uncertain Young's modulus with COV 10%, (c) uncertain Young's modulus and density with COV 1%, and (d) uncertain Young's modulus and density with COV 10%.

is clear that significant changes in the group speeds are introduced both in the axial and flexural cases, where the total scatters in axial and flexural speeds are about 25% and 20%, respectively when compared to the deterministic responses. In terms of speed, this change amounts to changes in group speeds of 3450 m/s and 350 m/s for the axial and flexural cases, respectively. Figure 3c is the flexural response for a case of COV 1%, from which it can be concluded that the variation in the time responses with the change in the number of input random variables from one to two is significantly less when the COVs of the input parameters are less. In summary, uncertainty in material parameters increases the total scatter in the group speeds. If the modulus alone is uncertain, then the flexural group speeds do not change significantly. However, when both the density and modulus are uncertain, flexural group speeds show a total scatter of nearly 20% with 10% COV in the input parameters. The variation in the time responses with the change in the number of input random variables from one to two is significantly less when the COVs of the input parameters are less.

4B. ***Comparison of efficiency of FEM and SEM using MCS.*** Here, to determine the efficiency of SEM under MCS, the same cantilever beam of the previous example is considered. The beam is modeled as a

single Timoshenko beam. Two different tone-burst loadings, one which samples at 5 kHz and the other at 50 kHz, are used for the study. Figure 4a shows the bending wave speed superimposed on the FFT spectrum of 5 kHz and 50 kHz loading. The 5 kHz load will travel at 1400 m/s while the 50 kHz pulse will travel at 1900 m/s, according to the figure. This means the 50 kHz pulse will travel faster than the 5 kHz loading. Hence, the reflection will arrive earlier under 50 kHz loading, which manifests itself in having a smaller time window compared to the 5 kHz loading. In other words, 50 kHz tone-burst loading needs a smaller time window, which means a smaller number of FFT points, compared to 5 kHz tone-burst loading. Hence, we can expect faster SEM solutions for 50 kHz loading than for 5 kHz loading.

In conventional FEM, when the frequency increases, the wavelength decreases; conventional FEM mandates that the element length should be comparable to its wavelength [Chakraborty and Gopalakrishnan 2004], and typically 6–10 elements should span a wavelength. Hence, increase in loading frequency, increases the problem size in conventional FEM, which will certainly increase the analysis time. This is quite different than the SEM solution. In the present case, increase in the frequency from 5 kHz to 50 kHz

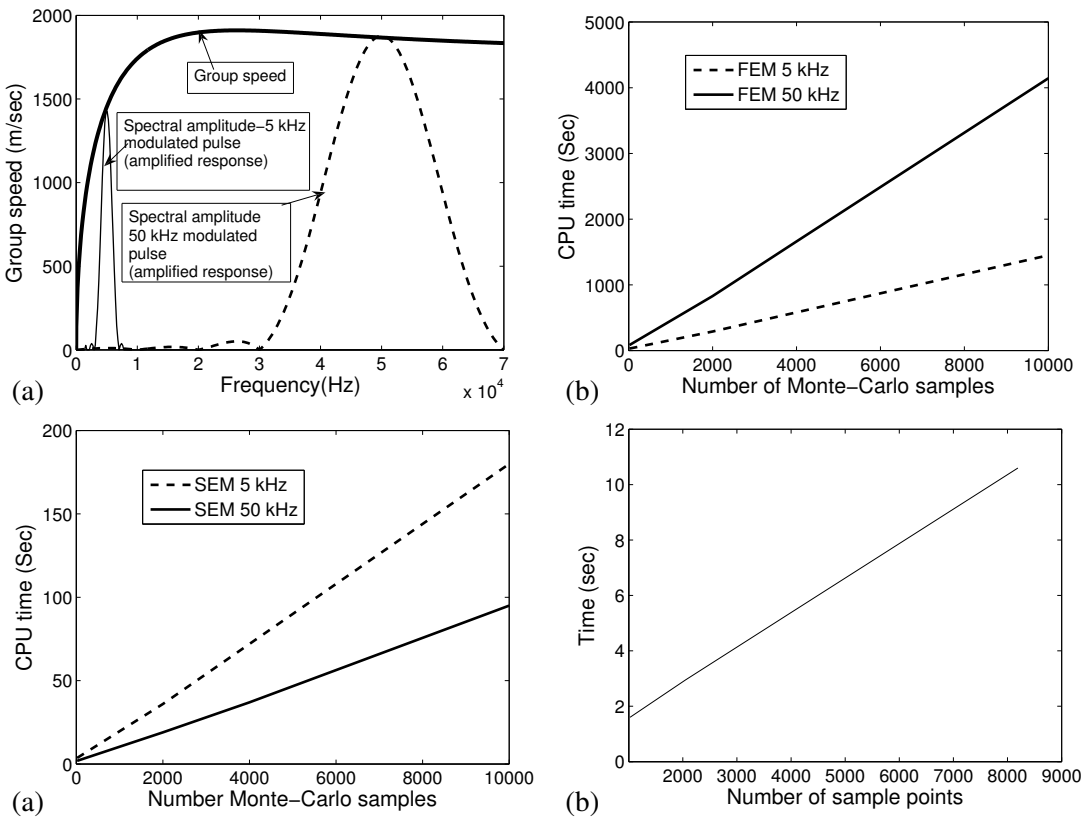

Figure 4. (a) Dispersion plot (bending group speed) of the beam, where the spectral amplitudes (amplitudes are amplified) of 5 kHz and 50 kHz tone-burst signals are superimposed onto it; CPU time as a function of the number of samples for different tone-burst signal frequencies (5 kHz and 50 kHz) with (b) FEM (c) SEM and (d) SEM for different numbers of FFT points for 100 samples.

increases the number of conventional elements required from 200 to 600 elements. Figures 4b and 4c compare the time taken by the MCS under FEM and SEM as a function of number of samples, for the transverse velocity response of a cantilever beam, using two different tone-burst signals. In SEM, a time sampling rate of 5 μs with 1024 FFT points is used for a 5 kHz signal loading; only 512 FFT samples are used for a 50 kHz load. For the conventional FEM we use 200 one-dimensional beam elements for a tone-burst pulse of modulated frequency 5 kHz, and 600 elements for a tone-burst pulse of frequency 50 kHz. Only the Young's modulus is assumed as a random variable; the randomness is modeled as normal distribution. From these figures, we can clearly see that SEM is faster than conventional FEM for both loadings. SEM is 8 times faster for 5 kHz loading and takes less than 200 seconds to compute the responses. The factor increases from 8 to 48 when the frequency content of the load is 50 kHz. Hence, using MCS under SEM cannot be thought of as a luxury.

One of the problems associated with SEM is that it cannot handle finite small dimension structures, which is due to enforced periodicity in the frequency domain used in the DFT. The enforced periodicity causes the responses to wrap around due to its inability to damp out all the responses within the chosen time window. To overcome this, we need to enlarge the time window, which can be done by increasing the time sampling rate, increasing the number of FFT points, or both. In the present case, for a 100 sample MCS simulation, the time taken by SEM as a function of the number of FFT points is shown in Figure 4d. The CPU time variation is linear and quite small. In summary SEM performs the simulations faster than conventional FEM, increasing with the increase in the frequency content of the load.

4C. ***Effect of variation on natural frequencies and modal amplitudes.*** Natural frequencies are functions of the material properties. If these properties are uncertain, then we will see significant variation in the responses predicted by the analysis. In particular, the shift in the natural frequency is used as a way to assess the presence of damage in the structure. There is difficulty in distinguishing the shift in the natural frequency due to damage with the shift in frequency due to material uncertainties, which makes it necessary to perform a detailed uncertainty analysis. SEM directly gives the FRF as a by-product, a plot of which will provide us with insight on how the frequencies are shifting due to material uncertainties.

We first consider a single elementary rod SEM model, fixed at one end. In the first case we consider the Young's modulus alone as uncertain, with its mean value at 70 GPa, and more than 10,000 samples are used in the MCS. In this study we assume only a normal distribution for all the input random variables. Figure 5a shows the FRF for a rod for 1% and 10% COV in the input parameter, the Young's modulus. For 1% COV the shifts in the first three modes are very small; thereafter, there is some increase in the shift. All modes exhibit negligible change in their modal amplitudes. This is also typical behavior of a metallic beam with small cracks. If the COV is increased to 10%, then the fundamental axial modes also change and the shifts in the second and higher frequencies are quite substantial. The changes in modal amplitudes are also significant.

Next, we plot the FRF for axial loading, when both the Young's modulus and density are considered random, as a function of increasing percentage of COV. This is shown in Figure 5b. The notable feature here is that even though the shift in the natural frequency increases drastically the modal amplitudes change little from their deterministic values.

Figures 6a and 6b show the beam FRF, which is modeled as a single Timoshenko beam for the cases of the Young's modulus being random and both the Young's modulus and density being random, respectively.

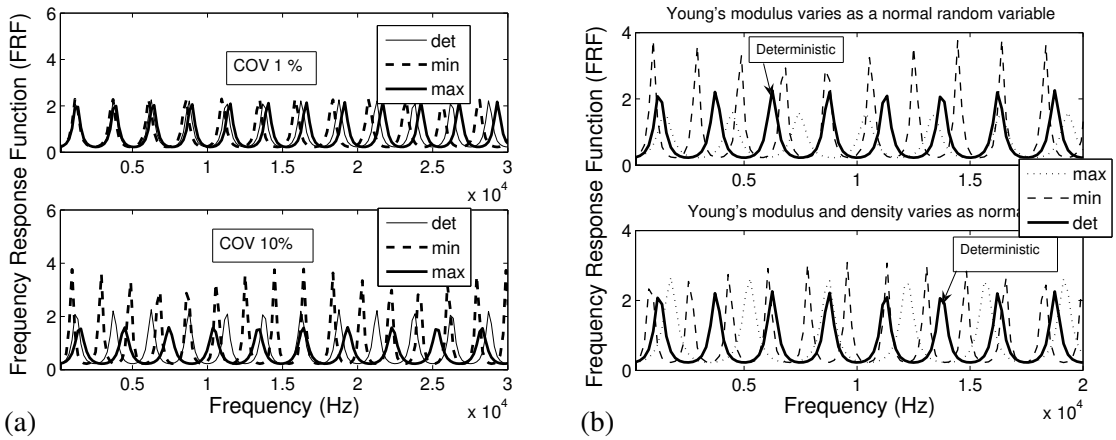

Figure 5. FRF of axial modes for 1% and 10% COV: (a) the Young's modulus is uncertain and (b) both the Young's modulus and density are uncertain (COV 10%).

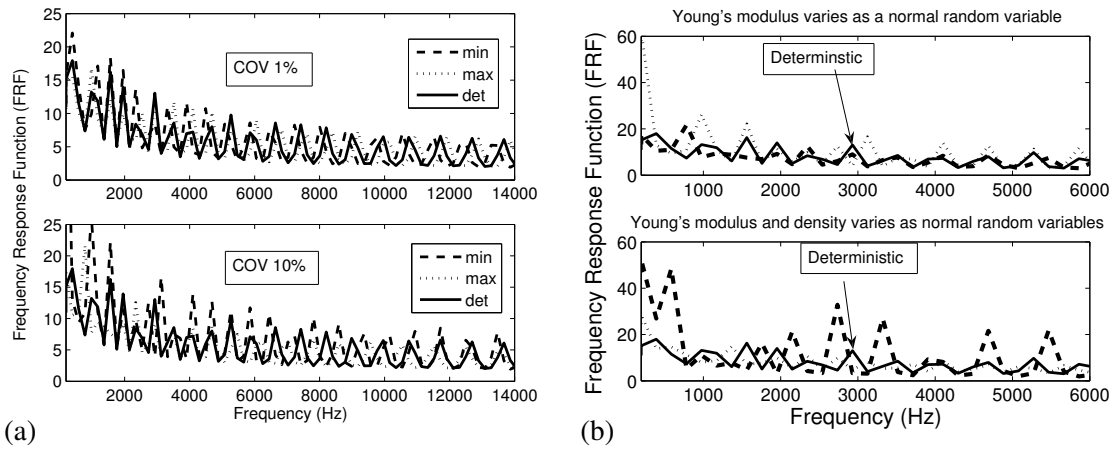

Figure 6. FRF of flexural modes for 1% and 10% COV: (a) the Young's modulus is uncertain and (b) both the Young's modulus and the density are uncertain (COV 10%).

For the case of a random Young's modulus, with 1% COV, as in the case of the rods, there is not much shift in the lower modes. Here, in the case of a beam model, the changes in the fundamental modes and the modal amplitude with the increase in COV to 10% is observed, as in the case of a rod. Figure 6b shows the FRF when both the Young's modulus and density are uncertain for a COV of 10%. When compared to the FRF with only the Young's modulus uncertain, significant shifts are visible for the natural frequencies. However, the modal amplitudes nearly double for most of the modes.

In summary, the frequency shifts for a small COV for both the axial and flexural modes are very small for lower-order modes, while the higher modes exhibit significant shifts. A higher COV not only shows a higher shift for the entire natural frequency spectrum, but also shows higher modal amplitudes.

4D. ***Distribution of time of arrival of first reflection.*** In Section 4A, we showed that the material uncertainties significantly changed the group speeds, where the group speed effects are quantified by computing

the speeds using the time of arrival of the first reflection. In this section, we would like to quantify the group speed changes in terms of the distribution of the time of arrival of the first reflection for two different input material property distributions, namely the normal and extreme value distributions. The extreme value type I distribution based on the smallest extreme values is used in this study, also referred to as the Gumbel distribution. In this case, only a flexural response is considered, where the cantilever beam is modeled as a single Timoshenko element subjected to a point impact load (see Figure 1). As before, 10,000 samples are used in the MCS. The objective here is, for an input COV of material variation, to determine the COV of time of arrival of first reflection.

In each figure, the label "Monte" means that the actual histogram from MCS, while "Normal" and "Extreme" indicate the ideal normal and extreme value distributions with the sample mean and standard deviations obtained from the simulated data. Figure 7 shows the distribution of the time of arrival of the first reflection for two different distributions of the Young's modulus with a COV of 10%. Here, density is assumed to be deterministic. The different input distributions predict similar COVs (about 2.9%) for the output. Next, we assume both the density and Young's modulus as uncertain; these distributions are modeled by normal and extreme value distributions with a COV of 10%. As in the previous case, the COV remains constant (around 3.9%) for the different distributions (Figure 8). For the different distributions, we see that the maximum and minimum limits of the output distribution are not significantly different. In summary, different distribution of material uncertainty does not significantly alter the total bound of variation of the group speed.

4E. ***Effect of loading frequency in time responses with uncertain material properties.*** A tone-burst modulated signal (Figure 1b) is normally used in structural health monitoring studies to detect the presence of cracks in structures since it travels nondispersively. These signals are modulated at certain frequencies, which depend on size of cracks, that is, the smaller the damage, the larger the value of the modulated frequency. The aim of this subsection is to understand and estimate the extend of the shift in the arrival of first reflection that is caused by material uncertainty for an increasing value of loading frequency. In health monitoring studies, this aspect is very critical in order to distinguish clearly the shift in the arrival of first reflection caused by the damage with that caused by the material uncertainties.

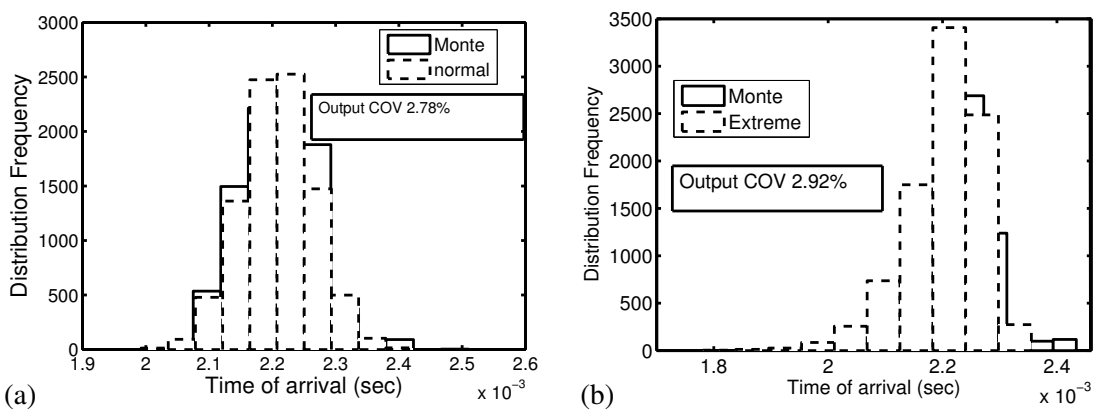

Figure 7. Histogram of distribution of time of arrival of first reflection, Young's modulus with an input COV 10% for different distributions: (a) normal and (b) extreme value.

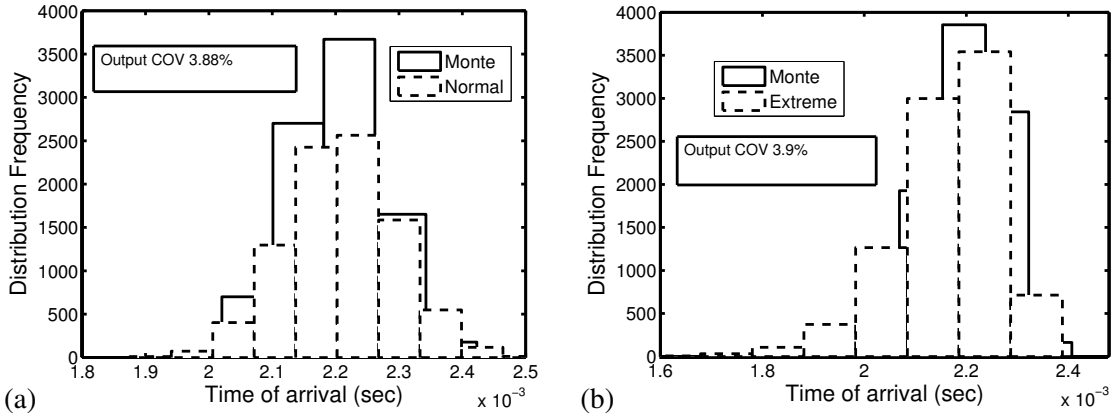

Figure 8. Histogram of distribution of time of arrival for first reflection with uncertain Young's modulus and density with a COV of 10% for different distributions: (a) normal and (b) extreme value.

We again model the same cantilever beam of the previous section with a single Timoshenko beam model and subject this beam to a tone-burst signal (Figure 1b), whose modulated frequencies are varied from 5 kHz to 50 kHz. In each case, results were obtained considering the Young's modulus as uncertain and both the Young's modulus and density as uncertain. In both these cases the COV was fixed at 10%. Figures 9a and 9b show the velocity history responses for frequencies of 20 kHz and 50 kHz, respectively. As in the earlier studies, in both cases the shift in the arrival of the first reflection is maximum when both the Young's modulus and density are uncertain. For 20 kHz loading, the variation in the group speed is about 720 m/s. This variation decreased to 660 m/s for 50 kHz loading. When we quantify these variations in group speed in terms of the percentage of its deterministic value, we can see an increase in the variation of group speed from 27% to 35.5% with the increase in the loading from 5 kHz to 20 kHz. However, for loading with a frequency of 50 kHz, the variation in group speed is about 35.5%. Beyond 50 kHz, we notice no further appreciable change in the group speed. Hence, in health monitoring studies, it is always necessary to use signals modulated at frequencies beyond 50 kHz, if the structure is uncertain, so that the shift in the reflected pulse due to material uncertainties can be factored into the damage location computation.

4F. ***Wavenumber COV for different material property distributions.*** Generally in wave analysis, the wavenumber, which acts as a scale factor on the position variable in the same way that the frequency acts on the time (Equations (2-6), (2-14), and (2-15)), and its variation with frequency are a major areas of study. Uncertainty in the material parameters scatters waves that are very different from the deterministic beam. This scatter will be quite different in the presence of flaws such as cracks, especially when the parameters are uncertain. Two parameters that will help us to differentiate the scattering of waves due to material uncertainties and damage are the wavenumber and group speed of waves. In the application of wave propagation analysis for structural health monitoring, the time of arrival of the first reflection is an important parameter, which directly depends on the group speed of the structure. However, we know that there is a direct relation between wavenumber and group speed, given in (2-5). It is essential to study the variation of wavenumber with the variability of the material properties, which will actually

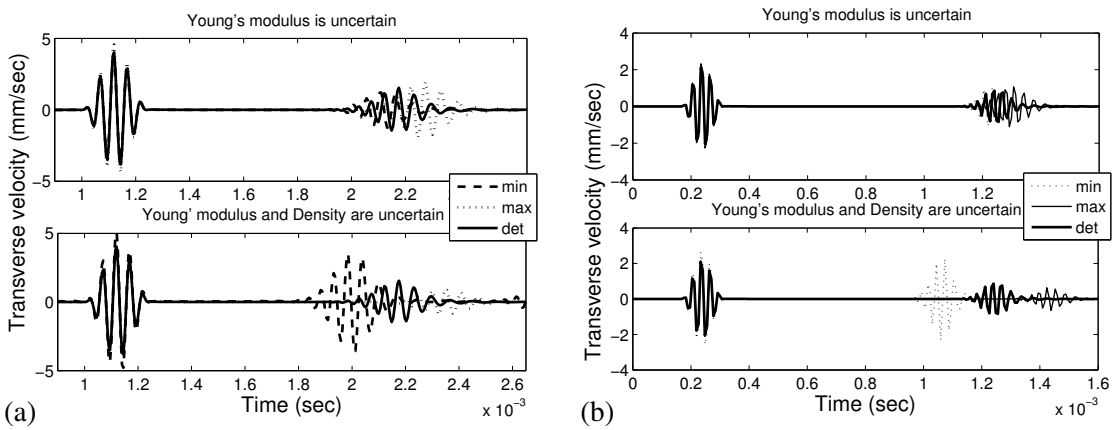

Figure 9. Transverse velocity variation with change in the modulation frequency for (a) 20 kHz loading and (b) 50 kHz loading.

help us in structural health monitoring by giving us insight into the type of variation of group speed and its dependence on the wavenumber. In this study, we try to quantify the variation of COV of the wavenumber with the variation of COV of the input parameters.

Here, we have assumed the material properties (modulus and density) to vary as normal, Weibull, and extreme value distributions. The wave number for the beam is calculated by solving the characteristic equation, (2-12), while for a rod (2-4) is used. As before, 10,000 randomly generated samples are used in the analysis. Figure 10 shows COV plots as a function of a few discrete frequencies for a normal distribution of the material property. From the figure, the following observation can be made. When the Young's modulus alone is uncertain (Figure 10a), the wavenumber COV variation decreases with the increase in frequency; on the other hand, if the density alone is uncertain (Figure 10b), the wavenumber COV variation is just the reverse of the previous case. Figures 11a and 11b show the flexural wavenumber COV variation for a Weibull distribution. These variation patterns follow that of the normally distributed wavenumber COV. No effect of frequency on the COV of wavenumber is noticed in a simple rod and beam model, where the term containing frequency, present in both the denominator and numerator of the expression for the COV, will cancel out. However, in a Timoshenko beam model the frequency has an effect on the variability of the wavenumber, which is explicit from the constant term (the third term) of the characteristic equation (Equation (2-12)). From the above two cases and also from the extreme value distribution of the input parameter, when both the Young's modulus and density are uncertain (Figures 10c, 11b, and 11c), the wavenumber COV is not heavily influenced by the frequency. In fact, compared to the case of a single uncertain input variable, in all these cases the variability in the wavenumber is very high even in the low frequency range, when the Young's modulus and density are uncertain. Figure 12 shows the wavenumber COV for an axial wavenumber. The figures show that the axial wavenumber COV is more than that of a flexural wavenumber COV for a given material distribution and, in contrast to the flexural case, the wavenumber COV does not show any variation with frequency.

4G. ***Distribution of wavenumber, for different types of input distributions.*** In the next few plots, the variation of the wavenumber by taking different probability density functions for the input parameters

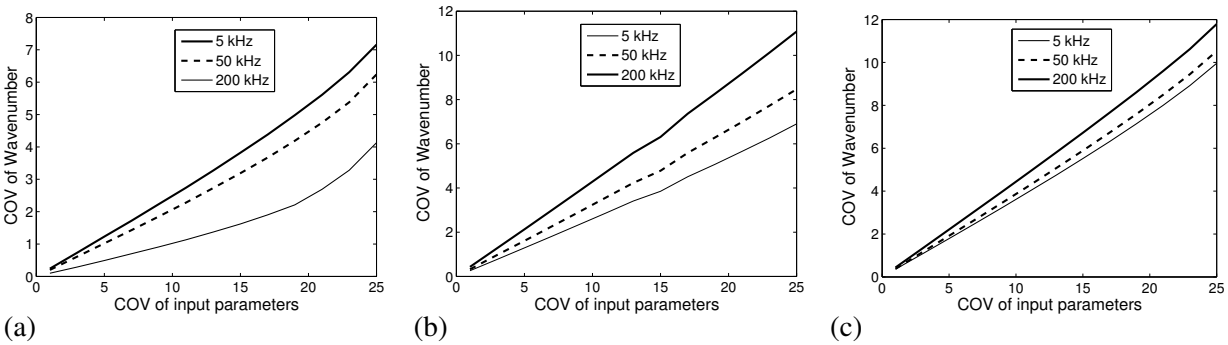

Figure 10. Variation of COV of wavenumber (flexural) with frequency where input parameters vary as normal random variables: (a) Young's modulus, (b) density, and (c) Young's modulus and density.

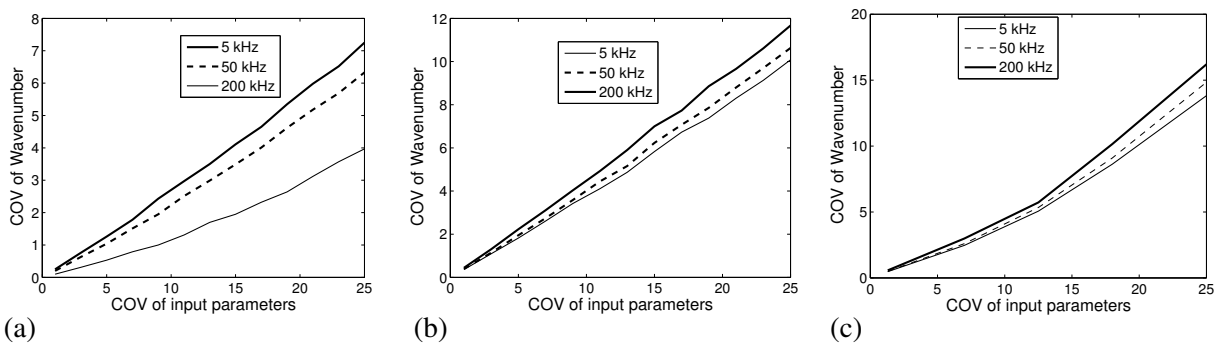

Figure 11. Variation of COV of wavenumber (flexural) with frequency where input parameters are taken as Weibull and extreme value random variables: (a) Young's modulus (Weibull), (b) Young's modulus and density (Weibull), and (c) Young's modulus and density (extreme value distribution).

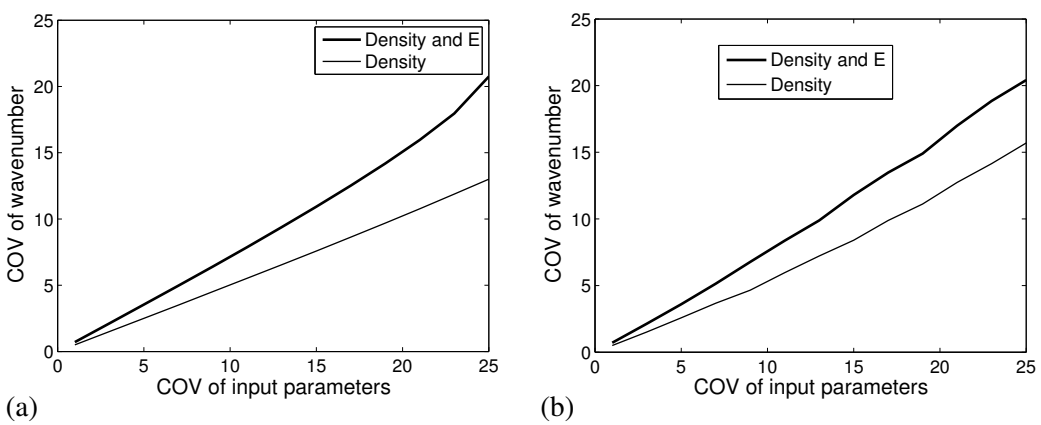

Figure 12. Variation of COV of wavenumber (axial) with input parameters (density and Young's modulus) varying as (a) normal and (b) Weibull random variables.

is shown to quantify the effects of material uncertainty. Here we are only studying the variation in the flexural wavenumber and the uncertain input parameters considered are the Young's modulus and density. Figures 13a and 13b show the change in the variation distribution of the flexural wavenumber at 10 kHz and 25 kHz, taking the input parameters as normal random variables with COV 7%. MCS is performed using 10,000 samples and the corresponding normal distributions of the output samples are obtained using the estimates of the MCS, for purposes of comparison. In Figure 14 the input parameters are taken as Weibull distributions and in Figure 15 the input parameter uncertainty is represented as an extreme value distribution. Here, the different discrete frequencies, where the wavenumber is calculated, are 25 kHz and 200 kHz. Similar to the previous case, the corresponding Weibull and extreme value distributions of the output are obtained using the estimates of the MCS. The results show that the distribution of the variation of the wavenumber at a particular frequency does not vary much with the change in the type

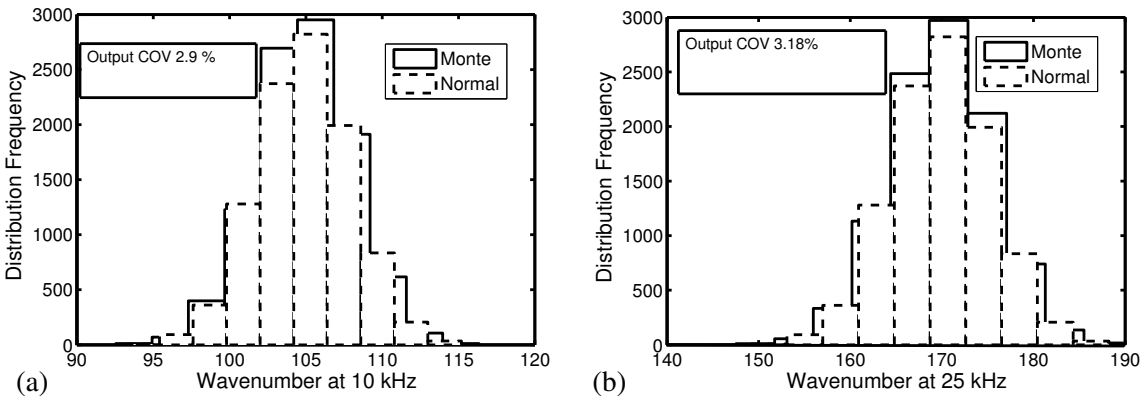

Figure 13. Histogram of distribution of wavenumber (flexural) at different frequencies, with both uncertain density and Young's modulus modeled as normal random variables with COV 7%: (a) 10 kHz and (b) 25 kHz.

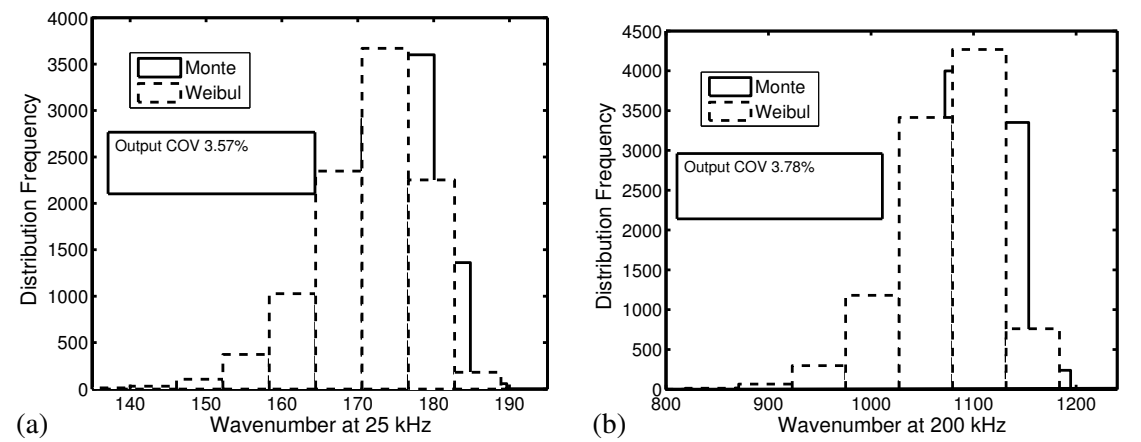

Figure 14. Histogram of distribution of wavenumber (flexural) at different frequencies, with both uncertain density and Young's modulus modeled as Weibull random variables with COV 7%: (a) 25 kHz and (b) 200 kHz.

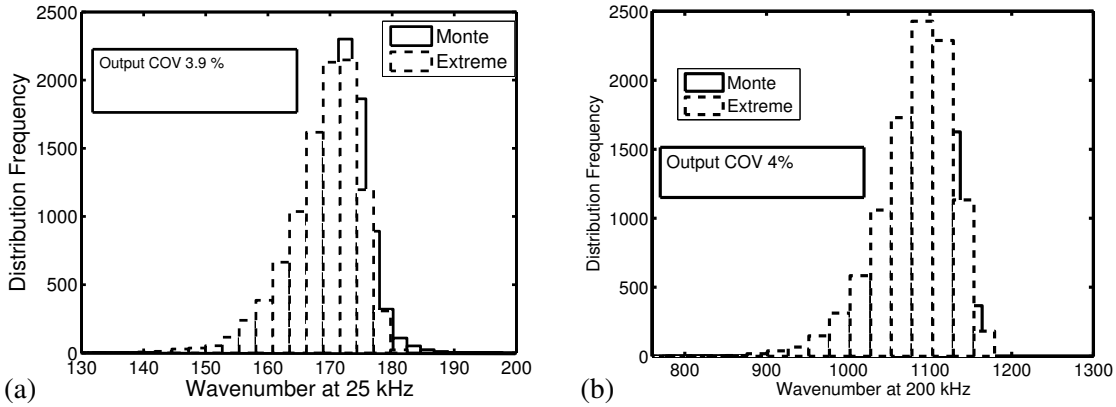

Figure 15. Histogram of distribution of wavenumber (flexural) at different frequencies, with both uncertain density and Young's modulus modeled as extreme value random variables with COV 7%: (a) 25 kHz and (b) 200 kHz.

of probability distribution function. The minimum and maximum limits obtained are similar in all cases, regardless of the type of distribution considered. Moreover, it can be seen that the COV of the variation of the wavenumber does not vary much with the increase in the corresponding frequency.

4H. ***Effect of uncertainty on wavenumber due to higher-order effects in metallic rods and beams.*** In Section 2 we have discussed in detail the computation of the wavenumber. In an elementary rod, there is only one mode due to axial deformation, which is propagating. The wavenumber varies linearly as frequency and hence is nondispersive. This model was used in all earlier simulations. An elementary beam, on the other hand, has a wavenumber which is a nonlinear function of frequency and hence dispersive. It has two modes, one of which is propagating and the other evanescent. Introducing higher-order effects to this elementary model completely alters the wave mechanics. The lateral higher-order effects in rods are introduced by adding an additional lateral motion attributed to the Poisson's ratio. The wavenumber computation for the model is given in Section 2. Higher-order effects introduce an additional propagating mode beyond a certain frequency called the cutoff frequency, which occurs at very high frequencies. In fact, the existence of a cutoff frequency determines the usage of a particular rod model, either an elementary or higher-order model. That is, if the frequency of interest falls below the cutoff frequency, one can still use an elementary model for analysis. Similarly, higher-order effects in beams can be introduced through the introduction of shear deformation, which makes the evanescent mode propagating after a certain cutoff frequency. The cutoff frequency is governed by the material and geometric properties of the structure. In light of the fact that the uncertainties involved in the determination of material properties of a real structure are greater, first we focus our study on the variation of the cutoff frequency of the structure with the variability in the material properties. Here, the geometric properties of the system are considered deterministic, and never initiate higher-order effects in the system. However, if the material properties are uncertain, the predicted cutoff frequencies may be quite misleading in deciding the type of analysis to be used. The aim of this section is to determine the range of shift in the cutoff frequencies due to material uncertainties so that proper theories can be used in the simulation process.

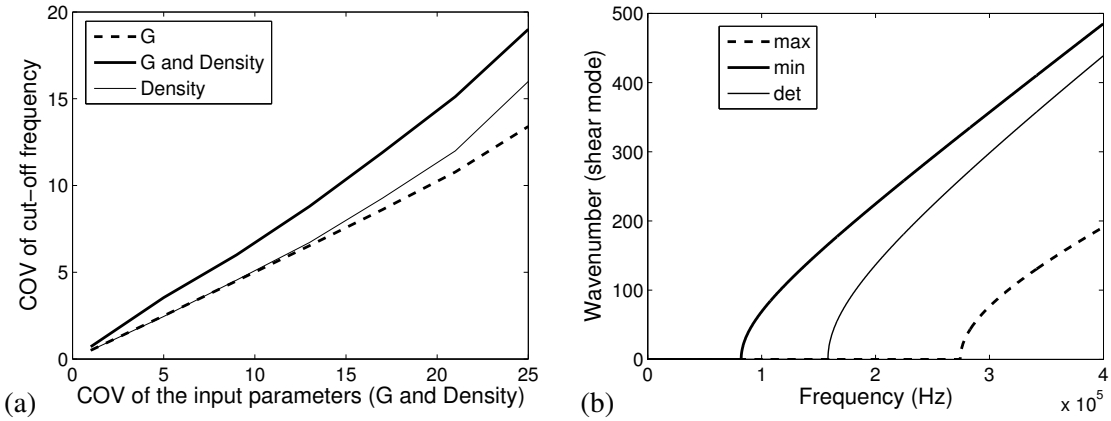

Figure 16. Variation of cutoff frequency of the shear mode of a Timoshenko beam, with both uncertain rigidity modulus and density normal with COV 20%: (a) variation of COV and (b) maximum and minimum bounds of cutoff frequency.

Figure 16a shows the variation of the cutoff frequency with the change in COV of the input parameters (density and G). When the number of random variables used increases from one (density or G) to two (both density and G), we can see that the COV of the cutoff frequency increases. The variation of the COV of the cutoff frequency is greater when the input random variable is density, especially when the COV of the input is high. Figure 16b shows the upper and lower bounds of the shear mode when the COV of the input random variable is 20% and the number of random variables is two (density and G). There is a variation from the deterministic value or 161 kHz to 78 kHz in the lower limit and 271 kHz in the upper limit. The lower limit of this result suggests that, when there is such a large variation in the input parameters, there is a chance for the shear mode to propagate at a lower frequency (here it is 78 kHz) than the expected frequency (161 kHz), which cannot be traced by a simple Euler–Bernoulli theory even for a thin beam. The distributions of the cutoff frequency for different distributions are shown in Figure 17.

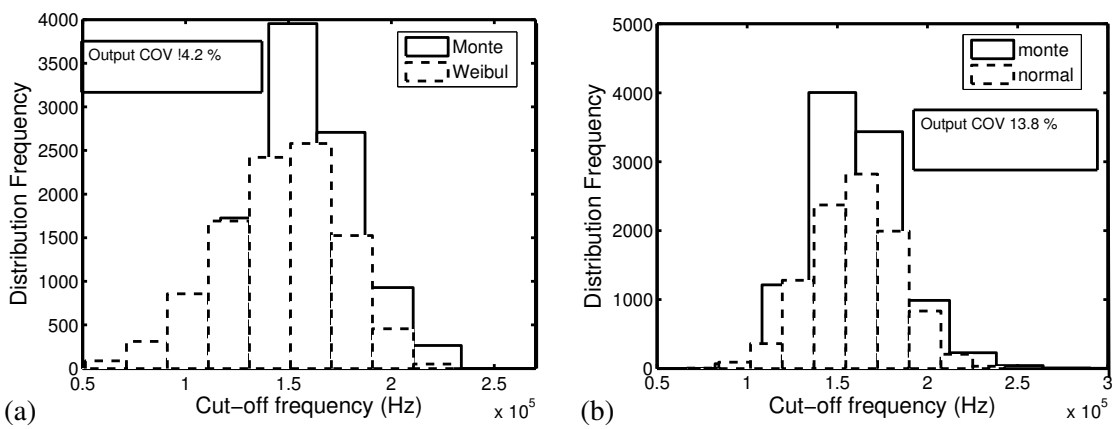

Figure 17. Histogram of the distribution of cutoff frequency of the shear mode of a Timoshenko beam, with both density and rigidity modulus uncertain using different input distributions with COV 20%: (a) normal and (b) Weibull input distribution.

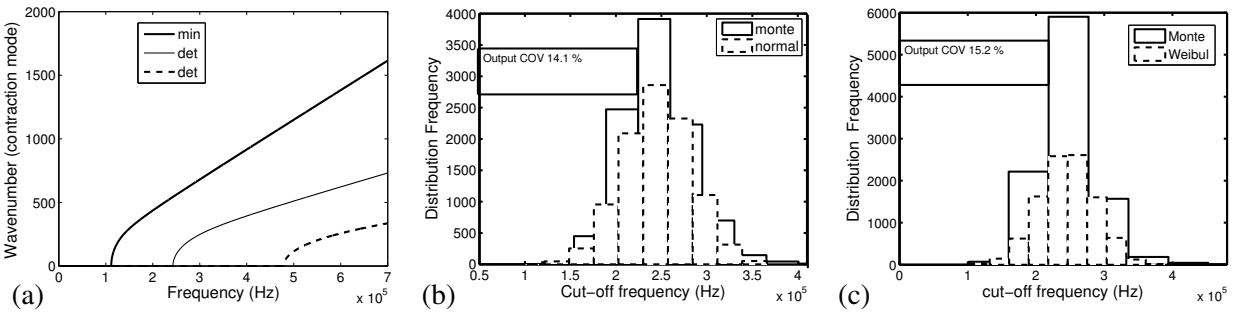

Figure 18. Variation of cutoff frequency for a higher-order rod for uncertain density and rigidity modulus, with COV 20% for different distributions: (a) maximum and minimum limit for normal; histograms of distribution of cutoff frequency for input distributions (b) normal and (c) Weibull.

	Normal		Weibull	
COV (%)	maximum	minimum	maximum	minimum
1	165.74	157.25	158.44	149.02
5	185.48	141.32	173.07	134.35
10	216.86	126.11	198.22	112.34
15	246.62	98.58	223.69	85.24
20	271.24	78.12	245.54	67.33

Table 1. Total bounds on variation of cutoff frequency (kHz) with different input COVs, when both the Young's modulus and density are uncertain, for a Timoshenko beam.

We can see the output distribution variation is almost the same for the two distributions considered and differs from the corresponding input distribution pattern in both cases, where the input parameters are taken as normal distributions and as Weibull distributions.

Figure 18a shows the variation in the contraction mode of a higher-order rod. From this figure, we can see the deterministic value of cutoff frequency for a higher-order rod is very much higher than that for the previous case of a higher-order beam. The uncertain response has the same impact as in the case of the beam in the maximum limit (here, 123 kHz) of frequency of the load, which can be used with the simple elementary rod model. The distribution of the cutoff frequency shows the same pattern of distribution as that of the beam model (Figures 18b and 18c). Finally, Tables 1 and 2 give us an idea of the total bounds on variation of the cutoff frequencies of a Timoshenko beam and a higher-order rod, as a function of the COV of the input parameter, when both the Young's modulus and density are uncertain.

5. Conclusions

Monte Carlo simulation coupled with the spectral finite element method (SEM) is applied to study the variation in the high frequency response of a metallic beam and rod with the variation in the material properties. It can be seen that the method using SEM is efficient and takes much less time than taken by

	Normal		Weibull	
COV (%)	maximum	minimum	maximum	minimum
1	278.66	262.82	280.74	260.47
5	314.21	233.04	327.71	229.84
10	364.65	201.93	395.65	191.93
15	398.69	168.42	423.69	152.42
20	455.38	123.46	495.53	98.34

Table 2. Total bounds on variation of cutoff frequency (kHz) with different input COVs, when both the Young's modulus and density are uncertain, for a higher-order rod.

the method using conventional FEM. The ratio between the CPU time taken for conventional FEM and SEM increases with the loading frequency (here, it increases from 8 to 48 as the frequency content of the load increases from 5 kHz to 50 kHz). Increase in the number of random variables used affects the responses considerably, but only when the coefficient of variation is large. The change in the variation of the time response and the dispersion relations with the increase in the frequency only depends on the uncertain input parameters considered. Regardless of the input parameter distributions considered, the maximum and minimum bounds on the time of first reflection and the wavenumber variation distributions almost match in all the cases. The variation of the shear mode in the beam and the contraction mode in the higher order rod suggest that the uncertainty enforces the use of higher-order theories at lower frequencies than the expected frequency, even for thin structures.

Finally, at this stage, it is very difficult to determine the reason for the shift in the arrival of the first reflection. For understanding the shift due to damage, uncertainties in damage location, size, and type of damage also need to be introduced into the formulation. This is indeed an open area of research and the authors are working towards their next article focusing on this very concept.

References

[Ang and Tang 1975] A. H. S. Ang and W. H. Tang, *Probability concepts in engineering planning and design, vol. 1: Basic principles*, Wiley, New York, 1975.

[Bhattacharyya and Chakraborty 2002] B. Bhattacharyya and S. Chakraborty, "NE MCS technique for stochastic structural response sensitivity", *Comput. Methods Appl. Mech. Eng.* **191**:49–50 (2002), 5631–5645.

[Cecchi and Sab 2009] A. Cecchi and K. Sab, "Discrete and continuous models for in plane loaded random elastic brickwork", *Eur. J. Mech. A Solids* **28**:3 (2009), 610–625.

[Chakraborty and Gopalakrishnan 2004] A. Chakraborty and S. Gopalakrishnan, "A higher-order spectral element for wave propagation analysis in functionally graded materials", *Acta Mech.* **172**:1–2 (2004), 17–43.

[Decker 1991] K. M. Decker, "The Monte Carlo method in science and engineering: theory and application", *Comput. Methods Appl. Mech. Eng.* **89**:1-3 (1991), 463–483.

[Doyle 1997] J. F. Doyle, *Wave propagation in structures: spectral analysis using fast discrete Fourier transforms*, Springer, New York, 1997.

[Ghanem and Spanos 2003] R. G. Ghanem and P. D. Spanos, *Stochastic finite elements: a spectral approach*, Dover, Minneola, NY, 2003.

[Gopalakrishnan et al. 2008] S. Gopalakrishnan, A. Chakraborty, and D. R. Mahapatra, *Spectral finite element method: wave propagation, diagnostics and control in anisotropic and inhomogenous structures*, Springer, London, 2008.

[Horr and Safi 2003] A. M. Horr and M. Safi, "Full dynamic analysis of offshore platform structures using exact Timoshenko pipe element", *J. Offshore Mech. Arct. Eng.* **125**:3 (2003), 168–175.

[James 1980] F. James, "Monte Carlo theory and practice", *Rep. Prog. Phys.* **43**:9 (1980), 1146–1189.

[Kleiber and Hien 1992] M. Kleiber and T. D. Hien, *The stochastic finite element method: basic perturbation technique and computer implementation*, Wiley, Chichester, UK, 1992.

[Lepage 2006] S. Lepage, *Stochastic finite element method for the modeling of thermoelastic damping in micro-resonators*, Ph.D. thesis, Université de Liège, 2006, Available at http://www.ltas-vis.ulg.ac.be/cmsms/uploads/File/Lepage_PhD.pdf.

[Li and Chen 2006] J. Li and J. B. Chen, "The probability density evolution method for dynamic response analysis of non-linear stochastic structures", *Int. J. Numer. Methods Eng.* **65**:6 (2006), 882–903.

[Liu et al. 1986a] W. K. Liu, T. Belytschko, and A. Mani, "Probabilistic finite elements for nonlinear structural dynamics", *Comput. Methods Appl. Mech. Eng.* **56**:1 (1986), 61–81.

[Liu et al. 1986b] W. K. Liu, T. Belytschko, and A. Mani, "Random field finite elements", *Int. J. Numer. Methods Eng.* **23**:10 (1986), 1831–1845.

[Martin et al. 1994] M. A. Martin, S. Gopalakrishnan, and J. F. Doyle, "Wave propagation in multiply connected deep waveguides", *J. Sound Vib.* **174**:4 (1994), 521–538.

[Mindlin and Herrmann 1952] R. D. Mindlin and G. Herrmann, "A one dimensional theory of compressional waves in an elastic rod", pp. 187–191 in *Proceedings of the First U.S. National Congress of Applied Mechanics* (Chicago, 1951), American Soc. Mech. Eng., New York, 1952.

[Nag et al. 2003] A. Nag, D. R. Mahapatra, S. Gopalakrishnan, and T. S. Sankar, "A spectral finite element with embedded delamination for modeling of wave scattering in composite beams", *Compos. Sci. Technol.* **63**:15 (2003), 2187–2200.

[Ostachowicz 2005] W. Ostachowicz, "Elastic wave propagation development for structural health monitoring", pp. 275–286 in *Mechanics of the 21st century: Proceedings of the 21st International Congress of Theoretical and Applied Mechanics* (Warsaw, Poland, 2004), Springer, Dordrecht, 2005.

[Pardoen 1989] G. C. Pardoen, "Effect of delamination on the natural frequencies of composite laminates", *J. Compos. Mater.* **23**:12 (1989), 1200–1215.

[Schueller 2001] G. I. Schueller, "Computational stochastic mechanics-recent advances", *Comput. Struct.* **79**:22-25 (2001), 2225–2234.

[Shinozuka 1972] M. Shinozuka, "Monte Carlo solution of structural dynamics", *Comput. Struct.* **2**:5-6 (1972), 855–874.

[Spanos and Zeldin 1998] P. D. Spanos and B. A. Zeldin, "Monte Carlo treatment of random fields: a broad perspective", *Appl. Mech. Rev.* (*ASME*) **51**:3 (1998), 219–237.

[Stefanou 2009] G. Stefanou, "The stochastic finite element method: past, present and future", *Comput. Methods Appl. Mech. Eng.* **198**:9-12 (2009), 1031–1051.

[Vinckenroy and De Wilde 1995] G. V. Vinckenroy and W. P. De Wilde, "The use of Monte Carlo techniques in statistical finite element methods for the determination of the structural behaviour of composite materials structural components", *Compos. Struct.* **32**:1-4 (1995), 247–253.

Received 28 Jul 2009. Revised 1 Jan 2010. Accepted 14 Jan 2010.

V. AJITH: ajith@aero.iisc.ernet.in
Department of Aerospace Engineering, Indian Institute of Science, Bangalore 560012, India

S. GOPALAKRISHNAN: krishnan@aero.iisc.ernet.in
Department of Aerospace Engineering, Indian Institute of Science, Bangalore 560012, India
http://www.aero.iisc.ernet.in/krishnan

JOURNAL OF MECHANICS OF MATERIALS AND STRUCTURES
Vol. 5, No. 4, 2010

ENERGY-MINIMIZING OPENINGS AROUND A FIXED HOLE IN AN ELASTIC PLATE

SHMUEL VIGDERGAUZ

The design of elastic structures to optimize the stress state of flat plates with appropriately shaped construction holes is a problem of considerable mathematical and industrial significance. This paper continues the shape optimization study previously reported in this journal, **1**:2 (2006), 307–406, for the energy-minimizing single hole under remote shear, and in **3**:7 (2008), 1341–1363 for two identical holes. Here, a challenging and more practical three-hole arrangement is considered, where the central hole is fixed, while the two identical side holes are varied not only in their shapes, but also in their areas.

This twofold novelty is resolved by enhancing a standard genetic algorithm combined with a general method of shape parametrization for multiconnected regions. The method employs conformal mapping of the outside of each optimized contour *separately* onto the outside of a unit circle, as was first proposed in the 2008 paper. We show here that this approach has a significant computational advantage over the common practice of mapping the entire domain under consideration. The numerical simulations present in detail the influence of sizes, shapes, and relative positions of the openings on the induced energy increment and, to a much smaller extent, on the local stresses. The main result is that, compared to a single hole, interacting optimal openings induce up to 15%–19% less energy, depending on the hole spacing and the central hole shape.

1. Introduction

In spite of intensive studies carried out over the last decades, the problem of diminishing the weakening effect of construction holes in a flat elastic plate remains an object of much attention in engineering the optimal design. Various strengthening technologies, such as auxiliary unloading holes, reinforcement rings, and others are known so far, each posing its own elastostatic problem. Of particular assistance here is proper shaping of holes, which may significantly improve the stress-strain state of perforated plates. This optimization scheme is all the more promising, as the hole area is usually of much more importance than its shape, which thus permits a certain design freedom.

In modelling the problem, the plate is infinite and linearly elastic. Furthermore, although the engineering ideal is to minimize the maximum hoop stress occurring along the holes' boundaries, we choose here the weaker and numerically easier integral criterion of the energy increment brought by the holes in the uniform stress state of an undamaged plate under the same load. Besides computational convenience, this choice is advocated by two reasonings. First, a plate with several holes may be thought of as the zeroth-order approximation to a regularly perforated plate, where the energy is directly associated with

Keywords: plane elasticity problem, Kolosov–Muskhelishvili potentials, shape optimization, effective energy, extremal elastic structures, genetic algorithm.

The preliminary results of the paper were presented at the 7th EUROMECH Solid Mechanics Conference (ESMC2009), Lisbon, September 7–11, 2009.

the physically measurable effective moduli of the structure. Second, our previous experience shows that the energy minimization for a single hole [Vigdergauz 2006], and for two interacting holes [Vigdergauz 2008a], is not achieved at the expense of the boundary stresses. On the contrary, the energy-minimizing holes maintain a rather favourable stress distribution, with no excessive peaks; we may cautiously conclude that this is also the case here.

For concreteness, the plate is taken to be loaded by pure shear at infinity. This is more challenging than bulk load, which permits an analytical solution in many situations (*the equistress contours*, see, for instance: [Vigdergauz 2008a] and references therein).

Geometrically, the plane contains the main hole and, equally spaced on both sides of it, two identical unloading holes. The main hole is fixed as either a circle or as a slightly rounded square, which, in absence of auxiliary holes, provides the minimally possible energy under remote shear [Vigdergauz and Cherkaev 1986]. Our aim is, at a given inter-distance, to identify the shape and the area of the side holes that will minimize the hole-induced energy increment. Determining the minimum for such a solid and characterizing the associated extremal structures is an important problem, which arises in homogenization of composites and in optimal design.

Compared to the earlier optimization problem for two identical holes, the arrangement at hand has two complicating features. First, the boundary is partially fixed, since only the shapes of the side holes are changing, and, second, the area of the holes is also optimized. Both features are in contrast to the two-holes geometry fully described (up to scaling) by a single dimensionless parameter, which is the ratio of the hole area to the squared distance between the holes. Nevertheless, both new properties are treated here by enhancing the same numerical framework that was developed for the two holes case. The essential points of this framework can be described in terms of a numerical optimization strategy, where a direct problem solver is repeated many times in a searching space, until a pre-set convergence criterion is reached.

Here, the solver uses complex-valued Kolosov–Muskhelishvili (KM) potentials [Muskhelishvili 1975], which are obtained from a specially derived system of linear algebraic equations involving no singularities and, hence, providing a fast and accurate assessment of each possible hole shape, as was shown previously in a similar context [Vigdergauz 2008a]. A standardly configured genetic algorithm (GA) then employs the above-described solver for fitness evaluation in a gradientless search of the global optimum. Of importance here is the novel encoding scheme, where a shape is presented by a sequence of the first N Laurent coefficients of the function, mapping it conformally onto a unit circle. By adding one more design variable for the hole area, we transform each shape into a chromosome, concatenated of $(N+1)$ genes in the $(N+1)$-dimensional bounded searching space. The fixed central hole remains untouched, while a given distance between the holes is preserved by simply displacing the side hole decoded from a chromosome. This approach has proved to be rather advantageous for numerical solution of the problem at hand, both for a circular and for a square-like central hole.

The paper is organized as follows. For reader convenience, Section 2 summarizes the analytical basics required for further development. Section 3 presents, in terms of these tools, the exact problem formulation and describes the fast and stable direct solver for evaluation of the energy criterion at fixed holes' shapes. Section 4 describes the efficient and adaptive shape parametrization. Together, these three sections provide, to the maximum extent possible, the theoretical backbone for effective numerical simulations. Section 5 describes the features of genetic algorithm, designed specifically for the current

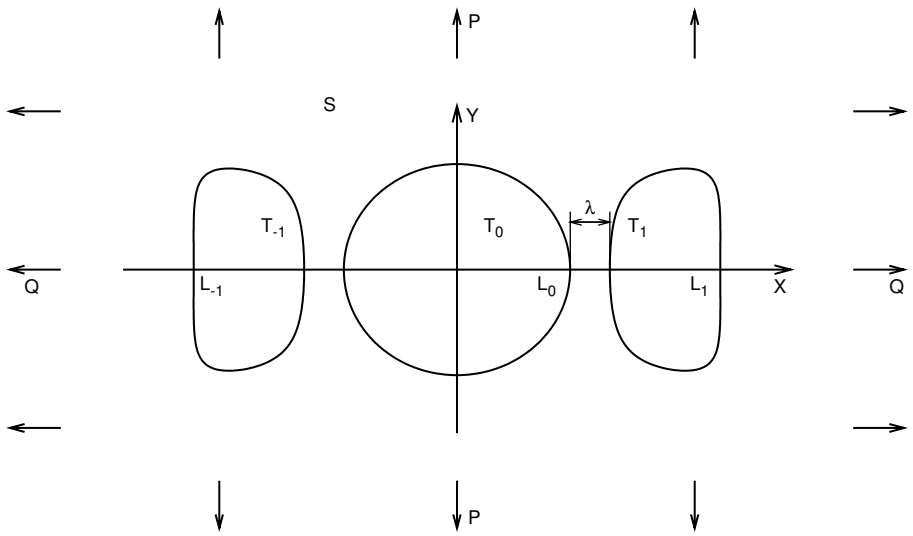

Figure 1. Problem schematic: an infinite plate with two identical holes under uniform stresses, cases $P = Q$ and $P = -Q$ correspond to remote bulk and shear, respectively. The piecewise smooth hole shape is symmetric about the x-axis and may have a finite number of angular points.

purposes. The numerical results are given at length in Section 6. Finally, Section 7 concludes the paper with a summary and remarks about future applications.

2. Analytical framework

Consider the setup in Figure 1, where a principal central hole T_0 in a thin elastic infinite plate interacts with two identical auxiliary holes T_{-1} and T_1, located symmetrically at a distance λ on each side of T_0. The areas of the holes are f_0 and $f_{-1} = f_1$, respectively. To fix the scale factor, we set $f_0 = \pi$.

For simplicity, the hole shapes L_j, $j = -1, 0, 1$, are traction-free, while the plate is remotely loaded by uniform nontangential stresses:

$$\sigma_{xx}^{\infty} = P, \quad \sigma_{yy}^{\infty} = Q, \quad \sigma_{xy}^{\infty} = 0. \tag{2-1}$$

The induced local stresses $\{\sigma_{xx}, \sigma_{yy}, \sigma_{xy}\}$ at any point $z = x + iy$ in the plate can be linearly expressed through a pair of complex-valued functions $\Phi_0(z)$ and $\Psi_0(z)$, holomorphic in the material-filled unbounded region S [Muskhelishvili 1975]:

$$\begin{aligned} \sigma_{xx}(z) + \sigma_{yy}(z) &= 4\,\mathrm{Re}\,\Phi_0(z), \\ \sigma_{yy}(z) - \sigma_{xx}(z) + 2i\sigma_{xy}(z) &= 2\big(\bar{z}\Phi_0'(z) + \Psi_0(z)\big). \end{aligned} \tag{2-2}$$

On account of symmetry, the potentials $\Phi_0(z)$, $\Psi_0(z)$ [Muskhelishvili 1975] are even functions of z:

$$\Phi_0(-z) = \Phi_0(z), \quad \Psi_0(-z) = \Psi_0(z) \qquad \text{for } z \in S, \tag{2-3}$$

with the asymptotics

$$\Phi_0(z) = B + \Phi(z), \quad \Psi_0(z) = \Gamma + \Psi(z) \qquad \text{with} \begin{cases} \Phi(z), \Psi(z) = O(|z|^{-2}) \ \text{ as } z \to \infty, \\ 4B = P + Q, \quad 2\Gamma = Q - P. \end{cases} \tag{2-4}$$

Hence, these potentials possess the following Laurent expansions [Alfors 1979], with purely real coefficients:

$$\Phi_0(z) - B = \Phi(z) = \sum_{k=2}^{\infty} \left(a_0^{(k)} \xi_k(z, 0) + a_1^{(k)} \xi_k(z, c)\right), \tag{2-5a}$$

$$\Psi_0(z) - \Gamma = \Psi(z) = \sum_{k=2}^{\infty} \left(b_0^{(k)} \xi_k(z, 0) + b_1^{(k)} \xi_k(z, c)\right), \tag{2-5b}$$

$$\xi_k(z, c) \equiv \frac{1}{(z-c)^k} + \frac{(-1)^k}{(z+c)^k}, \quad \xi_k(z, c) = \xi_k(-z, c) \quad \text{for } z \in S, \tag{2-5c}$$

$$\xi_k(z, 0) = \frac{2}{z^k} \ \text{ for } k = 2, 4, \ldots, \quad \xi_{2k+1}(z, 0) = 0 \ \text{ for } k = 3, 5, \ldots, \tag{2-5d}$$

where c is a fixed point on the X-axis inside the hole L_1.

It should be noted that only the first coefficients in (2-5a) and (2-5b) define the stress energy increment Δw brought by the holes into a given outer stress field (2-1) [Muskhelishvili 1975]:

$$\Delta w = 2\pi \left(2\Gamma_0 (a_0^{(2)} + 2a_1^{(2)}) + B_0 (b_0^{(2)} + 2b_1^{(2)})\right) E^{-1}, \tag{2-6}$$

where E is the Young modulus of the plate. This is in clear contrast to the local stresses (2-2), which involve all the coefficients (2-5a). This difference provides a great computational advantage.

The increment is a strictly positive definite bilinear form of B, Γ [Muskhelishvili 1975]:

$$\Delta w = B^2 \omega_{11} + 2B\Gamma\omega_{12} + \Gamma^2 \omega_{22} > 0 \quad \Longrightarrow \quad \omega_{11}, \ \omega_{22} > 0, \ \omega_{11}\omega_{22} > \omega_{12}^2 \tag{2-7}$$

and depends on all the parameters involved in the problem. For future convenience, we normalize Δw by the total holes area $(\pi + 2f_1)$ and by E,

$$\Delta w = E\Delta w/(\pi + 2f_1) = B^2 w_{11} + 2B\Gamma w_{12} + \Gamma^2 w_{22}, \tag{2-8a}$$

$$w_{ij} = w_{ij}(L_0, L_1, \lambda, f_1) \quad \text{for } i, j = 1, 2, \ i \le j. \tag{2-8b}$$

Finally, the traction-free condition links the potentials along the holes' boundaries, in the following form:

$$2\frac{\partial \bar{t}}{\partial t} \operatorname{Re} \Phi(t) + \bar{t}\, \Phi'(t) + \Psi(t) = -2B \frac{\partial \bar{t}}{\partial t} - \Gamma, \quad t \in L; \quad L = L_{-1} + L_0 + L_1; \tag{2-9}$$

see [Muskhelishvili 1975], observing that identity (2-9) is specifically rearranged for future use.

Though mathematically simple, the increment Δw can be obtained only by finding the stress state in the plate at a given geometry. Using (2-2), this full-size direct elastostatic problem is equivalently replaced by the uniquely solved boundary value problem (2-9)+(2-4)+(2-1) in $\Phi_0(z)$ and $\Psi_0(z)$; see again [Muskhelishvili 1975]. It can be solved numerically, amongst many other possibilities, by substituting

the expansions (2-5) into (2-9), to arrive at an infinite system of algebraic equations in vector $\{x\}$ of the unknown Laurent coefficients:

$$\sum_{j=1}^{\infty} p_{ij} x_j = q_i \quad \text{for } i = 1, 2, \ldots. \tag{2-10}$$

The system matrix, $\{p_{ij}\}$, and the right hand side, $\{q_i\}$, are obtained by integrating specific combinations of the power terms and their conjugates in (2-5) over the boundaries of the holes. Analytically, this is a difficult problem, highly dependent on specific geometry, because only a circle $\{t : |t - c| = r\}$, that is,

$$(\bar{t} - \bar{c}) = r^2 (t - c)^{-1}, \tag{2-11}$$

possesses the simple relations between shape points t and $\bar{t}$ used for reducing the integrals to a closed form. Otherwise, numerical methods are called for. In a similar context we have proposed in [Vigdergauz 2006; 2008a] a fast and stable computational scheme employing the special parametric shape representation, as detailed in the next section.

3. Problem formulation and fast direct solver

Our aim now is to use the scheme sketched above as an inner solver, within the following optimization problem:

Given a central hole L_0 at an inter-distance λ from its neighbors, and given a far stress field, B, Γ, find the shape L_1 and the area f_1 of the Δw-optimal auxiliary holes, on which

$$\Delta w(B, \Gamma, L_0, L_1, \lambda, f_1) \xrightarrow[\{L_1\},\quad f_1 \le f]{} \min(B, \Gamma, L_0, \lambda), \tag{3-1}$$

where $\{L_1\}$ denotes the set of all closed curves with area less than a specified constant f. The curves are to have no cusps and no self-intersections.

The variable hole area is a rather novel feature in shape optimization in elasticity. This additional degree of freedom may provide certain advantages in minimizing the criterion (3-1). To be more specific, we suppose that the auxiliary holes may not be larger than the principal one,

$$f_1 \le f = f_0 = \pi. \tag{3-2}$$

Preparatory to solving the optimization problem (3-1), we prove the following elementary assertion:

Let the functions $f_1(z)$, $f_2(z)$ be holomorphic in the same domain D of the complex plane z. Also, let them be equal in all their derivatives at some interior point $z_0 \in D$:

$$f_1^{(k)}(z_0) = f_2^{(k)}(z_0) \qquad \text{for } k = 0, 1, \ldots. \tag{3-3}$$

Then both functions coincide identically throughout their common region of analyticity:

$$f_1(z) = f_2(z) \qquad \text{for all } z \in D. \tag{3-4}$$

Indeed, a holomorphic function is represented in a sufficiently small neighborhood of any interior point by a Taylor series [Alfors 1979]:

$$f_j(z) = c_{j,0} + c_{j,1}(z - z_0) + c_{j,2}(z - z_0)^2 + \cdots \quad \text{for } z, z_0 \in D \text{ with } \|z - z_0\| \le r_j, \tag{3-5}$$

where $j = 1, 2$. Considering (3-5) in $\|z - z_0\| \le \min(r_1, r_2)$, we conclude, in view of (3-3), that both Taylor series are the same: $c_{1,k} = c_{2,k}$ for $k = 0, 1, \ldots$, and, hence,

$$f_1(z) \equiv f_2(z) \quad \text{if } \|z - z_0\| \le \min(r_1, r_2). \tag{3-6}$$

The extended identity (3-4) now follows from (3-6) by the principle of analytical continuation [Alfors 1979].

Next, as in [Vigdergauz 2008a], we specifically employ the loading boundary condition (2-9). Integration of the both sides with the Cauchy kernel $dt/(t - z)$ over the holes' boundaries L gives

$$2\int_L \frac{\operatorname{Re}\Phi(t)\,d\bar{t}}{t-z} + \int_L \frac{\bar{t}\,\Phi'(t)\,dt}{t-z} + \int_L \frac{\Psi(t)\,dt}{t-z} = -2B\int_L \frac{d\bar{t}}{t-z} - \Gamma\int_L \frac{dt}{t-z}. \tag{3-7}$$

Inside either of the holes, each item in (3-7) represents a holomorphic function of z [Muskhelishvili 1975]. It is crucial for further derivations that the last left integral identically disappears, since its integrand $\Psi(t)$ is the boundary value of a holomorphic function *outside* the holes and vanishes at infinity [Alfors 1979]. In addition, the symmetry relations (2-3) allow for replacing the integral path L_{-1} with L_1, while the second right integral is simply $2\pi i\Gamma$, by the residue theorem. By virtue of all of the above, (3-7) is rewritten, after routine algebra, as

$$2\int_{L_0} \frac{\operatorname{Re}\Phi(t)\,d\bar{t}}{t-z} + \int_{L_0} \frac{\bar{t}\,\Phi'(t)\,dt}{t-z} + 2\int_{L_1} \operatorname{Re}\Phi(t)\eta_1(t,z)\,d\bar{t} + \int_{L_1} \bar{t}\,\Phi'(t)\eta_1(t,z)\,dt$$
$$= 2B\int_{L_0} \frac{d\bar{t}}{t-z} + \int_{L_1} \eta_1(t,z)\,d\bar{t} + 2\pi i\Gamma, \tag{3-8}$$

where $\eta_1(t, z)$ is defined similarly to (2-5c):

$$\eta_1(t,z) \equiv \frac{1}{t-z} + \frac{1}{t+z}, \quad \eta_1(t,-z) = \eta_1(t,z) \quad \text{for } z \in L_0, L_1. \tag{3-9}$$

The most common way of further transforming identity (3-7) is to obtain an equivalent *singular* integral equation, where z tends from the inside of the holes to their boundary $L_0 + L_1$ [Muskhelishvili 1975]. Alternatively, we employ (3-3)+(3-4) to equivalently recast (3-8) into a set of *regular* identities at $z_0 = c$:

$$2\int_{L_0} \frac{\operatorname{Re}\Phi(t)\,d\bar{t}}{(t-c)^k} + \int_{L_0} \frac{\bar{t}\,\Phi'(t)\,dt}{(t-c)^k} + 2\int_{L_1} \operatorname{Re}\Phi(t)\eta_k(t,c)\,d\bar{t} + \int_{L_1} \bar{t}\,\Phi'(t)\eta_k(t,c)\,dt$$
$$= 2B\int_{L_0} \frac{d\bar{t}}{(t-c)^k} + 2B\int_{L_1} \eta_k(t,c)\,d\bar{t} + 2\pi i\Gamma\delta_{k,1}, \tag{3-10}$$

and at $z_0 = 0$:

$$2\int_{L_0} \frac{\operatorname{Re}\Phi(t)\,d\bar{t}}{t^k} + \int_{L_0} \frac{\bar{t}\,\Phi'(t)\,dt}{t^k} + 2\int_{L_1} \operatorname{Re}\Phi(t)\eta_k(t,0)\,d\bar{t} + \int_{L_1} \bar{t}\,\Phi'(t)\eta_k(t,0)\,dt$$
$$= 2B\int_{L_0} \frac{d\bar{t}}{t^k} + 2B\int_{L_1} \eta_k(t,0)\,d\bar{t} + 2\pi i\Gamma\delta_{k,1}. \tag{3-11}$$

Here $\delta_{k,1}$ is the Kronecker delta and we have set, for $k = 0, 1, 2 \ldots$,

$$\eta_{k+1}(t,c) \equiv \frac{1}{(k)!}\frac{\partial^k \eta_1(t,z)}{\partial z^k}\bigg|_{z=c} = \frac{1}{(t-c)^{k+1}} + \frac{(-1)^k}{(t+c)^{k+1}}; \tag{3-12}$$

in particular, $\eta_{2k+1}(t,0) = 2/t^{2k+1}$ and $\eta_{2k+2}(t,0) = 0$. As prescribed by the symmetry of the problem, the kernels ξ_k and η_{k+1} differ in the sign of their second term.

Finally, substitution of the Laurent expansion (2-5) transforms (3-10)+(3-11) into the linear system (2-10) in the unknowns $x_{2k-1} = a_1^{(k)}$, $x_{2k} = a_0^{(2k)}$, $k = 1, 2, \ldots$

$$\begin{aligned}
p_{2k-1,2l-1} &= 2\int_{L_0+L_1} \operatorname{Re}\xi_{l+1}(t,c)\eta_k(t,c)\,d\bar{t} \qquad + \int_{L_0+L_1} \bar{t}\xi'_{l+1}(t,c)\eta_k(t,c)\,dt,\\
p_{2k-1,2l} &= 2\int_{L_0+L_1} \operatorname{Re}\xi_{2l-1}(t,0)\eta_k(t,c)(t,c)\,d\bar{t} + \int_{L_0+L_1} \bar{t}\xi'_{2l-1}(t,0)\eta_k(t,c)\,dt,\\
p_{2k,2l-1} &= 2\int_{L_0+L_1} \operatorname{Re}\xi_{l+1}(t,c)\eta_{2k-2}(t,0)\,d\bar{t} \qquad + \int_{L_0+L_1} \bar{t}\xi'_{l+1}(t,c)\eta_{2k-2}(t,0)\,dt,\\
p_{2k,2l} &= 2\int_{L_0+L_1} \operatorname{Re}\xi_{2l-1}(t,0)\eta_{2k-2}(t,0)\,d\bar{t} \qquad + \int_{L_0+L_1} \bar{t}\xi'_{2l-1}(t,0)\eta_{2k-2}(t,0)\,dt,\\
q_{2k-1} &= -2B\int_{L_0+L_1} d\bar{t}\,\eta_k(t,c) + \Gamma\delta_{k,1},\\
q_{2k} &= -2B\int_{L_0+L_1} d\bar{t}\,\eta_e t a_{2k-2}(t,0) + \Gamma\delta_{k,1}.
\end{aligned} \tag{3-13}$$

The kernels $\xi_k(t,c)$, $\xi_k(t,c)$, $\eta_k(t,c)$, $\eta_k(t,0)$ and, hence, the above integrals are regular. All entries in (3-13) are divided by $2\pi i$. Again, along circular shapes (2-11) they take a closed, though cumbersome, typical form of binomial coefficients and powers of c.

Remarkably, the resolving system (3-13) involves no Laurent coefficients $b_1^{(k)}$, $b_0^{(2k)}$ of $\Psi(z)$. Once the system is solved, they can be found by directly integrating the boundary condition (2-9),

$$2\pi i b_1^{(k)} = \int_{L_1} (t-c)^{2k-1} \operatorname{Re}\Phi(t)\,d\bar{t} + \int_{L_1} (t-c)^{2k-1}\bar{t}\,\Phi'(t)\,dt, \tag{3-14a}$$

$$2\pi i b_0^{(2k)} = \int_{L_0} t^{2k-1} \operatorname{Re}\Phi(t)\,d\bar{t} + \int_{L_0} t^{2k-1}\bar{t}\,\Phi'(t)\,dt. \tag{3-14b}$$

This halves the computational efforts compared to the commonly used approaches, where both potentials are solved simultaneously rather than in tandem.

4. Shape parametrization scheme

We are now in a position to enhance the proposed sequential solution of KM potentials by a numerical scheme for effectively evaluating the contour integrals (3-13). Within the optimization framework, this raises the question of how to validly encode an arbitrary hole. The commonly used discretization with nodal points is computationally expensive, due to their double use as design variables and as integration points. For reasonably accurate results, one should keep a needlessly large number of nodes, thus causing a dramatic slowdown of the optimization convergence.

In a similar, though more simple, context of free-boundary problems for a single elastic inclusion [Vigdergauz 2006], and for two identical holes [Vigdergauz 2008a], we devised an alternative shape parametrization scheme, which can also be used for the current purposes. For reader's convenience we briefly summarize this latter paper's approach, in which the design variables are *separated* from the integration points.

For this purpose, we narrow our focus to smooth closed curves L_1 that can be conformally mapped onto the unit circle $\gamma = \{\tau = e^{i\theta} : 0 \le \theta \le 2\pi\}$, by means of an analytic function $\Omega(t)$ with a small number N of initial nonzero Laurent terms [Alfors 1979]:

$$t \equiv \Omega(\tau) = \tau + \sum_{j=1}^{N} d_j \tau^{-j} \quad \text{with } t \in L_1,\ \tau \in \gamma \tag{4-1}$$

(note that $\tau^{-1} = \bar{\tau}$). The area of the region enclosed by L_1 is then

$$F_N = \pi\left(1 - \sum_{j=1}^{N} j|d_j|^2\right). \tag{4-2}$$

Thus, the novel feature of varying the area is realized simply by scaling the hole with the factor

$$f_1/F_N, \quad f_1 \le f. \tag{4-3}$$

It is quite significant that, in contrast to common practice, neither the elastic domain nor the stress-strain equations are really transformed. The mapping is used for the purely geometrical purpose of effectively presenting the searched shapes. Put otherwise, the novel shape representation involves a conformal mapping of a *single hole*, rather than of *all holes simultaneously*. This feature is especially useful for the partially fixed boundary, where the major hole simply remains unmapped.

Taken in this case as design variables, the mapping coefficients have the following substantial advantages over the nodal points representation:

- They are naturally ordered, in the sense that the higher the coefficient, the smaller its global impact on the inclusion shape. Indeed, geometrically, the high-order mapping coefficients are responsible mainly for forming large curvature isolated shape points and, thus, have little effect on the *integral*-type energy increment Δw. In practice, this provides a rapid convergence to the global optimum at small values of N (typically, $N \le 7$, as shown in Section 6). This convenience disappears for the problem of minimizing the *local* stresses, where N should be sufficiently large to accurately compute possible stress concentration at large curvature points. For this reason, the stress optimization remains beyond the current scope.
- They fall into the successfully narrowing intervals,

$$-\frac{1}{\sqrt{j}} \le d_j \le \frac{1}{\sqrt{j}} \quad \text{for } j = 1, 2, \ldots, \tag{4-4}$$

  as a result of the uniqueness of conformal mapping [Alfors 1979]. This allows us to treat these intervals and the two-sided inequality (3-2) for the noncentral hole area as linear constraints in the optimization problem (3-1), which is reformulated in the following manner:

For a given finite number N of mapping coefficients and fixing the other parameters involved in (3-1), find the energy-minimizing shape and area of the auxiliary hole L_1,

$$\Delta\omega(B, \Gamma, L_0, L_1, \lambda, f_1) \xrightarrow[\{L_1\}_N, \quad f_1 \le f]{} \min_N(B, \Gamma, L_0, \lambda). \tag{4-5}$$

Put differently, we simplify the initial shape optimization problem by replacing the comprehensive pool $\{L_1\}$ of all admissible curves by its N-mapped subset

$$\big\{\{L_1\}_N : \{L_1\}_N \subset \{L_1\},\ \min_N(B, \Gamma, L_0, \lambda) \ge \min(B, \Gamma, L_0, \lambda).\big\}$$

By taking the differential of (4-1) and its conjugate, and using the identity (2-11), we get

$$dt = \Omega'(\tau)\, d\tau = i\left(\tau - \sum_{j=1}^{N} j d_j \tau^{-j}\right) d\theta, \quad d\bar{t} = -i\left(\tau^{-1} - \sum_{j=1}^{N} j d_j \tau^{j}\right) d\theta. \tag{4-6}$$

Any integration path $L_1 \in \{L_1\}_N$ in (3-13) is transformed to the unit circumference γ, independently of the design variables $\{d_1, d_2, \ldots, d_N\}$. The resultant regular integrals along γ can be evaluated by any appropriate numerical scheme. We employ the standard Gaussian quadrature rule with N_p equally spaced points. The design variables here are fully separated from the integration points.

Our experience suggests that the reformulation (4-5) of the optimization problem is well suited to be solved by the genetic algorithm (GA).

5. GA scheme: related results and current specifics

Devised by Holland [1975], the genetic algorithm (GA) exploits the heuristic that simulates natural evolution processes, such as selection and mutation. It evolves candidate solutions for problems that have large solution space and are not amenable to exhaustive search or traditional optimization techniques.

Typically, GA starts with a random population of encoded candidate solutions, called chromosomes. Then the fitness of each candidate solution in the current population is evaluated to select the fittest candidate solutions as parents of the next generation of candidate solutions. After being selected for reproduction, parents are recombined (using a crossover operator) and mutated (using a mutation operator) to generate offspring. The fittest parents and the new offsprings form a new population, for which the process is repeated to create new populations.

As applied to the problem at hand, the GA operators are specified in the following way:

Each chromosome concatenates $N+1$ two-byte integers I_j in the range $-M \le I_j \le M$ where $M = 2^{15} - 1$ and $j = 0, 1, \ldots, N$. In view of (3-2), (4-4), and (4-3) the chromosomes encode a possible shape $L_1 \in \{L_1\}_N$ through its area and its Laurent coefficients:

$$f_1 = (1 + I_0/M) f/2, \tag{5-1a}$$

$$d_j = I_j/M\big/\sqrt{j} \quad \text{for } j = 1, 2 \ldots, N. \tag{5-1b}$$

Substitution of (5-1) into (4-1) decodes the corresponding shape. However, self-intersecting shapes may appear, since the inequalities (4-4) are only necessary, not sufficient, to guarantee their absence. To our knowledge, no conditions on the coefficients d_j are known which trim out only self-intersecting curves.

Therefore, we check each decoded curve for possibly breaking monotonicity, demanding that

$$\frac{d \arg \Omega(\tau)}{d\theta} \geq 0 \quad \text{for } 0 \leq \theta \leq 2\pi; \tag{5-2}$$

this corresponds to the more restrictive shape property of star-shapeness. Physically, it is clear anyway that only star-shaped holes are promising for optimization. In the numerical simulations (Section 6) this is attested to by the fact that the optimal values of d_j, $j = 1, 2, \ldots, N$, are rather distant from the limiting values in (4-4).

Inequality (5-2) is verified at each integration point along the unit circle $\gamma : |\tau| = 1$. Wherever (5-2) is violated, the corresponding shape obtains a penalty as its fitness, and the GA process takes the next candidate. The idea is to assign the penalty by measuring the squared violation and multiplying it by a very large constant. A shape allowed by (5-2) is further scaled with respect to (5-1b) and is displaced from the origin at the distance

$$c = \lambda + \min\big(\operatorname{Re} L_0(x, y) - \operatorname{Re} L_1(x, y)\big), \tag{5-3}$$

to satisfy the given geometry. The displacement value c from (5-3) serves as the parameter in (3-13) and in all the relative transformations. After that, the fitness of a feasible candidate is evaluated by (1) solving first the system (3-13) truncated to size $K \times K$; (2) restoring the second potential $\Psi(z)$ by use of (3-14); and (3) substituting the first few Laurent coefficients into the resulting expression (2-6) for the energy increment. Step (1) is the most time-consuming phase of GA; hence, all the economy reasoning should be applied here. First, due to symmetry, the system is pure real. Second, the coefficients $b_0^{(2)}$, $b_1^{(2)}$

GA parameter	Parameter value(s)
Gene	Integer in $[-32767; 32767]$
Individual	Interface shape
Population size	1000–25000, depending on inter-distance
Number of genes, $N + 1$	up to 8
Initial population	1000–25000 random individuals
Selection	Tournament
Elitism	Four best individuals
Crossover	1-point
Crossover rate	0.99
Creep mutation	By randomly changing a bit
Creep mutation rate	0.35
Jump mutation	By adding a random integer, typically in the range $[-4; 4]$
Jump mutation rate	0.35
Stopping criterion	After M iterations, M in the range [100; 150]
Resolving system size	$K = 36$
Number of integration points	$N_p = 720$ (in the interval $[0, \pi]$)

Table 1. GA operator types, their probability rates and related parameters typically used in further optimizations.

of $\Psi(z)$ disappear from the energy increment (2-6) when the remote load is pure shear ($B = 0$). This allows for avoiding step (2) calculations and for truncating the system (3-13) at relatively moderate size, since only the two first unknowns, $a_0^{(2)}$ and $a_1^{(2)}$, define the increment (2-6). Namely, in such a way a single energy minimizing hole [Vigdergauz 2006] and two interacting holes [Vigdergauz 2008a] were identified earlier. In the first case, additionally, the unknowns partly vanish due to four-fold symmetry, while the equations (3-13) acquire a finite-difference form [Levy and Lessman 1959] that is resolved analytically, with no truncation.

The main result so obtained in [Vigdergauz 2006] is that the energy-minimizing singular hole under remote shear L_* looks like a square with slightly rounded corners, and provides the global increment minimum

$$\Delta w_{22}(0, 1, \lambda, L_*) \approx 0.928623, \tag{5-4}$$

which is somewhat less than the value for a circle γ [Muskhelishvili 1975],

$$\Delta w_{22}(0, 1, \lambda, \gamma) = 1.00. \tag{5-5}$$

In what follows, we also suppose that the plate is subject to pure shear at infinity, using both values (5-4) and (5-5) for future comparison. An immediate conclusion can be drawn here about the behavior of the corresponding increment (2-8), when the inter-distance λ tends to infinity. In this case, the resultant energy is simply a weighted sum of the energies (5-4) and (5-5) with the optimized side holes nearing L_*. Therefore, we have

$$\min_{\{L_1\}} \lim_{\lambda\to\infty} w_{22} = \min_{\{f_1\le f_0\}} w_{22}(L_0, L_*, f_1) \tag{5-6}$$

$$= \begin{cases} \min\limits_{\{f_1\le f_0\}} \dfrac{f_0+2\times 0.928623 f_1}{f_0+2f_1} = 0.952416 \text{ (achieved for } f_1 = f_0) & \text{when } L_0 = \gamma, \\ \min\limits_{\{f_1\le f_0\}} \dfrac{0.928623(f_0+2f_1)}{f_0+2f_1} = 0.928623 \text{ (achieved for any } f_0, f_1) & \text{when } L_0 = L_*. \end{cases}$$

It is worthy of note that, when f_1 tends to infinity, the upper expression in (5-6) is a decreasing function of f_1 everywhere in the interval $0 \le f_1 < \infty$, with the limit (5-4). Therefore, in the absence of the inequality constraint (3-2), the optimized hole area grows infinitely large with the distance, as observed in numerical simulations. The lower expression, naturally, is independent of the areas f_0, f_1, and assumes the constant value (5-4).

Though many schemes are suggested to enhance GA, the relatively small number N of design variables allows us to use a rather simple configuration, with a number of heuristic parameters. For achieving better efficiency, these need to be adjusted by preliminary numerical tests for assessing the GA's stability and convergence speed. Table 1 on the previous page gives the chosen values of the parameters.

6. Numerical results

A wide set of GA-based simulations was performed to numerically solve the optimization problem (4-5) in the representative inter-distance interval $0.2 \le \lambda \le 5.0$. To ensure the accuracy of the results, all output data were computed several times, randomly starting each GA process and stopping it after a rather large number M of iterations, when there is no more variation of the results. At a fixed inter-distance λ, the computed minimum w_{22} depends on both N and M, and should converge separately with increase of

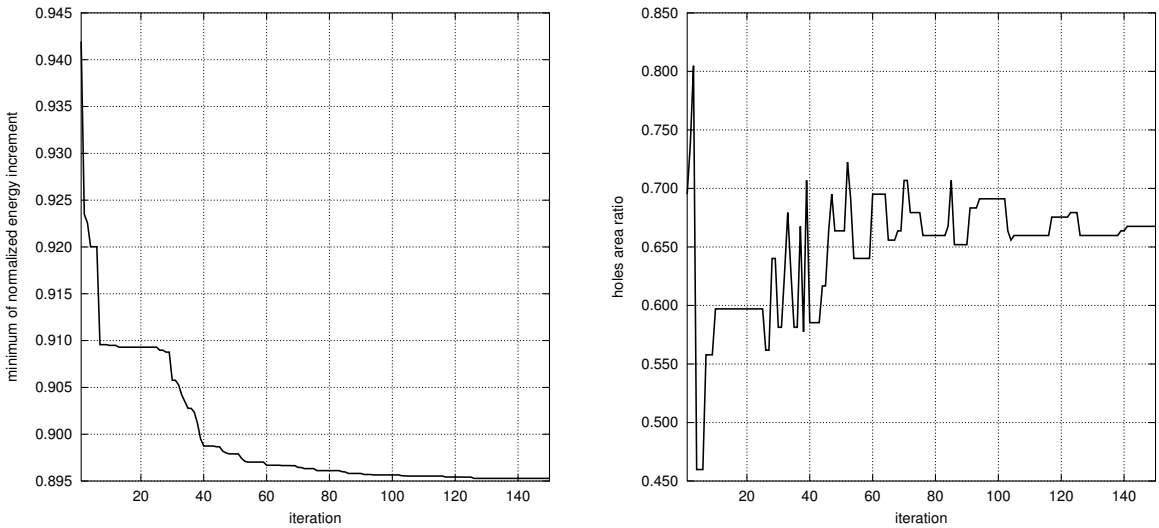

Figure 2. Hole shape identification: progress of a typical genetic optimization run with increasing M for the energy increment (left) and for the side hole area (right).

either of them. A typical iteration convergence for the GA scheme is shown in Figure 2. The convergence to the global optimum with increasing number N of mapping terms was assessed by the relative proximity of the optimal values for the first successive values of N, as shown in Table 2, at the hard-to-compute value $\lambda = 0.2$. The evolution of the optimized shape with M and N is presented in Figure 3. The right part of the figure illustrates the fact, already noted, that the higher mapping coefficients change the optimized shape only locally.

The remaining results are displayed in parallel for the circular and the square-like central hole. The most labor-intensive is Figure 4, which demonstrate the dependence of the energy increment minimum

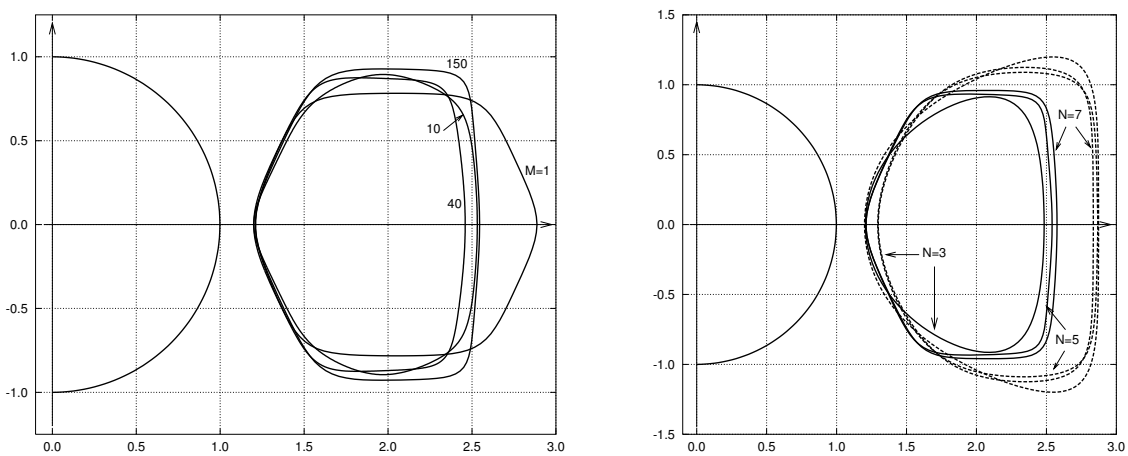

Figure 3. Hole shape identification: progress of a typical genetic optimization run at $\lambda = 0.2$ with M (left) and with N (right). The dashed lines show the optimal shapes at the fixed side hole area $f_1 = f_0$.

N	d_1	d_2	d_3	d_4	d_5	d_6	d_7	f_1/f_0	$\min \delta w_{22}$
1	−0.2039							0.3892	0.9367
2	−0.1843	−0.0804						0.5539	0.9204
3	−0.1686	−0.0902	−0.0144					0,5892	0.9200
4	−0.1804	−0.0412	−0.0118	−0.0343				0.5931	0.9113
5	−0.1863	−0.0627	−0.0484	−0.0284	0.0282			0.6990	0.8963
6	−0.1863	−0.0627	−0.0484	−0.0284	0.0282	0.0000		0.6990	0.8963
7	−0.1843	−0.0627	−0.0497	−0.0314	0.0282	0.0026	0.0022	0.6873	0.8955

Table 2. Circular central hole case: optimal mapping coefficients for the side hole and the corresponding min Δw_{22} for different values of N.

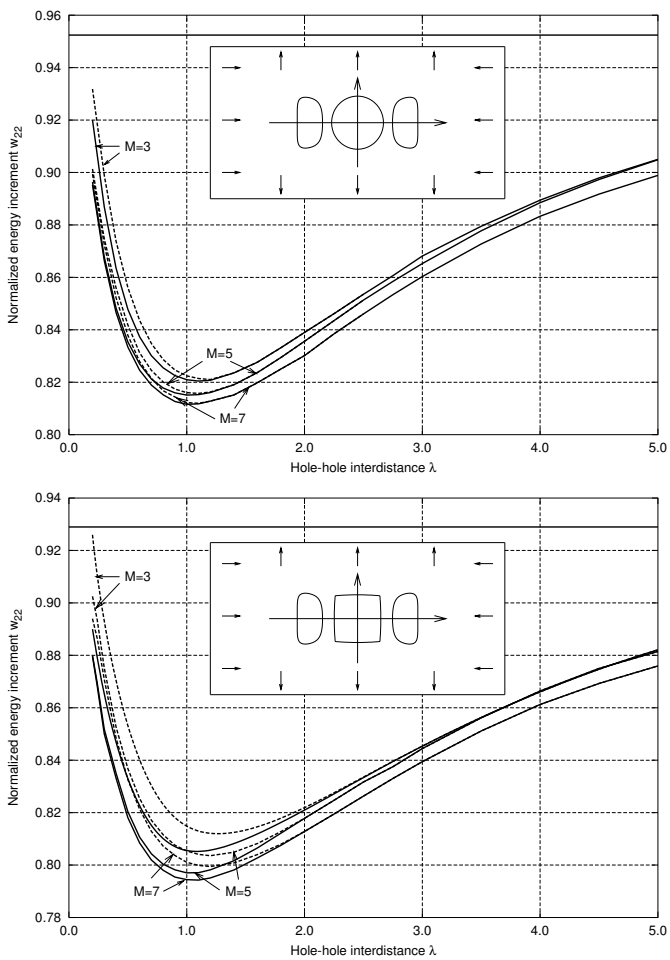

Figure 4. Values of min w_{22} as a function of the inter-distance λ with dependence on the problem mapping size N, with (solid lines) and without (dashed lines) optimization of the hole area. The value (5-6) of the minimum energy increment induced by the widely spaced holes is also added for comparison (straight line). Top: circular central hole case. Bottom: square-like central hole case.

w_{22} on the distance λ between the central and the side holes. Comparison to the limiting values (5-6) of the widely spaced optimal holes (straight lines) shows that the interaction of the holes provides an appreciable energy gain at any inter-distance λ, except at very small ones. Clear optima are observed in both cases for λ in the range 1.05–1.10, with a relative decrease in the energy of $\approx 15\%$, as compared to the values (5-6) for the corresponding case of the noninteracting holes. Compared to the increment (5-5) of a single circular hole, the auxiliary holes raise the gain to $\approx 19\%$, while a pair of identical interacting optimal holes conserves $\approx 12\%$ of the energy [Vigdergauz 2008a]. We note that the pre-optimization levels (5-4), (5-5), and, hence, the energy gain are both less for the square-like central hole. The difference between the solid and the dashed lines reflects the contribution related solely to the hole area variation in interval (5-1a), which remains small even near the global increment minimum. This indicates that the potential of changing the area of the hole for energy optimization is rather limited at the current geometry.

Figure 5 exhibits the shape evolution with the increasing distance λ. As expected, in both cases the optimal shape grades into the square-like optimal hole of the area $f_1 = f_0 = \pi$, in accordance with (5-6) and (3-2).

The dependence $f_1(\lambda)$ of the optimal hole area on the spacing between the holes is shown in Figure 6.

Finally, we try to qualitatively evaluate the hoop stresses induced along the energy optimal and the fixed central hole. When L_0 is a unit circle, the angular stress distribution obtained as a by-product of

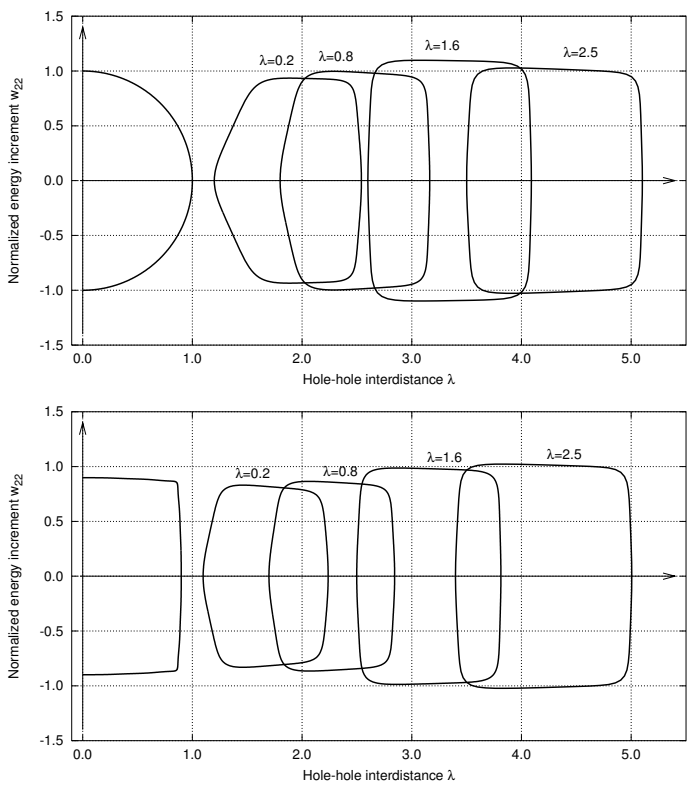

Figure 5. Evolution of the energy-minimizing hole with the distance d at $N = 7$, for the circular (top) and square-like (bottom) central hole.

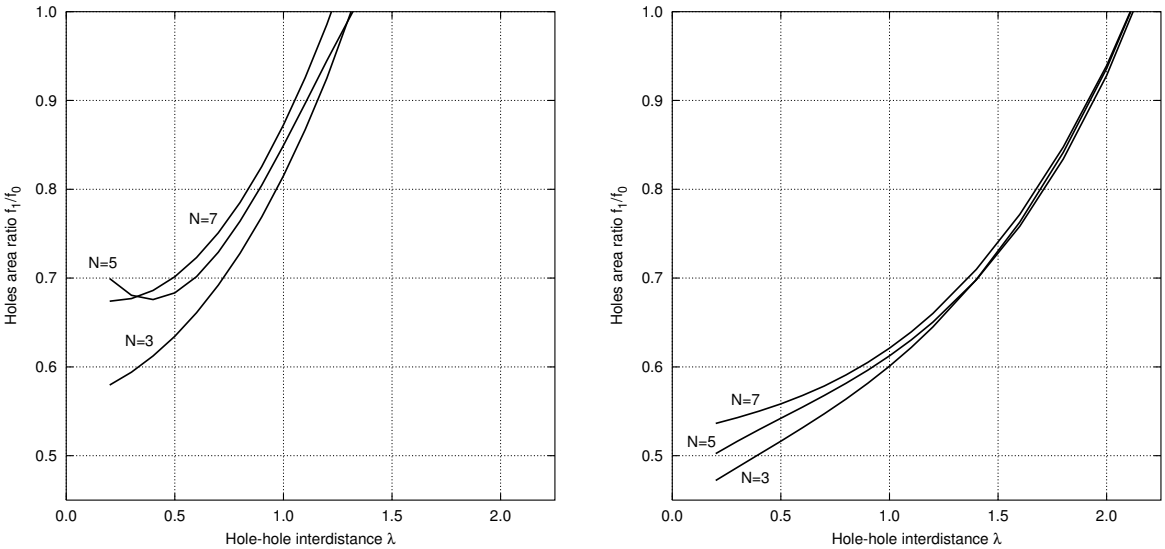

Figure 6. Ratio of the optimal and fixed hole areas as a function of their inter-distance for the circular (left) and the square-like (right) central hole.

the energy optimization is shown in Figure 7. The nonphysical oscillations observed indicate that the currently configured optimization scheme is not adequate for quantitative assessment of the stresses. On the other hand, the oscillations occur well away from the global extrema, so the latter can be cautiously used to conclude that, as N increases, the stresses maxima show a decrease (though not monotonic) in parallel with the energy (Table 3).

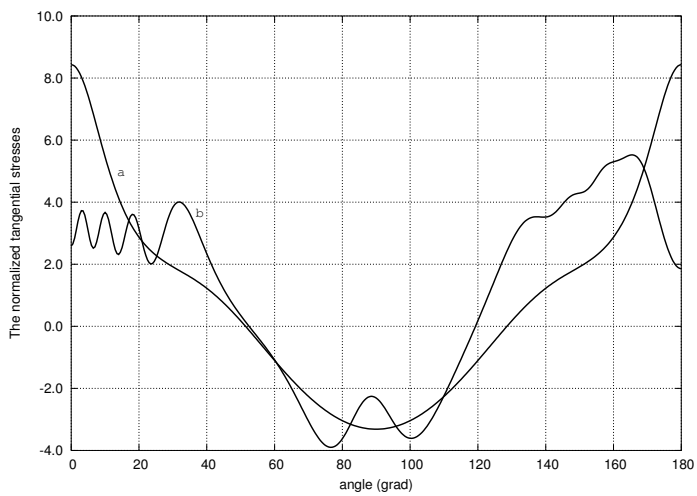

Figure 7. Circular central hole case: hoop stresses distribution along the central (a) and the energy-minimizing side holes (b), for $N = 7$ and $\lambda = 0.2$. The holes themselves are depicted in Figure 3, left.

	N	0	1	2	3	5	7
L_0	maximum	14.0200	9.6408	8.6397	9.2894	8.4561	8.4309
	minimum	−3.1456	−3.6886	−3,4341	−3.4155	−3.3545	−3.3145
L_1	maximum	11.0186	7.3296	6.6463	7.1169	5.6460	5.5241
	minimum	−6.2377	−3.9310	−4.2924	−4.2819	−3.9522	−3.9000

Table 3. Extremal values of the hoop stresses along the central circular and side energy-minimizing holes at $\lambda = 0.2$ with increasing number N of the mapping terms from $N = 0$ (a circle) and on.

7. Closure and future applications

The paper presented a GA-based study of a rather difficult shape optimization problem in an infinite 2D elastic region with partially fixed boundary. This was done by combining the complex variable technique with a novel shape representation specially tailored for the current purposes. For clarity, we repeat here the essential points of the approach.

First, the advanced direct solver is employed for a fast and stable fitness evaluation. The solver engine is based on a standard numerical treatment of a specially derived system of linear algebraic equations in Laurent coefficients for the first KM potential only. The system entries involve boundary integrals of a regular, rather than a singular, type.

Second, an efficient shape encoding scheme is used within the GA framework. Based on a separate conformal mapping of each free contour, it has a twofold benefit over the commonly used nodal points representation. First, as design variables, the mapping coefficients drastically reduce the computational size of the problem, because even a small number of them provides a representative pool of admissible curves. Possible excessive smoothing of angular points through neglecting the high-order coefficients is counteracted by the integral nature of the energy-related criterion. Second, any mutual arrangement of the mapped shapes is straightforwardly met by displacing and scaling.

The approach described works well also when elastic inclusions are taken instead of holes [Vigdergauz 2008b], and may be applied to similar problems in other fields of continuum mechanics. In elastostatics, it seems promising to use the proposed scheme for yet unsolved shape optimization problems in *finite* domains. We are now pursuing this issue.

References

[Alfors 1979] L. Alfors, *Complex analysis*, 3rd edition ed., McGraw-Hill, New York, 1979.

[Holland 1975] J. H. Holland, *Adaptation in natural and artificial systems*, University of Michigan Press, Ann Arbor, MI, 1975.

[Levy and Lessman 1959] H. Levy and F. Lessman, *Finite difference equations*, Pitman, London, 1959.

[Muskhelishvili 1975] N. I. Muskhelishvili, *Some basic problems of the mathematical theory of elasticity*, 2nd ed., Noordhoff, Leiden, 1975.

[Vigdergauz 2006] S. B. Vigdergauz, "Energy-minimizing hole in an elastic plate under remote shear", *J. Mech. Mater. Struct.* **1**:2 (2006), 387–406.

[Vigdergauz 2008a] S. B. Vigdergauz, "Shape optimization in an elastic plate under remote shear: from single to interacting holes", *J. Mech. Mater. Struct.* **3**:7 (2008), 1341–1363.

[Vigdergauz 2008b] S. B. Vigdergauz, "Stress-minimizing inclusion in an elastic plate under remote shear", *J. Mech. Mater. Struct.* **3**:1 (2008), 63–83.

[Vigdergauz and Cherkaev 1986] S. B. Vigdergauz and A. V. Cherkaev, "A hole in a plate optimal for its biaxial extension-compression", *J. Appl. Math. Mech.* **50**:3 (1986), 401–404.

Received 1 Aug 2009. Revised 26 Dec 2009. Accepted 28 Dec 2009.

SHMUEL VIGDERGAUZ: smuel@iec.co.il
Research and Development Division, The Israel Electric Corporation Ltd., P.O.Box 10, 31000 Haifa, Israel

JOURNAL OF MECHANICS OF MATERIALS AND STRUCTURES
Vol. 5, No. 4, 2010

INFLUENCE OF DIFFERENT INTEGRAL KERNELS ON THE SOLUTIONS OF BOUNDARY INTEGRAL EQUATIONS IN PLANE ELASTICITY

Y. Z. CHEN, X. Y. LIN AND Z. X. WANG

A modified integral kernel is introduced for boundary integral equations (BIE). The formulation for the modified kernel is based on a representation in pure deformable form of the fundamental solution of concentrated forces. It is found that the modified kernel can be applied to any case, even if the loadings on the contour are not in equilibrium in an exterior boundary value problem. The influence of different integral kernels on solutions of BIE, particularly in the Neumann problem and Dirichlet problem, are addressed. Numerical examples are presented to prove the assertion proposed. Properties of solutions from the usage of the modified integral kernel are studied in detail. The influence of different integral kernels on the degenerate scale are discussed and numerical results are provided. It is found that the influence of the constants involved in the integral kernels is significant. For the cases of the elliptic and rectangular contour, the influence on the degenerate scale is studied with numerical results.

1. Introduction

The boundary integral equation (BIE) is widely used in elasticity. The fundamentals of BIE are found in [Rizzo 1967; Cruse 1969; Jaswon and Symm 1977; Brebbia et al. 1984]. Recent development of the boundary element method is summarized in [Cheng and Cheng 2005].

There are still some problems in the study of BIEs. The first is the regularity condition in the exterior boundary value problem (BVP) [Brebbia et al. 1984]. Generally, Betti's reciprocal theorem or the Somigliana identity is used for the formulation of the BIE. In the exterior BVP, if a mutual work difference integral (MWDI) on a sufficient large circle vanishes, the regularity condition is satisfied. However, this condition has not been studied clearly. Once the BIE in plane elasticity is formulated for the exterior region, one must meet the MWDI (the terms $D^{*1}_{i(CR)}(\xi)$ and $D^{*2}_{i(CR)}(\xi)$ in Equations (8) and (17)). If the MWDI vanishes, the regularity condition at infinity is satisfied. In fact, the MWDI is the difference of two works: the work done by the fundamental field on the physical stress field and vice versa. Therefore, the properties of the MWDI depend on the representation of the fundamental field and the properties of the physical stress field. A general expression for the MWDI from the two stress fields was obtained in [Chen 2003]. This will be the theoretical basis of the present study.

In fact, it has been proved that if the loadings applied on the contour in the exterior BVP are not in equilibrium, instead of using the usual integral kernel $U^{*2}_{ij}(\xi, x)$ (see (14)) one should use a modified one $U^{*1}_{ij}(\xi, x)$ (see (6)). The two integral kernels have a difference of a constant. Clearly, the two different integral kernels will influence the properties of solutions obtained.

Keywords: boundary integral equation, exterior boundary value problem, regularity condition, numerical method, degenerate scale problem.

The second problem in this field is the degenerate scale problem [He et al. 1996; Chen et al. 2002; 2005; Vodicka and Mantic 2008; Chen and Shen 2007]. In the degenerate scale problem, an improper solution in the Dirichlet problem for BIE exists if the used size is near the critical value. Clearly, the degenerate scale for the individual problem must depend on the used integral kernel, (for example, $U_{ij}^{*1}(\xi, x)$ or $U_{ij}^{*2}(\xi, x)$). This problem has also not been investigated in detail.

This paper complements the usual integral kernel $U_{ij}^{*2}(\xi, x)$ (see (14)) with a modified one, $U_{ij}^{*1}(\xi, x)$ (see (6)). The formulation for the modified kernel is based on a representation in pure deformable form of the fundamental solution of concentrated forces. The two kernels $U_{ij}^{*1}(\xi, x)$ and $U_{ij}^{*2}(\xi, x)$ have a difference of a constant. It is found that $U_{ij}^{*1}(\xi, x)$ can be used to any case, even if the loadings on the contour are not in equilibrium in an exterior BVP. The influence of the different integral kernels on solutions of the BIE, particularly in the Neumann problem and the Dirichlet problem, are addressed. The properties of solution using $U_{ij}^{*1}(\xi, x)$ are discussed in detail. Numerical examples are presented to prove the assertion proposed. The influence of the used integral kernels on the degenerate scale is discussed and numerical results are provided. It is found that the influence of the constant in the integral kernels on the degenerate scale is significant. For the cases of elliptic and rectangular contours, the influence is studied with numerical results.

2. Influence of different kernels on the solutions of exterior BIE

2.1. ***Formulation of kernels $U_{ij}^{*1}(\xi, x)$ and $U_{ij}^{*2}(\xi, x)$ and the relevant BIEs.*** The following analysis depends on the complex variable function method in plane elasticity [Muskhelishvili 1953]. In this method, the stresses $(\sigma_x, \sigma_y, \sigma_{xy})$, the resultant forces (X, Y), and the displacements (u, v) are expressed in terms of the two complex potentials $\phi(z)$ and $\psi(z)$ such that

$$\sigma_x + \sigma_y = 4\,\mathrm{Re}\,\phi'(z), \quad \sigma_y - \sigma_x + 2i\sigma_{xy} = 2[\bar{z}\phi''(z) + \psi'(z)], \tag{1}$$

$$f = -Y + iX = \phi(z) + z\overline{\phi'(z)} + \overline{\psi(z)}, \tag{2}$$

$$2G(u + iv) = \kappa\phi(z) - z\overline{\phi'(z)} - \overline{\psi(z)}, \tag{3}$$

where $z = x + iy$ denotes a complex variable, G is the shear modulus of elasticity, $\kappa = (3 - \nu)/(1 + \nu)$ for the plane stress problems, $\kappa = 3 - 4\nu$ for the plane strain problems, and ν is Poisson's ratio. In the present study, the plane strain condition is assumed throughout. In the following, we occasionally rewrite the displacements u and v as u_1 and u_2; σ_x, σ_y, and σ_{xy} as σ_{11}, σ_{22}, and σ_{12}; and x and y as x_1 and x_2, respectively.

It is emphasized that we only consider the exterior BVP. Also, the remote tractions σ_x^∞, σ_y^∞, and σ_{xy}^∞ are assumed to tend to zero.

The formulation of the BIE is introduced below. If the concentrated forces (P_x, P_y) are applied at the point $z = t$ (Figure 1a), the relevant complex potentials are defined by

$$\phi_{(\alpha)}(z) = F\ln(z - t), \quad \psi_{(\alpha)}(z) = -\kappa\bar{F}\ln(z - t) - \frac{F\bar{t}}{z - t} \tag{4}$$

(see [Muskhelishvili 1953]), where

$$F = -\frac{P_x + iP_y}{2\pi(\kappa + 1)}. \tag{5}$$

In (4), the subscript (α) denotes the fundamental solution initiated by concentrated forces.

Note that the relevant complex potentials shown in (4) are expressed in a pure deformable form [Chen and Lin 2008].

A direct substitution from the complex potentials shown in (4) in the proper place will lead to the following kernel [Chen and Lin 2008]:

$$U_{ij}^{*1}(\xi, x) = \frac{1}{8\pi(1-\nu)G}\big(-(3-4\nu)\ln(r)\delta_{ij} + r_{,i}r_{,j} - 0.5\delta_{ij}\big), \tag{6}$$

which is used in a BIE mentioned below.

Without losing generality, we can introduce the BIE for the region between the elliptic contour Γ and a large circle CR (Figure 1b). The observation point ξ is assumed on the elliptic contour $\xi \in \Gamma$. For the plane strain case, the suggested BIE can be written as follows [Brebbia et al. 1984]:

$$\tfrac{1}{2}u_i(\xi) + \int_\Gamma P_{ij}^*(\xi, x)u_j(x)\,ds(x) = \int_\Gamma U_{ij}^{*1}(\xi, x)p_j(x)\,ds(x) + D_{i(\mathrm{CR})}^{*1}(\xi) \quad (i = 1, 2,\ \xi \in \Gamma), \tag{7}$$

where $D_{i(\mathrm{CR})}^{*1}(\xi)$ is a MWDI on a large circle CR and is defined by

$$D_{i(\mathrm{CR})}^{*1}(\xi) = -\int_{\mathrm{CR}} P_{ij}^*(\xi, x)u_j(x)\,ds(x) + \int_{\mathrm{CR}} U_{ij}^{*1}(\xi, x)p_j(x)\,ds(x) \quad (i = 1, 2,\ \xi \in \Gamma). \tag{8}$$

In (8), CR denotes the sufficient large circle with radius R.

In addition, the kernel $P_{ij}^*(\xi, x)$ is defined by [Brebbia et al. 1984]

$$P_{ij}^*(\xi, x) = -\frac{1}{4\pi(1-\nu)}\frac{1}{r}\big\{(r_{,1}n_1 + r_{,2}n_2)\big((1-2\nu)\delta_{ij} + 2r_{,i}r_{,j}\big) + (1-2\nu)(n_i r_{,j} - n_j r_{,i})\big\}, \tag{9}$$

where the Kronecker delta δ_{ij} is defined as $\delta_{ij} = 1$ for $i = j$, $\delta_{ij} = 0$ for $i \neq j$, and

$$r_{,1} = \frac{x_1 - \xi_1}{r} = \cos\alpha, \quad r_{,2} = \frac{x_2 - \xi_2}{r} = \sin\alpha, \qquad n_1 = -\sin\beta, \quad n_2 = \cos\beta, \tag{10}$$

where angles α and β are indicated in Figure 1.

Even the physical field is caused by a nonequilibrium force on the elliptic contour. We have proved in [Chen and Lin 2008] that $D_{i(\mathrm{CR})}^{*1}(\xi) = 0$ $(i = 1, 2)$:

$$D_{i(\mathrm{CR})}^{*1}(\xi) = -\int_{\mathrm{CR}} P_{ij}^*(\xi, x)u_j(x)\,ds(x) + \int_{\mathrm{CR}} U_{ij}^{*1}(\xi, x)p_j(x)\,ds(x) = 0 \quad (i = 1, 2,\ \xi \in \Gamma). \tag{11}$$

Therefore, (7) can be reduced to

$$\tfrac{1}{2}u_i(\xi) + \int_\Gamma P_{ij}^*(\xi, x)u_j(x)\,ds(x) = \int_\Gamma U_{ij}^{*1}(\xi, x)p_j(x)\,ds(x) \quad (i = 1, 2,\ \xi \in \Gamma). \tag{12}$$

Note that the displacements $u_j(x)$ on the left side of (12) should be expressed in pure deformable form.

In addition, if the same concentrated forces (P_x, P_y) are applied at the point $z = t$ (Figure 1a), the relevant complex potentials can be defined alternatively by [Muskhelishvili 1953]

$$\phi_{(\alpha)}(z) = F\ln(z - t), \qquad \psi_{(\alpha)}(z) = -\kappa\bar{F}\ln(z - t) - \frac{F\bar{t}}{z - t} + \bar{F}. \tag{13}$$

The complex potentials shown in (13) differ from those in (4) by a constant $\bar{F}$ in the function $\psi_{(\alpha)}(z)$.

Comparing (4) with (13), an additional pair of complex potentials $\phi(z) = 0$ and $\psi(z) = \bar{F}$ is presented in (13). Clearly, this pair causes no stresses anywhere, and represents a rigid translation. Therefore, it is said that the complex potentials in (13) are expressed in an impure deformable form.

A direct substitution from the complex potentials in (13) in the proper place will lead to the following kernel [Chen and Lin 2008]:

$$U_{ij}^{*2}(\xi, x) = \frac{1}{8\pi(1-\nu)G}\big(-(3-4\nu)\ln(r)\,\delta_{ij} + r_{,i}r_{,j}\big). \tag{14}$$

The two kernels have the relation

$$U_{ij}^{*2}(\xi, x) - U_{ij}^{*1}(\xi, x) = \frac{1}{16\pi(1-\nu)G}\delta_{ij}. \tag{15}$$

The kernel $U_{ij}^{*2}(\xi, x)$ is found in [Brebbia et al. 1984]. Similarly, from the kernel $U_{ij}^{*2}(\xi, x)$ in (14), we obtain the BIE

$$\tfrac{1}{2}u_i(\xi) + \int_\Gamma P_{ij}^*(\xi, x)u_j(x)\,ds(x) = \int_\Gamma U_{ij}^{*2}(\xi, x)p_j(x)\,ds(x) + D_{i(\mathrm{CR})}^{*2}(\xi) \quad (i = 1, 2,\ \xi \in \Gamma), \tag{16}$$

where $D_{i(\mathrm{CR})}^{*2}(\xi)$ is a MWDI on a large circle and is defined by

$$D_{i(\mathrm{CR})}^{*2}(\xi) = -\int_{\mathrm{CR}} P_{ij}^*(\xi, x)u_j(x)\,ds(x) + \int_{\mathrm{CR}} U_{ij}^{*2}(\xi, x)p_j(x)\,ds(x) \quad (i = 1, 2,\ \xi \in \Gamma). \tag{17}$$

It was proved in [Chen and Lin 2008] that when the physical field is caused by a nonequilibrium force on the elliptic contour, we have $D_{i(\mathrm{CR})}^{*2}(\xi) \neq 0$ for $i = 1, 2$ (so the BIE (16) cannot be reduced further), while in the opposite case — when the physical field is caused by an equilibrium force on the elliptic contour — we have $D_{i(\mathrm{CR})}^{*2}(\xi) = 0$ for $i = 1, 2$, and then the BIE (16) can be reduced to the form

$$\tfrac{1}{2}u_i(\xi) + \int_\Gamma P_{ij}^*(\xi, x)u_j(x)\,ds(x) = \int_\Gamma U_{ij}^{*2}(\xi, x)p_j(x)\,ds(x) \quad (i = 1, 2,\ \xi \in \Gamma). \tag{18}$$

Note that in the exterior BVP, the BIE using the kernel $U_{ij}^{*1}(\xi, x)$, shown by (6), can always be used, even if the applied loadings on the elliptic contour are not in equilibrium. However, in the exterior BVP, the BIE using $U_{ij}^{*2}(\xi, x)$, shown by (14), can only be used when the applied loadings on the elliptic contour are in equilibrium.

2.2. ***General properties of the solutions of BIEs.*** As claimed previously, the kernel $U_{ij}^{*1}(\xi, x)$ can always be used, without regard to the loading condition on the elliptic contour. Therefore, for the exterior BVP we suggest the BIE (12), which we repeat here for convenience:

$$\tfrac{1}{2}u_i(\xi) + \int_\Gamma P_{ij}^*(\xi, x)u_j(x)\,ds(x) = \int_\Gamma U_{ij}^{*1}(\xi, x)p_j(x)\,ds(x) \quad (i = 1, 2,\ \xi \in \Gamma). \tag{19}$$

The problem of the equivalence of the solution of the BIE and an elasticity solution is studied below. As stated previously, the physical stress field is assumed in pure deformable form. Therefore, if the functions $u_i(\xi)$, $u_j(x)$, and $p_j(x)$ in (12) are boundary values of an elasticity solution expressed in pure deformable form, these functions must satisfy the BIE in (12); if $u_i(\xi)$, $u_j(x)$, and $p_j(x)$ in (12) are

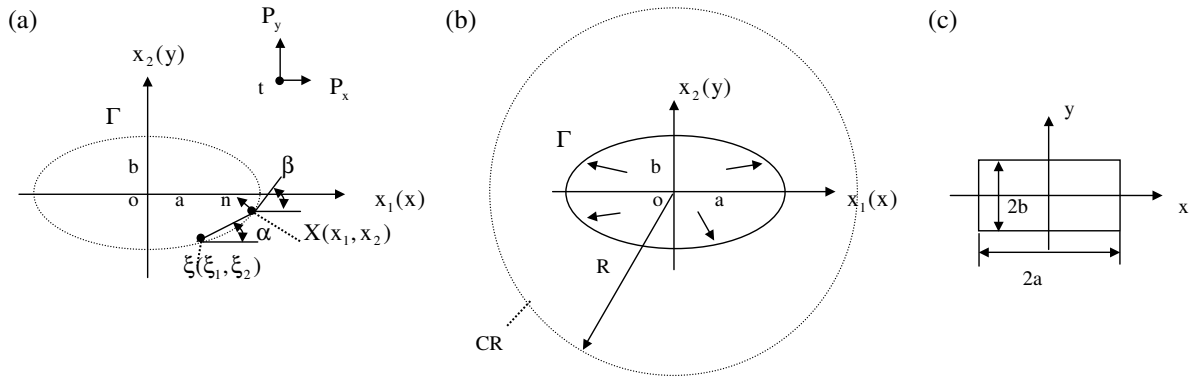

Figure 1. (a) A concentrated force applied at point $z = t$, or the loading condition for the α-field. (b) Some loadings having resultant forces applied on the elliptic contour, or the loading condition for the β-field or physical stress field. (c) A rectangular notch.

boundary values of an elasticity solution expressed in an impure deformable form, they must not satisfy the BIE shown by (12).

This situation can be seen from the following example. It is known that there are three particular elasticity solutions:

$$\begin{aligned}
&\begin{Bmatrix} u_1^{(1)} \\ u_2^{(1)} \end{Bmatrix} = \begin{Bmatrix} b_1^{(1)} \\ b_2^{(1)} \end{Bmatrix} = \begin{Bmatrix} 1 \\ 0 \end{Bmatrix}, && \sigma_{ij}^{(1)} = 0 \text{ and } p_i^{(1)} = 0, \\
&\begin{Bmatrix} u_1^{(2)} \\ u_2^{(2)} \end{Bmatrix} = \begin{Bmatrix} b_1^{(2)} \\ b_2^{(2)} \end{Bmatrix} = \begin{Bmatrix} 0 \\ 1 \end{Bmatrix}, && \sigma_{ij}^{(2)} = 0 \text{ and } p_i^{(2)} = 0, \\
&\begin{Bmatrix} u_1^{(3)} \\ u_2^{(3)} \end{Bmatrix} = \begin{Bmatrix} b_1^{(3)} \\ b_2^{(3)} \end{Bmatrix} = \begin{Bmatrix} -y_t \\ x_t \end{Bmatrix}, && \sigma_{ij}^{(3)} = 0 \text{ and } p_i^{(3)} = 0 \quad (t = x_t + i y_t \in \Gamma).
\end{aligned} \tag{20}$$

Clearly, the stress fields shown by (20) represent translations or rotation for the body. It has been proved that substituting those displacements on the contour into the left-hand term of (12) yields

$$\tfrac{1}{2} u_i(\xi) + \int_\Gamma P_{ij}^*(\xi, x) u_j(x)\, ds(x) \Big|_{u_i \to b_i^{(k)}} = b_i^{(k)} \neq 0 \quad (k = 1, 2, 3). \tag{21}$$

Substituting the tractions $p_j(x)$ on the contour shown by (20) into right-hand term of (12) yields

$$\int_\Gamma U_{ij}^{*1}(\xi, x) p_j(x)\, ds(x) \Big|_{p_j \to p_j^{(k)} = 0} = 0. \tag{22}$$

Comparing (21) and (22), which are the left and right sides of (12) respectively, proves the assertion.

In the Neumann problem, the boundary tractions $\tilde{p}_j(x)$ $(j = 1, 2)$ are given beforehand. Therefore, in the case of the kernel $U_{ij}^{*1}(\xi, x)$, from (12) we can obtain the BIE

$$\tfrac{1}{2} u_i(\xi) + \int_\Gamma P_{ij}^*(\xi, x) u_j(x)\, ds(x) = g_i(\xi) \quad (i = 1, 2,\ \xi \in \Gamma), \tag{23}$$

where

$$g_i(\xi) = \int_\Gamma U_{ij}^{*1}(\xi, x)\tilde{p}_j(x)\,ds(x) \quad (i = 1, 2,\ \xi \in \Gamma). \tag{24}$$

In (24), $\tilde{p}_j(x)$ $(j = 1, 2)$ are the boundary tractions which are given beforehand.

It is known that the BIE in (23) possesses the invertible property; that is, it can be solved for any right-hand term $g_i(\xi)$. However, the obtained $u_j(x)$ $(j = 1, 2)$ belong to some boundary values of displacements in an elasticity solution expressed in pure deformable form.

Similarly, in the Dirichlet problem, the boundary displacements $\tilde{u}_j(x)$ $(j = 1, 2)$ are given beforehand. Therefore, in the case of the kernel $U_{ij}^{*1}(\xi, x)$, from (12) we can obtain the BIE

$$\int_\Gamma U_{ij}^{*1}(\xi, x)p_j(x)\,ds(x) = h_i(\xi) \quad (i = 1, 2,\ \xi \in \Gamma), \tag{25}$$

where

$$h_i(\xi) = \tfrac{1}{2}\tilde{u}_i(\xi) + \int_\Gamma P_{ij}^{*}(\xi, x)\tilde{u}_j(x)\,ds(x) \quad (i = 1, 2,\ \xi \in \Gamma). \tag{26}$$

In (26), $\tilde{u}_i(\xi)$ $(i = 1, 2)$ and $\tilde{u}_j(x)$ $(j = 1, 2)$ are the boundary displacements, which are given beforehand.

It is known that the BIE shown by (25) processes the invertible property only if the degenerate scale has not been reached [Vodicka and Mantic 2008]. In other words, the BIE shown by (25) can be solved for any right-hand term $h_i(\xi)$ only if the degenerate scale has not been reached. However, the obtained $p_j(x)$ $(j = 1, 2)$ belong to some boundary values of tractions in an elasticity solution. Generally, those tractions, $p_j(x)$ $(j = 1, 2)$, may have a resultant force along the contour.

2.3. ***Numerical investigation of the kernels $U_{ij}^{*1}(\xi, x)$ and $U_{ij}^{*2}(\xi, x)$ in the case of nonequilibrium loadings on the contour.*** In order to examine the behavior of the kernels $U_{ij}^{*1}(\xi, x)$ and $U_{ij}^{*2}(\xi, x)$, the relevant BIEs are repeated:

$$\tfrac{1}{2}u_i(\xi) + \int_\Gamma P_{ij}^{*}(\xi, x)u_j(x)\,ds(x) = \int_\Gamma U_{ij}^{*1}(\xi, x)p_j(x)\,ds(x) \quad (i = 1, 2,\ \xi \in \Gamma), \tag{27}$$

$$\tfrac{1}{2}u_i(\xi) + \int_\Gamma P_{ij}^{*}(\xi, x)u_j(x)\,ds(x) = \int_\Gamma U_{ij}^{*2}(\xi, x)p_j(x)\,ds(x) \quad (i = 1, 2,\ \xi \in \Gamma). \tag{28}$$

In all the problems studied subsequently, one knows a closed-form solution beforehand. Substituting the results from the known solution, say for $p_j(x)$ $(j = 1, 2)$, into the right-hand term of (12) will yield a BIE for $u_j(x)$ $(j = 1, 2)$. The displacements $u_j(x)$ $(j = 1, 2)$ can be obtained from the BIE, and then compared with those from the closed-form solution. In the solution of the BIE, the scale used is assumed to be sufficient large to avoid the used scale coinciding with the degenerate scale.

In the examples below, the ellipse has major semiaxis a and minor semiaxis b (Figure 1b). The plane strain condition and $\nu = 0.3$ are assumed. The elliptic contour is divided into 120 intervals. For the BIE solution, constant displacement and traction are assumed for each interval.

Example 1. We propose the complex potentials

$$\phi(z) = q_0 A \ln z, \quad \psi(z) = -\kappa q_0 \bar{A} \ln z, \quad \text{where } A = A_1 + i A_2, \tag{29}$$

where q_0 is a unit loading. From the complex potentials shown by (29) and (2), it can be seen that the following resultant forces are applied:

$$\{X + iY\}_{\text{re}} = -2\pi(\kappa + 1)q_0 A, \tag{30}$$

on the contour. In this case, the exact solution for the displacements and stresses on the boundary contour can be easily obtained from (1), (3) and (29).

In this example, the examination is performed from the viewpoint of the Neumann problem. The loadings applied on the contour, p_j $(j = 1, 2)$, are computed from the complex potentials in (29), and are then substituted into the right-hand term of (18). Standard numerical techniques are used to solve (18), and the boundary displacements u_j $(j = 1, 2)$ can be evaluated immediately. The calculated boundary displacements using the kernels $U_{ij}^{*1}(\xi, x)$ and $U_{ij}^{*2}(\xi, x)$, and those from the exact solution are expressed by

$$u_1 = \frac{q_0}{2G(1+\nu)} f_1(\theta), \qquad u_2 = \frac{q_0}{2G(1+\nu)} f_2(\theta), \qquad \text{(at the points } x = a\cos\theta,\ y = b\cos\theta). \tag{31}$$

For the case of $b/a = 0.25$, $a = 40$, $A_1 = 1$, and $A_2 = 0.5$, the results calculated using the kernels $U_{ij}^{*1}(\xi, x)$ and $U_{ij}^{*2}(\xi, x)$, and the exact results from the closed-form solution are shown in Figure 2, where $f_1(\theta)_{\text{ex}}$ and $f_2(\theta)_{\text{ex}}$ are from the exact solution, or from the complex potentials (29) directly; $f_1(\theta)_{*1}$ and $f_2(\theta)_{*1}$ are from the usage of the kernels $U_{ij}^{*1}(\xi, x)$; and $f_1(\theta)_{*2}$ and $f_2(\theta)_{*2}$ are from the usage of the kernels $U_{ij}^{*2}(\xi, x)$.

It is found from Figure 2 that the results computed for $f_1(\theta)_{*1}$ and $f_2(\theta)_{*1}$ using the kernel $U_{ij}^{*1}(\xi, x)$ are very accurate, coinciding with the results from the exact solution (denoted by $f_1(\theta)_{\text{ex}}$ and $f_2(\theta)_{\text{ex}}$). However, the results computed for $f_1(\theta)_{*2}$ and $f_2(\theta)_{*2}$ using the kernel $U_{ij}^{*2}(\xi, x)$ are very different from

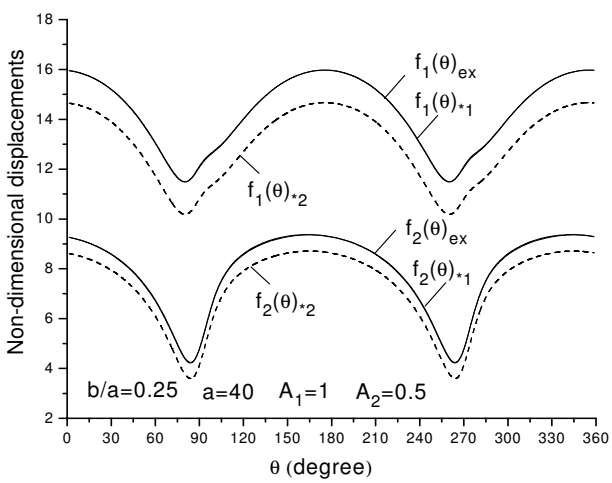

Figure 2. Nondimensional displacements for an exterior problem with nonequilibrium loadings on contour: $f_1(\theta)_{\text{ex}}$ and $f_2(\theta)_{\text{ex}}$ from the exact solution, $f_1(\theta)_{*1}$ and $f_2(\theta)_{*1}$ from the kernel $U_{ij}^{*1}(\xi, x)$, from $f_1(\theta)_{*2}$ and $f_2(\theta)_{*2}$ using $U_{ij}^{*2}(\xi, x)$, with $b/a = 0.25$, $a = 40$, $A_1 = 1$, and $A_2 = 0.5$ in (29) (see Figure 1b and (31)).

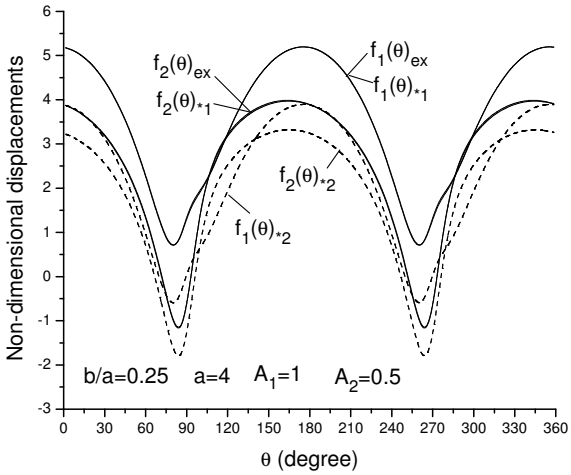

Figure 3. Nondimensional displacements for an exterior problem with nonequilibrium loadings on contour: $f_1(\theta)_{\rm ex}$ and $f_2(\theta)_{\rm ex}$ from the exact solution, $f_1(\theta)_{*1}$ and $f_2(\theta)_{*1}$ from the kernel $U_{ij}^{*1}(\xi, x)$, and $f_1(\theta)_{*2}$ and $f_2(\theta)_{*2}$ from $U_{ij}^{*2}(\xi, x)$, with $b/a = 0.25$, $a = 4$, $A_1 = 1$, and $A_2 = 0.5$ in (29) (see Figure 1b and (31)).

those from the exact solution. It is also found that the results computed for $f_1(\theta)_{*2}$ and $f_2(\theta)_{*2}$ have a constant difference from $f_1(\theta)_{\rm ex}$ and $f_2(\theta)_{\rm ex}$.

Similarly, in the case of $b/a = 0.25$, $a = 4$, $A_1 = 1$, and $A_2 = 0.5$, the results calculated using the kernels $U_{ij}^{*1}(\xi, x)$ and $U_{ij}^{*2}(\xi, x)$ and the exact results from the closed-form solution are shown in Figure 3. Similar phenomena as in the previous case can be observed.

Example 2. All the conditions used in Example 1 are still used in this example. However, in this example, the examination is performed from the viewpoint of the Dirichlet problem. The displacements on the contour, u_j $(j = 1, 2)$, are computed from the complex potentials shown by (29), and the obtained displacements u_j $(j = 1, 2)$ are substituted into the left-hand term of (12) (or (18)). Standard numerical technique is used to solve (12) (or (18)), and the boundary tractions p_j $(j = 1, 2)$ can be evaluated immediately. The calculated boundary tractions are expressed by

$$p_1 = q_0 g_1(\theta), \quad p_2 = q_0 g_2(\theta) \qquad \text{(at the points } x = a\cos\theta,\ x = b\cos\theta). \tag{32}$$

For the case of $b/a = 0.25$, $a = 40$, $A_1 = 1$, and $A_2 = 0.5$, the results calculated using the kernels $U_{ij}^{*1}(\xi, x)$ and $U_{ij}^{*2}(\xi, x)$, and the exact results from the closed-form solution are shown in Figure 4, where $g_1(\theta)_{\rm ex}$ and $g_2(\theta)_{\rm ex}$ are from exact solution, or from the complex potentials (29) directly, $g_1(\theta)_{*1}$ and $g_2(\theta)_{*1}$ are from the usage of the kernels $U_{ij}^{*1}(\xi, x)$, and $g_1(\theta)_{*2}$ and $g_2(\theta)_{*2}$ are from the usage the kernels $U_{ij}^{*2}(\xi, x)$.

It is found from Figure 4 that the results computed for $g_1(\theta)_{*1}$ and $g_2(\theta)_{*1}$ using the kernel $U_{ij}^{*1}(\xi, x)$ are very accurate, which coincides with the results from the exact solution (denoted by $g_1(\theta)_{\rm ex}$ and $g_2(\theta)_{\rm ex}$). However, the results computed for $g_1(\theta)_{*2}$ and $g_2(\theta)_{*2}$ using the kernel $U_{ij}^{*2}(\xi, x)$ are very different from those from the exact solution (denoted by $g_1(\theta)_{\rm ex}$ and $g_2(\theta)_{\rm ex}$).

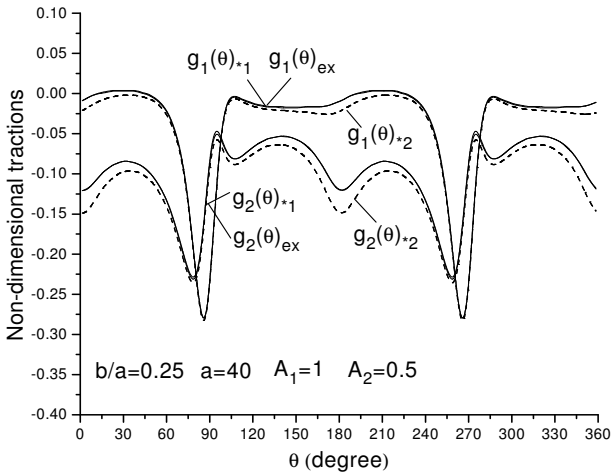

Figure 4. Nondimensional tractions for an exterior problem with nonequilibrium loadings on contour: $g_1(\theta)_{\text{ex}}$ and $g_2(\theta)_{\text{ex}}$ from the exact solution, $g_1(\theta)_{*1}$ and $g_2(\theta)_{*1}$ from the kernel $U_{ij}^{*1}(\xi, x)$, and $g_1(\theta)_{*2}$ and $g_2(\theta)_{*2}$ from $U_{ij}^{*2}(\xi, x)$, with $b/a = 0.25$, $a = 40$, $A_1 = 1$, and $A_2 = 0.5$ in (29) (see Figure 1b and (32)).

Similarly, in the case of $b/a = 0.25$, $a = 4$, $A_1 = 1$, and $A_2 = 0.5$, the results calculated using the kernels $U_{ij}^{*1}(\xi, x)$ and $U_{ij}^{*2}(\xi, x)$ and the exact results from the closed-form solution are shown in Figure 5. Similar results as in the previous case have been found. Particularly, in this case, the deviation of the result using the kernel $U_{ij}^{*2}(\xi, x)$ can reach a higher value. For example, in the case of $\theta = \pi$ we have $g_1(\theta)_{\text{ex}} = -1.195$ from the exact solution, $g_1(\theta)_{*1} = -1.200$ using the kernel $U_{ij}^{*1}(\xi, x)$, and $g_1(\theta)_{*2} = -2.842$ using the kernel $U_{ij}^{*2}(\xi, x)$; see Figure 5.

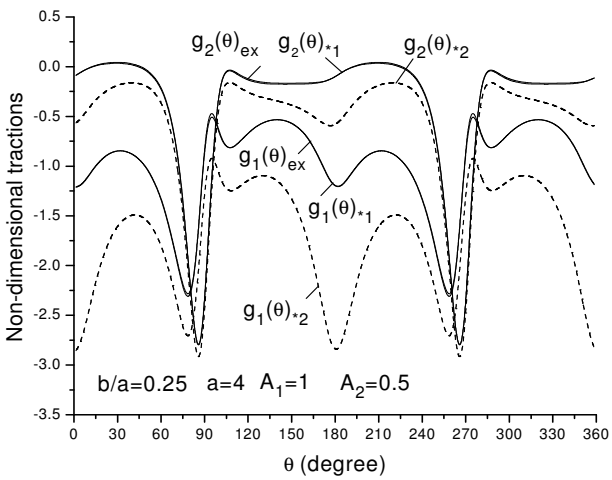

Figure 5. Nondimensional tractions for an exterior problem with nonequilibrium loadings on contour: $g_1(\theta)_{\text{ex}}$ and $g_2(\theta)_{\text{ex}}$ from the exact solution, $g_1(\theta)_{*1}$ and $g_2(\theta)_{*1}$ from the kernel $U_{ij}^{*1}(\xi, x)$, and $g_1(\theta)_{*2}$ and $g_2(\theta)_{*2}$ from $U_{ij}^{*2}(\xi, x)$, with $b/a = 0.25$, $a = 4$, $A_1 = 1$, and $A_2 = 0.5$ in (29) (see Figure 1b and (32)).

2.4. ***Numerical investigation of the kernels $U_{ij}^{*1}(\xi, x)$ and $U_{ij}^{*2}(\xi, x)$ in the case of equilibrium loadings on the contour.*** As mentioned previously, in the case of equilibrium loadings on the contour, the solutions obtained from the two kinds of BIE shown in (12) and (18) must be the same. This conclusion is also examined in the following examples.

Example 3. In this example, we propose the complex potentials

$$\phi(z) = q_0 \frac{A}{z}, \quad \psi(z) = q_0 \frac{B}{z}, \quad \text{where } A = A_1 + iA_2, \quad B = B_1 + iB_2, \tag{33}$$

where q_0 is a unit loading. From the complex potentials in (33) we see that the loadings applied on the contour must be in equilibrium [Muskhelishvili 1953].

Similarly, in the Neumann problem, the calculated boundary displacements using the kernel $U_{ij}^{*1}(\xi, x)$ or $U_{ij}^{*2}(\xi, x)$ and those from the exact solution are expressed by

$$u_1 = \frac{q_0}{2G(1+\nu)} f_1(\theta), \quad u_2 = \frac{q_0}{2G(1+\nu)} f_2(\theta) \quad \text{(at the points } x = a\cos\theta,\ x = b\cos\theta). \tag{34}$$

For the case of $b/a = 0.25$, $a = 40$, $A_1 = 1$, $A_2 = 0.5$, $B_1 = 1$, and $B_2 = 0.5$ the calculated results using the kernels $U_{ij}^{*1}(\xi, x)$ and $U_{ij}^{*2}(\xi, x)$ and the exact results from the closed-form solution are shown in Figure 6, where $f_1(\theta)_{\text{ex}}$ and $f_2(\theta)_{\text{ex}}$ are from exact solution, or from the complex potentials (33) directly; $f_1(\theta)_{*1}$ and $f_2(\theta)_{*1}$ are from the usage of the kernels $U_{ij}^{*1}(\xi, x)$, while $f_1(\theta)_{*2}$ and $f_2(\theta)_{*2}$ are from the usage of $U_{ij}^{*2}(\xi, x)$.

It is found from Figure 6 that the results computed using the kernel $U_{ij}^{*1}(\xi, x)$ or $U_{ij}^{*2}(\xi, x)$ and those from the exact solution are merged into the same curves.

Example 4. All the conditions used in Example 3 are still used in this example. However, in this example, the examination is performed from the viewpoint of the Dirichlet problem. The displacements on the

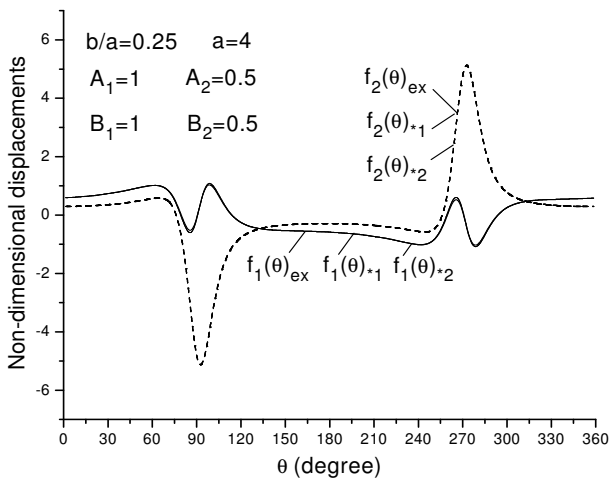

Figure 6. Nondimensional displacements for an exterior problem with nonequilibrium loadings on contour: $f_1(\theta)_{\text{ex}}$ and $f_2(\theta)_{\text{ex}}$ from the exact solution, $f_1(\theta)_{*1}$ and $f_2(\theta)_{*1}$ from the kernel $U_{ij}^{*1}(\xi, x)$, and $f_1(\theta)_{*2}$, and $f_2(\theta)_{*2}$ from $U_{ij}^{*2}(\xi, x)$, with $b/a = 0.25$, $a = 4$, $A_1 = 1$, $A_2 = 0.5$, $B_1 = 1$, and $B_2 = 0.5$ in (33) (see Figure 1b and (31)).

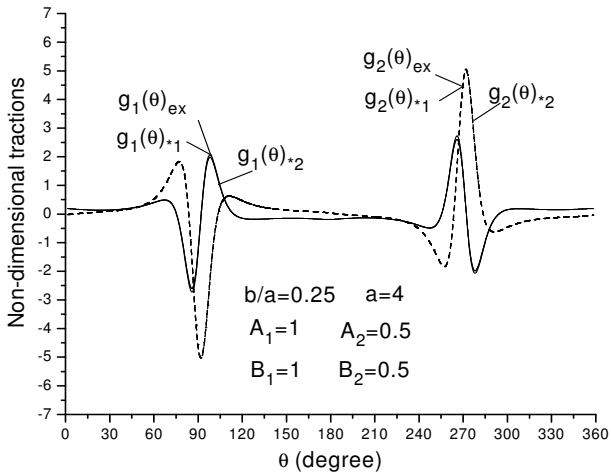

Figure 7. Nondimensional tractions for an exterior problem with nonequilibrium loadings on contour: $g_1(\theta)_{\text{ex}}$ and $g_2(\theta)_{\text{ex}}$ from the exact solution, $g_1(\theta)_{*1}$ and $g_2(\theta)_{*1}$ from the kernel $U_{ij}^{*1}(\xi, x)$, and $g_1(\theta)_{*2}$, and $g_2(\theta)_{*2}$ from $U_{ij}^{*2}(\xi, x)$, with $b/a = 0.25$, $a = 4$, $A_1 = 1$, $A_2 = 0.5$, $B_1 = 1$, and $B_2 = 0.5$ in (33) (see Figure 1b and (32)).

contour, u_j $(j = 1, 2)$, are computed from the complex potentials in (33), and the obtained displacements u_j $(j = 1, 2)$ are substituted into the left-hand term of (12) (or (18)). The calculated boundary tractions are expressed by

$$p_1 = q_0 g_1(\theta), \quad p_2 = q_0 g_2(\theta) \quad \text{(at the points } x = a\cos\theta,\ x = b\cos\theta). \tag{35}$$

For the case of $b/a = 0.25$, $a = 40$, $A_1 = 1$, $A_2 = 0.5$, $B_1 = 1$, and $B_2 = 0.5$ the results calculated using the kernels $U_{ij}^{*1}(\xi, x)$ and $U_{ij}^{*2}(\xi, x)$ and the exact results from the closed-form solution are shown in Figure 7, where $g_1(\theta)_{\text{ex}}$ and $g_2(\theta)_{\text{ex}}$ are from exact solution, or from the complex potentials (33) directly; $g_1(\theta)_{*1}$ and $g_2(\theta)_{*1}$ are from the usage of the kernels $U_{ij}^{*1}(\xi, x)$, while $g_1(\theta)_{*2}$ and $g_2(\theta)_{*2}$ are from the usage of $U_{ij}^{*2}(\xi, x)$.

It is found from Figure 7 that the results computed from the usage of kernel $U_{ij}^{*1}(\xi, x)$ or $U_{ij}^{*2}(\xi, x)$ and those from the exact solution are merged into the same curves.

3. Numerical evaluations for degenerate scale problems for different kernels $U_{ij}^{*g}(\xi, x)$

Instead of the two kernels $U_{ij}^{*1}(\xi, x)$ and $U_{ij}^{*2}(\xi, x)$, a kernel $U_{ij}^{*g}(\xi, x)$ in a more general form is defined as

$$U_{ij}^{*g}(\xi, x) = \frac{1}{8\pi(1-\nu)G}\left(-(3-4\nu)\ln(r)\delta_{ij} + r_{,i}r_{,j} - s\delta_{ij}\right), \tag{36}$$

where s can take any real value.

Clearly, a homogeneous equation for the degenerate scale problem using the kernel $U_{ij}^{*g}(\xi, x)$ can be formulated:

$$\int_{\Gamma_d} U_{ij}^{*g}(\xi, x)\, p_j(x)\, ds(x) = 0 \quad (i = 1, 2,\ \xi \in \Gamma). \tag{37}$$

In the formulation, one wants to find a particular size such that (37) has a nontrivial solution for $p_j(x)$, or $p_j(x) \neq 0$. By using relevant solutions in the normal scale problem, the degenerate scale problem can be solved [Chen et al. 2005; Vodicka and Mantic 2008].

In [Chen et al. 2009], after using two fundamental solutions in the normal scale, the degenerate scale problem can be solved. In this paper, the method suggested in [Chen et al. 2009] is used to solve the problems in the next two examples. Clearly, the degenerate scale must depend on the assumed constant s in (36).

Example 5. In the example, the ellipse has major semiaxis a and minor semiaxis b (Figure 1b). In computation, the plane strain condition and $\nu = 0.3$ are assumed. The elliptic contour is divided into 120 intervals. For the BIE solution, the constant displacement and traction are assumed for each interval. We vary s from -0.5 to 1.5 in steps of 0.5, and b/a from 0.1 to 1.0 in steps of 0.1, and list in Table 1 the two degenerate scales

$$a_{d1} = f_1(s, b/a), \quad a_{d2} = f_2(s, b/a). \tag{38}$$

We see that as the value of s increases from -0.5 to 1.5, the degenerate scale becomes smaller and smaller.

Example 6. In the example, the rectangular notch has width $2a$ and height $2b$ (Figure 1c). For the same ranges of s and b/a as in the previous example, we list in Table 2 the two degenerate scales

$$a_{d1} = g_1(s, b/a), \quad a_{d2} = g_2(s, b/a). \tag{39}$$

Again, as s increases from -0.5 to 1.5, the degenerate scale becomes smaller and smaller.

$a_{d1} = f_1(s, b/a)$										
$b/a =$	0.1	0.2	0.3	0.4	0.5	0.6	0.7	0.8	0.9	1.0
s										
-0.5	2.52541	2.41447	2.30954	2.21105	2.11897	2.03305	1.95295	1.87824	1.80853	1.74340
0	1.91291	1.82888	1.74940	1.67479	1.60504	1.53997	1.47929	1.42270	1.36990	1.32057
0.5	1.44896	1.38531	1.32511	1.26860	1.21577	1.16647	1.12051	1.07765	1.03765	1.00028
1	1.09754	1.04932	1.00372	0.96092	0.92090	0.88356	0.84875	0.81628	0.78598	0.75768
1.5	0.83135	0.79483	0.76029	0.72786	0.69755	0.66927	0.64290	0.61830	0.59535	0.57392
$a_{d2} = f_2(s, b/a)$										
$b/a =$	0.1	0.2	0.3	0.4	0.5	0.6	0.7	0.8	0.9	1.0
s										
-0.5	3.97868	3.49681	3.11489	2.80545	2.55005	2.33597	2.15411	1.99784	1.86219	1.74340
0	3.01371	2.64871	2.35942	2.12503	1.93158	1.76942	1.63166	1.51329	1.41054	1.32057
0.5	2.28278	2.00631	1.78718	1.60963	1.46310	1.34027	1.23593	1.14627	1.06844	1.00028
1	1.72913	1.51971	1.35373	1.21924	1.10825	1.01521	0.93617	0.86826	0.80930	0.75768
1.5	1.30975	1.15112	1.02540	0.92353	0.83946	0.76899	0.70912	0.65767	0.61302	0.57392

Table 1. The degenerate scale $a_{d1} = f_1(s, b/a)$ and $a_{d2} = f_2(s, b/a)$ for an ellipse notch (see (38) and Figure 1b).

$a_{d1} = g_1(s, b/a)$										
$b/a =$	0.1	0.2	0.3	0.4	0.5	0.6	0.7	0.8	0.9	1.0
s										
−0.5	2.40472	2.22301	2.07631	1.95320	1.84796	1.75521	1.67343	1.60015	1.53398	1.47394
0	1.82149	1.68385	1.57273	1.47948	1.39977	1.32951	1.26756	1.21206	1.16194	1.11646
0.5	1.37971	1.27546	1.19129	1.12066	1.06028	1.00706	0.96014	0.91809	0.88013	0.84568
1	1.04508	0.96612	0.90236	0.84886	0.80312	0.76281	0.72727	0.69542	0.66666	0.64057
1.5	0.79162	0.73180	0.68351	0.64298	0.60834	0.57780	0.55088	0.52676	0.50498	0.48521
$a_{d2} = g_2(s, b/a)$										
$b/a =$	0.1	0.2	0.3	0.4	0.5	0.6	0.7	0.8	0.9	1.0
s										
−0.5	3.61122	3.04801	2.66064	2.37149	2.14534	1.96172	1.80951	1.68074	1.57017	1.47394
0	2.73537	2.30876	2.01534	1.79632	1.62502	1.48593	1.37064	1.27310	1.18935	1.11646
0.5	2.07195	1.74881	1.52655	1.36065	1.23090	1.12554	1.03821	0.96433	0.90089	0.84568
1	1.56943	1.32466	1.15631	1.03065	0.93236	0.85256	0.78641	0.73045	0.68239	0.64057
1.5	1.18879	1.00338	0.87587	0.78068	0.70623	0.64578	0.59568	0.55329	0.51689	0.48521

Table 2. The degenerate scale $a_{d1} = g_1(d, b/a)$ and $a_{d2} = g_2(d, b/a)$ for a rectangular notch (see (39) and Figure 1c).

4. Conclusions

From the our theoretical analysis and numerical examples we get the following conclusions. The kernel $U_{ij}^{*1}(\xi, x)$ can be used for arbitrary loading on the contour. However, the kernel $U_{ij}^{*2}(\xi, x)$ can only be used when the loading on the contour is in equilibrium. This is an effective way to examine a suggested boundary integral equation (BIE) by using a known solution, particularly through a solution expressed in complex potentials. In this case, since the solution is known beforehand, one can easily judge whether the formulation used in the computation is correct or not.

In the case of using the kernel $U_{ij}^{*1}(\xi, x)$, the properties of solutions of the BIE are clearly studied. If the degenerate scale has not been reached, the Dirichlet problem has a unique solution. Generally, the computed tractions on the boundary may result in resultant forces along the contour. In the Neumann problem, the computed displacements must belong to the boundary values of the displacement field expressed in pure deformable form.

In the degenerate scale problem, the constant s involved in the integral kernel $U_{ij}^{*g}(\xi, x)$ has a significant influence to the final results of the degenerate scale.

References

[Brebbia et al. 1984] C. A. Brebbia, J. C. F. Telles, and L. C. Wrobel, *Boundary element techniques – theory and applications in engineering*, Springer, Heidelberg, 1984.

[Chen 2003] Y. Z. Chen, "Analysis of L-integral and theory of the derivative stress field in plane elasticity", *Int. J. Solids Struct.* **40** (2003), 3589–3602.

[Chen and Lin 2008] Y. Z. Chen and X. Y. Lin, "Regularity condition and numerical examination for degenerate scale problem of BIE for exterior problem of plane elasticity", *Eng. Anal. Bound. Elem.* **32** (2008), 811–823.

[Chen and Shen 2007] J. T. Chen and W. C. Shen, "Degenerate scale for multiply connected Laplace problems", *Mech. Res. Commun.* **34** (2007), 69–77.

[Chen et al. 2002] J. T. Chen, S. R. Kuo, and J. H. Lin, "Analytical study and numerical experiments for degenerate scale problems in the boundary element method of two-dimensional elasticity", *Int. J. Numer. Meth. Eng.* **54** (2002), 1669–1681.

[Chen et al. 2005] J. T. Chen, S. R. Lin, and K. H. Chen, "Degenerate Scale problem when solving Laplace's equation by BEM and its treatment", *Int. J. Numer. Meth. Eng.* **62** (2005), 233–261.

[Chen et al. 2009] Y. Z. Chen, X. Y. Lin, and Z. X. Wang, "Numerical solution for degenerate scale problem for exterior multiply connected region", *Eng. Anal. Bound. Elem.* **33** (2009), 1316–1321.

[Cheng and Cheng 2005] A. H. D. Cheng and D. S. Cheng, "Heritage and early history of the boundary element method", *Eng. Anal. Bound. Elem.* **29** (2005), 286–302.

[Cruse 1969] T. A. Cruse, "Numerical solutions in three-dimensional elastostatics", *Int. J. Solids Struct.* **5** (1969), 1259–1274.

[He et al. 1996] W. J. He, H. J. Ding, and H. C. Hu, "Degenerate scale and boundary element analysis of two dimensional potential and elasticity problems", *Comput. Struct.* **60** (1996), 155–158.

[Jaswon and Symm 1977] M. A. Jaswon and G. T. Symm, *Integral equation methods in potential theory and elastostatics*, Academic Press, London, 1977.

[Muskhelishvili 1953] N. I. Muskhelishvili, *Some basic problems of mathematical theory of elasticity*, Noordhoof, Amsterdam, 1953.

[Rizzo 1967] F. J. Rizzo, "An integral equation approach to boundary value problems in classical elastostatics", *Quart. J. Appl. Math.* **25** (1967), 83–95.

[Vodicka and Mantic 2008] R. Vodicka and V. Mantic, "On solvability of a boundary integral equation of the first kind for Dirichlet boundary value problems in plane elasticity", *Comput. Mech.* **41** (2008), 817–826.

Received 22 Sep 2009. Revised 15 Feb 2010. Accepted 28 Feb 2010.

Y. Z. CHEN: chens@ujs.edu.cn
Division of Engineering Mechanics, Jiangsu University, Xue Fu Road 301, Jiangsu 212013, China

X. Y. LIN: xiaoyun39527@yahoo.com
Division of Engineering Mechanics, Jiangsu University, Xue Fu Road 301, Jiangsu 212013, China

Z. X. WANG: wzx-5566@163.com
Division of Engineering Mechanics, Jiangsu University, Xue Fu Road 301, Jiangsu 212013, China

SUBMISSION GUIDELINES

ORIGINALITY

Authors may submit manuscripts in PDF format online at the Submissions page. Submission of a manuscript acknowledges that the manuscript is original and has neither previously, nor simultaneously, in whole or in part, been submitted elsewhere. Information regarding the preparation of manuscripts is provided below. Correspondence by email is requested for convenience and speed. For further information, write to one of the Chief Editors:

Davide Bigoni	bigoni@ing.unitn.it
Iwona Jasiuk	ijasiuk@me.concordia.ca
Yasuhide Shindo	shindo@material.tohoku.ac.jp

LANGUAGE

Manuscripts must be in English. A brief abstract of about 150 words or less must be included. The abstract should be self-contained and not make any reference to the bibliography. Also required are keywords and subject classification for the article, and, for each author, postal address, affiliation (if appropriate), and email address if available. A home-page URL is optional.

FORMAT

Authors can use their preferred manuscript-preparation software, including for example Microsoft Word or any variant of TEX. The journal itself is produced in LATEX, so accepted articles prepared using other software will be converted to LATEX at production time. Authors wishing to prepare their document in LATEX can follow the example file at www.jomms.org (but the use of other class files is acceptable). At submission time only a PDF file is required. After acceptance, authors must submit all source material (see especially Figures below).

REFERENCES

Bibliographical references should be complete, including article titles and page ranges. All references in the bibliography should be cited in the text. The use of BibTEX is preferred but not required. Tags will be converted to the house format (see a current issue for examples); however, for submission you may use the format of your choice. Links will be provided to all literature with known web locations; authors can supply their own links in addition to those provided by the editorial process.

FIGURES

Figures must be of publication quality. After acceptance, you will need to submit the original source files in vector format for all diagrams and graphs in your manuscript: vector EPS or vector PDF files are the most useful. (EPS stands for Encapsulated PostScript.)

Most drawing and graphing packages—Mathematica, Adobe Illustrator, Corel Draw, MATLAB, etc.—allow the user to save files in one of these formats. Make sure that what you're saving is vector graphics and not a bitmap. If you need help, please write to graphics@mathscipub.org with as many details as you can about how your graphics were generated.

Please also include the original data for any plots. This is particularly important if you are unable to save Excel-generated plots in vector format. Saving them as bitmaps is not useful; please send the Excel (.xls) spreadsheets instead. Bundle your figure files into a single archive (using zip, tar, rar or other format of your choice) and upload on the link you been given at acceptance time.

Each figure should be captioned and numbered so that it can float. Small figures occupying no more than three lines of vertical space can be kept in the text ("the curve looks like this:"). It is acceptable to submit a manuscript with all figures at the end, if their placement is specified in the text by means of comments such as "Place Figure 1 here". The same considerations apply to tables.

WHITE SPACE

Forced line breaks or page breaks should not be inserted in the document. There is no point in your trying to optimize line and page breaks in the original manuscript. The manuscript will be reformatted to use the journal's preferred fonts and layout.

PROOFS

Page proofs will be made available to authors (or to the designated corresponding author) at a Web site in PDF format. Failure to acknowledge the receipt of proofs or to return corrections within the requested deadline may cause publication to be postponed.

Journal of Mechanics of Materials and Structures
Volume 5, No. 4 April 2010

Mechanical behavior of silica nanoparticle-impregnated kevlar fabrics
ZHAOXU DONG, JAMES M. MANIMALA and C. T. SUN 529

A generalized plane strain meshless local Petrov–Galerkin method for the micromechanics of thermomechanical loading of composites
ISA AHMADI and MOHAMAD AGHDAM 549

Effective medium theories for wave propagation in two-dimensional random inhomogeneous media JIN-YEON KIM 567

A numerical model for masonry-like structures
MAURIZIO ANGELILLO, LUCA CARDAMONE and ANTONIO FORTUNATO 583

A coupled honeycomb composite sandwich bridge-vehicle interaction model
MIJIA YANG and A. T. PAPAGIANNAKIS 617

Spectral element approach to wave propagation in uncertain beam structures
V. AJITH and S. GOPALAKRISHNAN 637

Energy-minimizing openings around a fixed hole in an elastic plate
SHMUEL VIGDERGAUZ 661

Influence of different integral kernels on the solutions of boundary integral equations in plane elasticity Y. Z. CHEN, X. Y. LIN and Z. X. WANG 679